

**MAX-PLANCK-INSTITUT FÜR RADIOASTRONOMIE  
BONN**

**Studies of the Envelopes of Evolved  
Stars using Millimetre and  
Submillimetre Spectroscopy**

Dissertation  
zur  
Erlangung des Doktorgrades (Dr. rer. nat.)  
der  
Mathematisch-Naturwissenschaftlichen Fakultät  
der  
Rheinischen Friedrich-Wilhelms-Universität Bonn

von  
**Manali Hemant Jeste**  
aus  
Pune, Indien

Bonn, 2024

Angefertigt mit Genehmigung der Mathematisch-Naturwissenschaftlichen Fakultät der Rheinischen  
Friedrich-Wilhelms-Universität Bonn

Gutachter/Betreuer: Prof. Dr. Karl M. Menten  
Gutachter: Prof. Dr. Pavel Kroupa  
Tag der Promotion: 30.04.2025  
Erscheinungsjahr: 2025

RHEINISCHE FRIEDRICH–WILHELMS–UNIVERSITÄT BONN

## *Abstract*

by Manali Hemant Jeste

for the degree of

*Doctor rerum naturalium*

Asymptotic giant branch (AGB) stars are low- to intermediate-mass stars at the end of their life. At this stage of the stellar evolution, these objects shed large amounts of matter in the form of gas and dust, forming a circumstellar envelope (CSE) around them and enriching the interstellar medium (ISM). At optical wavelengths, such CSEs had largely remained unexplored as the opacity of the circumstellar material blocks emissions from such wavelengths from passing through. However, advancements in observing facilities in the millimetre and sub-millimetre wavelength regime have allowed us to gain a deeper understanding of the physical and chemical processes that take place in these envelopes.

This thesis focuses on probing the envelopes using carbon-bearing species, the C atom, and various molecules, with observations from different single dish telescopes. We use the rotational lines of the HCN molecule arising from its ground and vibrationally excited states to study sixteen carbon-rich AGB stars. Our study provided us with constraints on the excitation temperature and column density using optically thin vibrationally excited HCN lines. We find that these lines originate in the innermost parts of the envelope and thus can be used as tools to probe its hotter regions. We also discover 23 new HCN masers, increasing the total number of known HCN masers towards carbon-rich AGB stars by a factor of almost five. Studies in these transitions of HCN had been sparse before and thus our work contributes significantly to exploring these inner regions of the envelope. Moving further away from the star, the outer parts of the envelope are exposed to the interstellar radiation field and drive the photo-chemistry in these regions. We use the fine-structure lines of atomic and ionised carbon ( $C^0$  and  $C^+$ ) to probe this region of the envelope of IRC +10216. This is an archetypal carbon-rich AGB star and provides an opportunity for a detailed study, as its CSE hosts a plethora of molecular species and it is located close to us. Our study places the distribution of  $C^0$  in a shell-like form in the envelope and constrains its location using sophisticated radiative transfer modelling. Additionally, the absence of detectable [C II] emission beyond a certain distance suggests that  $C^0$  is distributed between CO and  $C^+$ , which is expected for an external far-ultraviolet radiation field.

Finally, for a comprehensive view of AGB stars as a population, we analysed 445 stars as part of the Nearby Evolved Stars Survey (NESS) collaboration. We observed transitions of the CO molecule (the main tracer of molecular gas) from multiple rotational states and derived mass-loss rates (MLRs) using an empirical formula. Based on these estimates, we infer that stars with higher MLRs produce dust more efficiently, confirming earlier theoretical speculations. The statistical distributions of the inferred physical parameters are discussed further, dividing the whole stellar sample into the three chemical types, namely, oxygen-rich, carbon-rich, and objects with similar abundance of O and C. These findings demonstrate how the statistical analysis of a stellar population can confirm and extend our understanding of its contribution to the cosmic cycle of matter.



---

# List of publications

---

## Publications related to this thesis

The research work presented in this thesis comprises of two peer-reviewed first-author publications, along with an additional manuscript that is prepared for submission. They are listed below:

1. NESS IV: Initial results from single-dish CO observations

**Jeste, M.** et al. *to be submitted*

*Contributions:* Acquired the data, performed data reduction and analysis, interpreted results, and wrote the manuscript. Co-authors helped with the analysis code, supervised the project, and helped with the manuscript.

2. [C I] and [C II] emission in the circumstellar envelope of IRC +10216.

I. Observational data and NLTE modelling of the [C I] emission

**Jeste, M.;** Wiesemeyer, H.; Menten, K. M.; Wyrowski, F.; 2023, *A&A*, 675, A139

DOI: [10.1051/0004-6361/202346034](https://doi.org/10.1051/0004-6361/202346034)

*Contributions:* Acquired the data, performed data reduction and analysis, interpreted results, and wrote the manuscript. Co-authors helped with the interpretation, supervised the project, and helped with the manuscript.

3. Vibrationally excited HCN transitions in circumstellar envelopes of carbon-rich AGB stars

**Jeste, Manali;** Gong, Yan; Wong, Ka Tat; Menten, Karl M.; Kamiński, Tomasz; Wyrowski, Friedrich; 2022, *A&A*, 666, A69

DOI: [10.1051/0004-6361/202243365](https://doi.org/10.1051/0004-6361/202243365)

*Contributions:* Acquired the data, performed data reduction and analysis, interpreted results, and wrote the manuscript. Co-authors helped with the interpretation, supervised the project, and helped with the manuscript.

## Other relevant publications

Below is a list of publications, to which I have contributed as a member of ATOMIUM and NESS collaborations.

1. ATOMIUM: Molecular inventory of 17 oxygen-rich evolved stars observed with ALMA  
[Wallström, S. et al 2024, A&A, 681, A50](#)  
DOI: [10.1051/0004-6361/202347632](#)  
*Contributions:* Provided with estimates of some parameters required from the single-dish data and commented on the manuscript.
2. The Nearby Evolved Stars Survey II: Constructing a volume-limited sample and first results from the James Clerk Maxwell Telescope  
[Scicluna, P. et al 2022, MNRAS, 512, 1091](#)  
DOI: [10.1093/mnras/stab2860](#)  
*Contributions:* Acquired single-dish telescope data as part of the collaboration which resulted in discussions for the publication and commented on the manuscript.
3. ATOMIUM: ALMA tracing the origins of molecules in dust forming oxygen rich M-type stars. Motivation, sample, calibration, and initial results  
[Gottlieb, C. A. et al 2022, A&A, 660, A94](#)  
DOI: [10.1051/0004-6361/202140431](#)  
*Contributions:* Conducted data reduction of the single-dish data as part of the collaboration and commented on the manuscript.

---

# Contents

---

<b>1</b>	<b>Introduction</b>	<b>1</b>
1.1	Evolution of a star . . . . .	1
1.1.1	Historical background . . . . .	1
1.1.2	A star's main sequence phase . . . . .	2
1.1.3	A star's post-main sequence phase . . . . .	4
1.1.4	Stellar life on the asymptotic giant branch phase . . . . .	5
1.1.5	Stellar life after the AGB phase . . . . .	6
1.2	Circumstellar envelopes . . . . .	7
1.3	The quintessential AGB star: IRC +10216 . . . . .	9
1.4	Radio Astronomy . . . . .	10
1.4.1	Telescope properties . . . . .	11
1.4.2	Telescopes used in this thesis . . . . .	14
1.5	Fundamentals of radiation and the radiative transfer of spectral lines . . . . .	18
1.5.1	Basic definitions . . . . .	18
1.5.2	Radiative transfer . . . . .	19
1.6	Atoms and molecules in the CSEs . . . . .	22
1.6.1	Thermal emissions . . . . .	22
1.6.2	Masers . . . . .	25
1.7	Radiative transfer analysis: RATRAN . . . . .	30
1.8	Outline of the thesis . . . . .	30
<b>2</b>	<b>Vibrationally excited HCN transitions in circumstellar envelopes of carbon-rich AGB stars</b>	<b>33</b>
2.1	Introduction . . . . .	33
2.2	Methods . . . . .	33
2.3	Results . . . . .	34
2.3.1	Our findings . . . . .	34
2.3.2	Population diagram analysis . . . . .	35
2.3.3	HCN masers . . . . .	35
2.4	Conclusions . . . . .	36
<b>3</b>	<b>[C I] and [C II] emission in the circumstellar envelope of IRC +10216</b>	<b>37</b>
3.1	Context . . . . .	37
3.2	Methods . . . . .	38
3.3	Results . . . . .	38
3.4	Conclusions . . . . .	40

<b>4</b>	<b>The Nearby Evolved Stars Survey: NESS</b>	<b>43</b>
4.1	Introduction . . . . .	43
4.2	Aims of the survey . . . . .	44
4.3	Sample selection . . . . .	46
4.4	Observations . . . . .	47
4.5	Summary of results . . . . .	47
<b>5</b>	<b>NESS: Initial results from single dish multi-<i>J</i> CO observations</b>	<b>49</b>
5.1	Introduction . . . . .	49
5.1.1	General background . . . . .	49
5.1.2	The Sample of NESS sources . . . . .	50
5.2	Observations and data reduction . . . . .	50
5.2.1	APEX observations . . . . .	50
5.2.2	IRAM-30m observations . . . . .	51
5.2.3	JCMT observations . . . . .	52
5.2.4	SEST and OSO observations . . . . .	52
5.2.5	Data reduction . . . . .	52
5.3	Data analysis . . . . .	52
5.4	Results and discussion of line-shape parameters . . . . .	56
5.4.1	APEX observations . . . . .	57
5.4.2	IRAM observations . . . . .	57
5.4.3	SEST and OSO observations . . . . .	59
5.5	Discussion . . . . .	59
5.5.1	Distributions of mass-loss rates and expansion velocities . . . . .	59
5.5.2	Correlation analysis . . . . .	60
5.6	Conclusions . . . . .	62
<b>6</b>	<b>Conclusions and Outlook</b>	<b>67</b>
<b>A</b>	<b>NESS: Tables presenting results of the soft-parabola line fitting procedure</b>	<b>71</b>
<b>B</b>	<b>NESS: Figures presenting soft-parabola line fitting of the spectra</b>	<b>97</b>
<b>C</b>	<b>Paper I: Vibrationally excited HCN transitions in circumstellar envelopes of carbon-rich AGB stars</b>	<b>137</b>
<b>D</b>	<b>Paper II: [C I] and [C II] emission in the circumstellar envelope of IRC +10216</b>	<b>175</b>
	<b>I. Observational data and NLTE modelling of the [C I] emission</b>	<b>175</b>
	<b>Bibliography</b>	<b>185</b>
	<b>List of Figures</b>	<b>195</b>
	<b>List of Tables</b>	<b>199</b>
	<b>Acknowledgements</b>	<b>201</b>

---

# Nomenclature

---

## Astronomical constants

$M_{\odot}$	solar mass	$1.989 \times 10^{30}$ kg
$R_{\odot}$	solar radius	$6.957 \times 10^8$ m
$L_{\odot}$	solar luminosity	$3.846 \times 10^{26}$ W
pc	parsec	$3.0857 \times 10^{16}$ m
AU	Astronomical Unit	$1.496 \times 10^{11}$ m

## Physical constants

$k$	Boltzmann's constant	$1.381 \times 10^{-23}$ J K <sup>-1</sup>
$h$	Planck's constant	$6.626 \times 10^{-34}$ J Hz <sup>-1</sup>
$c$	speed of light	$2.9979 \times 10^8$ m sec <sup>-1</sup>
$\sigma$	Stefan-Boltzmann constant	$5.67 \times 10^{-8}$ W m <sup>-2</sup> K <sup>-4</sup>

## Frequently used symbols

yr	year
$\nu$	frequency
$\lambda$	wavelength
$J$	orbital angular momentum
$\tau$	optical depth
$R_*$	stellar radius
$S_{\nu}$	flux density
$\Omega$	solid angle
dB	decibel
$T_{\text{ex}}$	excitation temperature
$N$ or $N_{\text{tot}}$	column density
$\theta$	angle



---

# Introduction

---

*General references: Habing and Olofsson (2003), Kippenhahn et al. (2013) and Karakas and Lattanzio (2014)*

## 1.1 Evolution of a star

### 1.1.1 Historical background

The first attempts to describe the interior of stars date back to the end of the 19th century. In 1870, Jonathan H. Lane formulated a differential equation for the hydrostatic equilibrium between the thermal pressure and the self-gravity of a star. Around the same time, Lord Kelvin and Hermann von Helmholtz formulated the time the Sun would take to radiate all its gravitational energy. However, their calculations revealed that the Sun would have been younger than the geological estimates of the age of the Earth. The advancements in physics and astronomical spectroscopy at the turn of the century aided in solving this puzzle. In 1900, Max Planck published his law of blackbody radiation. His discovery was preceded by various empirical findings and approximations, such as Wien's displacement law, which states that the wavelength at the maximum of a blackbody spectral energy distribution,  $\lambda_{\max}$ , and the temperature are inversely related as  $\lambda_{\max} [\mu\text{m}] = 2898/T [\text{K}]$ . In addition, the Stefan-Boltzmann law relates the temperature to the radiated total power (luminosity  $L$ ), that is, determined by defining an effective photospheric temperature,  $T_{\text{eff}}$ , of a blackbody as  $L_* = 4\pi R_*^2 \sigma T_{\text{eff}}^4$ , where  $R_*$  is the radius of the star. Thus, correlations describing the stars can be made between the state variables, such as luminosity, mass, radius, and temperature. With the availability of a meaningful sample of stars with known distances and spectral types, it became possible to empirically establish these correlations and subsequently compare them with theoretical predictions.

In 1911 Ejnar Hertzsprung and in 1914 Henry N. Russell represented the absolute brightness or luminosity of stars of known distance against their spectral types or colours. The correlation between the stellar luminosity and effective photospheric temperature (determined by the Stefan-Boltzmann law) is demonstrated by the main sequence of the Hertzsprung-Russell (HR) diagram, on which stars spend most of their lifetime (> 90%). For stars that are at least as massive as the Sun, one can approximate the underlying relation by  $L/L_{\odot} \approx (T/T_{\odot})^{5.9}$ , showing that a small increase in temperature results in a significant increase in luminosity<sup>1</sup>. These empirical findings and how young

---

<sup>1</sup> As a caveat, one should note that this approximative description of the main sequence holds only for a given metallicity and

stars find their location on the main sequence were only understood later; yet the foundations of star formation were laid as early as 1902 when Sir James Jeans formulated his criterion for the stability of a self-gravitating gas cloud. Additionally, the conundrum of the too-short Kelvin-Helmholtz time scale of the Sun was solved in 1920 when Arthur S. Eddington suggested the mass difference between four hydrogen atoms and a helium atom as the principal source of energy of the Sun. He also hypothesised that elements are synthesised in stellar interiors. The detailed theory of hydrogen burning was later established by Hans Bethe and, independently, by Carl Friedrich von Weizsäcker. An extensive account of these and later developments is given in the review by Burbidge et al. (1957, further references therein), including the nucleosynthesis of elements beyond the main sequence.

Fig. 1.1 shows a simplified version of the HR diagram, plotting luminosity versus effective surface temperature and depicting the various phases of stellar evolution. In the following sub-sections, we will go through the different stages of stellar evolution, from the main sequence to its end, with a focus on the later stages due to their relevance to this thesis.

### 1.1.2 A star's main sequence phase

As mentioned above, stars spend most of their life in the main-sequence (MS) stage, where hydrogen burning takes place in their core to fuse into helium. The initial stage of a star on the main sequence, when the core hydrogen starts burning, is referred to as the zero-age main sequence. The rate of nuclear fusion and the amount of material available for burning depend on the mass of the star. It is an important determinant of the star's fate. Once the hydrogen is converted to helium in the core, the star leaves the MS and forms a hydrogen burning shell around the core.

Fig. 1.2 presents a simplistic version of the HR diagram, which focuses on the evolution of a low-mass star. As seen for the MS phase, the star appears to not go through any substantial change, except for its chemical composition, which for a star of super-solar mass entails a shift of its locus in the HR diagram away from the zero-age MS. The next phases are more dynamic and take place on short timescales, as will be discussed later in the following sub-sections.

MS stars are in a state of hydrostatic equilibrium, where the inward gravitational force is balanced by the force due to pressure gradients acting outwards. In the case of a massive star, the gravitational pull acting inwards would be greater, heating the opaque gas and thus increasing the thermal pressure. In addition to the enhanced gas pressure, the higher temperature in the core accelerates the nuclear fusion reaction rate, releasing more energy. As a result, the stellar interior will adjust to a new equilibrium. With increasing stellar mass, the radiation pressure becomes important. While it plays no role in the solar core, in the most massive stars it exceeds the thermal pressure (where the ratio between both pressures scales with approximately  $M_*^2$ ) until a stable configuration is not possible anymore (due to the Eddington mass limit).

The enhanced nuclear fusion rate leads to massive stars having much shorter lifetimes since they use up the material much faster compared to their lower-mass counterparts. A typical  $1 M_\odot$  star, like the Sun, will spend about  $10^{10}$  years in the MS phase, whereas a  $10 M_\odot$  star will have a life span of about  $2 \times 10^7$  years in this phase<sup>2</sup>.

---

under exclusion of fully convective stars. It results from the combination of exact laws (Planck's law and its implications) and empirical relations fitted to the state variables obtained from stellar models or eclipsing spectroscopic binaries (for further discussion see e.g., Eker et al., 2018; Serenelli et al., 2021; Eker et al., 2024).

<sup>2</sup> [https://www.atnf.csiro.au/outreach/education/senior/astrophysics/stellarevolution\\_mainsequence.html#mslifespan](https://www.atnf.csiro.au/outreach/education/senior/astrophysics/stellarevolution_mainsequence.html#mslifespan)

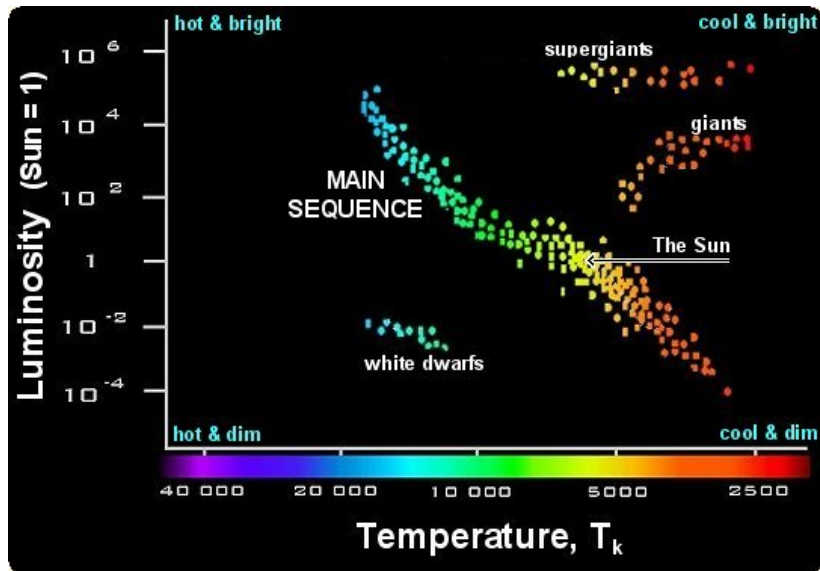


Figure 1.1: A simplified Hertzsprung-Russell (HR) diagram with surface temperature (in Kelvin) on the X-axis and luminosity (in solar units) on the Y-axis. Credit: Western Washington University ([https://astro101.wvu.edu/a101\\_hrdiagram.html](https://astro101.wvu.edu/a101_hrdiagram.html)).

The process through which the fusion reaction takes place varies with the stellar mass as well. Low-mass stars go through the proton-proton (pp-) chain reaction, where two hydrogen nuclei first form a deuteron followed by a proton capture forming  ${}^3\text{He}$ . For the subsequent production of  ${}^4\text{He}$  the most important path (out of three) yields a  ${}^4\text{He}$  nucleus (and two protons) from the reaction of two  ${}^3\text{He}$  nuclei. This is the most important nuclear reaction to convert hydrogen to helium in stars with masses below  $1.5 M_{\odot}$ ; side chains are less likely to occur.

Stars with masses higher than  $1.5 M_{\odot}$  produce their energy via the carbon-nitrogen-oxygen (CNO) cycle. In this process, a proton and  ${}^{12}\text{C}$  react to form  ${}^{13}\text{N}$ , an isotope of nitrogen that is unstable and undergoes  $\beta^+$  decay to form  ${}^{13}\text{C}$ . The latter reacts with another proton to form the stable main isotope of nitrogen,  ${}^{14}\text{N}$ , followed by another proton capture forming  ${}^{15}\text{O}$  which decays to  ${}^{15}\text{N}$ . The final reaction continues with a proton forming an  $\alpha$  particle and restoring the  ${}^{12}\text{C}$  nucleus that started the cycle. In summary, this process ultimately fuses four hydrogen nuclei (i.e., protons) to one helium nucleus (the resulting  $\alpha$  particle), while the  ${}^{12}\text{C}$  nucleus acts as a catalyst for the next CNO cycle. Likewise, if the cycle had started with the  ${}^{14}\text{N}$  nucleus, it would have acted as a catalyst. Less important variants of this cycle also involve  ${}^{16}\text{O}$ . We note that the Sun drives a CNO cycle as well but it contributes only  $\sim 1\%$  to its energy production (Borexino Collaboration et al., 2020).

Regardless of the type of process, the MS phase comes to an end when the hydrogen in the core is depleted and converted to helium. With regards to our star, the Sun is currently still burning hydrogen in its stellar core. The pp-chain is fairly slow at the temperature of the Sun's core ( $\sim 15 \times 10^6$  K) and efficient only owing to the sheer number of protons. For the Sun, the resulting nuclear time scale is  $\tau_N \sim 10$  Gyr; the star has been on the MS for 4.6 Gyr (meteoritic age, Desch et al., 2023). For comparison, it took the Sun only  $\sim 40$  Myr to move from the pre-MS T Tauri phase to the MS (Guenther, 1989).

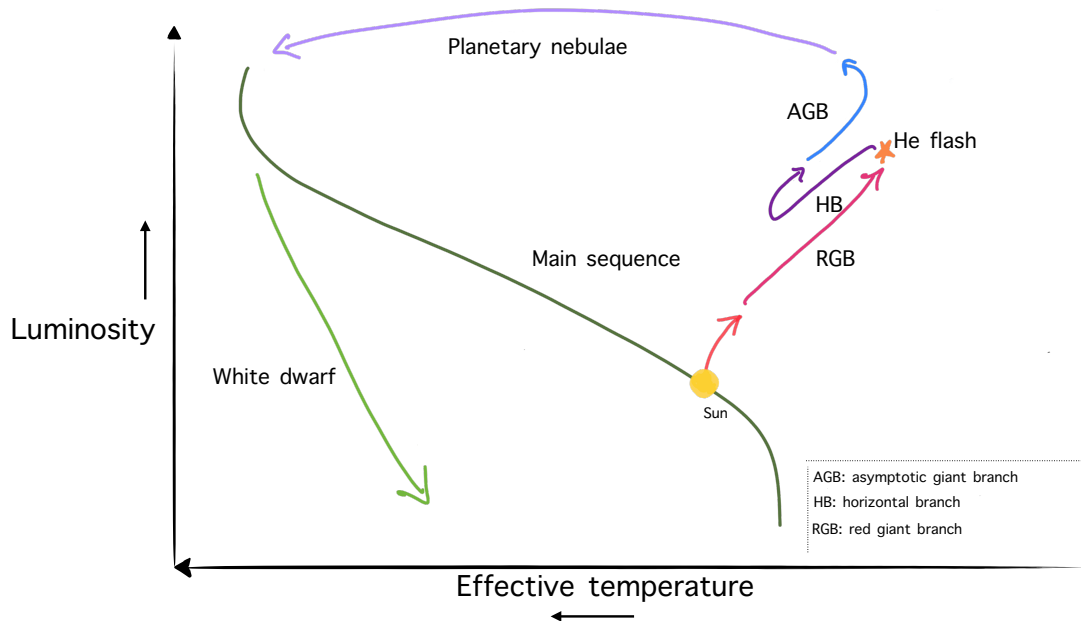


Figure 1.2: A sketch presenting a simplified version of the HR diagram. The figure shows the evolutionary path for a solar-mass star marked with its important phases. The Sun's current position is also illustrated on the HR diagram as a reference (Created based on [https://www.astro.uu.se/deathstar/agn\\_stars.html](https://www.astro.uu.se/deathstar/agn_stars.html)).

### 1.1.3 A star's post-main sequence phase

After the core hydrogen burning phase, stellar evolution proceeds through different mass-dependent processes. Low-mass stars ( $0.8\text{--}2 M_{\odot}$ ) have a degenerate helium core after the MS phase. Stars with intermediate masses ( $\approx 2\text{--}8 M_{\odot}$ ) have a non-degenerate helium core. Both eventually convert to a carbon-oxygen core, but intermediate-mass stars do so more gently owing to the non-degenerate conditions. At the end of their life, stars from both groups shed their material due to stellar winds and become compact white dwarfs, consisting of an electron-degenerate carbon-oxygen (C-O) mixture. On the other hand, high-mass stars ( $> 8 M_{\odot}$ ) burn carbon in their non-degenerate cores due to their higher temperatures and masses. High-mass stars also undergo burning phases for heavier elements such as oxygen. Since this thesis deals with low- and intermediate-mass stars, hereafter the focus of our discussion will be on the evolution of these stars. Their post-main-sequence evolutionary path is shown in Fig. 1.2.

As discussed earlier, stars are in balance with the gravitational pull and the pressure gradient acting outwards. When a star runs out of hydrogen fuel in its core, it leaves the MS. In low-mass stars, fusion ceases in the core, leading to a reduced pressure. As a result, gravitational forces start to dominate, causing the helium core to contract. The contraction increases the temperature igniting the hydrogen shell present around the core and releases more energy. The increase in radiation and thermal pressure subsequently causes the outer layers of the star to expand and cool, making the star much larger and thus more luminous. At this stage, the gravitational pull is quite weak and hence it is easier for the outer layers of the star to be expelled. This stage is known as the *red giant phase*. Stars on the red

giant branch have a convective envelope with a hydrogen-burning shell inside it. When the convective layer mixes with the products of the nucleosynthesis elements that are produced in the MS phase, the products are brought up to the outer layer through convection. This process is called the *first dredge-up*.

The hydrogen shell burning provides additional helium to the core of the star, which increases the mass and temperature in the core. When the temperature reaches  $10^8$  K, the kinetic energy becomes sufficient to initiate the fusion of helium, where two  $^4\text{He}$  nuclei (or  $\alpha$ -particles) fuse together to form beryllium ( $^8\text{Be}$ ). When the unstable  $^8\text{Be}$  is hit with a third  $^4\text{He}$  nuclei,  $^{12}\text{C}$  is formed. This process is referred to as the *triple-alpha process* or helium fusion reaction. For low-mass stars, the degenerate nature of the core leads to a sudden burst of helium fusion known as a *helium flash*, lasting for at most a few minutes (in intermediate and high-mass stars, helium burning ignites more gently, due to the non-degenerate conditions in the core).

The initial and subsequent helium flashes increase the temperature in the core causing it to progressively become non-degenerate and to expand under the thermal pressure, resulting in quiescent helium burning. As a result, the star heats up but the envelope shrinks, thus maintaining a similar luminosity. At this stage, the star moves to the *horizontal branch* of the HR diagram, where the helium-burning core is surrounded by a hydrogen-burning shell, but where the star as a whole is unstable.

#### 1.1.4 Stellar life on the asymptotic giant branch phase

*References: Vassiliadis and Wood (1993), Karakas and Lattanzio (2007) and Höfner and Olofsson (2018)*

The asymptotic giant branch (AGB) phase is an important stage in the evolution of a star as it produces essential elements that enrich the universe. The helium fusion in the core leads to the formation of a carbon-oxygen core. Once the helium in the centre is exhausted, the core starts to contract. For further fusion to occur in the core, the star needs a temperature higher than  $10^8$  K, which is not possible for low- to intermediate-mass stars. The contraction of the core releases enough energy to ignite the surrounding helium produced by the hydrogen-burning shell. As a result, the star has two shells driving fusion reactions, a helium-burning shell and a hydrogen-burning shell surrounding it (see Fig. 1.3 for an illustration). The ignition of the former defines the start of the AGB phase of the star, where the evolution in the HR diagram follows a path that is asymptotically located above the red giant branch (see Fig. 1.2).

For intermediate-mass stars, the so-called double-mirror principle takes place during this phase, where the core contracts with an expanding helium shell and a contracting hydrogen shell. As the helium shell expands, it reduces the temperature in the hydrogen shell until the burning stops. The constant expansion and cooling of layers lead to the process of the *second dredge-up* when the convective layer reaches the helium-rich region of the centre. The dredged-up material – mainly helium – is mixed with the outer convective layer and brought up to the surface. In low-mass stars, the hydrogen shell burning prevents the second dredge-up from taking place.

During the second dredge-up, hydrogen makes contact with the helium-burning shell, which heats up the hydrogen until the hydrogen-burning shell is re-ignited. With time, the helium-burning shell becomes thin making it difficult to maintain nuclear burning and thus becomes thermally unstable. The hydrogen-burning shell also adds mass to the region between the two burning shells called the

intershell region. Over time, the increase in pressure and temperature at the bottom of the intershell region (or above the helium-burning shell) leads to the ignition of the helium shell in a thermonuclear runaway called the *helium shell flash* or thermal pulse (TP).

The rapid release of energy due to the helium shell flash expands the intershell region. As the helium shell starts to expand and cool, it extinguishes the hydrogen shell again. The expansion and cooling of the intershell region facilitate the process of convection to take place. The intershell material is mixed with the outer layers as they penetrate through the hydrogen shell. Consequently, products from helium burning (mostly  $^{12}\text{C}$ ) are brought up to the surface, which indicates that the star has undergone the *third dredge-up* process.

After this, the hydrogen shell is re-ignited and the helium shell is extinguished. The hydrogen burning becomes stable for some time, which then leads to an increase of mass in the intershell region and re-ignition of the helium shell, and the TP is generated again. This process repeats various times and the stars enter the TP-AGB phase. The cycle time  $\tau_p$  between successive pulses decreases with increasing mass of the degenerate C-O core (Kippenhahn et al., 2013). For a core with  $0.5 M_{\odot}$ ,  $\tau_p$  would last for about  $10^5$  years and for a  $1.4 M_{\odot}$  core  $\sim 10$  years. The total number of thermal pulses on the AGB varies between six for a star of initial solar mass, and 200 for an  $8 M_{\odot}$  star (Rees et al., 2024).

The third dredge-up is crucial for the enrichment of the interstellar medium (ISM) as it brings fresh nucleosynthesis products (mainly carbon, but also heavier elements produced by slow neutron capture) from the interior of AGB stars to their surface. AGB stars start as M-type stars ( $C/O \approx 0.5$  in the solar neighbourhood) in the initial phase, but the third dredge-up changes the ratio to  $C/O$  to values  $> 1$ , forming a carbon-rich AGB star. This formation is limited by the initial mass of the AGB star through the process of *hot-bottom-burning* (HBB). For stars with mass above  $4 M_{\odot}$ , the convective envelope extends down to the hydrogen-burning shell where the high temperature drives the proton capture reaction to convert  $^{13}\text{C}$  (from the CNO cycle) into  $^{14}\text{N}$ . This process prevents the formation of a carbon star (or carbon-rich star), causing relatively massive AGB stars to remain oxygen-rich with  $C/O < 1$ . For initial masses below  $1.5 M_{\odot}$ , the stellar core has not grown enough when the first thermal pulse occurs, inhibiting the third dredge-up. When the elemental abundances of carbon and oxygen are similar,  $C/O \sim 1$ , the stars are classified as S-type stars. In brief, AGB stars are initially oxygen-rich objects (with spectral type M), and later, when the initial mass ranges from  $1.5\text{--}4 M_{\odot}$ , they become carbon-rich via the triple- $\alpha$  process. The exact mass range depends on metallicity, where metallicity is the measurement of the abundance of elements heavier than hydrogen and helium (Decin, 2021).

### 1.1.5 Stellar life after the AGB phase

*General reference: Habing and Olofsson (2003)*

When a star is on the AGB, it has high luminosity and low effective temperature with a large radius. These properties enable the star to shed its stellar material into the atmosphere due to its low surface gravity. The ejected material forms an envelope around the star called the circumstellar envelope (CSE), which is composed of gas and dust condensing out of the gaseous material. This envelope is rich in molecular species and plays a crucial role in enriching the ISM with its constituents. The mechanisms and properties of the envelope will be discussed in Sect. 1.2.

As soon as the continuous mass loss has depleted the stellar envelope to the point where its mass falls below that of the core, the star leaves the AGB path on the evolutionary track. When the star's envelope mass reaches  $\sim 1\%$  of its core mass, it starts to shrink under the gravitational pull by its core,

but its luminosity remains constant because the effective temperature ( $T_{\text{eff}}$ ) increases. The evolution of the star, therefore, follows a horizontal line on the HR diagram towards higher  $T_{\text{eff}}$ , lasting up to  $\sim 10^4$  years (depending on the initial stellar mass and metallicity). Photons from the stellar core are scattered by the remainder of the envelope which in visible light starts to appear as a faint nebulosity (protoplanetary nebula). When the temperature reaches about 30,000 K, the ultraviolet (UV) radiation from the star ionises the expanding circumstellar material, forming a planetary nebula (PN) appearing in a wealth of atomic emission lines. It has recently been revealed that the morphologies seen in the stellar winds have counterparts in the observed planetary nebulae (PNe), implying that the mechanisms responsible for shaping both are similar (Decin et al., 2020; Decin, 2021). As the mass of the envelope decreases ( $10^{-5} M_{\odot}$ ), all the fusion processes cease, leaving a degenerate carbon-oxygen core at the centre. At this stage, the object cools off as a white dwarf with very low luminosity.

## 1.2 Circumstellar envelopes

*General Reference: Habing and Olofsson (2003)*

AGB stars are known to exhibit heavy mass loss in the form of gas and dust. This is one of the most distinguishing properties of these objects. The mass that is shed forms a circumstellar envelope around the star. This process is largely driven by the radiation pressure on the dust grains and the stellar pulsations. Empirically, the efficiency at which this material is being lost, known as the mass-loss rate (MLR), was shown to increase with the duration  $P$  of a single pulsation period. This trend, however, is implicitly related to the parameters of the star. The pulsation of AGB stars in the fundamental mode (i.e., long-period variable stars like Mira) is related to their radius  $R_*$  and mass  $M_*$  through  $P = QR_*^{3/2} M_*^{-1/2}$  ( $Q$  being the pulsational constant), to first order. Comparisons with empirically deduced relations need to account for the decrease of  $M_*$  through heavy mass loss in the later evolutionary stages at the tip of the AGB. Stellar pulsations create shocks and push the gaseous material towards a larger radius, also increasing the density in the atmosphere. Habing and Olofsson (2003) report that an MLR of up to  $10^{-4} M_{\odot} \text{ yr}^{-1}$  can be measured from the winds of these objects. Consequently, the atmospheres of such stars are enshrouded with dust and gas, making them difficult to observe at optical or even near-infrared wavelengths. Thus, telescopes operating at longer wavelengths, in the millimetre and sub-millimetre regimes, are useful tools for studying the physical and chemical properties of these regions. More on this will be discussed in Sect. 1.4. Generally, the MLR ranges from  $10^{-9}$  to  $10^{-4} M_{\odot} \text{ yr}^{-1}$  with expansion velocities  $V_{\text{exp}}$  (that is, the terminal velocities of the stellar winds) between 3 and 30  $\text{km s}^{-1}$ . This large range of velocities is also explicitly dependent on the chemical composition of the star (Höfner and Olofsson, 2018), which in turn probes its evolution on the AGB.

At a radius of about  $1-2 R_*$ , the temperature in the atmosphere is low enough to allow the dust particles to condense out of the gas. At this particular stage of the evolution of the AGB star, the luminosity is also high, which helps accelerate the dust particles through radiation pressure creating a wind. Dust comprises  $\sim 1\%$  of the total mass in the CSE but it is one of the major drivers for high mass-loss in stars. The strongly bound CO molecule is one of the first molecules to be formed and the element that is left and is not locked in to form CO condenses to form dust. By studying the composition of the dust, we can get an insight into the physical and chemical processes in the stellar envelope and additionally, the chemical composition of the central star. Depending on the chemistry of the star, we also find typical dust species in abundance. For example, oxygen-rich CSEs (O-CSEs)

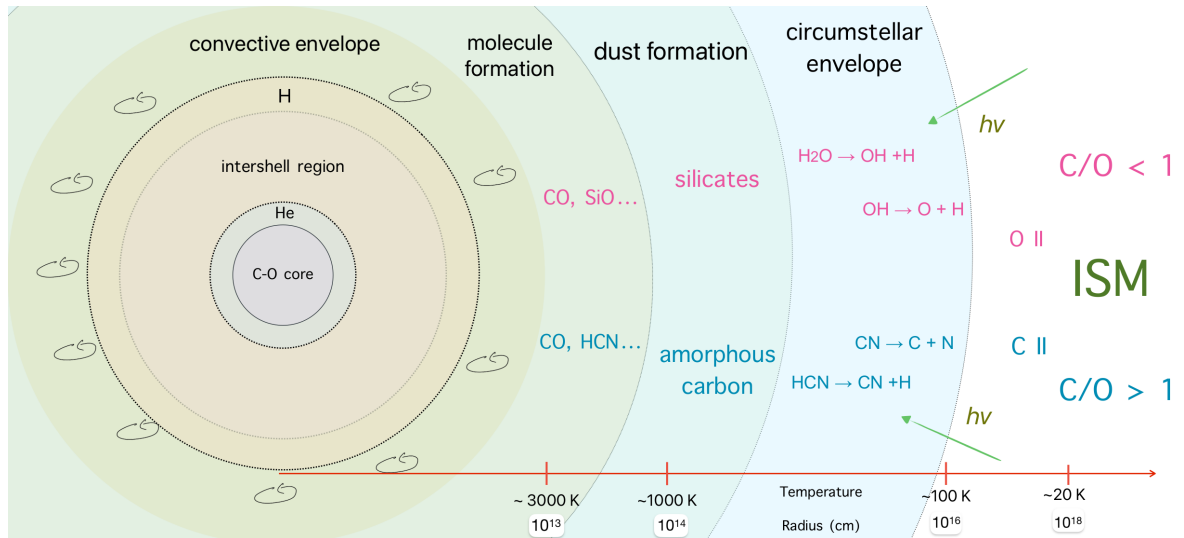


Figure 1.3: A schematic diagram of an AGB star and the composition of its CSE (Created based on Soria-Ruiz 2006; Höfner and Olofsson 2018).

mainly form amorphous silicates and carbon-rich CSEs (C-CSEs) amorphous carbon (Habing and Olofsson, 2003).

The CSE is divided into multiple regions (see Fig. 1.3) which are explained as follows:

- *Molecule formation zone:* The molecule formation zone is located after the convective envelope, where molecules form under LTE conditions ( $\sim 3000 - 1500$  K). These are often referred to as the parent molecules from which daughter species are formed in the outer parts of the envelope and are responsible for influencing the chemical type of the star.
- *Dust formation zone:* In this region, dust condensation occurs along with grain growth and wind acceleration. The radiation pressure from the star acts on the dust grains pushing the gas and the wind starts to accelerate here. The temperatures in the dust formation zone range from  $\sim 1500 - 500$  K.
- *Outer envelope:* In the outer parts of the envelope the wind expands at a constant velocity. Processes such as photodissociation and ion-neutral reactions occur in this region. The temperature in these parts of the envelope falls below 500 K.
- *Interaction with the ISM:* Beyond the outer parts of the CSE, the region is interacting with the ISM and forming a bow shock (see Sahai and Chronopoulos (2010) for the case of IRC +10216).

To fully understand the origin of individual molecules or atomic species in the CSEs and to use them as probes for the physical conditions in their environment, excitation analyses of the observed transitions are conducted. Other parameters, such as the expansion velocity of the gas, are inferred by modelling the spectra and comparing them to the observations. While for line profiles of emissions from CO one can use semi-empirical expressions (see Chapter 5), for other species radiative transfer calculations (explained in Sect. 1.7) are required and demonstrated, for the fine-structure line emissions from atomic carbon, in Chapter 3 and Appendix D.

### 1.3 The quintessential AGB star: IRC +10216

IRC +10216 or CW Leonis is an archetypal carbon-rich AGB star, known for being the brightest object at  $5\ \mu\text{m}$  outside the solar system at the time of its discovery (Becklin et al., 1969). Since then, it has been subjected to a tremendous amount of deep studies. One of the key features of the star is its high mass-loss rate of  $2\text{--}4 \times 10^{-5}\ M_{\odot}\ \text{yr}^{-1}$  (Crosas and Menten, 1997; De Beck and Olofsson, 2018; Fonfría et al., 2022) and its proximity to us (120–140 pc, Crosas and Menten 1997; Groenewegen et al. 2012). This makes the star an exceptional object for a wide range of observational studies across various wavelengths, facilitating an opportunity to constrain different parameters.

Menten et al. (2012) studied the star’s photosphere in the radio regime using Very Large Array at 7 mm wavelength. Their study adopted a distance of 130 pc and accurately determined the radio brightness temperature of the star to be 1660 K, the radio-emitting size to be 80 mas, and the average stellar luminosity to be  $8640\ L_{\odot}$ .

Richichi et al. (2003) used lunar occultations in the  $H$  and  $K$  bands to measure the near-infrared diameter as 7.1 AU. The star has also been extensively studied in the UV by Sahai and Chronopoulos (2010) using the *Galaxy Evolution Explorer* (GALEX) space telescope. The authors used near-UV and far-UV images from the GALEX archive to trace the extent of the CSE in the ISM. It is found that as the star moves through the ISM at a velocity of  $\gtrsim 91\ \text{km}\ \text{s}^{-1}$ , a shock structure of  $24'$  in diameter is formed as a result of the interaction between the ISM and the wind of the star. They identify structures due to the interaction including the termination shock, the astrosheath, the astropause, the bow shock, and an astrotail.

Work conducted by Maun and Huggins (1999) showed evidence of the star’s envelope out to  $200''$  through their  $B$ - and  $V$ - band observations with the Canada-France-Hawaii Telescope (CFHT) in the dust emission. Similar estimates were confirmed by Dharmawardena et al. (2018) using the James Clerk Maxwell Telescope (JCMT). Maun and Huggins (1999) reports that the envelope has discrete  $\sim 1''\text{--}2''$  thin concentric shells but the envelope is almost spherically symmetric as a whole. Similarly, multiple arcs were measured out in the envelope up to  $\sim 5.2'$ .

Studies conducted at (sub)-millimetre wavelengths revealed that the CSE of IRC +10216 is exceptionally molecule-rich, being host to more than 80 different molecular species (see, e.g., Cernicharo et al. 2000; De Beck et al. 2010; Agúndez et al. 2014; Höfner and Olofsson 2018; Pardo et al. 2022 and several references therein). Not only does this include the parent molecules but also various daughter species including carbon chain molecules.

Cernicharo et al. (2015a) studied the envelope using the 30m telescope of the Institut de Radioastronomie Millimétrique (IRAM) in the  $^{12}\text{CO}$  (1–0),  $^{13}\text{CO}$  (1–0), and  $^{12}\text{CO}$  (2–1) lines. The authors

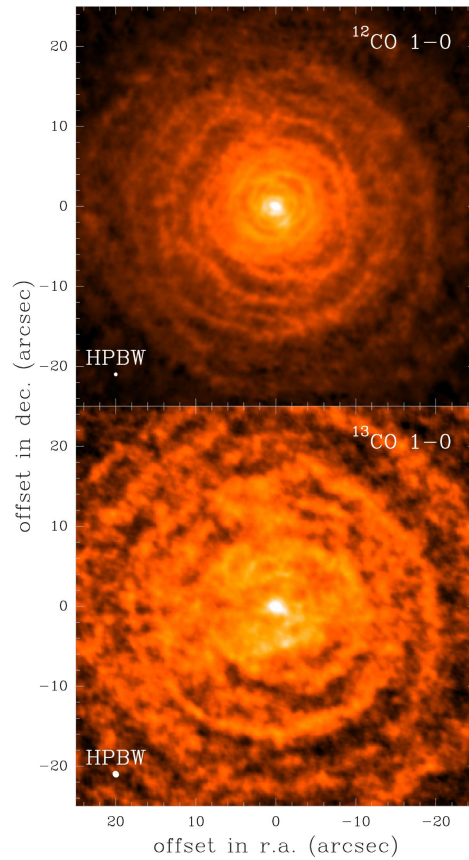


Figure 1.4: Line area brightness distributions of  $^{12}\text{CO}$  (1–0) (top) and  $^{13}\text{CO}$  (1–0) (bottom) lines from the ALMA and IRAM-30m data (Credit: Guélin et al. 2018).

mapped the  $^{12}\text{CO}$  (2–1) emission in the envelope with a resolution of  $11''$  (half power beam width, HPBW) up to the photodissociation radius of  $\approx 180''$ . They confirm that the envelope stays well inside the aforementioned bow shock (Sahai and Chronopoulos, 2010). The work also showed the presence of concentric dense shells expanding at a uniform velocity. To further understand the shell structure of the envelope, Guélin et al. (2018) conducted interferometric observations using the Submillimeter Array (SMA), the Plateau de Bure Interferometer (PdBI), and the Atacama Large Millimeter Array (ALMA) to achieve better angular resolution. They report that towards the outer parts of the envelope the separation between the brightest, regularly spaced shells is  $16''$ . As one moves closer to the star (about  $< 40''$ ), the shells appear to be more dense and irregular with arcs present (see Fig. 1.4 for the distribution of CO around the star). They also confirmed the expansion velocity of the gas closer to the star (but outside of the dust acceleration zone) to be constant at  $14.5 \text{ km s}^{-1}$ . The authors argue that the structure of the shells in the envelope could be a result of an interaction of a companion star of a much lower mass but detailed and prolonged observations are needed to confirm such a scenario.

Reach et al. (2022) discuss the distribution of atomic carbon ( $\text{C}^0$ ), resulting from the photodissociation of CO, and that of its photoionisation product  $\text{C}^+$ . In this thesis (Chapter 3), we study the distribution of atomic carbon in the CSE of IRC +10216 using dedicated observations and the aforementioned radiative-transfer analysis. While fine-structure emissions from  $\text{C}^0$  and  $\text{C}^+$  are also detected and analysed in the PNe phase (Young, 1997; Bernard-Salas and Tielens, 2005) characterised by a strongly ionising central star, the appearance of the  $\text{C}^+$  line in the inner envelope of IRC +10216 is still an enigma.

Similar to CO, though not as extensively, other molecules are also probed in the star's envelope, e.g. HCN. Cernicharo et al. (2011) use emissions from vibrationally highly excited states of HCN to understand the physical conditions in the gas acceleration and dust formation zone of the envelope. Shinnaga et al. (2009) use extended SMA observations to resolve the components of the HCN maser emission. They divide the envelope into two distinct regions, one where molecules are forming and dust is accelerated, and the other one where the gas is reaching its terminal velocity. Chapter 2 summarises the published work (see Appendix C for details), where we also use vibrationally excited HCN lines to probe these distinct regions in IRC +10216 (among other carbon-rich AGB stars) and discuss the physical conditions in the envelope.

## 1.4 Radio Astronomy

*General references: Wilson et al. (2013) and Condon and Ransom (2016)*

For centuries, the field of observational astronomy was restricted to the optical wavelengths of the electromagnetic spectrum. Karl Jansky, an American physicist, discovered, in 1931, the radio emission of astronomical objects. Since then, this field has dramatically evolved as the whole sky was to be observed with new eyes. Not only the tool to observe was different now, but also the objects hosting varied physical mechanisms can be studied due to the different nature in which radio astronomy operates, compared to the optical regime.

Astronomy in the millimetre/sub-millimetre wavelengths began relatively recently, in the 1970s. This region lies between the infrared and radio waves of the electromagnetic spectrum (see Fig. 1.5). Studying astronomical objects in these wavelengths provides a unique technique to observe phenomena, where other wavelengths fall short. For example, millimetre and sub-millimetre wavelengths penetrate regions obscured by dust extinction, allowing us to study stellar birth in molecular clouds, CSEs

around dying stars, high-redshifted sub-millimetre galaxies, and even dust-enshrouded Active Galactic Nuclei (AGNs).

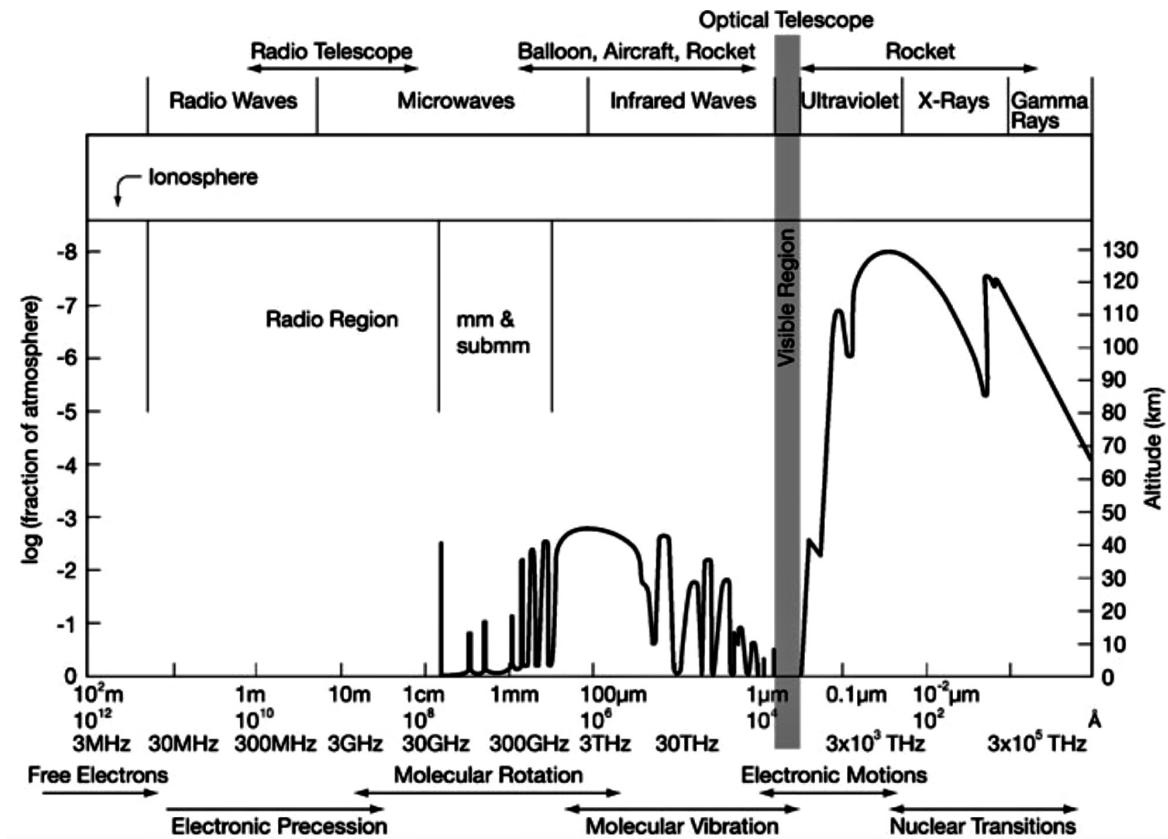


Figure 1.5: The figure presents the transmission through the earth's atmosphere for the electromagnetic radiation (Image from Wilson et al., 2013).

### 1.4.1 Telescope properties

*General references: Wilson et al. (2013) and Downes (1989)*

Before diving into the properties of single-dish radio telescopes, we first look into the parameters required to reliably convert the measured output signals into quantities describing the radiation field received from the observed astronomical objects. We refer to the determination and application of these parameters as calibration.

A simple way to describe the setup of a radio telescope (see on the left of Fig. 1.6 for a sketch of a Cassegrain telescope) comprises a single parabolic dish (referred to as an antenna) where the incoming electromagnetic radiation from the source is focused and collected in the receiver located in a Cassegrain, Gregorian, Nasmyth or primary focus, depending on the telescope design.

The telescope's response to the incoming radiation is described by its power pattern. Fig. 1.6 (right) presents a typical power pattern, where the maximum is referred to as the *main lobe* and the adjacent lobes are called the *side lobes*. In general, for the uniformly illuminated circular aperture of a parabolic dish (or another focusing optical device), this power pattern is given by the Airy pattern (more precisely, the Fourier transform of the transfer function). Strictly speaking, this result only

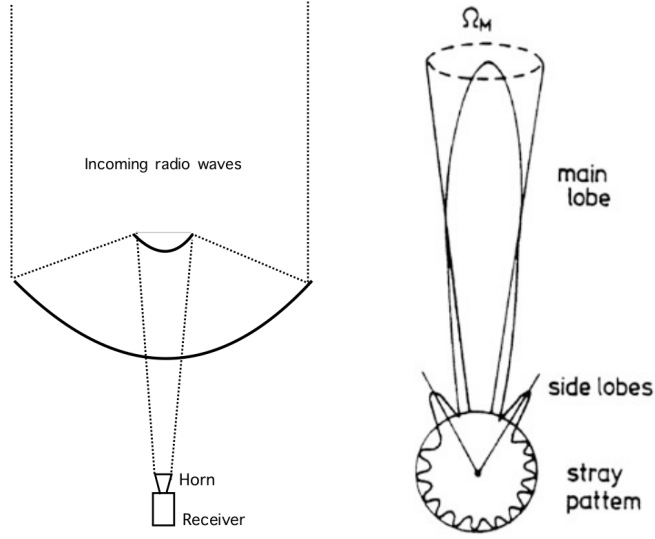


Figure 1.6: *Left*: A sketch of a single dish Cassegrain radio telescope. (Image created from Greve, 2000). *Right*: The figure represents the antenna power pattern with the main lobe and side lobes, along with the stray pattern generated due to non-uniformities of the dish. (Image is taken from Wilson et al., 2013).

holds for optical telescopes. For radio telescopes, with their low focal ratios  $f/D$  and their feed horns characterised by a Gaussian apodization of the aperture, this description is not correct anymore, while the basic principles still apply. In particular, using diffraction theory it can be shown that for a receiver feed horn illuminating the sub-reflector with a taper falling to  $-10$  to  $-14$  dB at its edge, the spatial resolution is characterised by a solid angle with an opening angle

$$\theta_{\text{HPBW}} = 1.2 \lambda/D, \quad (1.1)$$

such that for a source filling the main lobe, half of the power is received within that solid angle (HPBW refers to the half-power beam width). The factor in Equation (1.1) of order unity accounts for the sub-reflector illumination given by the feed horn design. Other illuminations are possible; receiver engineers usually select a pragmatic trade-off between spatial resolution and side lobe suppression. In practice, HPBW is measured on a strong, spatially unresolved source.

## Antenna and brightness temperature

The flux density received by an antenna is given by,

$$S_\nu = \iint I_\nu(\theta, \phi) P_n(\theta, \phi) d\Omega, \quad (1.2)$$

where  $I_\nu$  denotes the brightness distribution of the observed astronomical source (the emission of Earth's atmosphere is assumed to be removed, via observations of a clean reference position). The power pattern  $P_n(\theta, \phi)$  is normalised such that its full solid angle integral ( $4\pi$ ) yields unity.

The power (per unit spectral bandwidth) passing through the antenna's aperture and optical path is

therefore given by,

$$P_\nu = A_e S_\nu \quad (1.3)$$

where  $A_e$  is the efficient antenna aperture, which falls below the geometric aperture  $A_{\text{geo}} = \pi D^2/4$ , owing to the apodization introduced above and then central blockage by the subreflector (the ratio  $A_e/A_{\text{geo}}$  of both apertures is referred to as aperture efficiency ( $\eta_{\text{ap}}$ )).

On the other hand, the temperature  $T$  of a resistor matched to exhibit the same power as Johnson noise is, according to Nyquist (1928),

$$P_\nu = kT \quad (1.4)$$

We note that the temperature in Equation (1.4) is to be considered a Rayleigh-Jeans equivalent temperature. Only at low frequencies and temperatures, it can be equated with the physical temperature of the resistor. Equating (1.3) and (1.4) yields the antenna temperature, for which various notations exist. The antenna temperature  $T_a^*$  corrects the signal for losses in Earth's atmosphere, and for power contributions that do not couple to the sky, and is given by,

$$T_a^* = S_\nu \exp(\tau_z/\sin \varepsilon) A_e/(2 k \eta_{\text{ff}}), \quad (1.5)$$

introducing the optical depth of the atmosphere at the zenith,  $\tau_z$ , the telescope's elevation  $\varepsilon$ , and the forward efficiency  $\eta_{\text{ff}}$ , quantifying the fraction of the power received from outside the receiver cabin, which can be retrieved from a skydip measurement of atmospheric emission against elevation. The factor 1/2 in Equation (1.5) arises from the fact that phase-coherent detection in a given heterodyne mixer is sensitive to one polarisation only (the orthogonal polarisation would be measured by a second mixer), such that for an unpolarised source the calibration yields Stokes I. The above correction for atmospheric transmission is for a plane-parallel atmosphere, which is a good approximation except for the lowest elevations where observing is not advisable anymore due to the low transmission or the pickup of thermal radiation from the ground. In practice,  $\tau_z$  is deduced from a model atmosphere emitting the same power as the measured one, which in turn is calibrated employing frequently observed loads at ambient and cold, e.g., liquid nitrogen, temperature. For the remainder of this section, we assume the flux density to be scaled to its value outside the atmosphere and replace  $S_\nu \exp(\tau_z/\sin \varepsilon)$  with  $S_\nu$ .

The so-defined antenna temperature is useful for specifying receiver performance, but not for astrophysical purposes. For a given celestial source the antenna temperature is system-dependent and therefore does not allow for straightforward comparisons with astrophysical models or between flux densities measured at different telescopes. One therefore introduces the brightness temperature  $T_b$ , which is the Rayleigh-Jeans equivalent temperature of a radiation field carrying the same power (after correction for the atmospheric attenuation of the signal), thus

$$S_\nu = 2 k/\lambda^2 \int T_b \, d\Omega_s \quad (1.6)$$

where the integration extends over the solid angle subtended by the source. We note that at 100 GHz frequency, a brightness temperature of 100 K can be considered the physical temperature of a blackbody emitting the same power, with a relative error of 2.4%. Below 25 K, however, the error quickly rises above 10%. Towards the sub-millimetre and far-infrared regimes, the errors increase unless the considered temperature increases linearly with frequency. In summary, the correct temperature scale for calibration and radiative transfer is  $T_b$  and not the physical temperature of a

blackbody emitting the same power.

However, due to the limited spatial resolution of the telescope, the observed brightness temperature does not correspond to that defined in Equation (1.6). One therefore introduces the main-beam brightness temperature, which is the Rayleigh-Jeans equivalent temperature of a source filling the main beam of the power pattern, such that

$$S_\nu = 2 k/\lambda^2 T_{\text{mb}} \Omega_{\text{mb}} \quad (1.7)$$

Combining Equations (1.5) and (1.7) yields

$$T_{\text{a}}^* = A_{\text{e}} \Omega_{\text{mb}} T_{\text{mb}}/(\eta_{\text{ff}} \lambda^2) = T_{\text{mb}} \eta_{\text{mb}}/\eta_{\text{ff}} \quad (1.8)$$

introducing the main beam efficiency  $\eta_{\text{mb}}$ .

While at the telescope the online calibration usually provides spectra on the  $T_{\text{a}}^*$  scale, the parameters  $\eta_{\text{mb}}$  and  $\eta_{\text{ff}}$  are available for each receiver due to dedicated calibration observations carried out by the observatory staff.

We close this section with a short discussion of the main beam efficiency. Using the above definition of the aperture efficiency  $\eta_{\text{ap}}$ , and the area of a Gaussian main beam of HPBW  $\theta$ ,

$$\Omega_{\text{mb}} = \pi \theta_{\text{HPBW}}^2/(4 \ln 2) \quad (1.9)$$

one obtains

$$\eta_{\text{mb}} = \eta_{\text{ap}} \pi^2/(16 \ln 2) [\theta_{\text{HPBW}}/(\lambda/D)]^2 \quad (1.10)$$

With an accurate measurement of  $\theta_{\text{HPBW}}$ , and  $\eta_{\text{ap}}$  measured on a point-like calibrator of known flux, one can determine  $\eta_{\text{mb}}$  with the same accuracy as  $\eta_{\text{ap}}$ . As discussed above, the quantity in the squared brackets of order unity contains the detail of the apodization of the illumination of the sub-reflector by the feed horn (e.g., 1.2 for a  $\sim 10$  dB taper).

## 1.4.2 Telescopes used in this thesis

We used data from various telescopes to conduct studies presented in this thesis. In the following sub-sections, we list these facilities and give a detailed explanation of the instruments used for our research.

### Atacama Pathfinder Experiment (APEX):

*This sub-section is based on Güsten et al. (2006) and the APEX telescope instrument website page<sup>3</sup> unless specified:*

The APEX telescope was conceived as the pathfinder for the ALMA interferometer being a prototype for the antennas of the latter. APEX is located at the Llano de Chajnantor in the Chilean High Andes at an altitude of 5107 m. The telescope has a 12 m diameter dish with two Nasmyth cabins and one Cassegrain cabin for receivers.

In the following, we give a brief overview of the instruments used in this thesis:

---

<sup>3</sup> <https://www.apex-telescope.org/ns/instruments/>



Figure 1.7: APEX telescope at the Llano de Chajnantor in Chile.

1. SEPIA180: SEPIA180 is a Swedish-ESO PI instrument (Billade et al., 2012; Immer et al., 2016) operating in the 159–211 GHz frequency range. It is a dual polarisation dual-side-band (SB) receiver on which ALMA Band 5 is based. The upper sideband (USB) and lower sideband (LSB) outputs cover the intermediate frequency (IF) 4–8 GHz range (Belitsky et al., 2018a; Belitsky et al., 2018b). This instrument covers the lowest frequency range at APEX and is useful for observing the water vapour line at 183 GHz. As the telescope is situated at one of the driest places on earth, this line, which is absorbed at other sites, is accessible to observations with this instrument under suitable weather conditions. In this thesis, we have used this instrument to observe various HCN lines in the ground and vibrationally excited states in the  $J = 2-1$  transition. See Chapter 2 and Appendix C for more details.
2. PI230<sup>4</sup>: Located in the Nasmyth-B cabin, this receiver covers a bandwidth of 1.11 to 1.54 mm (195–270 GHz) with the IF range of 4–12 GHz and 32 GHz bandwidth per tuning (Brinkmann et al., 2020), operating in a single polarisation since 2020. It is widely used in the Event Horizon Telescope campaigns. For our work, we used this instrument to observe the CO (2–1) line at 230.538 GHz and various HCN lines in the ground and vibrationally excited states in the  $J = 3-2$  transition. See Chapters 2 and 5 for more details.
3. nFLASH230: Covering a range of 196–281 GHz, this instrument was used to conduct the observations of the CO (2–1) line (in both isotopologues) for our Nearby Evolved Stars Survey (NESS; see Chapter 4 and 5). With an extended IF range of 4 to 12 GHz, it covers 32 GHz instantaneous bandwidth, including two sidebands with a separation of 16 GHz and dual polarisations.
4. SEPIA345: This is a dual polarisation 2SB receiver operating in the 272–376 GHz range with an IF range of 4–12 GHz (Meledin et al., 2022). Due to its wide bandwidth (7.9 GHz + 7.9 GHz), this instrument is very favourably used for line surveys. We used it to observe CO lines in the  $J = 3-2$  transition (see Chapter 5).

<sup>4</sup> <https://www.eso.org/public/teles-instr/apex/pi230/>

5. FLASH345<sup>5</sup>: The First Light APEX Submillimeter Heterodyne (FLASH345/FLASH+) was a PI instrument (Klein et al., 2014) operating simultaneously in the 345 GHz and the 460 GHz atmospheric windows. We used this instrument for our high- $J$  HCN observations where the instrument operated in the frequency range of 268–374 GHz, with an IF range of 4–8 GHz and single polarisation. It has been decommissioned since December 2019 due to being replaced by a new generation of heterodyne receivers.
6. LAsMA<sup>6</sup>: The Large APEX sub-Millimeter Array (LAsMA) instrument is a 7-pixel array operating in the frequency range of 268–375 GHz. The six pixels surround the central pixel in a hexagonal manner. The on-sky separation between the pixels is about 40 arcsec. The IF bandwidth is 4–8 GHz for each of the two sidebands. This 345 GHz multi-beam receiver was used for our CO (3–2) observations discussed in Chapter 5.
7. nFLASH460: This is a 2SB receiver with two polarisations covering a frequency range of 378–507 GHz. The IF range is from 4–8 GHz. This band of the nFLASH receivers shows strong absorption features in the atmospheric transmission. We used this instrument to study the [C I] line at a frequency of 492.160700 GHz (see Chapter 3 and Appendix D for more details).

### Institut de Radioastronomie Millimétrique (IRAM) 30-m telescope<sup>7</sup>:



Figure 1.8: The IRAM 30-m telescope in the Spanish Sierra Nevada (Credit: IRAM/ K. Zacher).

The 30-m telescope operated by IRAM is located on the Pico Veleta in the Spanish Sierra Nevada. It is one of the leading telescopes operating at mm wavelengths. The telescope is located at an altitude of 2850 m and operates between 80 and 370 GHz (3 to 0.8 mm).

where we could cover  $^{12}\text{CO}$  and  $^{13}\text{CO}$  observations in their  $J = 1-0$  transitions and additional  $^{12}\text{CO}$  observations of the  $J = 2-1$  transition simultaneously. We used this facility to collect data for the NESS project. See Chapter 5 for more details.

We used the Eight MIXer Receiver (EMIR) for our heterodyne observations, which allows dual-band observations and provides two sideband and two polarisation outputs (8 GHz wide each). We observed in dual-band mode E0/E2, where we could cover  $^{12}\text{CO}$  and  $^{13}\text{CO}$  observations in their  $J = 1-0$  transitions and additional  $^{12}\text{CO}$  observations of the  $J = 2-1$  transition simultaneously. We used this facility to collect data for the NESS project. See Chapter 5 for more details.

### James Clerk Maxwell Telescope (JCMT)<sup>8</sup>:

Built close to the summit of Mauna Kea, Hawai'i, USA at an altitude of 4092 m, JCMT is a 15 m single dish telescope operating at sub-millimetre wavelengths. We have used data from this telescope only for preliminary statistical analysis. Only the sources observed in  $\delta < -30^\circ$  are included in the work presented in Chapter 5. For CO (2–1) observations we used the receiver RxA3, which operated

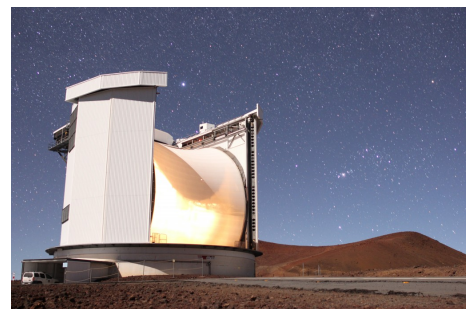


Figure 1.9: The JCMT telescope close to Mauna Kea, Hawai'i, USA (Credit: EAO observatory/ William Montgomerie).

<sup>5</sup> <https://www.eso.org/public/spain/teles-instr/apex/flash-plus/>

<sup>6</sup> <https://www.mpifr-bonn.mpg.de/5278286/lasma>

<sup>7</sup> <https://iram-institute.org/observatories/30-meter-telescope/>

<sup>8</sup> <https://www.eaobservatory.org/jcmt/about-jcmt/>

in the frequency range of 212–274 GHz. The receiver has been decommissioned since 2018. For higher- $J$  CO (3–2) observations, we used the Heterodyne Array Receiver Program (HARP), tunable between 325–375 GHz with an IF of 5 GHz. Similar to previous sub-sections, data from this telescope has been used for the NESS project (Chapter 5).

### Onsala Space Observatory (OSO)<sup>9</sup>:

The Swedish 20 m telescope is located about 45 km from Gothenburg, Sweden, and operates in the lower frequency range of up to 116 GHz, well equipped for observations of molecules in comets, CSEs, the ISM, and also extragalactic objects. We have used archival data for CO (1–0) emissions, which is presented in Chapter 5.



Figure 1.10: The Onsala 20 m telescope (Credit: Chalmers/ J-O Yxell).

### Stratospheric Observatory For Infrared Astronomy (SOFIA)<sup>10</sup>:



Figure 1.11: SOFIA with its telescope door open during a test flight (Credit: NASA/ Jim Ross).

The SOFIA telescope was a 2.7 m reflecting dish aboard the Boeing 747SP aircraft, designed to observe objects in the infrared wavelengths from the Earth’s stratosphere at altitudes of 38,000 – 45,000 feet (12 – 14 km). The observatory was decommissioned in September 2022. For this thesis, we used the upGREAT 7-pixel receiver to observe the ionised carbon line emission from the CSE of IRC +10216. The receiver operated between 1.9 – 2.5 THz and the [C II] fine-structure line lies at 1900.5369 GHz. Our results and the instrumentation are explained in detail in Chapter 3 and Appendix D.

### Swedish-ESO Submillimetre Telescope (SEST)<sup>11</sup>:

SEST was a 15 m diameter sub-millimetre telescope operating in the frequency range of 70 – 365 GHz. It saw the first light in 1987 and was built on the European Southern Observatory (ESO) site of La Silla in Chile at an altitude of 2375 m<sup>12</sup>. It was the only sub-millimetre telescope at the time in the southern hemisphere. The telescope was decommissioned in 2003 and has been superseded by the APEX and ALMA telescopes. For our work, we have used



Figure 1.12: The SEST telescope at La Silla, Chile (Credit: F. Kerschbaum/ ESO).

<sup>9</sup> <https://www.chalmers.se/en/infrastructure/oso/telescopes-and-instruments/radio-astronomy-facilities/onsala-20-m-telescope/>

<sup>10</sup> <https://science.nasa.gov/mission/sofia/>

<sup>11</sup> <https://www.apex-telescope.org/sest/>

<sup>12</sup> <https://www.eso.org/public/teles-instr/lasilla/swedish/>

archival data obtained from observations with SEST and used it for our statistical analysis for the NESS project (Chapter 5).

## 1.5 Fundamentals of radiation and the radiative transfer of spectral lines

General references: Cannon (1985), Wilson et al. (2013) and Condon and Ransom (2016)

### 1.5.1 Basic definitions

Exact definitions have been established for the measurement of radiation from astronomical sources. Radiation travels in straight lines or *rays* if the system under study is larger than the wavelength ( $\lambda$ ) of the radiation. Fig. 1.13 shows systematically the arrangement of a measurement of the specific intensity.

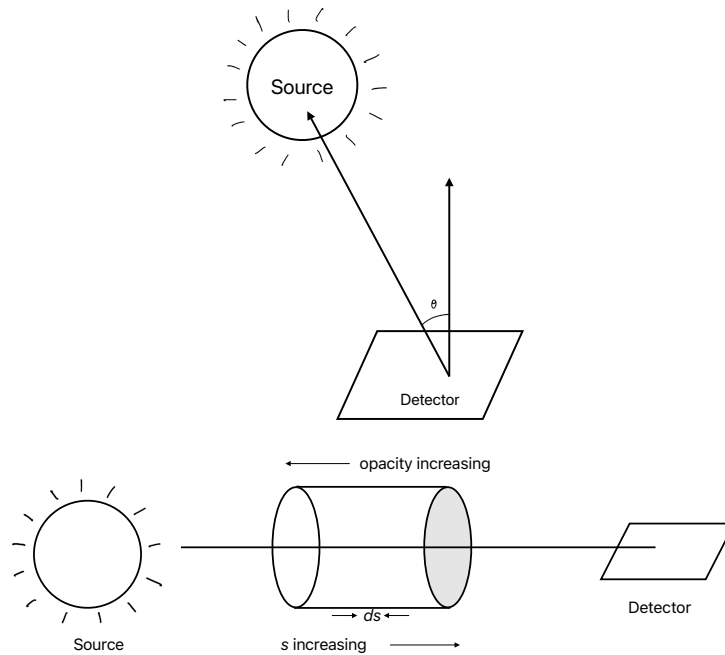


Figure 1.13: *Top*: Measurement of specific intensity. *Bottom*: Radiative transfer arrangement, here opacity refers to the optical depth ( $\tau$ ). Credit: Adapted from figures from Condon and Ransom (2016).

*Specific intensity* is defined as the brightness per unit frequency, denoted as  $I_\nu$ , where the frequency is indicated by  $\nu$ . To generalise the specific example, an infinitesimal power received from a given direction by an infinitesimal surface is given by,

$$dP = I_\nu \cos \theta d\Omega d\sigma d\nu, \quad (1.11)$$

where,  $dP$  is the infinitesimal power in watts,  $I_\nu$  is the brightness or specific intensity in  $\text{W m}^{-2} \text{Hz}^{-1} \text{sr}^{-1}$ ,  $d\Omega$  is the infinitesimal solid angle,  $d\sigma$  is the infinitesimal surface area in  $\text{cm}^2$ ,  $\theta$  is the angle between the normal to  $d\sigma$  and  $d\Omega$ , and  $d\nu$  is the infinitesimal bandwidth in Hz.

Furthermore, *flux density* is obtained by integrating Equation 1.11 over the total solid angle  $\Omega_s$  that is subtended by the source. Then we have,

$$S_\nu = \int_{\Omega_s} I_\nu(\theta, \phi) \cos \theta \, d\Omega \quad (1.12)$$

This quantity is measured in  $\text{W m}^{-2} \text{Hz}^{-1}$ . Since the flux densities of radio sources tend to be small, a new unit of Jansky (Jy) is introduced,

$$1 \text{ Jy} = 10^{-26} \text{ W m}^{-2} \text{Hz}^{-1} = 10^{-23} \text{ erg s}^{-1} \text{cm}^{-2} \text{Hz}^{-1} \quad (1.13)$$

### 1.5.2 Radiative transfer

The specific intensity  $I_\nu$  of radiation, in free space, is conserved, i.e. it is independent of the distance along the ray. This quantity is altered only when there is a medium present in between, which allows radiation to be absorbed or emitted locally, and such a phenomenon is described by the *radiative transfer equation*.

The conservation of the specific intensity along a ray without sinks and sources of radiation is defined by,

$$\frac{dI_\nu}{ds} = 0 \quad (1.14)$$

where  $ds$  is the infinitesimal sightline element.

Fig. 1.13 (bottom) shows a sketch explaining the radiative transfer arrangement, where the medium is present between the astronomical source and the detector. The *coordinate* of the ray increases in the direction of the detector when it passes through the medium, whereas the opacity  $\tau$  increases in the opposite direction, i.e. as we move away from the detector.

When the ray propagates through the medium, assuming that only absorption and emission processes affect the ray (neglecting the scattering process), the radiative transfer equation becomes,

$$\frac{dI_\nu}{ds} = -\kappa_\nu I_\nu + \epsilon_\nu, \quad (1.15)$$

where,  $\kappa_\nu$  is the absorption coefficient, and  $\epsilon_\nu$  is the emissivity.

In some cases, this equation is simplified if:

- only absorption takes place ( $\epsilon_\nu = 0$ ), then the equation becomes:

$$\frac{dI_\nu}{ds} = -\kappa_\nu I_\nu \quad (1.16)$$

- only emission takes place ( $\kappa_\nu = 0$ ), then we get:

$$\frac{dI_\nu}{ds} = \epsilon_\nu \quad (1.17)$$

In a closed system, radiation and matter are characterised by the same temperature ( $T$ ) and it is thus referred to as being in thermal equilibrium (TE). For example, in the following discussion, we will consider a two-level system, which can also be generalised for a multi-level system, with populations  $N_l$  and  $N_u$  and energies  $E_l$  and  $E_u$  for lower and upper states, respectively. In such a system, known as “black body” Planck’s formula describes the specific intensity of the radiation,

$$B_\nu(T) = \frac{2h\nu_{ul}^3}{c^2} \frac{1}{e^{\frac{h\nu_{ul}}{kT}} - 1}, \quad (1.18)$$

where  $h\nu_{ul}$  is the energy difference  $E_u - E_l$ , and the populations  $N_l$ ,  $N_u$  follow the Boltzmann distribution,

$$\frac{N_u}{g_u} = \frac{N_l}{g_l} e^{-\frac{h\nu_{ul}}{kT}} \quad (1.19)$$

Albert Einstein in 1917 (Einstein, 1917) first introduced the process that matter and radiation permanently exchange energy:

The upper energy level of a particle can be populated by absorption of a photon of energy  $\Delta E_{ul} = E_u - E_l = h\nu$ , at a rate  $B_{lu} \times J_\nu$ , where  $J_\nu$  is the solid-angle averaged specific intensity of the radiation field. The upper level is depopulated by spontaneous emission of a photon of energy  $h\nu$ , at a rate  $A_{ul}$ , or by stimulated emission at a rate  $B_{ul} \times J$ . In the state of equilibrium, the rate  $dN_{lu}/dt$  of upward transitions should be equal to that of the downward transitions,  $dN_{ul}/dt$ , where

$$\dot{N}_{ul} = A_{ul}N_u + B_{ul}N_uJ_\nu \quad (1.20a)$$

$$\dot{N}_{lu} = N_lB_{lu}J_\nu \quad (1.20b)$$

$$\dot{N}_{ul} = \dot{N}_{lu} \quad (1.20c)$$

This principle is referred to as detailed balancing. Substituting  $N_u$  by  $\exp(-h\nu/kT) \times N_l \times g_u/g_l$ , equations (1.20) yield,

$$J_\nu = \frac{A_{ul}}{\frac{g_l}{g_u}B_{lu}e^{\frac{h\nu_{ul}}{kT}} - B_{ul}} \quad (1.21)$$

The Planck formula (1.18) describes the radiation field  $J$  since the system is closed. The equality of Equations (1.18) and (1.21) yields,

$$A_{ul} = \frac{2h\nu_{ul}^3}{c^2}B_{ul} \quad (1.22)$$

and

$$g_lB_{lu} = g_uB_{ul} \quad (1.23)$$

If the density is sufficiently high, collisions between the particles become important and occur at rates (per particle)  $C_{lu}$  (excitation) and  $C_{ul}$  (de-excitation), and Equations (1.20) must be correspondingly

extended which leads to:

$$N_u(A_{ul} + B_{ul}J_\nu + C_{ul}) = N_l(B_{lu}J_\nu + C_{lu}) \quad (1.24)$$

Due to the thermal equilibrium, the level populations continue to follow a Boltzmann distribution. Thus combining Equations (1.20c) and (1.24),

$$C_{lu} = C_{ul} \frac{N_u}{N_l} = C_{ul} \frac{g_u}{g_l} e^{-\frac{h\nu_{ul}}{kT}} \quad (1.25)$$

In astrophysics, the concept of a closed system in thermal equilibrium is often an approximation, which is accurate enough for practical applications (e.g., for describing stellar interiors). It can still be useful if it is applied to small volume elements where almost no radiation can escape from the boundary. The thermodynamic equilibrium is then referred to as “local” (LTE). As soon as radiative losses become important, the Planck formula cannot describe the resulting radiation anymore. Here a solution of the radiative transfer equation (1.15) comes of use, as developed in the following:

The first term on the right-hand side of equation (1.15) describes the net absorption of radiation (per sightline element  $ds$ ) by stimulated processes and  $\kappa_\nu$  is given by,

$$\kappa_\nu = \frac{h\nu_{ul}}{4\pi} \phi(\nu) (N_l B_{lu} - N_u B_{ul}) \quad (1.26)$$

where  $\phi(\nu)$  is the profile function and it accounts for the monochromatic radiation that is considered, while the emitting and absorbing particles follow a (usually Maxwellian) velocity distribution.

The source term  $\varepsilon_\nu$  (from spontaneous emission) can be written out as

$$\varepsilon_\nu = \frac{h\nu_{ul}}{4\pi} \phi(\nu) N_u A_{ul} \quad (1.27)$$

Since the radiative transfer equation must reproduce the limiting case of a closed system, the condition  $dI_\nu/ds = 0$  entails

$$\varepsilon_\nu = \kappa_\nu I_\nu \quad (1.28)$$

which, using (1.26) and (1.27), correctly yields  $I_\nu = B_\nu$  and Kirchhoff’s law of radiation,

$$\varepsilon_\nu = \kappa_\nu B_\nu \quad (1.29)$$

And for the general case of non-LTE (NLTE), one can introduce a source function,

$$\Sigma_\nu = \frac{\varepsilon_\nu}{\kappa_\nu} \quad (1.30)$$

which can be parametrised through Planck’s law, by an equivalent excitation temperature  $T_{\text{ex}}$  such that the level populations are given by a Boltzmann distribution at  $T_{\text{ex}}$ , which in NLTE differs from the gas temperature  $T_{\text{kin}}$ .

The radiative transfer equation then becomes

$$\frac{dI_\nu}{ds} = \kappa(\Sigma_\nu - I_\nu) \quad (1.31)$$

If the medium is isothermal in nature (i.e.,  $\Sigma$  is constant along the sightline), the solution of

equation (1.31) becomes

$$I_\nu(s) = I_\nu(0) + \Sigma_\nu(1 - e^{-\tau_\nu}) \quad (1.32)$$

introducing the optical depth,

$$\tau_\nu(s) = \int_0^s \kappa_\nu(z) dz \quad (1.33)$$

If the optical depth is high, radiation from the interior of the considered medium and the background radiation  $I_\nu(0)$  behind it does not penetrate toward the surface, and the result simply becomes

$$I_\nu(s) = \Sigma_\nu(T_{\text{ex}}) \quad (1.34)$$

In view of the apparent simplicity of this limiting case, it is important to note again that this solution is not necessarily represented by a Planck function at gas temperature  $T_{\text{kin}}$ . Even if the level populations at the surface layer were set by collisions trying to enforce  $T_{\text{ex}} = T_{\text{kin}}$ , loss (through the surface of the medium) of radiation from the spontaneous de-excitation of collisionally excited atoms or molecules would lead to efficient cooling and therefore a different source function.

## 1.6 Atoms and molecules in the CSEs

As preceded by radio astronomy applications, atoms and molecules can be used as important tools to understand the chemical and physical compositions of the atmospheres of AGB stars. These regions provide an abundance of molecular and atomic species. Here, we provide information on three such species that are important constituents of the envelope and the ISM and whose emissions serve as crucial tools for scientific analysis in the subsequent chapters.

### 1.6.1 Thermal emissions

#### Hydrogen cyanide (HCN)

HCN is a linear molecule, where C and H are linked by a single bond, and C and N are linked by a triple bond. Snyder and Buhl (1971) detected the HCN molecule in its main molecular isotopic form  $\text{H}^{12}\text{C}^{14}\text{N}$  in the interstellar medium at 88.6 GHz in the  $J=1-0$  transition. Numerous studies showed detections of the molecule in the atmospheres of AGB stars. It is one of the most abundant species in the CSEs of carbon-rich AGB stars forming close to the star (see Fig. 1.3 for reference). HCN is also a parent molecule for the subsequent chemistry and therefore an important probe for the inner envelope regions.

Molecules as a whole exhibit vibrational and rotational motions and the vibrational modes depend on the number of atoms and the geometry present in the molecule (e.g., Atkins and Friedman, 2011). Diatomic molecules perform in only one vibration mode. For a polyatomic molecule, an atom can move in 3 different directions. This gives  $3N$  degrees of freedom that are available, where  $N$  is the number of atoms. Subtracting the motions translating or rotating the molecule as a whole leaves us with the number of vibrational modes. If the molecule is nonlinear, the latter is given by  $3N - 6$ , whereas in the case of a linear molecule, it is given by  $3N - 5$ .

For the HCN molecule ( $N = 3$ ), it would be  $3 \times 3 - 5 = 4$ , which corresponds to two vibrational stretching modes and one doubly-degenerate bending mode. Changes in the bond length and the angle between bonds are termed as stretching and bending modes, respectively. From Menten et al. (2018)

and references within, the notation for the vibrational modes is  $(\nu_1, \nu_2^l, \nu_3)$ , where  $\nu_2^l$  represents the bending mode. The CH stretching mode,  $\nu_1$  [(1, 0, 0)], is at a wavelength of  $3.0 \mu\text{m}$  and at 4765 K above ground, the doubly degenerate bending mode,  $\nu_2^l$  [(0, 1, 0)], is present at  $14.0 \mu\text{m}$  and at 1027 K, and the CN stretching mode,  $\nu_3$  [(0, 0, 1)] is at a wavelength of  $4.8 \mu\text{m}$  with a temperature of 3017 K (measurements from Mellau, 2011). The band emissions from these modes are challenging to observe from the ground due to absorption in Earth’s atmosphere, especially with a strong continuum emission underneath.

A multitude of rotational transitions arise from these vibrational states, which are expressed by the angular momentum quantum number  $J$ . The rotational transitions ( $J \rightarrow J - 1$ ) are easily observable from ground-based telescopes and can reveal structures with high-resolution imaging when observed with interferometers such as ALMA or the IRAM NOthern Extended Millimeter Array (NOEMA) (Menten et al., 2018). The vibrational bending mode results in the bending of the bonds in two orthogonal directions, which makes  $\nu_2$  doubly degenerate. This degeneracy is lifted when the molecule is bending and spinning at the same time, causing  $l$ -type doubling, where each rotational level splits into two sub-levels (Menten et al., 2018, and references therein).

A schematic representation of the energy diagram of the HCN molecule is shown in Fig. 1.14. Upper-level energies are indicated on the left in Kelvin. The vibrational and rotational states are indicated by the quantum numbers  $\nu$  and  $J$ , respectively. The splitting of the rotational state into two sub-levels due to  $l$ -type doubling is indicated by 1e and 1f. The red arrows show direct  $l$ -type transitions, whereas,  $J = 2-1$  ( $0, 1^{1e}, 0$ ) and  $J = 2-1$  ( $0, 1^{1f}, 0$ ) transitions are indicated by blue and purple arrows, respectively. It is important to note that the separation between the two sub-levels is not drawn to scale and is only presented as an indicator. Cyan arrows show the wavelengths at which the photons are pumped from ground state to highly vibrational state. More detailed discussions can be found in Chapter 2 and Appendix C.

## Carbon monoxide (CO)

Carbon monoxide is a simple molecule composed of one carbon atom and one oxygen atom, bound together by a triple bond. This molecule was first discovered in space by Wilson et al. (1970) towards the Orion Nebula in the  $J = 1-0$  transition at a frequency of 115.2712 GHz. It is also the second most abundant molecule after molecular hydrogen ( $\text{H}_2$ ) with a relative abundance of  $[\text{CO}/\text{H}_2] \approx 10^{-4}$  (Saber et al., 2019). Since  $\text{H}_2$  is not easily observable (lacking, as homo-nuclear molecule, a permanent dipole moment), CO is considered to be the most useful tracer for not only measuring the mass-loss in evolved stars but also for tracing molecular gas in various other regions in the ISM.

In the case of evolved stars, it is crucial to use this molecule in the analyses as it serves to trace the structure of the cool regions in the envelope. According to Bieging et al. (2002), the dissociation energy for this molecule (11.1 eV) is quite high. It is assumed to form in the atmospheres of cool giants and supergiants, where the abundance of the molecule is close to the value predicted by the chemical thermodynamic equilibrium. CO, in the atmospheres of evolved stars, is formed by binding together nearly all available carbon and oxygen atoms (see below for more discussion). This allows a more reliable estimation of the abundance of the molecule as it can be based on the particular atomic abundance. The CO fundamental line present at  $4.6 \mu\text{m}$  gives optically thick emission, whereas the first overtone line is already not optically thick. Models considering large MLRs and extended atmospheres imply that these lines are particularly useful to trace the entire envelope, especially when combined with the reliability of the molecule’s stability in its abundance (Winters et al., 2000; Bieging

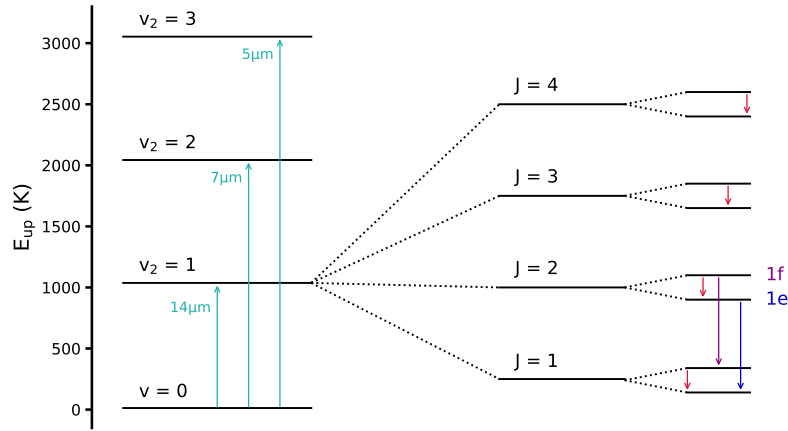


Figure 1.14: Energy diagram of the HCN molecule from Jeste et al. (2022) showing the rotational transitions, arising from vibrational states indicated by  $J$  and  $\nu$ , respectively. The splitting of every rotational level into two sub-levels, 1e and 1f, caused by the  $l$ -type doubling is also indicated in the figure above. We also show the  $J = 2-1$  ( $0, 1^{1e}, 0$ ) and  $J = 2-1$  ( $0, 1^{1f}, 0$ ) transitions marked with blue and purple arrows, respectively. Cyan arrows denote the pumping photons from the ground state to highly vibrational excited states. Red arrows indicate the direct  $l$ -type transitions. It is important to note that the separations of the  $l$ -type transitions are not drawn to scale.

et al., 2002).

Höfner and Olofsson (2018) discussed the circumstellar emission of the CO rotational line in more detail. Due to collisional processes and high abundances and densities, the energy levels are easily excited and yield bright lines for easier detection. The rotational lines of this molecule prove advantageous as they probe an extended energy range, allowing us to trace different regions of the envelope using these lines. Moreover, the line profile provides us with information about the expansion velocity of the gas, the optical depth, and the emission extent in the envelope.

Another aspect discussed in Höfner and Olofsson (2018) is the fractional abundance of CO ( $f_{\text{CO}}$ ), a parameter estimating the total MLR from the loss-rate inferred from CO. The formation of CO is complete when it uses up all of the C or O atoms to form the molecule. Because this is limited by the species that is depleted first, it highly depends on the elemental abundance in the photosphere, i.e., whether it is O-rich or C-rich. It is not well estimated as to how much of these elements are locked in CO. Interestingly, the change in the molecular abundance of CO is based on the chemical type of the star and the processes that take place in the CSE. In C-rich stars, the CO abundance depends on the O abundance and the metallicity. In low-mass O-rich stars, metallicity plays a role in the abundance, and for more massive O-rich stars, the hot bottom burning process (see Sect. 1.1.4) lowers the abundance of C, which dramatically affects the CO abundance. Thus, it should be noted that the MLRs determined using the  $f_{\text{CO}}$  parameter may show larger uncertainties for S-type and more massive O-rich stars compared to C-rich stars.

These quantities, along with others, are particularly useful for understanding and performing radiative transfer models. To numerically calculate the CO line radiative transfer, numerous studies

have been done using non-LTE excitation models (see examples in Groenewegen, 1994; Schöier and Olofsson, 2001; Decin et al., 2006). Studies such as Ramstedt et al. (2008) and De Beck et al. (2010) show observations and modelled spectra of CO lines. They use a new formula to calculate MLR (building on the one presented in Knapp and Morris 1985), based on parameters such as  $f_{\text{CO}}$ , expansion velocities, integrated line intensities, and other observational quantities. The two formulae differ as the one put forth by Ramstedt et al. (2008) have a smaller range for the MLR estimates as compared to De Beck et al. (2010). In this thesis, Chapter 5 makes use of these empirical formulae to determine the MLRs of a large sample of AGB stars using high- $J$  CO lines.

### Atomic carbon (C I)

One of the important processes to understand the chemistry in the CSEs is the photodissociation of molecules. In these regions, the interstellar radiation field dominates the dissociation process. This radiation can vary from the Lyman limit at an extreme UV wavelength (912 Å) to infrared wavelengths (Jorgensen, 1994). The second most abundant molecule, CO, has a dissociation energy of 11.09 eV (= 1118 Å) and it photodissociates to form atomic carbon (C I) and subsequently ionised carbon (C II) via photodissociation. The photodissociation of CO is believed to be the major contributor for the production of atomic carbon (Huggins and Glassgold, 1982; Keene et al., 1993; van der Veen et al., 1998).

Studying the atom in the CSEs of AGB stars is more or less straightforward as, to a certain extent, the envelope can be considered spherically symmetric with the material expanding at a constant velocity from the star (Keene et al., 1993). Stars such as IRC +10216 are rich in molecular species both in the inner and outer parts of the envelope. After CO, the photodissociation of molecules such as  $\text{C}_2\text{H}_2$  and HCN is thought to produce a considerable amount of atomic carbon, especially  $\text{C}_2\text{H}_2$  is responsible for a stronger emission of [C I] present in the inner parts of the CO dissociation region due to the higher temperature and density there (Huggins and Glassgold, 1982; Keene et al., 1993, and references therein). Reach et al. (2022) studied the ionised carbon distribution in the envelope of IRC +10216 using observations with the SOFIA and Herschel telescopes and compared them to their models predicting the emitting size and column densities. The abundances of the photodissociation products of CO are shown below in Fig. 1.15 taken from Reach et al. (2022).

Extensive studies are yet to be done for this atom in the CSEs of various AGB stars. The electronic ground state of C I has a fine-structure triplet with two transitions, at 492 and 809 GHz. van der Veen et al. (1998) conducted a study for several evolved stars and were successful in detecting the fine-structure line in IRC +10216 and  $\alpha$  Orionis using the JCMT telescope. They used the 609  $\mu\text{m}$  ground-state fine-structure line at 492 GHz to constrain [C I] in their envelopes. In addition to the CO dissociation in IRC +10216, processes such as the freeze-out of [C I] in the inner parts of the envelope and shocks are also responsible for the production of [C I] (in the case of  $\alpha$  Orionis, Glassgold and Huggins, 1986; van der Veen et al., 1998).

In this thesis, we use the fine-structure line to constrain the distribution of atomic carbon with more sensitive observations and sophisticated non-LTE radiative transfer modelling.

## 1.6.2 Masers

### Basic principles

*General References: Elitzur (1982), Elitzur et al. (1983) and Gray (2012)*

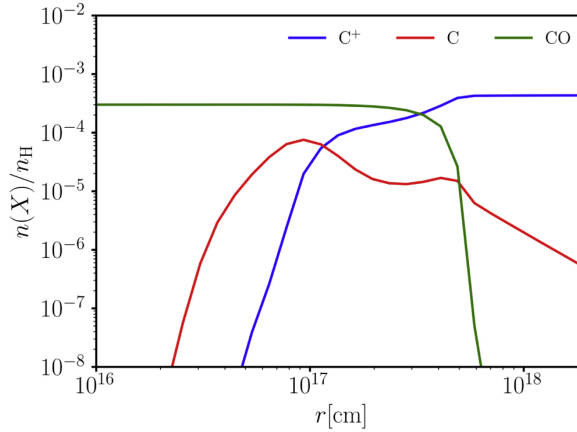


Figure 1.15: Abundances of CO, C, and C<sup>+</sup> in the outer envelope of IRC +10216 from the model presented in Reach et al. (2022).

Referring to the concept of stimulated emission (see Sect. 1.5), from Equation (1.15), it is seen that the incident seed radiation field,  $I_\nu$ , can be amplified if  $\kappa_\nu$  becomes negative. Taking into account Equations (1.23) and (1.26), radiation can be amplified by stimulated processes if

$$\frac{N_u}{g_u} > \frac{N_l}{g_l} \quad (1.35)$$

(i.e., only the populations per sub-state matter for inversion). Evidently, a Boltzmann distribution (i.e., thermalisation of the level populations, Equation (1.19)) cannot fulfil this requirement. However, by pumping the levels of the maser through the excitation of particles from a reservoir (i.e., states not directly involved in the maser action), level inversion can be achieved. In the following, this is demonstrated with a three-level maser (Fig. 1.16), following Elitzur et al. (1983), but many other configurations are possible.

For the purposes of demonstration, the rates of spontaneous emissions and collisional transitions between the three levels are assumed to be negligible in comparison to those of the stimulated transitions,  $R_{ij} = B_{ij} J_{ij}$ . The pump rates into the levels are denoted with  $P_j$  ( $j=1,2,3$ ), and the losses out of them (into states outside the three-level maser) by  $\Gamma_j N_j$ .

The detailed balancing introduced in Sect. 1.5 (Equations (1.20)) then yields,

$$P_1 + R_{21}N_2 = \Gamma_1 N_1 + R_{12}N_1 \quad (1.36a)$$

$$P_2 + R_{12}N_1 + R_{32}N_3 = R_{21}N_2 + R_{23}N_2 + \Gamma_2 N_2 \quad (1.36b)$$

$$P_3 + R_{23}N_2 = \Gamma_3 N_3 + R_{32}N_3 \quad (1.36c)$$

Making use of the identity Equation (1.23), and introducing the differences  $n_{ij}$  between the sublevel populations,

$$n_{ij} = \frac{N_i}{g_i} - \frac{N_j}{g_j} \quad (1.37)$$

we get,

$$n_{32} = \frac{(P_3 - \Gamma_3 N_3)}{R_{32} g_3} \quad (1.38a)$$

$$n_{21} = \frac{(\Gamma_1 N_1 - P_1)}{R_{21} g_2} \quad (1.38b)$$

and, since the total pump rate should equal the total loss rate out of the three-level system,

$$n_{32} R_{23} g_2 = n_{21} R_{21} g_2 + \Gamma_2 N_2 - P_2 \quad (1.39)$$

The explicit solutions for  $n_{32}$  and  $n_{21}$  after elimination of  $N_1$ ,  $N_2$ , and  $N_3$  are rather evolved, but from the above expressions, one can already infer that a level inversion ( $n_{32} > 0$ ) is maintained if the pump rate into level 3 exceeds the loss rate out of it, irrespective of the radiative transitions between levels 2 and 3. Similarly, the populations of levels 1 and 2 are inverted if the loss rate out of the lower level is larger than the pump rate into it. On the other hand, even if levels 1 and 2 are not inverted, the inversion of levels 2 and 3 can be maintained if the net rate of the depopulation of level 2 towards the external reservoir ( $\Gamma_2 N_2 - P_2$ ) is fast enough.

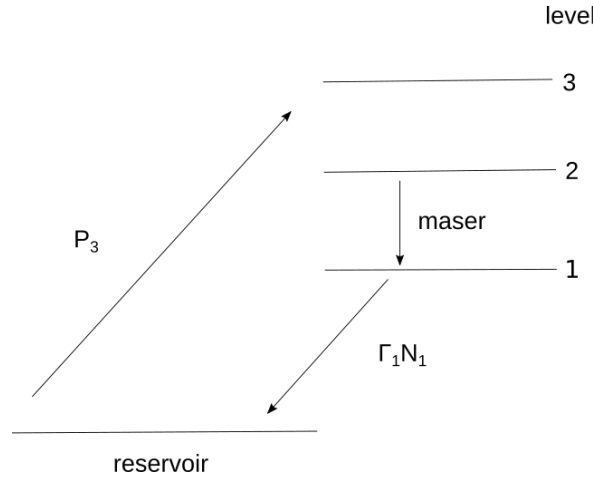


Figure 1.16: Simple three-level maser. For clarity, only selected pathways for pumping and losses are shown and indicated by the arrows labelled with  $P_3$  and  $\Gamma_1 N_1$  respectively. Further details are mentioned in the text.

## Astrophysical masers

*General Reference: Elitzur (1992)*

Naturally occurring masers were discovered in 1965 from hydroxyl (OH) in giant molecular clouds. The distinction between the thermal and non-thermal emission (maser) was confirmed by Weaver et al. (1965). The authors assigned the narrow emission line observed at 1665 MHz in W3 and Orion A as ‘mysterium’, which set the stage for the next discoveries and subsequent classifications of OH masers. While OH masers are also present in the circumstellar envelopes around AGB stars, here we will focus more on the discussion of masers found in the atmospheres of evolved stars that are relevant to this work.

When masers are mentioned in the context of evolved stars, the SiO molecule comes to the forefront for consideration. Kaifu et al. (1975) found SiO masers towards 12 of the objects from their survey and works by Deguchi (2007) reported that about 2000 stars (RGB, Mira variable, OH/IR, and semi-regular type) host SiO masers. After the formation of CO, in O-rich stars, oxygen that is available in surplus, forms SiO, whereas in the C-rich stars, excess carbon leads to the formation of HCN, giving rise to SiO and HCN masers as dominants, in O- and C-rich stars, respectively. Even though SiO and HCN masers are considered similar, they differ based on their location and main pumping mechanisms.

Masers from SiO, OH, and H<sub>2</sub>O in O-rich stars are typically found at low frequencies, which makes them easier to study. Maser emission is characterised by narrow, bright, variable and asymmetric line profiles (Bieging, 2001). Masers found in the atmospheres of C-rich stars are paving their way recently, especially with HCN, SiS, and CS molecules, which have been unsurprisingly found in IRC +10216 (e.g., Fonfría Expósito et al., 2006; Gong et al., 2017; Schilke and Menten, 2003, and many more). Maser emission from HCN was first discovered by Guilloteau et al. (1987) towards the carbon-rich late-type star CIT 6. This maser is considered similar to the SiO maser since it occurs in the rotational transition of  $J = 1-0$  in a vibrationally excited state, 2030 K above ground, as compared to 1770 K above ground for SiO. Soon after, Lucas and Cernicharo (1989) detected a strong maser in the  $J = 2-1$  transition from another vibrationally excited state. Shinnaga et al. (2009) find the  $J = 3-2$  HCN maser from a high vibrationally excited state to be present at a distance of  $15 R_*$  from IRC +10216. Schilke et al. (2000) and Schilke and Menten (2003) discovered the HCN maser lines at 804.751 GHz and 890.761 GHz towards multiple C-rich stars. For the archetypal C-rich star, IRC +10216, the lines are very bright, where the peak flux density is  $\sim 800$  Jy and 8000 Jy at 804.751 GHz and 890.761 GHz, respectively. Schilke and Menten (2003) identified the  $J = 9-8$  transition to be masing and inferred it to be present closer to the star. Because the  $(0, 4^0, 0)$  line has a lower energy of 4200 K above the ground state, it arises from the innermost part of the envelope. Wong (2019) imaged these lines with ALMA, confirming the maser region to be  $\sim 10-30$  AU size for V Hya and IRC +10216 (Humphreys et al., 2024). Similarly, we also discover numerous HCN masers in various C-rich stars using APEX and some of them can be deduced to be situated in the dust formation zone. More on that will be discussed in Chapter 2 and Appendix C.

The physical and chemical environment around the star, which is a fingerprint of its evolutionary stage, largely influences the various properties of the CSEs, which give rise to maser emissions. These emissions can be used to understand the evolutionary phase of the star. Baud and Habing (1983) analyse 1612 MHz maser stars to demonstrate that the OH maser properties are strongly related to the MLR, of which the evolution can be generalised if the time elapsed since the onset of the OH maser emission is referred to the lifetime of the latter. They discuss that MLR and the residual mass of the convective envelope are inversely proportional to each other at any given time. This relation was also confirmed by the study performed by de Jong (1983). Lewis (1989) approached the topic by using the infrared colours from the IRAS point-source catalogue as an indicator for the evolutionary sequence from Mira stars to protoplanetary nebulae. He then associated the IRAS point sources with known masers and inferred the chronological order of their appearance in a given expanding shell, namely, SiO, H<sub>2</sub>O, OH main-line and 1612 MHz masers. With the thickening of the shell, the masers disappear in the reverse order of their appearance, except for the 1612 MHz line. Interestingly, the main lines seem to reappear once the mass-loss process ceases and the shell is detached until it is so much dilated that this maser emission disappears as well.

Thus, if maser stars are treated as a stellar population, we are provided with an opportunity to perform statistical analysis and receive information about the end-of-life phases of the stars on the

AGB, which are scarcely available. Such analytical studies are crucial for constructing productive stellar evolution models for AGB objects. The use of interferometry is also proving to be essential to understanding the maser processes and overall physical and kinematical structure of the star. For instance, Chapman and Cohen (1986) reconstructed the velocity field using SiO, H<sub>2</sub>O, and OH masers and described the shell structure and the wind acceleration of the maser species. This study is complementary to studies of the dynamics of CSEs using thermal emissions (mainly from CO as discussed in Chapter 5 of this thesis), but for OH one has to distinguish between the main lines at 1665 and 1667 MHz and the satellite lines at 1612 and 1720 MHz. The underlying transitions are all located in the rotational ground state, but the main lines connect states of the same hyper-fine quantum number  $F$ , and the satellite lines those of different  $F$  (the designations “main” and “satellite” are due to the LTE line ratios, and not due to NLTE line ratios in CSEs). The main lines arise from the same zone as the water masers. However, to keep the inferred MLRs close to those determined from CO, one assumes a two-phase medium with a hotter, denser phase for the water maser emission, and a cooler, more tenuous one for the OH main lines (Richards et al., 2011; Gray, 2012). The satellite lines arise farther out in the CSE, where the abundance of CO has significantly decreased due to its photodissociation by the interstellar radiation field. This is why studies of CSE kinematics using CO thermal and OH maser emissions are complementary. For example, in the oxygen-rich AGB star W Hya, the abundance of CO drops due to its photo-dissociation to 50% at  $3 \times 10^{16}$  cm from the star (Mamon et al., 1988; Khouri et al., 2014), whereas even the main-line maser emission of OH, which is a photo-dissociation product of H<sub>2</sub>O, arises at  $1.5 \times 10^{17}$  cm from the star (Vlemmings et al., 2003). On the other hand, SiO masers (for oxygen-rich AGBs) and HCN masers (for their carbon-rich equivalents) trace the kinematics and physical conditions in the extended stellar photosphere, up to the dust-forming zone (Gray, 2012).

Besides their location, these masers also differ in their pumping mechanisms. OH masers were shown to be mainly pumped radiatively under far-infrared line overlap, but pumping routes involving collisional transitions within a given lambda-doublet are also at work (Gray et al., 2005). Water masers in star-forming regions were shown to originate in shocks and the 22 GHz maser line was shown to be collisionally pumped (de Jong, 1973). Later, Neufeld and Melnick (1991) demonstrated that collisional pumping drives millimetre and submillimetre-masers as well, also in CSEs. This statement is also valid for the recently detected THz water masers (Neufeld et al., 2017; Neufeld et al., 2021). In contrast, SiO masers are predominantly radiatively pumped, although collisionally pumped excitation pathways are also possible. The correlations between the stellar optical and near-infrared variability and the short phase-lags are taken as evidence in favour of radiative pumping. In turn, the latter cannot explain why VLBI observations locate different maser lines at different distances from the star (Gray, 2012, further references therein). The pumping of HCN masers is still uncertain. Menten et al. (2018) point out that the stellar infrared emission is sufficient for radiative pumping, but the missing correlation between the stellar and maser variability suggests that collisional pumping is also at work. This is also supported by the higher densities in the extended photospheres of C-rich AGB stars driving a stronger mass loss than their O-rich equivalents. We note that the hydrogen-abstraction reaction of CN offers a potential path towards chemical pumping, leaving the HCN molecule in a variety of vibrationally excited states. The mechanism is thought to drive astronomical and laboratory masers alike (Schilke et al., 2000, further references therein). Further details will be given in Chapter 2. Methanol masers, widespread in star-forming regions, are not discussed here because they are not detected towards AGB stars. The first thermal emissions were detected with ALMA towards the post-AGB star HD 101584 (Olofsson et al., 2017). Likewise, from ammonia, only thermal emissions

were detected (e.g., Justtanont et al., 2012, further references therein) while maser lines are reserved to environments forming high-mass stars.

## 1.7 Radiative transfer analysis: RATRAN

*General references: Rybicki and Hummer (1991), Rybicki and Hummer (1992), Hubeny (2003), Hogerheijde and van der Tak (2000) and Maercker et al. (2008).*

To correctly interpret the observed data, it is necessary to compare it with the predictions from CSE models. This can be achieved by solving the radiative transfer equation numerically for which a number of codes are available. These codes allow one to account for various astrophysical conditions, including various geometrical shapes. One such numerical code is publicly available for the 1D approach, called RATRAN (Hogerheijde and van der Tak, 2000). The authors use the flexibility offered by the Monte Carlo (MC) method. This method uses a large number of test photons to statistically describe their probability to propagate from one grid point to the next, or of being absorbed locally. The random approach of this method for the direction of integration is quite useful but it tends to get slow at high opacities ( $\tau \gtrsim 100$ ).

An important aspect in radiative transfer analysis is the non-local coupling between matter and radiation. In fact, the statistical equilibrium between exciting and de-exciting collisional and radiative processes requires an iterative approach to the solution. This is because the radiation from spatially separated volume elements that are coupled due to resonant Doppler shifts alters the level populations non-locally, which in turn modifies the emerging radiation field. *Lambda Iteration* (LI) was used to consistently solve for level populations and the radiation field (Rybicki and Hummer, 1991). This method is, however, quite slow as the photons get trapped in the cases of high opacities due to short mean free paths. Sometimes the solution is shown to converge to a local minimum before a proper global convergence is reached (see, for e.g., Hubeny, 2003). This problem is solved by introducing the *Accelerated Lambda Iteration* (ALI) technique. ALI simplifies the process by making the diagonal elements of the matrix (lambda operator) easier to handle and invert, compared to the ordinary LI method. In LI, the matrix can be large and cumbersome to invert, making ALI a more efficient alternative (Hubeny, 2003).

We use the publicly available code called RATRAN<sup>13</sup> to calculate the radiative transfer for our molecular and atomic lines. The authors of this code combine the MC and ALI methods to efficiently converge on a solution. We use this radiative transfer code in the publication presented in Appendix D, which is summarised in Chapter 3.

## 1.8 Outline of the thesis

The thesis is organised as follows: Chapter 2 summarises the published work presented in Appendix C on the vibrationally excited HCN transitions that are observed in the CSEs of 16 C-rich stars. We describe the observations conducted for the project, the population diagram analyses constraining the excitation temperatures and column densities for several sources. We also discuss the numerous discovered HCN masers, their temporal variability, and their possible pumping mechanisms.

---

<sup>13</sup> <https://personal.sron.nl/~vdtak/ratran/frames.html>

Chapter 3 summarises the work where we observe and analyse  $C^0$  and discuss its distribution in the CSE of IRC +10216 using observations and sophisticated radiative transfer modelling. Our finding places the  $C^0$  distribution in a thick-shell in the CSE. We also briefly discuss the presence of  $C^+$  in the central part of the envelope and how it signifies the distribution of these two atoms in the CSE. The published work is presented in its entirety in Appendix D.

Chapter 4 provides an overview of the Nearby Evolved Stars Survey (NESS), where we describe the survey's aims and motivation along with initial results. Chapter 5 deals with the third project in regards to this thesis, where we analyse the acquired dataset of 445 stars from various single dish telescopes, primarily APEX, and conduct statistical analysis on the data as AGB population using multi- $J$  CO transitions. In this work, we use an empirical formula to calculate MLRs for our sample and compare these MLRs with the literature. Appendices A and B provide tables presenting the line-fitting results including the calculated MLRs and the soft-parabola line fits of the observations, respectively.

Chapter 6 concludes the work presented in this thesis. This is followed by an outlook, which discusses how further observations can expand our knowledge of CSEs.



---

# Vibrationally excited HCN transitions in circumstellar envelopes of carbon-rich AGB stars

---

*This chapter summarises the contents of the published article (Jeste et al., 2022) presented in its entirety in Appendix C:*

## **Vibrationally excited HCN transitions in circumstellar envelopes of carbon-rich AGB stars**

Manali Jeste; Yan Gong; Ka Tat Wong; Karl M. Menten; Tomasz Kamiński; Friedrich Wyrowski

[Astronomy & Astrophysics, 2022, 666, A69 \(DOI: 10.1051/0004-6361/202243365\).](#)

## **2.1 Introduction**

Stellar winds from AGB stars are responsible for enriching the interstellar medium with an abundance of molecules, which are formed in the extended photospheres and envelopes of the AGB stars. Of these molecules, molecular hydrogen ( $\text{H}_2$ ) is the most abundant, followed by carbon monoxide (CO) in carbon- and oxygen-rich AGB stars. The third most abundant molecule found in the circumstellar envelopes of carbon-rich stars is hydrogen cyanide (HCN). Being one of the parent molecules in the envelopes, it is present in the innermost regions of the CSE and also in the outer shells before it is photo-dissociated into H and CN. The rotational lines arising from the vibrationally excited levels of HCN are extremely useful to trace the innermost region and are accessible to ground-based telescopes operating at millimetre and sub-millimetre wavelengths.

Hence, we use these lines to constrain the physical conditions in the inner regions of the CSE. In addition, the HCN molecule is known to exhibit maser emissions, introduced in the previous chapter. We use this opportunity to search for new HCN masers and explore the potential temporal variations using our data and previous studies. We also discuss the various pumping mechanisms at work.

## **2.2 Methods**

For our study, we selected 16 carbon-rich stars and observed them with the APEX telescope. The selection criteria were mainly based on two following conditions: (1) the sources should be observable with APEX; (2)

the carbon-rich nature of these stars has been confirmed by the detection of the HCN molecule in their CSEs. Out of the 16 stars, three were taken from Menten et al. (2018), three from Rau et al. (2017), and the rest of the 10 stars are from Massalkhi et al. (2018). Our sources vary in different parameters, with mass-loss rates ranging from  $10^{-7}$  to  $10^{-4} M_{\odot} \text{ yr}^{-1}$ , distances from 140 – 3300 pc, and with a large range of luminosities. We have also measured and discussed briefly, the pulsation phase of the stars during different observation periods.

We conducted observations of 26 rotational transitions of HCN,  $J = 2-1$ ,  $J = 3-2$ , and  $J = 4-3$ , in various vibrationally excited states, comprising a total observing time of 185.06 hours. The observational data was reduced using the GILDAS<sup>1</sup> software package (Pety, 2005). In the data reduction, a first polynomial order baseline was subtracted from each spectrum, and the spectra were smoothed to increase the signal-to-noise ratios (S/N).

## 2.3 Results

Below I summarise and briefly discuss the main results obtained from this project:

### 2.3.1 Our findings

Our large data-set presented us with a detection of 68 vibrationally excited lines of HCN from 13 carbon-rich AGB stars. Of these lines, 39 were found to be thermal while 29 were identified as maser in nature. In the following sections, I describe this phenomenology and observational distinction. Ground-state HCN transitions were detected in all the stars, where the emission line showed a parabolic shape, a characteristic feature of an optically thick line emitted from an expanding, spatially resolved CSE (Olofsson et al., 1982).

As for the vibrationally excited lines, the emission features more varied and complex line shapes, pertaining to its origin of thermal or maser emission in nature. The former lines exhibit Gaussian-shaped line profiles with FWHM  $> 8 \text{ km s}^{-1}$  and thus we fitted a single Gaussian component to derive the observed physical parameters, the results of which are presented in Table 6 of Jeste et al. (2022). Two of our sources, IRC +10216 and CRL 3068, exhibit a large number of thermal vibrationally excited HCN lines, allowing for a comparison of their fitted parameters. Interesting to note are the  $v_2 = 3$  lines in IRC +10216, which show a very narrow feature with expansion velocities of  $\sim 5 \text{ km s}^{-1}$ , which are well below the terminal wind speed of  $14 - 15 \text{ km s}^{-1}$ . We conclude that these lines form in the inner part of the envelope in agreement with their high energy levels. Comparing these lines with models of the velocity structure (e.g. in Decin et al., 2015), we inferred that they arise from the wind acceleration zone which is about  $8 - 10 R_{*}$  from the star.

This region of the envelope is very interesting and important to study as it is a host to high-temperature, volume-density, and extinction environments. It is not straightforward to study these regions due to the complexity introduced by photon-trapping and self-absorption.

In our study, we detected a number of non-thermal vibrationally excited lines (masers). We characterised the emission lines as masers because of their atypically high peak intensities and/or asymmetrical line profiles overlaid on a broader line. One of the indications for a maser action can be seen in the emission from  $J = 2-1$  ( $0, 1^{1e}, 0$ ) and ( $0, 1^{1f}, 0$ ) lines. The upper-level energies for the vibrational states are similar 1037.1 K and 1037.2 K, respectively, yet they show a vast difference in their peak intensity and line shape. Under LTE conditions, they should be identical but the deviation from such behaviour indicates maser action (see Fig. 1 from Appendix C). According to literature (see, e.g., Henkel et al., 1983; Schilke et al., 2000; Fonfría Expósito et al., 2006; Gong et al., 2017; Fonfría et al., 2018), these asymmetrical profiles with peaks at unique velocities seem to arise from a specific region in the CSE, as expected for maser action.

<sup>1</sup> <https://www.iram.fr/IRAMFR/GILDAS/>

### 2.3.2 Population diagram analysis

Despite these numerous detections of vibrationally excited lines, only those from two sources were detected with enough sensitivity to allow us to construct useful population diagrams, which were IRC +10216 and CRL 3068. The vibrationally excited lines, characterised by energy levels above 1000 K, exhibit narrow velocity ranges. As discussed above, this indicates that the observed line emissions arise from regions closer to the stellar surface, where the stellar outflow has not reached its terminal velocity yet. This region of the envelope, as discussed before, has not been probed very well. To better understand and constrain this region, we use the population diagram method to estimate the excitation temperature and the column density of the HCN molecule in this region. The results are presented in Table 7 of Appendix C.

For optically thin emission from a sufficient number of spectral lines from an ensemble of molecules whose excitation can be described by a Boltzmann distribution (Equation (1.19)), one can determine the column density and the excitation temperature. For a source function that is constant along the sightline, the specific intensity is given by Equation (1.32), which for  $\tau \ll 1$  can be approximated to first order in  $\tau$ ,

$$I_\nu = \Sigma_\nu \tau_\nu \quad (2.1)$$

Using Equations (1.30), (1.27), (1.26), (1.23), one can show that the frequency-integrated line area is given by

$$\int I_\nu d\nu = A_{ul} h_\nu N_u / (4\pi) \quad (2.2)$$

where  $A_{ul}$  is the Einstein coefficient and  $N_u$  is the column density of molecules in the upper state (the subscripts  $u$  and  $l$  refer to the upper and lower state of the transition, respectively).

The Boltzmann distribution (Equation (1.19)) can be written as

$$N_u = g_u N \exp(-E_u/k T_{\text{ex}}) / Q(T_{\text{ex}}) \quad (2.3)$$

where the partition function  $Q$  normalises the above equation such that the sum of  $N_u$  over all occupied states yields the total column density of the molecule,  $N$ . For rotational transitions characterised by a rotational constant  $B$ ,

$$Q(T_{\text{ex}}) = k T_{\text{ex}} / (h B) \quad (2.4)$$

which applies only for rotational levels within a given vibrational state, but is tabulated for the more general situation of ro-vibrational excitation in the JPL molecular spectroscopy and CDMS databases.

Combining the above expressions yields

$$\ln N_u = \ln \left( \int I_\nu d\nu 4\pi / (A_{ul} h_\nu) \right) = \ln(g_u N / Q(T_{\text{ex}})) - E_u/k T_{\text{ex}} \quad (2.5)$$

such that plotting  $\ln N$  against  $E_u/k$  yields a straight line of slope  $-1/T_{\text{ex}}$ . With the thus determined temperature and looking up the corresponding partition function, the ordinate intercept then yields  $N$ . In practice (e.g., Fig. 2.1), the data points will scatter around a straight line and one obtains  $T_{\text{ex}}$  and  $N$  from a linear regression analysis. When the prerequisites mentioned above are not fulfilled anymore, population diagrams across a larger number of energy levels become non-linear (e.g., the discussion in Nicolaes et al. 2018). The same happens if frequency- or instrument-dependent beam-filling factors are not correctly taken into account. We can safely exclude the latter situation, since our vibrationally excited emissions studies are spatially unresolved and therefore appear point-like in the APEX main beams.

### 2.3.3 HCN masers

We also studied the time variability shown by HCN masers by comparing their profiles with those of previous studies (2015, 2018, and 2021). We obtained data from 3 stars, IRC +10216, II Lup and RAFGL 4211 (Menten

et al., 2018). There is an increase of 86% in the flux density between the three epochs for IRC +10216, and of 25% and 63% in the first two epochs for II Lup and RAFGL 4211, respectively. These dramatic temporal variations are observed in the  $J = 2-1$  ( $0, 1^{1e}, 0$ ) transition, whereas the  $J = 2-1$  ( $0, 1^{1f}, 0$ ) transition does not change much. However, the time span between the observations of the HCN masers studied for the temporal variations is too large and we cannot conclusively associate them with stellar pulsation periods or other periodic variations. Fig. 2.1 shows an example of such variability in IRC +10216. Refer to Fig. 7 in Appendix C for time variability spectra seen in more sources.

An advantage of detecting such a large number of masers is the opportunity to study their pumping mechanism, which is detailed in Sect. 1.6.2. Infrared pumping is known to be an acceptable mechanism responsible for vibrationally excited HCN masers (Lucas and Cernicharo, 1989; Menten et al., 2018). By comparing the isotropic maser luminosities  $L_M$  and their corresponding infrared luminosities  $L_{IR}$ , we find that the ratio is more than 50 for all the HCN masers. This indicates that infrared photons are more than adequate to pump these HCN masers. Hence, the HCN masers are likely unsaturated in nature, because only in a saturated maser each pump photon is converted to a maser photon. The temporal variation in the masers can also be explained by this mechanism as the brightness temperature increases quadratically with decreasing source size (Shinnaga et al., 2009).

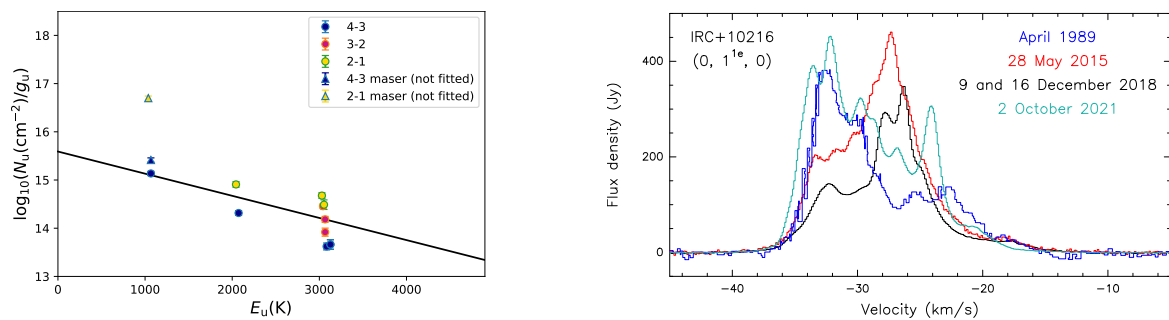


Figure 2.1: *Left*: Rotation diagram of IRC +10216 using vibrationally excited HCN lines. Some masers are plotted in the diagram for viewing purposes, shown by triangles, but are excluded from the linear least-square fit. *Right*: Temporal variations in the  $J = 2-1$  ( $0, 1^{1e}, 0$ ) line in IRC +10216. The spectrum in black shows observations from 2018, cyan from 2021, red from 2015 (Menten et al., 2018), and blue from 1989 (Lucas and Cernicharo, 1989). Figures are taken from Jeste et al. (2022).

## 2.4 Conclusions

1. Vibrationally excited HCN lines are ubiquitous in carbon-rich stars. Our observations detected 39 thermal and 29 non-thermal vibrationally excited lines. We expanded the total number of known masers by 47%. This study broadens the spectrally resolved detection of vibrationally excited HCN transitions beyond the very well-known and studied star, IRC +10216.
2. The population diagram analysis shows that the excitation temperatures for IRC +10216 and CRL 3068, 700 – 1000 K, are consistent with previous studies. Our source-averaged HCN column densities range from  $0.18-10.8 \times 10^{19} \text{ cm}^{-2}$  for six stars and the HCN abundance (relative to  $\text{H}_2$ ) is  $\sim 7.4 \pm 5.5 \times 10^{-5}$ .
3. Our study of the pumping mechanism of HCN masers indicates that the masers are unsaturated in nature, which we derive from the ratio of isotropic maser luminosities to infrared luminosities. The time variability of masers observed in our study can also be explained by their unsaturated nature as they vary exponentially in intensity on shorter timescales.
4. From a comparison between the photon luminosities of HCN masers and those of SiO masers, and because of their origin in the extended photosphere, we conclude that HCN masers in carbon-rich stars may serve as an analogue to SiO masers in oxygen-rich stars.

---

# [C I] and [C II] emission in the circumstellar envelope of IRC +10216

---

*This chapter summarises the contents of the published article (Jeste et al., 2023) presented in its entirety in Appendix D:*

**[C I] and [C II] emission in the circumstellar envelope of IRC +10216. I. Observational data and NLTE modelling of the [C I] emission**

Manali Jeste; Helmut Wiesemeyer; Karl M. Menten; Friedrich Wyrowski.

*Astronomy & Astrophysics*, 2023, 675, A139 (DOI: [10.1051/0004-6361/202346034](https://doi.org/10.1051/0004-6361/202346034)).

## 3.1 Context

IRC +10216 (also known as CW Leonis) is an archetypal carbon-rich AGB star, at a distance of 120 pc – 140 pc (Crosas and Menten, 1997; Groenewegen et al., 2012) from us, undergoing an episode of heavy mass-loss at a rate of  $2\text{--}4 \times 10^{-5} M_{\odot} \text{ yr}^{-1}$  (Crosas and Menten, 1997; De Beck and Olofsson, 2018; Fonfría et al., 2022). Imaging of its radio photosphere with the Very Large Array revealed the star’s luminosity as  $8600 L_{\odot}$  (Menten et al., 2012). IRC +10216 has a large extended envelope as seen in the ultraviolet images taken from GALEX (Sahai and Chronopoulos, 2010), bounded by its interaction with the ISM. The star is also very well known for hosting more than 80 molecular species in its CSE (see Cernicharo et al., 2000; Agúndez et al., 2014; De Beck and Olofsson, 2018; Pardo et al., 2022, and many other publications cited therein).

The large extent of the star’s CSE can be impressively seen in the work by Cernicharo et al. (2015b) and Guélin et al. (2018), who mapped the CO emission using the IRAM 30m telescope, followed by interferometric imaging at higher resolution. The emission reaches out to  $180''$  (distance from the star), beyond which CO undergoes photodissociation producing atomic carbon and, subsequently, ionised carbon. A detailed introduction to this star and the exceptional abundance of molecular species present in its CSE is discussed in Sect. 1.3.

In this publication, we aim to constrain the distribution of atomic carbon ( $C^0$ ) in the envelope of IRC +10216, with support from a dedicated photo-chemical model (Reach et al., 2022). We also shortly discuss the observations of ionised carbon ( $C^+$ ) emission conducted towards the star.

## 3.2 Methods

We performed single-dish observations of the [C I] line at 492.160700 GHz towards IRC +10216 in the  $^3P_1 \rightarrow ^3P_0$  transition using the APEX telescope. The observations were performed at the central position and then in a cross-cut manner in right ascension and declination, initially with a regular spacing of  $6.5''$  up to  $26''$  from the star, and then of  $13''$  up to  $78''$ . To further understand the line profiles, we fit Gaussian profiles to the line emission and also performed radiative transfer analysis.

Additionally, we also observed the fine-structure [C II] line at 1900.5369 GHz in the  $^2P_{3/2} \rightarrow ^2P_{1/2}$  transition with the SOFIA telescope using the upGREAT receiver at the central position of the star and also at  $32''$  from it. Details of the observations and instruments used are discussed in the article presented in Appendix D.

Data from both of these fine-structure lines were reduced and analysed using the CLASS software from the GILDAS package.

## 3.3 Results

### [C I] emission

In order to completely understand the distribution of the [C I] emission, we analysed the spectra qualitatively and, through non-LTE modelling, quantitatively. The observed spectra are presented in Fig. 3.2 and in the publication of Appendix D. Up to a  $13''$  (projected distance from the center), there is a clear distinction between the two emission peaks: the red-shifted peak from the receding rear hemisphere and its blue-shifted counterpart from the front hemisphere approaching us. Beyond this offset, the two peaks start to merge as the sightline-projected expansion velocity decreases. We compare our observational parameters with those from Keene et al. (1993) and see that, despite a  $\approx 30$  year gap between the two studies, the flux of our line emission is  $3.1 \text{ K km s}^{-1}$ , in agreement with Keene et al. (1993). In our model described below, the kinematical spacing of 90 AU corresponding, at the expansion speed of the CSE, to this time-lapse would lead to no change in the predicted line profiles, because the gas is flowing through the stationary [C I] emitting zone defined by the photodissociation radius of CO and the photoionisation radius of  $C^0$ . The line profile would change only if the [C I] emission originated from a freely expanding, thin shell. However, such a scenario does not reproduce the observed line shapes (see Fig. 2 in Appendix D).

The analysis of the neutral carbon distribution in the envelope is further investigated through NLTE excitation modelling using the radiative transfer code RATRAN. The model assumes a spherically symmetric envelope, with the star located at a distance of 130 pc and a mass-loss rate of  $2 \times 10^{-5} M_{\odot} \text{ yr}^{-1}$  (Cernicharo et al., 2015a; Reach et al., 2022; Fonfría et al., 2022). The expansion velocity of the gas is assumed to be  $V_{\text{exp}} = 14 \text{ km s}^{-1}$ , confirmed by the line-profile fits overlaid in Fig. 3.2. The input parameters are shown in Table 3.1. We use the  $C^0$  abundance profile of Reach et al. (2022) (see their Fig. 3) as input in our model to see how it affects the distribution of the [C I] emission compared to a model with constant abundance. The models are overlaid on the observed spectra in Fig. 3.2 to verify whether the observed spectra can be well reproduced by the adopted models. At the sensitivity of our data, it is not possible to favour either model; however we find a reasonable fit to our observations with a constant abundance of  $n(C^0)/n(H) = 4 \times 10^5$  and  $r_{\text{in}} = 4 \times 10^{16} \text{ cm}$ .

The figure shows a weakly self-absorbed blue-shifted peak in the spectrum of the central sightline. Both models are unable to reproduce this asymmetry, but otherwise describe the observed spectra quite well, except at the position of  $19.5''$ . Here, the variable abundance model, in green, underestimates the emission closer to the systematic velocity by  $1-2 \sigma_{\text{rms}}$  but the constant abundance model works quite well. At an offset of  $26''$ , both models overpredict the emissions close to  $\pm V_{\text{exp}}$ . Beyond these positions, the differences between the line profiles predicted by both models stay within the noise level of the observed spectra. In summary, the model proposed by Reach et al. (2022) represents the [C I] emission well, at least on seven out of nine sightlines.

Table 3.1: Input parameters for the RATRAN model of the [C I] emission

D	$M_{\odot}$	$r_{\text{in}}$	$r_{\text{out}}$	$n_{\text{H}_2}(r_{\text{in}})$	$T(r_{\text{in}})$	$v_{\text{exp}}$	$\Delta\nu$
[pc]	$[M_{\odot} \text{ yr}^{-1}]$	[cm]	[cm]	$[\text{cm}^{-3}]$	[K]	$[\text{km s}^{-1}]$	
130	$2 \times 10^{-5}$	$2.3 \times 10^{16}$	$1.9 \times 10^{18}$	$4.5 \times 10^4$	156	14.0	1.0

**Notes.**  $D$  = distance to the source,  $r_{\text{in}}$  and  $r_{\text{out}}$  = inner and outer radius, respectively, of the shell,  $v_{\text{exp}}$  = expansion velocity, and  $\Delta\nu$  = line width (1/e half-width).

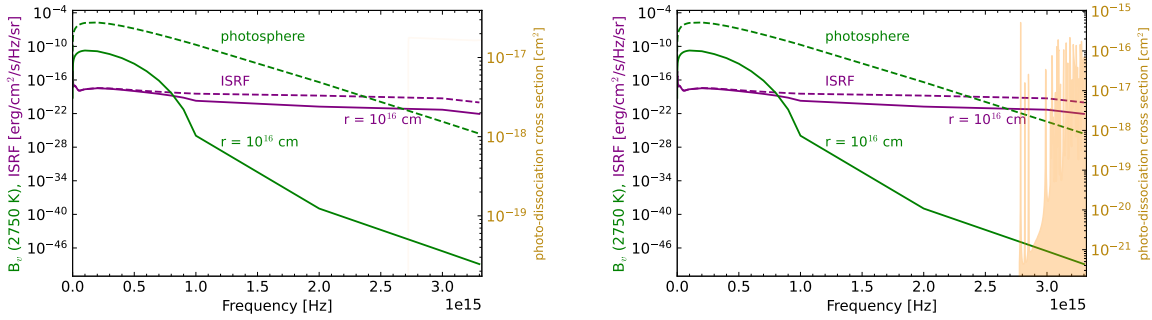


Figure 3.1: Cross-sections (right ordinates) for the photo-ionisation of C I and the photo-dissociation of CO, shown in *gold* (left and right figure, respectively). The solid *green* and *purple* lines show the SEDs (with left ordinates) of the attenuated stellar photosphere and ISRF respectively. The corresponding dashed lines are the unattenuated and undiluted radiation fields. The X-axis refers to the linear frequency scale. Figures are taken from Jeste et al. (2023).

## [C II] emission

The average spectra for [C II] emission are displayed in Fig. 3 of Appendix D. The line is only detected at the central position. The instrument's off-centre pixels, offset from the central one by  $32''$ , do not detect any emission from ionised carbon, even not upon averaging their spectra. The double-peaked profile of the line exhibits an asymmetrical shape, with FWHMs of  $8.1 \text{ km s}^{-1}$  and  $13.4 \text{ km s}^{-1}$  in the blue- and red-shifted velocities, respectively. This asymmetry, along with the non-detection at the off-centre position, is evidence that the [C II] emission could not only originate from the outer parts of the envelope exposed to the interstellar radiation field. The presence of [C II] emission in the central pixel raises the discussion about the possibility of an ionising source close to the star. At a distance of  $10^{16} \text{ cm}$  (700 AU), the diluted and attenuated photospheric emission from the star can't drive the photo-chemistry. This is demonstrated in Fig. 3.1, where the cross-sections for photo-ionisation of C I and the photodissociation of CO are shown together with the spectral energy distributions of the stellar and interstellar radiation fields. Reach et al. (2022) speculate that a companion could supply the ionising flux. Such a companion is indeed adopted by several works (e.g., Maunon and Huggins 1999; Cernicharo et al. 2015a; Siebert et al. 2022; Reach et al. 2022) to explain various shell structures observed in the CSE of this star but is not yet confirmed. We also see an emission feature present at a velocity of  $15 \text{ km s}^{-1}$ , which we attribute to the HNC  $J = 21-20$  transition. Due to its narrow line width of  $\sim 5 \text{ km s}^{-1}$ , significantly less than the terminal velocity of the expanding CSE of IRC +10216, we suggest that the line must originate close to the stellar photosphere (see Patel et al., 2009; Patel et al., 2011, for more discussion.)

### 3.4 Conclusions

#### [C I]

Our observations of the [C I] line of IRC+ 10216 show that the emission is optically thin, emerging from an extended and expanding envelope. On the inner sightlines significant emission is seen at red-shifted and blue-shifted velocities, displaying the characteristic "double-horn" profile. Only the spectra at 0'' and 6.5'' offset can be fitted by a model that consists of a thin, constant-abundance shell (with inner and outer radii of  $10^{17}$  and  $1.6 \times 10^{17}$  cm, respectively); nevertheless, it is unable to produce the emission found around the systemic velocity at distances of 13'' to 39'' (see Fig. 2 in Appendix D). Additionally, the modelled double-peak profile remains excessively strong and pronounced at 52'' and beyond, where the shell begins to emit at zero sightline-projected velocity, and the measured emission begins to fall below the detection limit. Our observations are more or less consistent with the literature (Keene et al., 1993) despite the 30 yr gap between both studies. Our models show that a constant, thick-shell abundance profile would best reproduce the line profiles observed at offsets from the star and places the inner boundary of the [C I]-emitting shell at  $\sim 10^{16}$  cm. While the photochemical model of Reach et al. (2022) for the  $C^0$  abundance works as well, its modification introducing a thin shell with co-spatial [C I] and [C II] emissions does not reproduce our observations.

#### [C II]

Interestingly, the presence of  $\sim 10 \text{ km s}^{-1}$  wide components of the line (FWHM), and the fact that the emission is present closer towards the star and not at distances  $\geq 20''-30''$  from it imply the presence of a source in the inner parts of the envelope, which is responsible for the ionisation of  $C^0$ . The speculation of the presence of a companion for this star has been ongoing for some time due to the star exhibiting multiple, partial shells in the optical (Mauron and Huggins, 1999), dust (Decin et al., 2011), and CO emissions (Cernicharo et al., 2015a; Decin et al., 2015; Guélin et al., 2018). Since our models are based on spherically symmetrical envelopes, we cannot infer a binary system being at play in this star. As evident in Fig. 3.1, the star itself is also not responsible for driving the photo-chemistry reactions, leaving interstellar UV photons entering the inner envelope on low-extinction sightlines through a patchy envelope as an attractive, but so far unconfirmed scenario. Interpreting the [C II] line profile with its two peaks, blue- and red-shifted with respect to the systemic velocity and with a weaker blue-shifted part (as compared to its red-shifted counterpart), is not straightforward either. As a matter of fact, this profile cannot be reproduced by any of the cases summarised in Table 5.2, and the line-centre optical depth is most likely too small to explain the asymmetry by self-absorption. A concrete conclusion can only be drawn with a full, critically sampled map of both tracers.

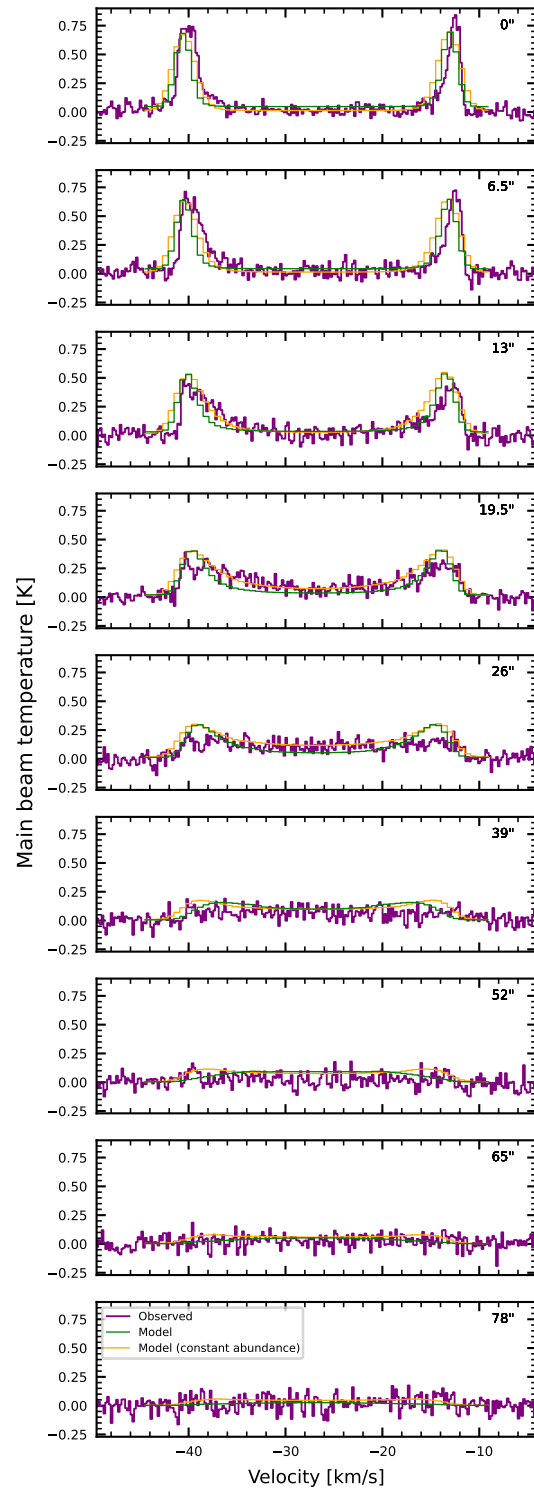


Figure 3.2:  ${}^3\text{P}_1 \rightarrow {}^3\text{P}_0$  emission of [C I] towards 9 offsets from the star (*in purple*), overlaid with modelled profiles with constant abundance (*in orange*) and variable abundance (*in green*). Figure from Jeste et al. (2023).



---

## The Nearby Evolved Stars Survey: NESS

---

*This chapter provides an overview of the NESS survey based on the publications by Scicluna et al. (2022) and Dharmawardena et al. (2018). Details about the methods and tools used are presented in these publications. My contributions to this survey are collecting and analysing new single dish telescope data and expanding the large sample as part of the NESS collaboration. The results and discussions will be presented in the next Chapter.*

### 4.1 Introduction

Having already established the importance of AGB stars and their vital role in the life cycle of the ISM, we now focus more on large-scale studies of these stars. The AGB phase is characterised by a succession of cycles consisting of helium-shell burning (thermal pulse, TP), a power-down phase, the third dredge-up and an interpulse phase whose duration depends on the mass of the stellar core. The third dredge up process is one of the main mechanisms that changes the chemistry on the surface of the star and subsequently its atmosphere. For more details, we refer to Sect. 1.1.4 and Karakas and Lattanzio (2014), with further references therein. Stars going through the TP-AGB phase expel material in the form of gas and dust. By studying their mass-loss rate (MLR), it is not only possible to constrain the star's mass and its evolutionary stage, but also to infer the composition of the dust, which governs the efficiency for converting the radiation pressure to the driving force launching the stellar wind. (e.g. Lagadec and Zijlstra, 2008; Uttenhaler et al., 2019).

As they are the major contributors of gas and dust to the ISM, numerous studies focus on AGB stars to get an estimate of the distribution of these products in galaxies. There is a missing link between the quantity of dust in the ISM and its sources. The contribution from AGB stars is not a major problem in the older galaxies like the Milky Way. In contrast, stars present in high-redshift galaxies are not evolved enough to be on the AGB yet, therefore more attention has to be paid closer to home. Srinivasan et al. (2016) and Riebel et al. (2012) have conducted studies on the dust production by AGB stars in the Small Magellanic Cloud (SMC) and Large Magellanic Cloud (LMC), respectively. Other sources responsible for dust production such as core-collapse supernova explosions are important to reconcile ultra-luminous infrared galaxies with their lack of AGB stars.

In Local Group galaxies, dust emissions have been successfully used as a tracer for evolved stars. But to use the gas as a tracer, they can only be studied by using molecular line emissions from bright stars (Groenewegen et al., 2016; Matsuura et al., 2016). In our Galaxy, this selection bias is much less severe, however, the interstellar extinction on sightlines through the Galactic disk and uncertain distances may lead to unreliable luminosity estimates.

Having established the need for large-scale studies to determine the return of products formed in the circumstellar envelopes (CSEs) to the ISM, and the importance of the AGBs' role in the chemical evolution of galaxies, we now proceed to discuss an overview of different studies. As mentioned before, CO is a very reliable tracer of mass-loss (see Sect. 1.6.1) and has been used for many decades to estimate MLRs. These

studies can be biased by the limited sensitivity of the telescopes at the time and thus the research was focused more on the brightest of these objects exhibiting a very high MLR. This bias takes place because such high mass-loss occurs only in the late evolution of more massive AGB stars. By limiting the studies to such objects, we are leaving out the low-mass AGB stars and earlier evolutionary stages. Very few research studies have been focused on targeting these objects. This is surprising because these stars make up a considerable number in other galaxies (see e.g. Boyer et al., 2015a; Boyer et al., 2015b) and for low-mass stars they represent the end-of-life phase (e.g. McDonald and Zijlstra, 2015).

Another shortcoming in the studies performed in the past is the lack of comparative studies across different types of stars. Some surveys targeted only a specific chemical type of stars: e.g., Olofsson et al. (1993) discussed a C-star sample while e.g., Sahai and Liechti (1995), Groenewegen and de Jong (1998) and Ramstedt et al. (2009) studied samples of S-type stars. Even though they offer large samples, comparing them is difficult owing to their varied sizes and volumes. Some of the studies have smaller sample sizes ( $\sim 10$ ) (e.g., Neri et al., 1998; Kemper et al., 2003; Teyssier et al., 2006; McDonald et al., 2018; Dharmawardena et al., 2018) while some have larger samples ( $\sim 100$  stars) (e.g. Kerschbaum and Olofsson, 1999; Olofsson et al., 2002; Loup et al., 1993; Kastner et al., 1993; Zuckerman et al., 1986; Zuckerman and Dyck, 1986a; Zuckerman and Dyck, 1986b; Zuckerman and Dyck, 1989). Despite the large sample sizes in some studies, the detection rates are often much lower.

The next factor to be considered is the transition to be preferred for such large-scale studies; CO (1–0) has been historically identified as a tracer of the “old” mass loss. Though it would give information on the oldest mass-loss events, there is potential contamination from the ISM when using telescopes with larger beam sizes. Therefore, lines from CO  $J = (2-1)$  and  $(3-2)$  provide a better solution. Naturally, for such studies, using interferometers offering high spatial resolutions may not be ideal because the completeness of the sample, difficult to achieve in such an approach, is quite important, and because extended molecular emissions may be missing in such data, which would require additional single dish maps. Hence single dish telescopes are preferred and those with large diameters provide high sensitivity. For instance, the JCMT with 15 m aperture provides angular resolutions of  $21''$  at 230 GHz and  $14''$  at 345 GHz. Similarly, the APEX with its 12 m aperture offers angular resolutions of  $25''$  at 230 GHz and  $17''$  at 345 GHz (for details see Sect. 1.4.2).

The factors mentioned above motivate the sample size, the telescopes used, and the objectives of the NESS project, which targets  $\sim 850$  AGB stars in the Milky Way. This project is also seen as a complement to other ongoing large programs toward AGB stars. For instance, DEtermining Accurate mass-loss rates for THERmally pulsing AGB STARS (DEATHSTAR)<sup>1</sup> is a survey using the Atacama Compact Array (ACA) observing  $\sim 180$  stars in medium spatial resolution  $5''.5/3-4''$  (Ramstedt et al., 2020). At the highest resolution, ALMA Tracing the Origins of Molecules forming dust In Oxygen-rich M-type stars (ATOMIUM)<sup>2</sup> uses Atacama Large Millimeter/submillimeter Array (ALMA) to observe 14 AGBs and red supergiants (Gottlieb et al., 2022; Decin et al., 2020). NESS complements these ongoing interferometric studies, with its much larger sample size and overarching goals which are mentioned below.

## 4.2 Aims of the survey

NESS targets a volume-limited sample of AGB stars in the Milky Way in CO molecular line and continuum emission. The main objectives can be broadly outlined as follows,

- To study the matter (gas and dust) that is being returned to the ISM by AGB stars
- To understand the physics of dust-driven stellar winds and their evolution

These can be further divided into following sub-groups:

---

<sup>1</sup> <http://www.astro.uu.se/deathstar>.

<sup>2</sup> <https://fys.kuleuven.be/ster/research-projects/aerosol/atomium>.

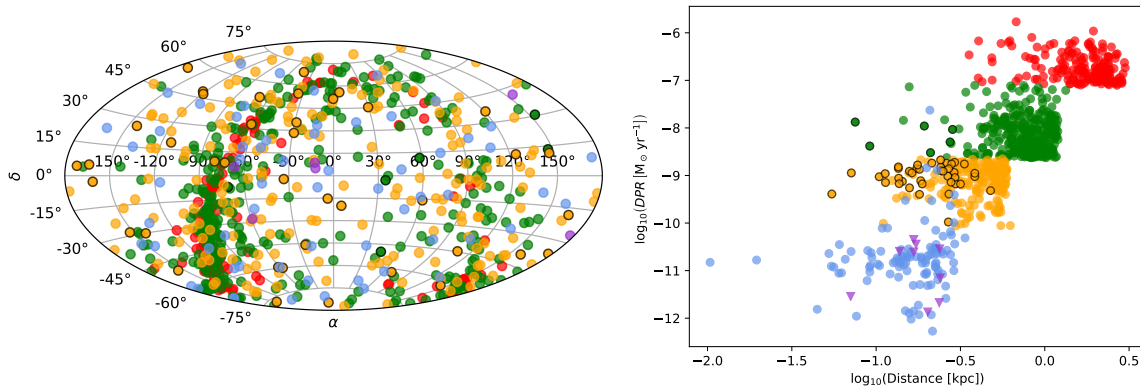


Figure 4.1: *left*: Total sky coverage of the NESS sample and *right*: NESS sample in the distance and DPR space. Tiers 0 to 4 are shown in purple, blue, orange, green, and red, respectively. Images taken from Scicluna et al. (2022).

1. *Statistics*: Since the sample is homogeneous and largely unbiased, the survey aims to be reliable for statistical studies.
2. *Return of the material to the ISM*: NESS aims to characterise the material returned by stars to the ISM when they are at different evolutionary stages on the AGB. It also aims to place better constraints on the return from stars with different chemical types, including stars with lower MLR, giving a fairer picture of the statistics of the population.
3. *Dust-to-gas ratio*: NESS aims to study variations of the dust-to-gas mass ratio across stars with different chemical types and at different evolutionary stages since previous studies have been limited by low sensitivity (Knapp and Morris, 1985).
4.  *$^{12}\text{CO}/^{13}\text{CO}$  abundance*: This ratio is quite important to study the efficiency of the dredge-up. Since our study also aims to cover the  $^{13}\text{CO}$  counterparts, there will be a significant increase in the sample size of the stars observed in lines from both isotopologues compared to previous studies. Most stars of the sample will be O-rich because of their high number in the Solar Neighbourhood and because they are in an earlier evolutionary stage. By studying the  $^{13}\text{CO}$  lines we can get information on the mixing processes and also the onset of the third dredge-up process.
5. *A new mass-loss formula*: NESS aims to provide a definite formula for measuring the mass-loss rate as previous studies have relied on empirical formulas. These formulae come with various uncertainties owing to, e.g., the sample size, the accuracy of the stellar parameters that are used, or the relationship between dust opacity and MLR. By using gas tracers, as NESS aims to, one can find a robust relationship between the MLR and the observable stellar parameters, which can be further used to constrain evolutionary models.
6. *Tracing mass-loss with better spatial resolution*: As part of the NESS project, various mapping procedures are also carried out to better understand the geometric variations in mass-loss. Additionally, the environmental impacts, such as external irradiation, on CO envelopes can provide insight into their influence on stellar ejecta.
7. *Dust*: Mapping the sources in continuum emission can reveal the historic mass-loss from dust and explore the evolution of dust grains and their interaction with the ISM.

### 4.3 Sample selection

As mentioned earlier, the sample for NESS should be a large volume-limited one, spanning a range of MLRs. Observations of CO lines *and* dust continuum ensures completeness and avoid biases. Taking this into account, several factors come into play. An appropriate sample selection requires carefully established criteria. The following subsections summarise such considerations. For further details see Scicluna et al. (2022) and references therein.

- *Distance measurements:* One of the key estimates for the sample selection is to have reliable estimates for distances. Maser parallaxes provide very accurate measurements for sources with the highest MLRs and are thus the priority for shortlisting the sources. Whenever these are not available, parallaxes from Gaia data release 1 (DR1) (Gaia Collaboration et al., 2016) and *Hipparcos* (van Leeuwen, 2007) are used.
- *Selecting the stars:* The point-source catalogue by the *Infrared Astronomical Satellite (IRAS)* is used as a reliable source for target selection (*Infrared Astronomical Satellite (IRAS) Catalogs and Atlases. Volume 1: Explanatory Supplement*. 1988). The *IRAS* photometry was matched with the 2MASS catalogue (Cutri et al., 2003) and sources within a distance of 30'' were selected. Further steps were taken in regards to applying a threshold for the distance, brightness, and the dust production rates (DPRs) resulting in about 60,000 stars. Sect. 2.3.2 of Scicluna et al. (2022) provides a detailed description of the procedure. Since the 60,000 stars are still too many to be observed in a reasonable amount of observing time, the authors structured a tiered system, which serves each tier with a representative sample in a DPR vs. distance plane (see Fig. 4.1). This reduced the number of stars to 2277, and further discarding the sources with inconsistent classifications (compared with entries in SIMBAD<sup>3</sup>), the final sample size consists of 852 stars.
- *Dust production rates:* This quantity (DPR or  $\dot{M}_{dust}$ ) is determined by matching the photometry from the *IRAS* 12, 25, and 60  $\mu\text{m}$  bands and 2MASS *J*, *H*, and *K<sub>s</sub>* bands and fitting them with the models presented in the Grid of Red supergiant and AGB ModelS (GRAMS; Srinivasan et al., 2011; Sargent et al., 2011). Another motivation to use this quantity is that  $\dot{M}_{dust} \sim \dot{M}$ , under certain assumptions (see Sect. 2.3.3 in Scicluna et al., 2022). The stars are divided into a staring sample and a mapping sample, depending on whether their CSEs are point-like or spatially resolved. The latter is less in number but will provide detailed information (see, e.g., Dharmawardena et al., 2018). GRAMS also provides the chemical information on the stars (O-/C-type). For the NESS sample, we assume that a source is O-rich unless it is confirmed by *IRAS* LRS or *Infrared Space Observatory (ISO)* Short Wavelength Spectrometer (SWS) spectra. This is also in order as M-stars are more numerous in the Milky Way. These claims are important as we perform a preliminary analysis of our NESS sample based on the classification in Chapter 5 and thus caution should be taken about this potential bias.
- *Staring sample:* We only mention the staring sample here as it is relevant to this thesis. The NESS sample is divided into several tiers as presented below based on distance and  $\dot{M}_{dust}$ :
  1. Tier 0 ('very low') DPR sources are located at a distance  $d < 250$  pc without any limit on  $\dot{M}_{dust}$ . These are special sources aimed at deriving mass-loss from RSGs and AGBs not producing dust.
  2. Tier 1 ('low') include 105 lowest DPR sources with  $\dot{M}_{dust} < 10^{-10} M_{\odot}\text{yr}^{-1}$  at  $d < 300$  pc,
  3. Tier 2 ('intermediate') includes 222 sources with  $10^{-10} M_{\odot}\text{yr}^{-1} \leq \dot{M}_{dust} < 3 \times 10^{-9} M_{\odot}\text{yr}^{-1}$  and  $d < 600$  pc,
  4. Tier 3 ('high') contains 324 sources with  $3 \times 10^{-9} M_{\odot}\text{yr}^{-1} \leq \dot{M}_{dust} < 10^{-7} M_{\odot}\text{yr}^{-1}$  at  $d < 1200$  pc,
  5. Tier 4 ('extreme') consists of 182 sources with  $\dot{M}_{dust} \geq 10^{-7} M_{\odot}\text{yr}^{-1}$  at  $d < 3000$  pc.

Fig. 4.1 presents the distribution of the sample in a DPR-versus-distance plot segregated based on the different tiers.

<sup>3</sup> <http://simbad.u-strasbg.fr/simbad/>

## 4.4 Observations

Observations for the above-mentioned sample are conducted in CO (2–1) and CO (3–2) lines along with continuum observations for  $\delta > -40^\circ$  with the JCMT telescope, which consists of 500 out of the 852 total sources. A detailed explanation is presented in Wallström et al. (in prep.) and Scicluna et al. (2022). The sample is complemented with APEX observations from the southern hemisphere consisting of 237 out of 852 sources. Chapter 5 deals with the observations and results obtained for the APEX sample.

## 4.5 Summary of results

*Since the thesis does not focus on the specific results obtained in the publication, below I briefly summarise the initial results from the survey, as a whole, based on Scicluna et al. (2022).*

1. The NESS sample ranges across AGB stars with varied masses and MLRs. The initial analysis of the whole sample shows that stars that show high DPR are present near the Galactic plane and are most likely massive AGBs/ RSGs.
2. Stars present at larger Galactic scale heights are part of the older population with lower DPRs.
3. O-rich stars dominate the dust production in the sample. Models fit to the Spectral Energy Distributions (SEDs) to get an estimate of the sample's DPRs, give an integrated value of  $4.7 \times 10^{-5} M_\odot \text{ yr}^{-1}$  for the total sample.
4. The initial analysis of the mapped sources shows that extended emission is present up to  $\sim 30''$  in the CO (3–2) line observations. These findings are particularly useful to trace the gas mass-loss history and will complement the dust mass-loss information presented in studies such as Dharmawardena et al. (2018) to determine the variance of the gas-to-dust ratio across the envelope.
5. A preliminary analysis of JCMT sub-mm continuum observations shows consistency of sub-mm emission with the blackbody emission in the Rayleigh-Jeans regime (except for two sources).

See Scicluna et al. (2022) for detailed information on the analysis results mentioned above. The work presented by NESS will be useful for future, more sensitive observing facilities (e.g., James Webb Space Telescope), offering a deeper understanding of nearby sources and enhancing our knowledge of more distant ones.



---

# NESS: Initial results from single dish multi-*J* CO observations

---

*This chapter presents the work conducted as part of the NESS collaboration. My contributions to this project consist of acquiring the observational data, combining various single dish observations spanning across multi-*J* CO transitions and analysing of the whole sample, along with performing statistical analysis, and writing the manuscript. This project is one of the main contributors to the NESS collaboration, as it includes sources from the southern hemisphere.*

## 5.1 Introduction

Stars with low and intermediate mass reach the AGB phase in the later stages of their life when the helium in their cores is exhausted (see Sect. 1.1.4 for more details). Throughout this phase, owing to a radiatively driven wind, they lose a substantial fraction of their mass, which creates a circumstellar envelope (CSE) around them. The material constituting the latter, a plethora of molecular species and dust, mixes with the interstellar medium (ISM). The chemical composition of the dust varies across the stellar evolution on the AGB and mainly depends on the oxygen-to-carbon ratio, which determines which species is left for the nucleation of dust after the less abundant of these species is used up for the production of CO.

### 5.1.1 General background

Starting from an oxygen-rich wind, the mixing of nucleosynthesis products into the convective envelope, known as the third dredge-up which accompanies each thermal pulse (e.g., Karakas and Lattanzio, 2014), increases the carbon fraction in the stellar photosphere, exceeding that of oxygen after a sufficient number of thermal pulses. Only recently it became clear that the underlying mass-loss and dust-production histories depend not only on the stellar mass and the evolutionary age on the AGB, but also on the complexity introduced by deviations from spherical symmetry (Decin, 2021), which are induced by shocks forming in response to the stellar pulsation and large-scale convective motions (Freytag and Höfner, 2023) and also by interaction with companions of stellar or sub-stellar mass (Aydi and Mohamed, 2022). Through the interplay between mass loss and dust production (see, e.g., Gail, 2003; Bladh et al., 2019), this complexity leaves its fingerprint in observable quantities. The identification and characterisation of these fingerprints are among the primary objectives of the Nearby Evolved Stars Survey (NESS) program (Scicluna et al., 2022) studying AGB stars within a distance of 3 kpc.

Ultimately, assisted by synthetic samples (e.g., Bladh et al., 2019), we expect answers to questions such as the chemical enrichment of the ISM by AGB stars, the connection between dust production and mass loss, and the role of binary companions.

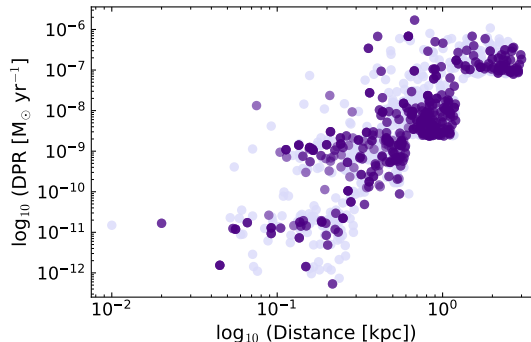


Figure 5.1: Sub-sample distribution (this work, in purple) overlotted on the complete sample of NESS.

### 5.1.2 The Sample of NESS sources

NESS comprises a volume-limited sample of  $\sim 850$  AGB stars within a distance of 3 kpc observed in submillimetre dust emission and various transitions of the CO molecule. An overview of the survey’s aims and first results are given by Scicluna et al. (2022) and a detailed catalogue explanation will be presented in McDonald et al. (in prep.). Various large single dish telescopes are used to observe the stars in both hemispheres. In the northern hemisphere, large-program observations of the CO 2–1 and 3–2 line with the James Clerk Maxwell Telescope (JCMT) towards  $\sim 500$  stars have been ongoing and will be discussed, along with a first analysis, in Wallström et al. (in preparation). The Atacama Pathfinder EXperiment (APEX) telescope has observed the southern part of the NESS sample in the same CO lines. We additionally observed the  $^{12}\text{CO}$  (1–0) line towards a small sample as this ground state line provides information about the most extended outer CO envelope, giving us an insight into the conditions in the oldest mass-losing state. For this, we used the IRAM 30-m telescope, which simultaneously provided the CO (2–1) line. Fig. 5.1 shows the dust-production rates in the total sample versus distance. The sources that are part of the sub-sample that is presented in this study are overlaid.

In brief, the work at hand contains a sample of 445 stars observed with the APEX, IRAM-30m, JCMT, SEST, and OSO telescopes, ranging over various tiers of mass-loss rates (see Scicluna et al. (2022) for more details). We first give an overview of the data (see Table 5.1 for a setup overview) and present the observational details for each telescope used, followed by the data reduction steps in Section 5.2. Section 5.3 provides the analysis method used in this research to determine various line parameters and an initial estimate of the mass-loss properties of the sample. The results and their discussion are presented in Sections 5.4 and 5.5, respectively. We then conclude our work in Section 5.6. Additionally, appendices A and B provide result tables and spectra for our large sample, respectively.

## 5.2 Observations and data reduction

We conducted observations with the IRAM-30m telescope in the northern and the APEX telescope in the southern hemisphere. We also used CO (1–0) data published by Olofsson et al. (1993) and Kerschbaum and Olofsson (1999) that were acquired with the OSO and the SEST telescopes. See Fig. 5.1 for the sample distribution. In the following, we describe the observed data and their reduction in detail.

### 5.2.1 APEX observations

We observed 237 sources in the southern hemisphere with the Atacama Pathfinder EXperiment (APEX), a 12 m diameter submillimeter telescope (Güsten et al., 2006) in the CO (2–1) and (3–2) lines under project IDs

Table 5.1: Receiver setups for observations with APEX, IRAM-30m, OSO, and SEST telescopes.

Telescope	Receiver	Tuning $\nu$ (SB) (GHz)	$J_u - J_l$	$\eta_{\text{mb}}$	$\theta_b$ ( $''$ )
APEX	PI230(a)	231.2 (USB)	2–1	0.74	27
	nFLASH230(a)	231 (USB)	2–1	0.68	27
	SEPIA345(a)	344.3 (USB)	3–2	0.72	18
	LAsMA(a)	344.29 (USB)	3–2	0.70	18
IRAM-30m	EMIR(b)	114 (UO)	1–0	0.78	21.3
	EMIR(b)	231.5 (UI)	2–1	0.59	10.7
JCMT	RxA3(c)	230.5	2–1	0.58	21
	HARP(c)	345.7	3–2	0.57	14
OSO(d)	–	–	1–0	0.3	33
SEST(d)	–	–	1–0	0.7	45

**Notes.** Column 3 refers to the tuning frequency (sideband), col. 4 to the observed CO transition, col. 5 to the main-beam efficiency, and col. 6 to the beam size (FWHM) at the respective transition. Main-beam parameters and further receiver information are from (a): <https://www.apex-telescope.org/ns/instruments/>, (b): <https://publicwiki.iram.es/EmirforAstronomers>, Carter et al. (2012), (c): <https://www.eaobservatory.org/jcmt/instrumentation/heterodyne/>, (d): Olofsson et al. (1993) and Kerschbaum and Olofsson (1999).

O-0101.F-9308A,B and M-0105.F-9534A,C. The observations were performed in 2018 and over two semesters from 2020 September 30 to 2021 November 17 under (for the APEX site) moderate weather conditions. The observations were scheduled when the precipitable water-vapour levels content was  $< 5$  mm and  $< 2$  mm for the CO (2–1) and (3–2) lines, respectively. We used various receivers for our observations. The lower- $J$  lines were observed with the nFLASH230 and PI230 instruments. For the higher- $J$  line, we made use of the SEPIA345 receiver and the Large APEX sub-Millimeter Array (hereafter: LAsMA), a 345 GHz 7-pixel multi-beam receiver.

To convert the antenna temperature scale  $T_A^*$  of the spectra to the main-beam temperature scale ( $T_{\text{mb}}$ ) we adopted a forward efficiency ( $\eta_f$ ) of 0.95 and the main-beam efficiencies from the APEX website (see Table 5.1 for the relevant values).

## 5.2.2 IRAM-30m observations

We performed staring-mode observations with the 30m telescope of the Institut de Radioastronomie Millimétrique (hereafter: IRAM-30m) towards 32 stars from our sample, in the CO (1–0) and CO (2–1) lines. They were conducted on 2021 March 5 and May 13 (project 142-20) and 2021 June 18–20 (project 062-21) in very good weather conditions with precipitable water-vapour levels ranging from 0.11 to 1.08 and from 0.19 to 1.02 mm, respectively. Total-power backgrounds were removed by wobbler switching except for three sources observed in frequency switching mode: 17361-2807, 17277-2356, and 18096-1003 to avoid CO contamination. We used the Eight Mixer Receiver (EMIR) (Carter et al., 2012) as frontend and the FTS200 Fast Fourier Spectrometer as backend, allowing us to observe the two CO lines simultaneously by combining the EMIR E090 and E230 bands. Main-beam parameters are reported in Table 5.1.

### 5.2.3 JCMT observations

The northern counterpart of the NESS sample is being discussed in Wallström, S. et al (in prep.), where the JCMT observations and data analysis are described in detail. They target  $\sim 500$  sources with declination  $\delta > -30^\circ$  in the CO (2–1) and CO (3–2) lines, along with their isotopologues. In addition to the new observations, they have also included archival data taken with RxA3 and HARP receivers, which contain sources at  $\delta < -30^\circ$ . We have included these 71 stars in our analysis as they belong to our southern NESS sub-sample.

### 5.2.4 SEST and OSO observations

Olofsson et al. (1993) and Kerschbaum and Olofsson (1999) have conducted large-scale surveys to study circumstellar envelopes in various CO transitions. We included their CO  $J = 1-0$  spectra in our analysis to correct for the flux missing in our resolved-out, single-pointing IRAM-30m observations. Their observations were conducted from 1986 to 1992 for the former work and from 1993 to 1998 for the latter. A complete list of telescopes, beams, and beam efficiencies is provided in Table 5.1.

### 5.2.5 Data reduction

After the acquisition of the APEX and IRAM-30m data from 2018 to 2022 and the construction of a homogeneous dataset, I performed the following data reduction steps using the GILDAS<sup>1</sup> software package (Pety, 2005): spectral resampling to  $1 \text{ km s}^{-1}$  resolution so as to be consistent with the JCMT observations, the conversion to main-beam brightness temperatures, and the subtraction of first-order baselines.

These steps are slightly altered while working with the SEST and OSO observations. We only used the sources that are also present in our catalogue (Scicluna et al., 2022)<sup>2</sup>. The data was provided in a reduced FITS format and reduced as per the aforementioned steps.

## 5.3 Data analysis

Wallström et al (in prep.) present the analysis of the JCMT observations in the NESS sample. Here, we perform a similar analysis for our complementary southern sample. The reduced data has run through a line-fitting script, the features of which we describe in the following.

For spatially unresolved observations, the line profile is controlled by the optical depth of the emission (Olofsson et al., 1993). The following analysis of line formation in an expanding circumstellar envelope is similar to the treatises by H. Olofsson (Chapter 7 in Olofsson (2004) and appendix to Olofsson et al. (1993)).

In the optically thin case, the solution of the radiative transfer equation for a constant source function (or excitation temperature), Equation (1.34), can be approximated to first order in optical depth,

$$I_\nu = \Sigma_\nu (1 - \exp(-\tau)) \approx \Sigma_\nu \tau = \Sigma_\nu \int \kappa_\nu ds, \quad (5.1)$$

where the integral extends over the sightline. The flux density received by emission at a sightline-projected velocity  $v_z$  from spatially unresolved observations is then proportional to

$$F_\nu(v_z) \propto \int_{p_1(v_z)}^{p_2(v_z)} 2\pi p N(p, v) dp, \quad (5.2)$$

where  $p$  is the impact parameter (the vertical distance from the central sightline), as shown in Fig. 5.2. Using

<sup>1</sup> <https://www.iram.fr/IRAMFR/GILDAS/>

<sup>2</sup> <https://evolvedstars.space/catalogue/>

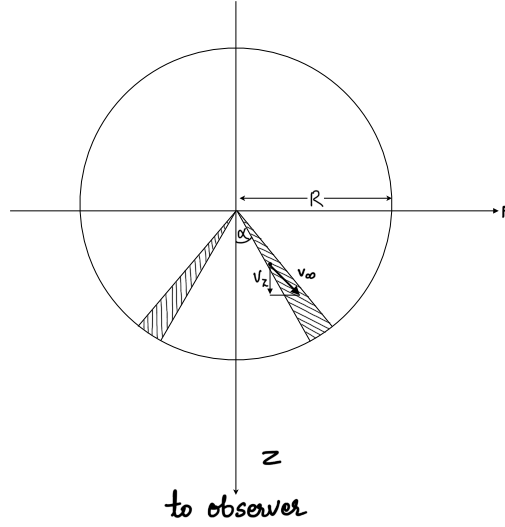


Figure 5.2: Sketch (in projection, viewed from above the sightline) of a circumstellar envelope of outer radius  $R$ , expanding at velocity  $v_\infty$ . The emission at a given velocity  $v_z$  originates from the surface of a cone with half opening angle  $\alpha = a \cos \frac{v_z}{v_\infty}$  (hatched area).

the radial expansion of the envelope, we can obtain the column density  $N$  of the gas as,

$$v_z = v_\infty \cos \alpha = v_\infty \frac{z}{\sqrt{p^2 + z^2}}, \quad (5.3)$$

i.e., the emission at that velocity arises from a cone (whose axis of symmetry coincides with the  $z$ -axis in Fig. 5.2, the sightline) with opening half-angle  $\alpha = \arccos(v_z/v_\infty)$ , where  $v_\infty$  is the expansion velocity of the envelope. The subscript refers to the fact that this velocity is reached asymptotically after the initial acceleration of the wind (see Sect. 1.2). In the following, we apply the scaling  $v = v_z/v_\infty$  without loss of generality; the same scaling applies to the linewidth  $\Delta v$ .

To allow for an analytical solution and by omitting constant prefactors, we assume a rectangular line profile of full width  $\Delta v$ . For each sightline (i.e., impact parameter  $p$ ), the coherence length for a given velocity  $v$  and hence the column density  $N(p, v)$  are given by,

$$N(p, v) = \int_{v-\Delta v/2}^{v+\Delta v/2} n(p, v) \frac{dz}{dv} dv = \begin{cases} n_0 r_0^2 \frac{\Delta v}{p(1-v^2)^{1/2}} & \text{where } p \leq R\sqrt{1-v^2} \\ 0 & \text{elsewhere,} \end{cases} \quad (5.4)$$

where we use the radial dependence of the volume density  $n$  of emitting molecules expected for mass conservation in a constant-velocity flow,  $n = n_0(r/r_0)^{-2}$ . The change of variables in the above sightline integral,  $z \rightarrow v$ , is unambiguous for all sightlines, except for the central one where  $v = 1$  at any position  $z$ . The case distinction asserts that the sightline under consideration contains gas moving at a projected velocity  $v$ . For a spatially unresolved observation, one obtains from Equation (5.2) a spectrum with a rectangular profile (Fig.5.3 (a)), because of

$$F_\nu(v) \propto \frac{1}{\Delta v} \int_0^{R\sqrt{1-v^2}} \frac{2\pi n_0 r_0^2 \Delta v}{(1-v^2)^{1/2}} dp = \begin{cases} 2\pi n_0 r_0^2 R & \text{where } |v| < 1 \\ 0 & \text{elsewhere.} \end{cases} \quad (5.5)$$

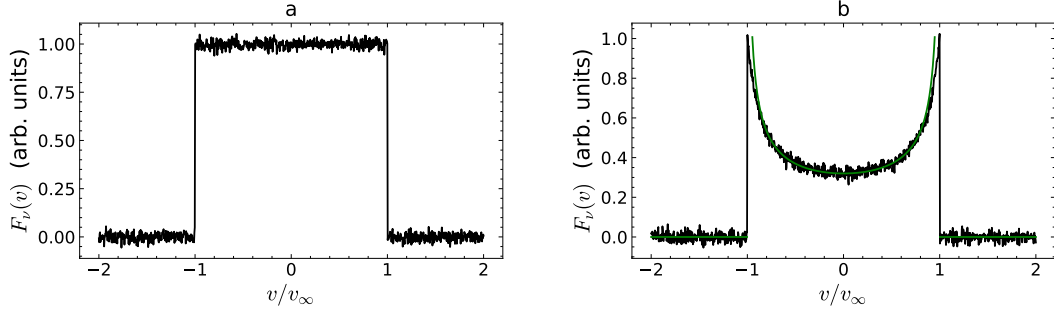


Figure 5.3: Line profile of optically thin emission from a circumstellar envelope expanding at a constant speed ( $v_\infty$ ), normalised to unity at maximum, for a signal-to-noise ratio of 50 at peak, for (a) a spatially unresolved observation, and (b)  $\theta = 0.6 R/D$  (from Eq. (5.6)), with an overlaid fit (green line profile) of the form  $F_\nu(v) = a/(1-v^2)^{0.5}$ .

A more realistic description would replace the rectangular line profile by the Gaussian one for a Maxwellian velocity distribution. The result of Equation (5.4), however, can be expressed in closed form only by introducing hypergeometric series of two variables (Appell, 1880). For a phenomenological description of the line formation in expanding envelopes, the above description is nevertheless useful since most of the line profiles from the NESS survey  $\Delta v \ll 1$ .

We therefore rather address an important generalisation of our line-formation analysis, namely, the coupling of the observing beam (of half-power width  $\theta$ , cf. Sect. 1.4.1) to the envelope, which matters as soon as  $R/D \sim \theta$ . We modify Equation (5.5) accordingly:

$$\begin{aligned}
 F_\nu(v) &\propto \int_0^{R\sqrt{1-v^2}} \exp(-4 \ln 2p^2/\theta D)^2 \frac{2\pi n_0 r_0^2}{(1-v^2)^{1/2}} dp \\
 &= \pi^{3/2} n_0 r_0^2 \theta D \frac{\text{Erf} \left( 2R \frac{\sqrt{\ln 2(1-v^2)}}{\theta D} \right)}{2\sqrt{\ln 2(1-v^2)}}
 \end{aligned} \tag{5.6}$$

The result for an envelope with  $\theta = 0.6 R/D$  is shown in Fig. 5.3 (b). In practice, for arguments  $> 1.986$  the error function deviates from unity by less than 0.5% and the line profile can be approximately expressed as,

$$F_\nu(v) \propto \frac{1}{2} \cdot \frac{\pi^{3/2} n_0 r_0^2 \theta D}{\sqrt{\ln 2(1-v^2)}} \tag{5.7}$$

except close to the singularity  $v = 1$ . We note that by applying de l'Hôpital's rule for  $|v| \rightarrow 1$  to Equation (5.6), one obtains,

$$F_\nu(|v| = 1) \propto 2\pi n_0 r_0^2 R \tag{5.8}$$

A similar demonstration can be provided for the case of an excitation gradient of the form  $T_{\text{ex}}(r) = T_{\text{ex}}(r_0) r_0/r$ , and yields, for a spatially resolved CSE,  $F(v) \sim 1/(1-v^2)^2$  (Olofsson, 2004). For comparison, the temperature gradient due to the adiabatic expansion of molecular gas expanding at constant velocity is  $T \sim r^{-4/3}$  (below 300 K, Crosas and Menten, 1997).

In the following, we address the optically thick case, which represents the majority of CO line profiles in the NESS survey. Since within a coherence length  $L(p, v) = \Delta v dz/dv$  we can assume uniform excitation conditions

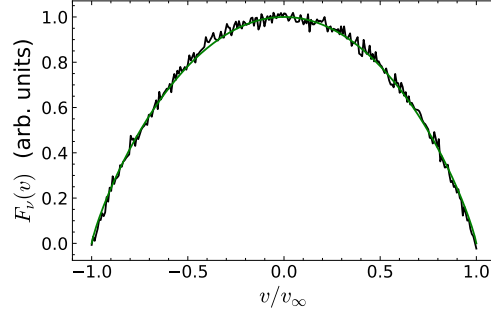


Figure 5.4: Optically thick emission ( $\tau_{R,0} = 4$ ) as observed in a beam of width  $\theta = 2R$  (FWHM), for a signal-to-noise ratio of 50 at peak. The green line is a soft-parabola with  $\beta = 1.7$  (from least-square fitting).

optical depth	spatially unresolved ( $\theta \gg R/D$ )	spatially resolved ( $\theta \ll R/D$ )
$\tau \ll 1$	$\beta = 0$ (rectangular)	$\beta = -1$ (double peak, $T_{\text{ex}} = \text{const.}$ ), $\beta = -2$ (double peak, $T_{\text{ex}} \sim 1/r$ )
$\tau \gg 1$	$\beta = 2$ (inverted parabola)	$\beta = 0$ (rectangular), $\beta = 1$ (“soft parabola”, $T_{\text{ex}} \sim 1/r$ )

Table 5.2: Table describing line shape parameters for cases with different optical depths and spatial resolution of the source.

and obtain, employing Equation (1.32),

$$F(v) = \int_0^{R\sqrt{1-v^2}} 2\pi p \left( 1 - \exp\left(\frac{-\tau_{0,R}R}{p\sqrt{1-v^2}}\right) \right) \exp\left(-4 \ln(2) \left(\frac{p}{\theta}\right)^2\right) dp, \quad (5.9)$$

where  $\tau_{R,0} = \tau(p = R, v = 0)$  is the line-centre optical depth at the outer boundary of the CSE. Equation (5.9) can be only partially expressed in closed form. Since the integrand is continuous in  $p$ , one can find a fitting function that allows us to evaluate Equation (5.9) in terms of error functions. For our applications,  $\tau_{0,R} > \sim 1$  and the following approximation describes integral in the interval:

$$F(v) \approx \int_0^{R\sqrt{1-v^2}} 2\pi p \exp(-a(p-b)^2) dp = \frac{\pi}{a} [\exp(-ab^2) - \exp(-a(b - R\sqrt{1-v^2})^2)] \\ + \pi b \sqrt{\frac{\pi}{a}} [\text{erf}((-b + R\sqrt{1-v^2})\sqrt{a}) + \text{erf}((b + R\sqrt{1-v^2})\sqrt{a})] \quad (5.10)$$

with parameters  $a$  and  $b$  fitting the integrand with a relative accuracy of  $\sim 10^{-3}$ . The result is shown in Fig. 5.4, along with a line-profile fit of the form  $F(v) = F(0) (1-v^2)^{\beta/2}$  (with  $\beta > 0$ , i.e., a “soft parabola”). For an excitation gradient of the form  $T_{\text{ex}} \sim 1/r$ , one can show in a similar way that  $\beta = 1$  (Olofsson, 2004). For the limiting case of a very high opacity ( $\tau_{R,0} \gg 1$ ) and a spatially unresolved observation ( $\theta \gg R/D$ ), one obtains from the then straightforward analytical solution of Equation (5.9)  $\beta = 2$ , i.e., an inverted parabola. For a spatially resolved observation ( $\theta \ll R/D$ ), the line profile becomes rectangular.

In summary, all cases described above can be approximated by  $F(v) = F(0) (1-v^2)^{\beta/2}$ , with  $\beta$  ranging from  $-2$  to  $+2$ . An overview is given in Table 5.2.

One can see that with a single observation of a rectangular profile, one can a priori not decide whether the

line is optically thick or thin. This ambiguity can be broken by observing several, half-beam spaced sightlines (e.g., a five-point cross) and/or an optically thin isotopologue.

In our case, i.e., single dish observations of optically thick lines, most profiles exhibit parabolic shapes, turning into a “soft parabola” for spatially resolved targets. We thus use the more general soft parabola model introduced above to determine the line-fitting parameters following De Beck et al. (2010):

$$T_v = T_{\text{MB}} \left[ 1 - \left( \frac{v - v_{\text{LSR}}}{v_\infty} \right)^2 \right]^{\beta/2}, \text{ with } |v - v_{\text{LSR}}| < v_\infty \quad (5.11)$$

where  $T_{\text{MB}}$  is the main-beam brightness temperature at the peak of the emission line,  $v_{\text{LSR}}$  the velocity of the star with respect to the local standard of rest (LSR),  $v_\infty$  the expansion velocity of the gas, and  $\beta$  the line shape parameter introduced above. Since this parameter is a fit to an observed line profile or an (analytically or numerically) computed one, its value does not entirely indicate whether we can integrate it analytically.

The line fit calculates the peak brightness temperature, expansion velocity, LSR velocity, and the root-mean-square deviation of the fit residuals, for each source, transition, and telescope. The errors for these parameters are then calculated using the EMCEE package (Foreman-Mackey et al., 2013) based on the MCMC method (Metropolis et al., 1953; Hastings, 1970; Speagle, 2019). In this, we create a sampler using arguments to specify the number of walkers (*nwalkers*), dimensions (*ndim*), and also to calculate the natural logarithm of the posterior probability for the determined parameter set. This sampler then passes through the MCMC sampling, taking into account the position and number of samples (*nsamples*) that are to be generated. We then analyse and reshape the outcome in an array containing the positions of the walkers and discard the initial samples that may not have reached the distribution we aimed for. For our calculations we have, *nwalkers* = 100, *nsamples* = 10000, and *ndim* = 4.

After we have obtained the line-fit parameters and their uncertainties, we calculate the velocity-integrated flux densities and inferred mass-loss rates (MLR) for the respective CO lines. For such a large sample, we use an empirical formula to determine the MLR, which is presented in Ramstedt et al. (2008) and will be discussed in Section 5.5,

$$\dot{M} = s_J (I_{\text{CO}} \theta_b^2 D^2)^{a_J} v_\infty^{b_J} f_{\text{CO}}^{-c_J}, \quad (5.12)$$

where  $\dot{M}$  is the MLR,  $I_{\text{CO}}$  the profile-integrated flux density (hereafter “line area”, in  $\text{K km s}^{-1}$ ),  $\theta_b$  the beam size in arcseconds (see Table 5.1 for our observations),  $D$  the distance in pc,  $v_\infty$  the expansion velocity, and  $f_{\text{CO}}$  the CO abundance with respect to  $\text{H}_2$ .  $a_J$ ,  $b_J$ ,  $c_J$ , and  $s_J$  are parameters for various transitions and are provided in Table A.1 of Ramstedt et al. (2008). They account for the applied unit conventions such that  $\dot{M}$  is given in  $M_\odot \text{ yr}^{-1}$ .

## 5.4 Results and discussion of line-shape parameters

In this work we present the initial analysis of 334 stars from the total NESS sample, applying the methods introduced in the previous section. Our total sample consisted of 445 stars but we filtered our observations due to possible contamination from the interstellar lines. 237 stars are observed with APEX and 71 stars with the JCMT in the CO (2–1) and CO (3–2) transitions, 32 stars with the IRAM-30m telescope in the CO (1–0) and CO (2–1) transition. We have additional data for the CO (1–0) line observed with the SEST telescope for 44 stars and OSO telescope for 22 stars. There is an overlap of observations with different telescopes for a number of sources, hence the total observed unique stars are 334.

Because for a given observing frequency the spatial extent of the CO-emitting area with respect to that covered by the main beam of the observations (hereafter called “beam-filling factor”) differs from telescope to telescope, we present the results separately for each telescope; they are summarised in the table presented in Appendix A. The JCMT data are discussed in detail in Wallström et al. (in prep.).

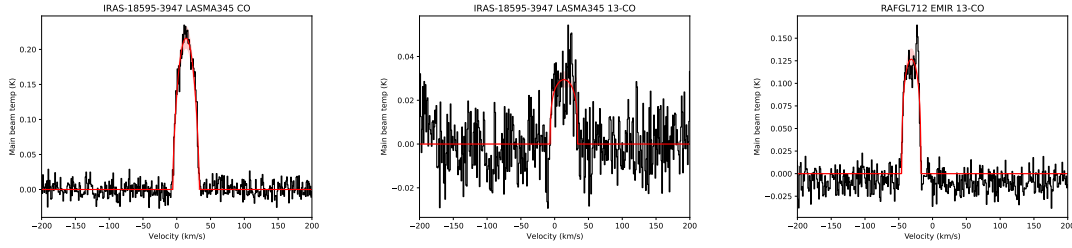


Figure 5.5:  $^{12}\text{CO}$  (3–2) (left) and  $^{13}\text{CO}$  (3–2) (centre) emission towards 18595-3947 (RAFGL 5552) observed with the APEX telescope.  $^{13}\text{CO}$  (1–0) (right) emission towards RAFGL 712 observed with the IRAM-30m telescope.

### 5.4.1 APEX observations

With the APEX telescope, we observed the CO (2–1) and (3–2) lines towards 237 sources. Note that there is an overlap of stars for which both lines are observed. After filtering, our sample consists of 168 stars. We have detection rates of 70% and 18% in the  $J = 2-1$  transitions of  $^{12}\text{CO}$  and  $^{13}\text{CO}$ , respectively, while 51% of  $^{12}\text{CO}$  and only 3% of  $^{13}\text{CO}$  is detected for the higher transition. Fig. 5.5 (left and centre) shows an example of the CO (3–2) transition from both isotopologues.

The  $^{12}\text{CO}/^{13}\text{CO}$  ratio is defined as the ratio between the line areas of the two profiles. Its distribution, shown in Fig. 5.6 (left), can be described as a log-normal distribution, mainly comprised in the range of 0 – 25 for both lines, in agreement with Olofsson et al. (2022) who obtain a similar distribution towards a sample of 22 high mass-loss targets in the inner Galactic Bulge (Olofsson et al., 2022). Whether this is a purely coincidental result or because both populations derive from AGB stars where most of the Galactic  $^{13}\text{C}$  is produced (e.g., Karakas and Lattanzio, 2014) remains to be confirmed. Owing to the saturated  $^{12}\text{CO}$  lines, the vast majority of these ratios fall below those of the Galactic  $^{12}\text{CO}/^{13}\text{CO}$  abundance distribution (Langer and Penzias, 1990), which in turn exceeds than seen in  $^{12}\text{CH}/^{13}\text{CH}$ , less affected by chemical fractionation (Jacob et al., 2020). We also observe a few optically thin  $^{12}\text{CO}$  lines where the top has multiple peaks or is flat-topped; high-sensitivity follow-up  $^{12}\text{CO}/^{13}\text{CO}$  observations of those targets might be a promising tool to unveil the underlying abundance distribution.

As for the line shape, the  $\beta$  parameter (Fig. 5.7, left) shows a bimodal distribution for an ensemble comprising both isotopologues: The optically thin  $^{13}\text{CO}$  emission peaks at  $\beta = 0.5$  (“soft-parabola”, almost rectangular profiles), while the optically thick  $^{12}\text{CO}$  emission has a higher  $\beta$  value of 1.5. Interestingly, the  $^{12}\text{CO}$  (3–2) line is described by a bimodal distribution. If this does not reflect an uncertainty due to the lower sensitivity of the CO (3–2) spectra, it could potentially be attributed to optical depth effects: In local thermodynamic equilibrium and under the same thermal line broadening, for an indicative gas temperature of 200 K, the optical depths of the (1–0), (2–1) and (3–2) transitions have ratios of 1:0.72:0.66. The medians for the CO (2–1) and (3–2) transitions are  $\beta = 0.7$  and 0.59, respectively.

Fig. 5.8 (top left) shows the MLR plotted against  $v_\infty$  for all the sources observed with APEX in the CO (2–1) and CO (3–2) transitions. The lowest MLR that was calculated in this sample is  $1.94 \times 10^{-11} \text{ M}_\odot \text{ yr}^{-1}$  and the highest is  $4.44 \times 10^{-5} \text{ M}_\odot \text{ yr}^{-1}$ . Our estimates of the MLR from the CO (2–1) transition tend to be higher compared to those of the CO (3–2) transition. The median for  $v_\infty$  for both lines is about  $15 \text{ km s}^{-1}$ .

### 5.4.2 IRAM observations

Observations in  $^{12}\text{CO}$  and  $^{13}\text{CO}$ ,  $J = 1-0$ , were conducted with the IRAM-30m telescope towards 32 stars (with  $^{12}\text{CO}$  (2–1) in parallel). The obtained line fit parameters and their calculated MLRs are again presented in Appendix A. In the  $^{12}\text{CO}$  (1–0) transition, no emission was detected in 18% of the 32 sources. About 34% show a parabolic (and often slightly optically thin) feature. 5 sources have single-channel emissions, which are most

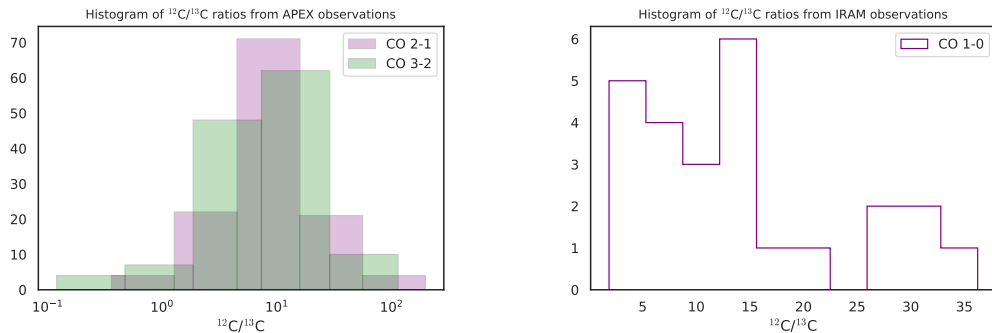


Figure 5.6: *Left:* Histogram showing the distribution of  $\log_{10}({}^{12}\text{CO}/{}^{13}\text{CO})$  ratio for APEX observations. *Right:*  ${}^{12}\text{CO}/{}^{13}\text{CO}$  ratio for IRAM observations

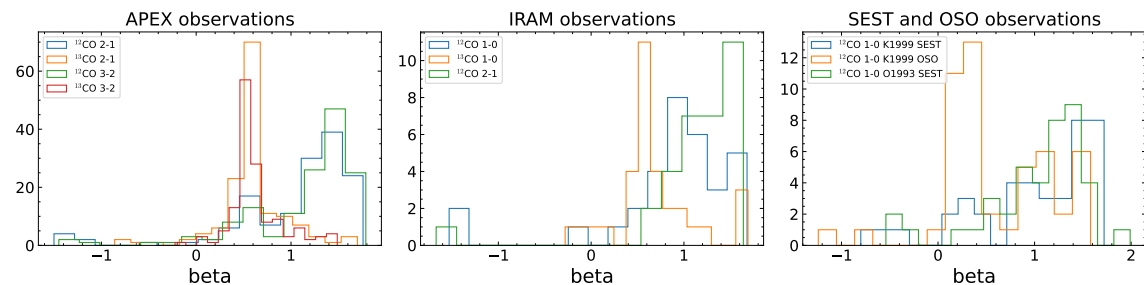


Figure 5.7: (*From left to right:*)  $\beta$  parameters for APEX, IRAM, SEST and OSO observations.

likely originating from loosely associated interstellar gas with narrow emission lines. For the  ${}^{13}\text{CO}$  emission in the same transition, we have 21 sources with non-detections, the same 5 sources with single channel emission, and two optically thin emission lines. Fig. 5.5 (right) shows optically thin  ${}^{13}\text{CO}$  emission in the (1–0) transition.

Fig. 5.6 shows the distribution of the  ${}^{12}\text{CO}/{}^{13}\text{CO}$  ratios in the CO (1–0) transition. The values are again largely contained between 0 and 20. Fig. 5.7 (centre) presents the histogram for the  $\beta$  parameter fitted in all three emission lines. The distribution shows that most of the  ${}^{13}\text{CO}$  emission is between  $-0.28$  and  $1.69$ , with the highest peak at  $0.5$ .  ${}^{12}\text{CO}$  emission in 1–0 and 2–1 transition is largely present in the higher end of the  $\beta$  parameter, implying optically thick emission. Considering Fig. 5.7, the optically thin emission line,  ${}^{13}\text{CO}$  (1–0), is fitted with a soft-parabolic line shape. Thus, caution should be exercised since it can be seen that the line-fitting procedure does not always fit the line well. This could be due to the lower signal-to-noise ratio, where the distinction between double-peaked and soft-parabolic line profiles is less definitive. Owing to the smaller sample size, the expected bimodal distribution that is apparent in the APEX sample of both isotopologues is less pronounced here.

Fig. 5.8 (*top right*) presents the MLR vs  $V_{\text{exp}}$  distribution for the CO (1–0) and CO (2–1) transitions. The MLRs obtained for the former transition fall systematically above those for the latter, at almost all expansion speeds. They range from  $7.23 \times 10^{-7}$  to  $1.72 \times 10^{-5} M_{\odot}/\text{yr}$  for the ground-state transition, while for the higher transition, the MLRs are comprised between  $2.59 \times 10^{-7}$  and  $8.25 \times 10^{-6} M_{\odot}/\text{yr}$ . We attribute this result to a potential flux loss in the CO 2–1 lines, due to the smaller beamwidth ( $10.''7$  vs.  $21.''3$ , cf. Table 5.1). The expansion velocities accumulate between 6 and  $17 \text{ km s}^{-1}$ , if one ignores outliers below  $5 \text{ km s}^{-1}$ , which we attribute again to interstellar CO emission (an alternative will be discussed in section 5.5).

### 5.4.3 SEST and OSO observations

#### CO 1–0 survey from Olofsson et al. (1993)

In this work, a CO survey of carbon stars within 900 pc from the Sun was performed using the SEST telescope. We obtained a part of their detections to extract crucial information on the CO 1–0 emission, which is prone to flux loss in our IRAM observations. Out of this sample, 15 stars are part of our NESS sample. We analysed the line profiles as described above. More than 70% of the sources exhibit a soft-parabolic shape, while some show two velocity components, indicating optically thin emission. Fig. 5.7 (*right*) shows (in green) the distribution of the deduced line-shape parameters  $\beta$ , most ranging from  $\beta = 0.1$  to 1.7, which implies optically thick emission. We also plot the distribution of the MLRs versus the expansion velocities in Fig. 5.8 (*bottom right*), which will be discussed below.

#### CO 1–0 survey from Kerschbaum and Olofsson (1999)

This survey was conducted towards oxygen-rich semiregular and irregular variables in various CO transitions for 109 stars. Here, we used a part of their sample, 51 stars, observed in the CO (1–0) transition using the SEST and OSO telescopes. The initial analysis shows that in a large portion of the OSO sample, the line-profile shape-parameter falls between  $\beta = 0$  and 0.5, as seen on the right panel of Fig. 5.7, and the parameter interval  $\beta = (1.0, 1.5)$  is the second-best populated one as expected due to the high opacities. The distribution of the MLR vs  $v_\infty$  is fairly narrow, with the highest  $V_{\text{exp}}$  at  $\approx 15 \text{ km s}^{-1}$  in the OSO sample (bottom-right panel of Fig. 5.8).

#### Comparison of the SEST/OSO surveys

There is a clear distinction between the samples from Olofsson et al. (1993) and Kerschbaum and Olofsson (1999). One part of the former coincides with the latter, another part – stars with high  $v_\infty$  and correspondingly high MLRs – has almost no equivalent sub-sample from Kerschbaum and Olofsson (1999). This is because the former survey specifically targets carbon stars and the latter oxygen-rich ones. It is interesting to note, however, that the respective mass-loss rates in the two samples do not differ by as much as an order of magnitude, a finding that we will discuss in the next section.

## 5.5 Discussion

### 5.5.1 Distributions of mass-loss rates and expansion velocities

Fig. 5.9 presents the distribution of the MLRs and expansion velocities for stars with different chemical types. There is a clear distinction in the distribution of expansion velocities. That of O-rich stars is mainly distributed between 2 and 20  $\text{km s}^{-1}$  peaking in the (10, 20)  $\text{km s}^{-1}$  interval, while for C-rich stars, the range of the distribution is larger and lies between 2–35  $\text{km s}^{-1}$ , peaking between 15–20  $\text{km s}^{-1}$ . As shown in Fig. 5.9 (*right*), our distribution agrees with that of Loup et al. (1993), who collected a comprehensive list of observations and stellar parameters from literature, for CO (1–0), CO (2–1), and HCN (1–0) lines. They found that O-rich stars tend to have a narrower distribution for  $V_{\text{exp}}$  compared to the C-rich ones. There is a clear cut-off for this range of O-rich stars, while the distribution for C-rich is more spread, which we also see in our results. There is a possibility of a bias towards O-rich stars, which will be discussed later.

For the MLR distribution, the normalised distributions for O-rich and C-rich stars differ as well, as expected and already visible in the foregoing inspection of the OSO/SEST data. Such a difference can be naturally explained by the larger opacity of carbon grains, hence leading to higher radiative accelerations and mass loss in C-stars, which was already observed by Ramstedt et al. (2009), and in the earlier studies of Loup et al. (1993). In our sample, the difference between the MLR distributions of the two compositions is moderate and not overwhelming, which, given the different opacities of carbon and silicate grains, might be surprising.

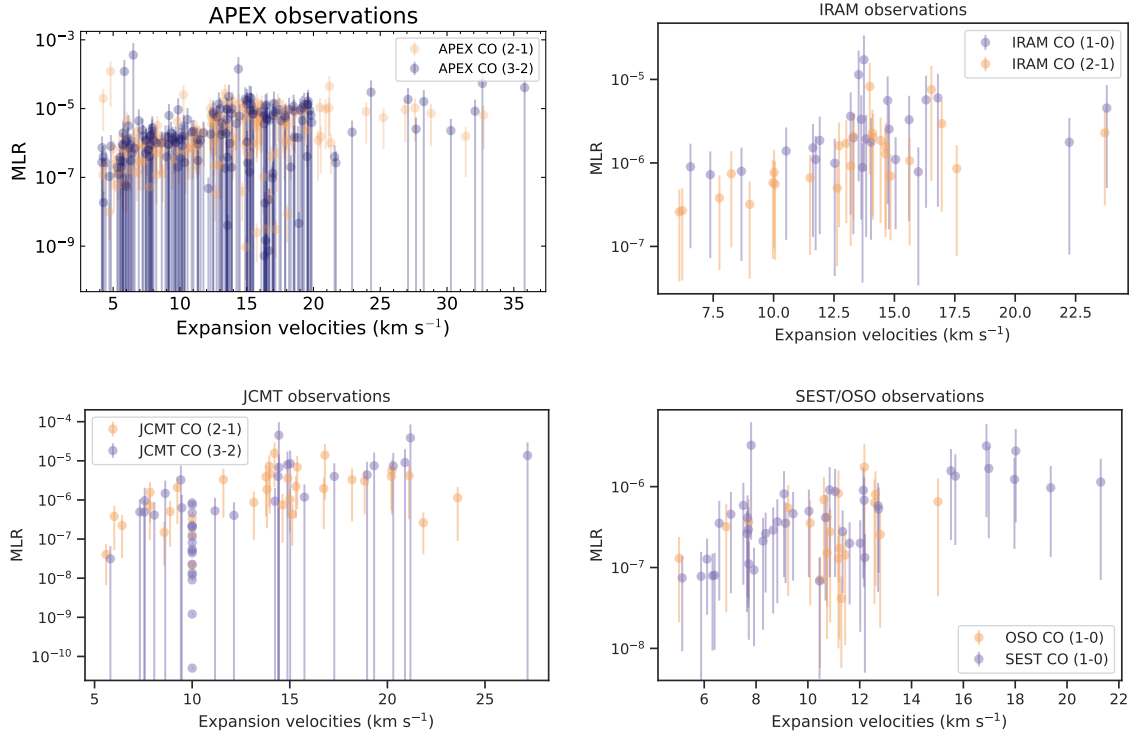


Figure 5.8: (Clockwise from top left:) MLR vs. expansion speed for APEX, IRAM, SEST/OSO, and JCMT observations. The latter are shown for completeness and discussed in Wallström et al. (in prep.).

The concern of how oxygen-rich AGB stars can efficiently power radiatively driven winds was expressed by Woitke (2006); solutions to that conundrum were presented later on. Höfner and Andersen (2007) combined a non-equilibrium dust nucleation model with radiation hydrodynamics. Their model predicts a population of carbon grains to be present in the atmospheres of O-rich stars as well and to efficiently drive their winds. In contrast, the natural Fe content of silicate grains (olivine and pyroxene) induces a steep grain absorption coefficient, setting an inner threshold for the condensation radius at  $\sim 10 R_*$ , which is too far away for efficient wind acceleration. Subsequently, Fe-free silicate grains were recognised to radiatively drive winds, thanks to the contribution of dust-scattered photons, and a feedback between grain growth and wind acceleration resulting in the formation of  $\sim 1 \mu\text{m}$ -sized dust particles as close as  $2\text{--}3 R_*$  from the star's centre (Höfner, 2008). This scenario was later confirmed by Bladh et al. (2019), whose work will be revisited in the following correlation analysis.

## 5.5.2 Correlation analysis

Although a correlation between the mass-loss rate and the expansion velocity is enforced by applying Equation (5.12) to the line profile fits, there are two reasons for further examination: First, the correlation could be deteriorated or cancelled by too large errors, or a potential irrelevance, for some spectra, of the fitting parameters deduced from the NLTE study (Ramstedt et al., 2008), or by potential anti-correlations introduced by the remaining observationally deduced quantities (such as beam-filling factors). Second, Equation (5.12) does not explicitly reflect the velocity dependence, because the latter is partially hidden in the line area  $I_{\text{CO}}$ . Morris (1975) has demonstrated that the line-centre optical depth (i.e., at the stellar systemic velocity) in a spherical shell expanding at constant velocity and mass-loss rate scales with  $\dot{M} f_{\text{CO}} / v_\infty^2$ . The  $1/v_\infty^2$  dependence

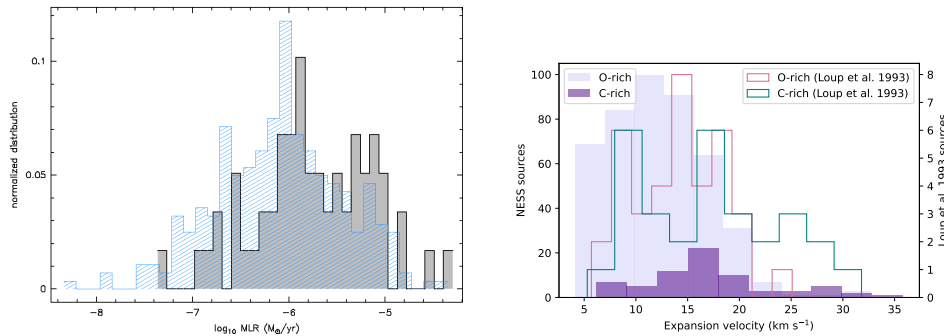


Figure 5.9: Histograms showing the distribution of MLRs (figure on the *left*), where blue indicates O-rich stars and grey indicates C-rich stars and (figure on the *right*) expansion velocities segregated based on their chemical types.

arises from the  $\nu_\infty^{-1}$  scalings of the coherence length and the gas density expressed under mass conservation by  $\dot{M}$ . For the CO (1–0) line observed towards a spatially unresolved envelope at a constant excitation temperature, this results in the expression

$$\dot{M} \simeq 1.2 \cdot 10^{-6} T_1 [\text{K}] \left( \nu_\infty [\text{kms}^{-1}] d [\text{kpc}] \right)^2 \left( f_{\text{CO}} \cdot 10^4 \right)^{-0.85} M_\odot \text{yr}^{-1} \quad (5.13)$$

(expressed in this form by Loup et al. (1993)), where  $T_1$  is the line-centre brightness temperature. For large surveys like the work at hand, the sensitivity among the observed targets is not uniform, and line areas ( $I_{\text{CO}}$  in Equation (5.12)) are more reliable than the line brightness temperatures at the systemic velocity. Ramstedt et al. (2008) showed that the dependence of  $\dot{M}$  on  $\nu_\infty$  is preserved but flattens (see their Table A.1).

In conclusion, a large sample like ours should exhibit a clear dependence of the MLR on the expansion velocity. The correlation between both quantities is shown in Fig. 5.10. Our sample and that of Loup et al. (1993) have 76 sources in common. Their estimates are taken from CO (1–0) observations and CO (2–1) when the CO (1–0) information was unavailable. For comparison, we overlay their values. The correspondence between them and those derived in our study is excellent. We, therefore, proceed now with the analysis of the latter.

We characterise the correlation between two quantities by the linear regression of their logarithms, which provides us with both a correlation coefficient (“Pearson  $r$ -value”) and, if the correlation is significant at the 1% level, the exponent of an underlying power law (i.e.,  $p < 1\%$ , where  $p$  is the “Pearson  $p$ -value”, or false-alarm probability). As inferred from our regression analysis (Fig. 5.8 and Table 5.3), all correlations of  $\log \dot{M}$  vs.  $\log \nu_\infty$  survive at a false-alarm probability of much less than 1%, except for the relatively small sample of  $J = 2-1$  lines of carbon-rich stars, displaying a false-alarm probability of  $p = 0.6\%$ . To avoid confusion with interstellar CO lines, we ignored lines with expansion speeds below  $4 \text{ km s}^{-1}$ , a cutoff that is inferred from the bimodal distribution of expansion speeds, separating circumstellar from interstellar lines.

Whether the deduced slopes reflect a genuine power-law exponent for an intrinsic dependence of the MLR on the expansion velocities is a priori uncertain, especially in view of the scatter among the line-specific values. We note, however, that the power-law exponents deduced from our sample,  $1.84 \pm 0.11$  for all stars ( $1/\sigma^2$ -weighted average of correlations that are significant at the 1% level) and  $1.72 \pm 0.13$  for the O-rich sample agree with those obtained from 2120 samples on a grid of DARWIN (Dynamic Atmosphere and Radiation-driven Wind models based on Implicit Numerics, (Höfner et al., 2016)) models for M-type AGB stars,  $1.82 \pm 0.03$  (Bladh et al., 2019), of which the winds are driven by the radiative acceleration of silicate dust. From the viewpoint of mass conservation, a linear relation between MLR and  $\nu_\infty$  would be expected. We conclude that there must still be a hidden, implicit velocity dependence, introduced e.g. by the sample selection or the distribution of gas densities at the wind onset. We also note that the mass-loss rate of the modelled DARWIN sample (when

referred to  $10 \text{ km s}^{-1}$  expansion velocity) falls a factor four above that of our O-rich sample as observed in CO (1–0), and a factor two in CO (2–1) and CO (3–2). This can be rationalised with the larger fraction of OH/IR stars in the former sample, with correspondingly higher expansion velocities, or, possibly, with a larger fraction of transition (S-type) stars in our sample: At nearly equal carbon and oxygen abundance, these elements are locked in CO rather than being available for the formation of dust and, by consequence, an agent different from carbon or silicate grains is required to drive the mass loss (solid iron and FeSi condensates, Gail, 2003, further references therein). This point is to be addressed by follow-up work. Ultimately, it should be kept in mind that such correlations, regardless of whether they derive from observed or modelled samples, can only describe general trends, rather than a universally valid law. Such a statement is also corroborated by the impact on mass-loss and dust-production histories under deviations from spherical symmetry (for a review see Decin, 2021, further references therein). The latter occurs both in single stars (Freytag and Höfner, 2023) and systems with companions of stellar or sub-stellar mass (Aydi and Mohamed, 2022).

The correlation between the dust-production and mass-loss rates, shown in Fig. 5.11, is easier to ascribe to the underlying physical mechanism, i.e., the mass loss triggered by the radiation pressure once the dust has condensed out. This is because both rates in our sample are determined independently: The former are obtained from the photometry of the 2MASS near-infrared and IRAS bands and evolutionary models (Sargent et al., 2011; Srinivasan et al., 2011; Scicluna et al., 2022), the latter from the CO spectroscopy presented here. All double-logarithmic correlations (i.e., for all transitions and chemical types) are significant, with false-alarm probabilities  $\ll 1\%$ , except for the small samples ( $< 20$  targets) of carbon-rich envelopes observed in CO (1–0) and (3–2). The power-law exponents vary from 0.7 for CO (1–0) to typically 1.0 for CO (3–2) and (2–1) (Table 5.3). Some of the significant power-law exponents (2 out of 7) differ significantly from one which implies that the gas-to-dust mass ratios (hereafter  $g/d$ ) depend on the mass-loss rate. Before we discuss this finding further, we provide  $g/d$  ratios that refer to the median mass-loss rates. We use only the CO (2–1) transition because it is the only one where the correlation between dust production and mass loss rates is significant for both O-rich and C-rich stars. This yields  $g/d = 180$  for the former group and 160 for the latter. We note that Wallström et al. (in prep., further references to previously determined values therein) obtain a  $g/d$  ratio of 210.

Indifferently analysing the whole sample would bias the resulting exponent because of different line-specific sample sizes. For a constant conversion efficiency between the radiative acceleration of dust and the mass loss, one would simply expect a linear relationship reflecting the average gas-to-dust mass ratio, as seen in the O-rich CO (2–1) and (3–2) samples. At mass-loss rates of  $\lesssim 10^{-5} \text{ M}_{\odot} \text{ yr}^{-1}$ , the nucleation of dust is incomplete, because the characteristic time for grain growth,  $\tau_{\text{gr}}/|\tau_{\text{gr}}^{\cdot}|$ , falls above that for the gas to accelerate from the local sound speed to  $v_{\infty}$  (Gail, 2003). Since a major fraction of the mass-loss rates in our sample falls below  $10^{-5} \text{ M}_{\odot} \text{ yr}^{-1}$  (90% and 86% for the O- and C-rich sample, respectively, as observed in CO (2–1) which has the largest number of samples), we would naturally expect a non-linear dependence of the dust-production rate from the mass-loss rate. If we only admit samples above a given MLR cutoff, the power law for expressing the dust-production rate through the mass-loss rate should steepen with increasing MLR cutoff, indicating a more efficient dust production at higher mass-loss rates. This behaviour is shown in Fig. 5.12, where such a trend is visible in CO (1–0), (2–1) and - for the O-rich sample - in (3–2). At the highest cutoff of  $2 \times 10^{-6} \text{ M}_{\odot} \text{ yr}^{-1}$  we observed again a decrement. Because the underlying DPR vs. MLR correlations are still significant at the 1% level, this decrement suggests that the efficiency of the dust production may depend on other factors than the mass-loss rate, e.g., chemical composition as discussed above, or non-linear grain growth (for a treatise of dust nucleation see e.g., supplement S3 of Decin, 2021, further references therein).

## 5.6 Conclusions

In this work, we presented the initial analysis and results obtained from CO observations with various telescopes as part of the NESS collaboration. We analysed 334 stars from our NESS sample and conclude the following:

1. With respect to the distribution of the mass-loss rates from carbon-rich stars, the corresponding distribution of oxygen-rich stars is shifted towards smaller values. We attribute this difference, which was already

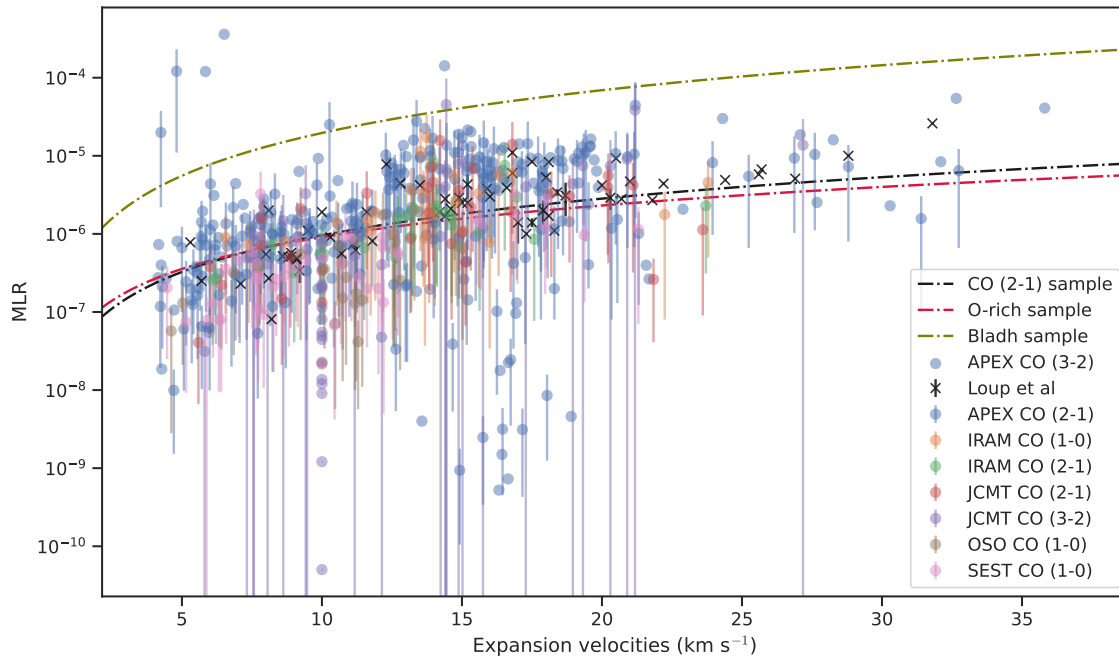


Figure 5.10: MLR vs. expansion velocities. The errorbars for CO (3–2) are not plotted for clarity. For CO (2–1), which offers the largest sample, the double-logarithmic linear regression is overlaid for the whole sample, the oxygen-rich sub-sample, and the synthetic Darwin sample from Bladh et al. (2019).

seen in previous studies, to the different properties of the condensates driving the wind, i.e., carbon and silicate grains, respectively.

2. Although the carbon-rich stars in our sample tend to higher mass-loss rates than the oxygen-rich stars, there is no evidence of a bimodal distribution of mass-loss rates, separating one chemical type from the other (i.e., the median values do not differ by an order of magnitude or more). This supports scenarios in which silicate grains can efficiently drive AGB winds, thanks to the contribution of scattered photospheric photons, and a feedback process between grain growth and radiative acceleration, forming micrometer-size, Fe-free silicate grains.
3. Consequently, a similar behaviour is seen in the distribution of expansion velocities, i.e., the circumstellar envelopes of carbon-rich stars tend to expand faster than those of their oxygen-rich equivalents, but also without an indication of a bimodal distribution. Even if present, we could hardly evidence one, given the bias in our sample, where carbon stars are under-represented.
4. We find a significantly non-linear correlation between mass-loss rates and expansion velocities. The power-law exponents for the latter are not unreasonably far from the exponent derived from a published sample of 1D-models of single M-type AGB stars, while our mass-loss rates are lower (by factors of two to four). We attribute this difference to selection biases in both samples. Beyond those, one may have to admit the impact of deviations from spherical symmetry or of undetected companions of stellar or sub-stellar mass.
5. In the CO (2–1) and (3–2) samples, we find an expected linear correlation between the dust-production and mass-loss rates, while in CO (1–0) it is sub-linear. However, we note a general trend that the correlation becomes predominantly superlinear when we introduce and gradually increase a lower

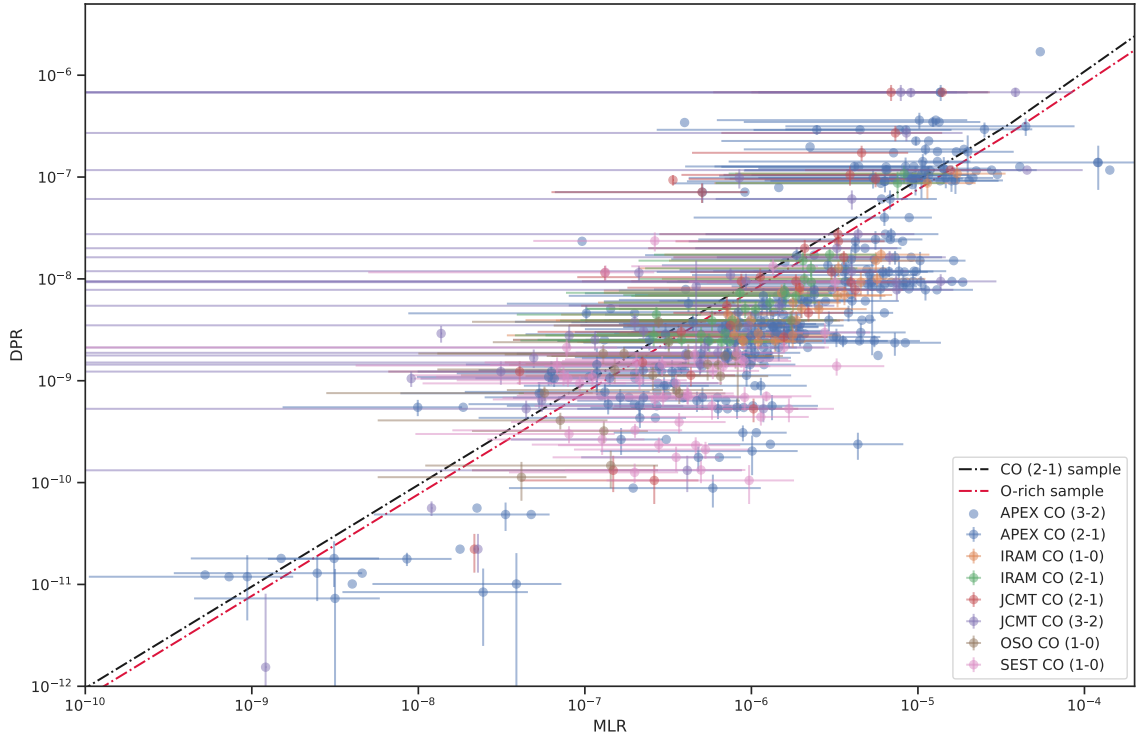


Figure 5.11: DPR vs. MLR. In CO (3–2), MLR values with missing errorbars are to be considered upper limits (errorbars suppressed for clarity). For CO (2–1), which offers the largest sample, the double-logarithmic linear regression is overlaid for the whole sample (in black) and for the oxygen-rich sub-sample (in red).

mass-loss cutoff. This finding may be tentatively attributed to the existence of a minimum mass loss required to build up a dust-driven wind, while the dust nucleation is complete only at the highest mass-loss rates of our sample, and otherwise affected by the chemical composition of the stellar atmosphere.

6. The distribution of the line-shape parameter  $\beta$  as deduced from the APEX observations is bimodal, clearly separating  $^{12}\text{CO}$  from  $^{13}\text{CO}$ . This result justifies that the parametrization of line profiles used by our and previous studies is adequate. The distribution of the  $^{12}\text{CO}/^{13}\text{CO}$  line-area ratio, although fraught with optical-depth and fractionation effects and sensitivity bias, agrees with that deduced from a sample of AGB stars in the Galactic bulge.
7. With the addition of this NESS sub-sample to the total NESS data, a significant portion being from the observations of the stars from the southern hemisphere, we can perform a more robust statistical analysis for a global view of AGB stars in our Local Galaxy.

The results of the regression analysis of mass-loss rates, expansion velocities and dust-production rates presented in this work should not be taken as genuine laws, since the deviations from the best fits are not only due to individual uncertainties in the correlated quantities, but also due to intrinsic variations from one source to another, each displaying its own mass-loss history. They can, however, be used to characterise large samples in a compact form, suited for comparison with modelled populations of AGB stars. In this respect, the sample presented in this work, and the NESS sample in general, are far from being fully explored.

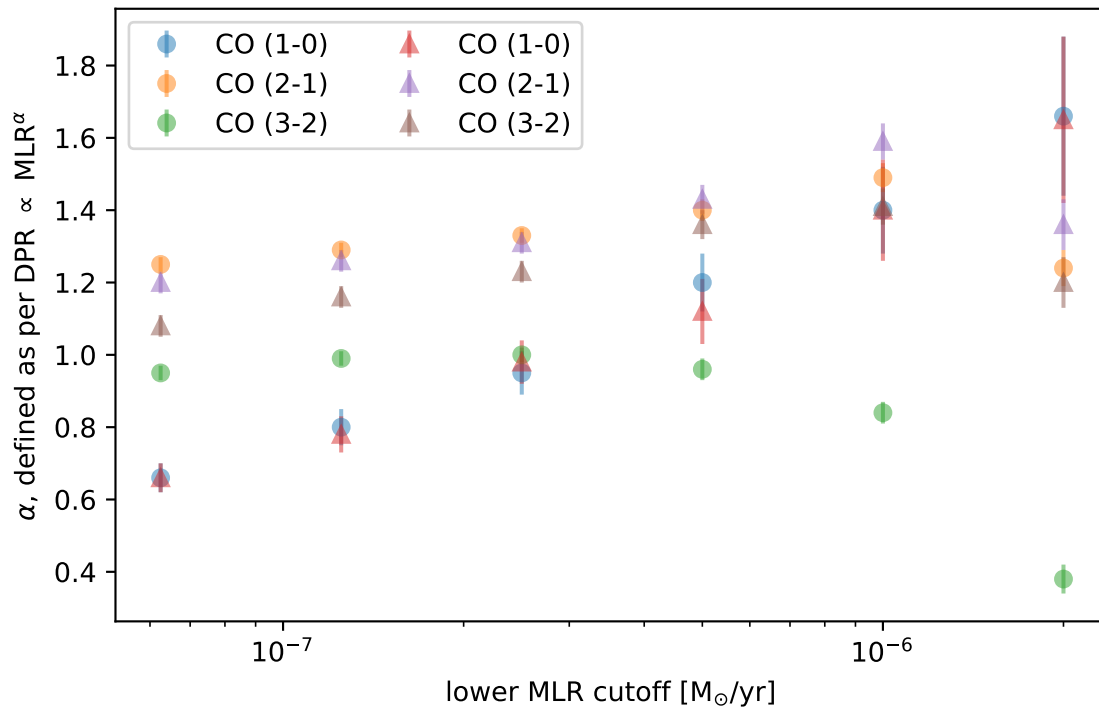


Figure 5.12: Power-law exponent for expressing the dust-production rate through the mass-loss rate, as a function of the lower MLR cutoff. CO transitions are labelled by different colours, for the whole sample (filled circles) and for the oxygen-rich sample (filled triangles).

Table 5.3: Correlation coefficients (Pearson  $r$ ), false-alarm probabilities (Pearson  $p$ ), and sample sizes for the double-logarithmic regression analysis of MLR vs.  $v_\infty$ , and of DPR vs. MLR.

chemical type	MLR (a) [ $10^{-7} M_\odot/\text{yr}$ ]	power-law exponent	$r$	$p$	DPR (b) $10^{-9} M_\odot/\text{yr}$	power-law exponent	$r$	$p$	$N$
CO (1–0)									
O, C	$4.93^{+4.84}_{-2.42}$	$2.27 \pm 0.29$	0.644	$\ll 0.01$	$0.527^{+0.045}_{-0.042}$	$0.66 \pm 0.04$	0.619	$\ll 0.01$	89
O	$5.20^{+6.30}_{-2.81}$	$2.30 \pm 0.35$	0.594	$\ll 0.01$	$0.617^{+0.056}_{-0.051}$	$0.65 \pm 0.04$	0.714	$\ll 0.01$	73
C	$3.64^{+13.96}_{-2.64}$	$2.62 \pm 0.64$	0.896	$\ll 0.01$	$0.152^{+0.044}_{-0.034}$	$0.95 \pm 0.11$	0.532	0.034	16
CO (2–1)									
O, C	$10.75^{+4.86}_{-3.34}$	$1.80 \pm 0.15$	0.502	$\ll 0.01$	$0.348^{+0.022}_{-0.021}$	$1.18 \pm 0.02$	0.832	$\ll 0.01$	205
O	$10.46^{+5.33}_{-3.52}$	$1.73 \pm 0.17$	0.457	$\ll 0.01$	$0.403^{+0.028}_{-0.026}$	$1.12 \pm 0.02$	0.837	$\ll 0.01$	176
C	$13.71^{+37.16}_{-9.46}$	$1.71 \pm 0.48$	0.496	0.00621	$0.080^{+0.021}_{-0.017}$	$1.52 \pm 0.05$	0.709	$\ll 0.01$	29
CO (3–2)									
O, C	$13.66^{+8.89}_{-5.36}$	$1.71 \pm 0.20$	0.432	$\ll 0.01$	$0.683^{+0.050}_{-0.047}$	$0.95 \pm 0.02$	0.740	$\ll 0.01$	188
O	$12.51^{+8.99}_{-5.20}$	$1.46 \pm 0.22$	0.361	$\ll 0.01$	$0.433^{+0.035}_{-0.032}$	$1.03 \pm 0.02$	0.806	$\ll 0.01$	164
C	$24.31^{+104.76}_{-17.76}$	$2.04 \pm 0.63$	0.640	$7.6 \times 10^{-4}$	$21.0^{+4.6}_{-3.8}$	$0.29 \pm 0.04$	0.226	0.29	24
Bladh et al. (2019)									
O	$19.60^{+1.54}_{-1.43}$	$1.82 \pm 0.03$	0.775	$\ll 0.01$					2120

**Notes.** Correlations that are insignificant at the 1% level are typeset in grey. (a) MLR for a reference expansion velocity of  $v_\infty = 10 \text{ km s}^{-1}$ . (b) DPR for a reference MLR of  $10^{-7} M_\odot/\text{yr}$ .

---

## Conclusions and Outlook

---

Our knowledge of the envelopes of AGB stars is biased: In oxygen-rich stars, the availability of SiO maser lines at millimetre wavelengths opened the path for spatially resolved (VLBI) observations of the extended photospheres early on (Moran et al., 1979), while OH-masers and H<sub>2</sub>O masers sounded the CSE (Reid et al. 1977, respectively Lane et al. 1987). With the improved instrumentation for millimetre astronomy, these studies were extended to the spectroscopy of CO lines, beginning with Solomon et al. (1971) in the CO  $J = 1-0$  transition. This detection was made towards IRC+10216, the archetypical carbon star. However, despite numerous follow-up studies, of which some data was also used for the work of this thesis, the link between the outer envelope and the extended photosphere of carbon stars remained difficult to establish, unlike the situation in oxygen-rich stars where the studies mentioned above could be established more easily (for a review on the early historical developments, we refer to Zuckerman 1980). For the carbon-rich stars, the question of whether the analysis of emissions from high-excited HCN lines ( $E_{\text{lower}} \sim 1000$  K) are the veritable equivalent to that of SiO masers in oxygen-rich stars therefore remained to be settled. As a matter of fact, the first detection of vibrationally excited HCN lines had to wait until 1986, when they were discovered in IRC+10216 (and Orion-KL, Ziurys and Turner 1986). Since then, the extension of astronomical spectroscopy to submillimetre and far-infrared wavelengths further improved the access to the innermost regions of the CSEs around carbon stars.

The main motivation of this thesis is to overcome this historical bias, by conducting three studies: First, to further confirm and complete our picture of the extended photospheres of carbon stars through the analysis of observations of HCN emissions excited to 1000 K and more. Additionally, to link it to their outer envelopes by including ground-state transitions as well, probing a region bounded by the photodissociation of HCN by the interstellar radiation field (ISRF). Second, to investigate the outer envelope (i.e., beyond the photodissociation of CO by the ISRF) in the two emission lines emitted by atomic carbon from its ground-state fine-structure triplet in the CSE of IRC+10216. A complementary observation of the emissions from the corresponding line of ionised carbon surprisingly turned out to serve the previous point, rather than insights into the photoionisation of the CSE by the ISRF. The third objective of this thesis is to set the obtained results in their more general context, namely, to compare them with the population of oxygen-rich AGB stars. For this, the first three rotational CO lines were observed towards a large sample of oxygen- and carbon-rich stars, along with targets in a transition phase between both.

Following are the conclusions of the studies conducted towards CSEs of AGB stars:

- In Chapter 2, we used the vibrationally excited transitions of HCN, a parent molecule, to have a closer look at the hotter regions of the CSEs belonging to 16 C-rich stars. The observations provided us with detections of 68 vibrationally excited lines originating from 13 out of the 16 stars from our sample, which demonstrates that vibrationally excited HCN lines are ubiquitous in C-rich stars. The large number of detected HCN masers (23 newly discovered; 29 in total) in our sample also aided in concluding that HCN masers in C-rich stars can be indeed regarded as analogous to SiO masers in O-rich stars. Additionally,

using the limited literature data for some of the HCN masers in three of our sources, along with our recent observations, we detected a large temporal variability in the  $J = 2-1$  ( $0, 1^{1e}, 0$ ) maser seen on the flux density scale as well as in the line shape. Comparing our results with the physical model for IRC +10216 presented in Agúndez et al. (2012), we infer that the HCN masers need regions with temperatures  $\gtrsim 700$  K to be formed. We also achieved our aim of constraining the physical conditions in the denser parts of the CSEs using vibrationally excited lines. Our results from the population diagram analyses show  $T_{\text{ex}} \sim 800$  K for IRC +10216 and CRL 3068 and source-average column densities of  $(0.18-10.8) \times 10^{19} \text{ cm}^{-2}$  for six of our C-rich stars. We also roughly estimate the corresponding HCN abundance with respect to  $\text{H}_2$  which is  $\sim 7.4 \pm 5.5 \times 10^{-5}$ .

- In Chapter 3 we closely look at the distribution of atomic carbon ( $\text{C}^0$ ) in the CSE of the archetypal star IRC +10216. Various studies such as Keene et al. (1993) and van der Veen et al. (1998) have been conducted to characterise the distribution of atomic carbon around stars. But for the first time, we use our more sensitive equipment to further constrain the [C I] emitting shell around the CSE, by observing cross-map samples out to a distance of up to  $78''$  from the star. Due to the evident centrosymmetric emission of CO (Cernicharo et al., 2015a), this makes for a valid strategy for our spatial sampling. The  $^3\text{P}_1 \rightarrow ^3\text{P}_0$  fine structure line shows a double-horned profile. Our observations separate the blue- and red-shifted wings of the line profile to up to  $13''$  distance from the star. We see a weak absorption in the blue-shifted peak in the central position observations because there are layers of decreasing excitation along the sightline through this hemisphere. Our measured line fluxes agree with those presented in Keene et al. (1993). The [C I] emitting shell is produced by photo-dissociation of CO and therefore stationary while the wind flows through it. Our analysis (see below) shows no evidence of a single thin [C I] emitting shell. Even if this was a valid scenario, the distance travelled by it in the time span between the two observations,  $\approx 30$  years, corresponds to 90 AU ( $0.7''$  for 130 pc distance, Cernicharo et al., 2015a), which, at our sensitivity and spatial resolution, would be inconsequential for the line profile. For further analysis, we conduct C I excitation modelling throughout the envelope. Using a radiative transfer analysis we determined the density and kinetic temperature profiles of C I. For this, we approached in two ways, first using a constant abundance model and another one with the variable abundance. We find that regardless of the approaches, both models reproduce the line profiles very well for the innermost positions. Using the distributions of C I and C II discussed in Reach et al. (2022), we place the inner boundary of the [C I]-emitting shell at  $\sim 10^{16}$  cm from the star. Our preliminary SOFIA observations of the [C II] fine structure line,  $^2\text{P}_{3/2} \rightarrow ^2\text{P}_{1/2}$  in IRC +10216 show an interesting aspect of its distribution. The emission is seen only at the central position and not in the averaged spectrum of the outer pixels of the receiver array, at  $32''$  offset. Additionally, the asymmetrical and broad components of the emission indicate that it does not originate uniquely from the outer parts of the envelope where it is exposed to the ISRF. Reach et al. (2022) suggest that the presence of a companion could explain the source of ionisation in the envelope. Cernicharo et al. (2015a) and Guélin et al. (2018) also hypothesise that the partial arcs in the envelope of IRC +10216 are generated by a companion. At the spatial resolution and sensitivity of our data, we cannot confirm such a scenario.
- In Chapter 5, we present a study of a sample of AGB stars, which is part of the NESS program. We analyse 334 stars, observed with various single dish telescopes. Due to the large sample size, we obtain the distributions of parameters such as the expansion velocity  $V_{\text{exp}}$ , the mass loss rate (MLR), and the dust production rate (DPR), also separating the sample into its chemical types. We find that the distribution of  $V_{\text{exp}}$  in C-rich stars is more widespread than that seen in O-rich stars. The envelopes of the former tend to expand at a higher speed than the latter. However, the larger sample of O-rich stars compared to that of their C-rich equivalents introduces a bias and a concrete conclusion cannot be drawn; though it does agree with samples shown in Höfner and Olofsson (2018). A similar distribution is seen for the MLRs of O-rich stars, which tend to be smaller. The difference to those of C-rich stars is less pronounced than expected, considering that carbon grains have larger opacities and are thus responsible for the larger radiative acceleration and mass loss in C-stars. Again, a part of the reason could be the bias in our sample.

Furthermore, our correlation analysis gives us a more concrete insight into our sample of AGB stars as a population. The non-linear correlation seen between MLR and  $V_{\text{exp}}$  is shown in Fig. 5.10. The comparison with Loup et al. (1993) shows a good agreement. However, if compared with the MLRs reported in Bladh et al. (2019) for a modelled sample, our values are generally lower. This can be rationalised with the possibility that their sample contains more OH/IR stars – which have higher MLRs – than our sample, or that the latter contains more stars in a transition phase of their evolution, i.e., S-type stars. In view of our correlation, the takeaway is that our sample reproduces the general trend and that a more concrete conclusion cannot be drawn yet.

In contrast, our analysis of the correlation between the DPR and the MLR is more reliable because both rates are determined independently, while they are connected by the underlying physical mechanism, i.e., the mass loss launched by the radiation pressure exerted on the condensed dust. Not unexpectedly, we see a linear correlation in our samples drawn from the CO (2–1) and CO (3–2) lines, but a sub-linear one for the CO (1–0) sample. For the latter our correlation becomes linear as well if we introduce a lower cutoff for the MLRs considered in the correlation (Fig. 5.12) and steadily increase it to  $\sim 10^{-6} M_{\odot} \text{ yr}^{-1}$ ; for the other transitions, it becomes super-linear. This behaviour can be explained by the fact that at MLRs  $\lesssim 10^{-5} M_{\odot} \text{ yr}^{-1}$  the dust nucleation is still incomplete when the wind reaches its terminal velocity (Gail, 2003) and that grain growth may be non-linear or depend on the chemical type.

In summary, the large size of our sample of AGB stars (most of them from the southern hemisphere) improves the robustness of the analysis and the significance of the inferred trends across the AGB population.

## Outlook

Due to continued improvements of the instrumentation that is available for the studies summarised in the previous paragraphs and based on the findings of this PhD thesis, it will be possible to gain further insight into CSEs and their host stars, ultimately aiming at their full understanding. The following points discuss exemplary projects that can be build based on the results reported in this work:

- Our HCN project confirms that the vibrationally excited lines of the molecule trace the innermost parts of the envelope of C-rich evolved stars. Following the importance of this molecule and the lack of extensive studies for a wider number of C-rich stars, we have acquired compact configuration data from the Submillimeter Array (SMA, Smithsonian Astrophysical Observatory) to image HCN emissions in the (3–2) and (4–3) transitions in three carbon-rich stars. These observations will help us to untangle the complex morphologies of the inner CSEs of these stars. HCN is also a more important coolant in these hot and dense environments than its mere abundance suggests, unlike  $^{12}\text{CO}$  which is hindered by its high opacity and remains an important coolant only due to its sheer abundance (Groenewegen, 1994). By modelling the excitation of HCN, following Crosas and Menten (1997), we plan to derive the temperature and density structure of the envelope close to the star. These inner regions have not been extensively explored for C-rich stars, except for IRC +10216 (Schöier et al., 2007; Shinnaga et al., 2009).
- The limitations that are set by the coarse sampling of our [C I] observations of IRC +10216 can be overcome by acquiring with APEX a full, critically sampled map of [C I]. Furthermore, interferometric observations would be useful to precisely pinpoint the location of the [C I]-emitting shell. For the distribution of the [C II] emission, which we unexpectedly locate in the inner envelope, such observations will not be possible in the near future. However, the latter emissions are seen to be variable on a timescale that roughly corresponds to the period of the stellar pulsation. An accurate determination of the phase lag between the near-infrared variability and that of the [C II] emission would allow us to more precisely locate the latter, even without high spatial-resolution data. Together with the [C I] map from the APEX telescope, a more complete photo-chemical network, and radiative transfer calculations beyond spherical

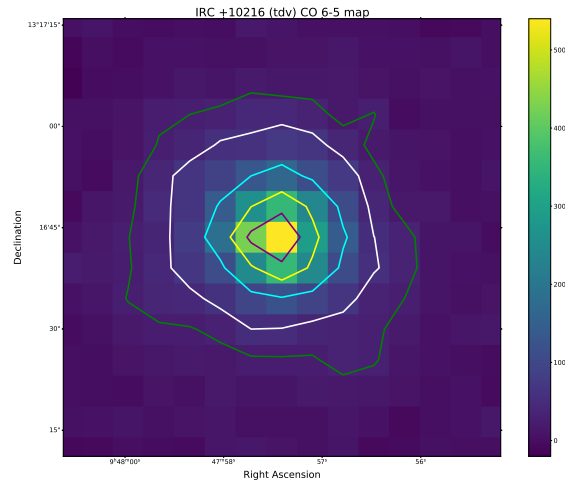


Figure 6.1: Integrated intensity map of IRC+10216 in CO (6–5) line emission observed with the APEX telescope. The contour levels are drawn at 5% intervals of peak emission.

symmetry, such monitoring observations would aid in understanding the nature of the ionising source in the inner envelope.

As discussed in this thesis, the extended envelope of IRC +10216 shows concentric shells in the emissions of the CO lines. We have acquired maps in the CO (2–1), (3–2), (4–3), and (6–5) transitions with the APEX telescope. Fig. 6.1 shows the line-area integrated intensity map of IRC +10216 in the CO (6–5) emission. The envelope shows compact emission in this line but is quite extended in the lower- $J$  transitions, as expected. We plan to use these observations to conduct excitation analyses, get additional constraints on the radial structure of the envelope, and trace the two-phase (i.e., shell and inter-shell) medium out to large radii.

- With the results presented in Chapter 5, we characterised the distributions of the CSE parameters across the NESS sample and used them to form a general understanding. The next step would be to perform radiative transfer modelling on individual stars, as shown in Chapter 3. We would use the initial constraints obtained from our current work and use them as input parameters to model the lines individually and analyse their excitation, providing us with a more robust MLR estimate. Additionally, our IRAM 30-m observations in the CO (1–0) transition provided us with a larger bandwidth, allowing us to detect various other molecular species in the CSEs of the stars from our sample. The analysis of their emissions by non-LTE radiative transfer modelling will shed light on the chemistry in the envelopes and further constrain the physical parameters in the emitting regions. We have also mapped some of our sources and we already see extended emissions in the preliminary line-area integrated intensity maps. In the CO (1–0) emission, this data traces the “old” mass loss and will thus be useful to address questions regarding the mass-loss history. We will also be able to see whether there is an influence of binary companions, if present, on our detections.

---

## NESS: Tables presenting results of the soft-parabola line fitting procedure

---

The following table presents the results obtained from the soft-parabola fitting of line profiles discussed in Chapter 5. The table mentions the IRAS name of the star (IRASPSC), the CO rotational transition  $J$ , the telescope used for the observation (Telescope), followed by the fit parameters: the peak temperature of  $^{12}\text{CO}$  ( $T_{\text{peak}}^{12}\text{CO}$ ), the peak temperature of  $^{13}\text{CO}$  ( $T_{\text{peak}}^{13}\text{CO}$ ), line-profile-integrated intensities of  $^{12}\text{CO}$  ( $I_{12\text{CO}}$ ) and  $^{13}\text{CO}$  ( $I_{13\text{CO}}$ ), LSR velocity ( $V_{\text{LSR}}$ ), terminal velocity  $V_{\text{inf}}$ , MLRs (with errors), and the  $^{12}\text{CO}/^{13}\text{CO}$  ratio.

Table A.1: Results of the soft-parabola fitting. Errors are estimated with a Markov-Chain Monte Carlo method. For details and reference see text.

IRASPSC	$J$	Telescope	RMS [1 km s <sup>-1</sup> ]	$T_{\text{peak}}^{12\text{CO}}$ [K]	$T_{\text{peak}}^{13\text{CO}}$ [K]	$I_{12\text{CO}}$ [K km s <sup>-1</sup> ]	$I_{13\text{CO}}$ [K km s <sup>-1</sup> ]	$V_{\text{LSR}}$ [km s <sup>-1</sup> ]	$V_{\text{inf}}$ [km s <sup>-1</sup> ]	MLR [M <sub>⊙</sub> yr <sup>-1</sup> ]	$\frac{^{12}\text{CO}}{^{13}\text{CO}}$
00193-4033	2-1	APEX	0.02	0.00 <sup>+0.01</sup> <sub>-0.01</sub>	0.0	0.4±0.1	0.0	18.6	8.2	(5.1±4.4) e-7	24.2
	2-1	JCMT	0.03	0.10 <sup>+0.00</sup> <sub>-0.00</sub>	0.0	0.8±0.1	–	0.0	8.9	(5.1±4.4) e-7	0.0
	3-2	APEX	0.01	0.00 <sup>+0.01</sup> <sub>-0.00</sub>	0.0	0.1±0.0	0.0	21.1	8.3	(1.0±1.2) e-7	-3.3
	3-2	JCMT	–	–	0.0	–	–	0.0	–	–	0.0
00245-0652	1-0	SEST	0.01	0.10 <sup>+0.01</sup> <sub>-0.01</sub>	0.0	0.6±0.1	0.0	8.5	7.5	(5.9±5.3) e-7	0.0
00254-3317	2-1	JCMT	0.04	0.00 <sup>+0.00</sup> <sub>-0.00</sub>	0.0	0.0±0.2	0.0	0.0	0.0	–	0.0
	3-2	JCMT	0.04	0.00 <sup>+0.00</sup> <sub>-0.00</sub>	0.0	0.0±0.2	0.0	0.0	0.0	–	0.0
01246-3248	1-0	SEST	0.38	0.90 <sup>+0.10</sup> <sub>-0.10</sub>	0.0	24.4±0.2	0.0	-21.1	17.0	(1.7±1.5) e-6	0.0
	2-1	JCMT	0.04	1.60 <sup>+0.00</sup> <sub>-0.00</sub>	0.0	50.3±0.2	3.2	0.0	15.0	(1.0±0.9) e-6	15.7
	3-2	JCMT	0.06	2.00 <sup>+0.00</sup> <sub>-0.00</sub>	0.0	62.5±0.3	–	0.0	15.8	(1.2±1.3) e-6	-0.1
01438+1850	1-0	SEST	0.01	0.00 <sup>+0.00</sup> <sub>-0.00</sub>	0.0	0.5±0.0	0.0	11.0	11.1	(8.7±7.9) e-7	0.0
02464-5915	2-1	APEX	0.02	0.00 <sup>+0.01</sup> <sub>-0.01</sub>	0.0	0.3±0.1	0.1	68.9	6.8	(1.4±1.2) e-7	5.6
	3-2	APEX	0.02	0.00 <sup>+0.00</sup> <sub>-0.00</sub>	0.0	0.0±0.1	0.1	25.0	15.8	(3.1±3.6) e-9	0.1
02522-5005	2-1	JCMT	0.07	1.60 <sup>+0.00</sup> <sub>-0.00</sub>	0.0	12.6±0.2	–	0.0	6.0	(3.8±3.3) e-7	0.0
	3-2	JCMT	–	–	0.0	–	–	0.0	–	–	0.0
03112-5730	1-0	SEST	0.02	0.10 <sup>+0.01</sup> <sub>-0.01</sub>	0.0	0.9±0.1	0.0	0.4	6.1	(1.3±1.0) e-7	0.0
	2-1	APEX	0.06	0.40 <sup>+0.03</sup> <sub>-0.03</sub>	0.0	3.3±0.1	-0.1	1.1	6.3	(1.7±1.3) e-7	-68.3
	3-2	APEX	0.02	0.10 <sup>+0.01</sup> <sub>-0.01</sub>	0.0	1.1±0.1	0.1	0.7	6.4	(4.8±5.1) e-8	15.2
03336-7636	2-1	APEX	0.03	0.10 <sup>+0.01</sup> <sub>-0.01</sub>	0.01	0.9±0.1	0.1	0.9	9.1	(1.4±1.2) e-6	10.4
	3-2	APEX	0.01	0.00 <sup>+0.00</sup> <sub>-0.01</sub>	0.0	0.2±0.1	0.1	-0.4	12.1	(2.0±2.3) e-7	1.3

03364-5533	2-1	APEX	0.02	$0.10_{-0.01}^{+0.01}$	0.0	$0.4\pm 0.1$	0.0	-12.5	5.6	$(1.6\pm 1.4) e^{-7}$	-10.6
	3-2	APEX	0.02	$0.00_{-0.00}^{+0.00}$	0.01	$0.1\pm 0.1$	-0.2	-4.9	16.1	$(4.3\pm 5.0) e^{-8}$	-0.5
03449+5041	1-0	IRAM	0.04	$0.00_{-0.01}^{+0.01}$	0.01	$0.6\pm 0.2$	0.1	-20.5	16.0	$(7.8\pm 7.5) e^{-7}$	4.4
	2-1	IRAM	0.05	$0.10_{-0.01}^{+0.02}$	0.0	$2.6\pm 0.2$	0.0	-17.2	12.6	$(5.0\pm 4.4) e^{-7}$	0.0
03479-7423	3-2	APEX	0.01	$0.00_{-0.00}^{+0.00}$	0.0	$0.1\pm 0.1$	0.1	-28.8	17.5	$(6.7\pm 8.0) e^{-10}$	1.6
03482-5213	2-1	APEX	0.01	$0.00_{-0.00}^{+0.00}$	0.0	$0.2\pm 0.0$	0.1	11.0	7.7	$(5.3\pm 4.5) e^{-8}$	3.6
	3-2	APEX	0.01	$0.00_{-0.00}^{+0.00}$	0.0	$0.0\pm 0.1$	0.0	17.4	16.5	$(5.3\pm 6.1) e^{-9}$	-13.8
03489-0131	1-0	OSO	0.03	$0.00_{-0.04}^{+1.09}$	0.0	$0.5\pm 0.2$	0.0	42.2	12.6	$(6.3\pm 6.0) e^{-7}$	0.0
	1-0	SEST	0.01	$0.00_{-0.00}^{+0.00}$	0.0	$0.1\pm 0.0$	0.0	53.8	8.7	$(2.9\pm 2.6) e^{-7}$	0.0
03511-4558	2-1	APEX	0.03	$0.10_{-0.01}^{+0.01}$	0.0	$0.7\pm 0.1$	0.0	-36.7	8.5	$(1.0\pm 0.9) e^{-6}$	-76.2
	3-2	APEX	0.02	$0.00_{-0.00}^{+0.00}$	0.0	$0.1\pm 0.1$	-0.1	-46.8	16.8	$(1.9\pm 2.2) e^{-7}$	-1.0
04094-2515	1-0	IRAM	0.04	$0.10_{-0.02}^{+0.02}$	0.01	$0.9\pm 0.1$	0.0	0.4	7.4	$(7.2\pm 6.5) e^{-7}$	36.2
	2-1	IRAM	0.06	$0.20_{-0.03}^{+0.03}$	0.0	$1.6\pm 0.2$	0.0	1.0	6.2	$(2.7\pm 2.3) e^{-7}$	0.0
04140-8158	3-2	APEX	0.02	$0.10_{-0.01}^{+0.01}$	0.0	$0.9\pm 0.1$	0.0	14.9	13.0	$(1.4\pm 1.7) e^{-7}$	149.9
04166+4056	1-0	OSO	0.04	$1.10_{-0.46}^{+0.12}$	0.0	$2.0\pm 0.1$	0.0	-3.9	1.2	$(2.9\pm 2.5) e^{-7}$	0.0
04328+2824	1-0	IRAM	0.03	$0.10_{-0.01}^{+0.01}$	0.01	$1.4\pm 0.1$	0.1	-3.1	6.6	$(9.0\pm 8.0) e^{-7}$	13.5
	2-1	IRAM	0.08	$0.40_{-0.03}^{+0.03}$	0.0	$4.8\pm 0.1$	0.0	-1.9	8.2	$(7.4\pm 6.4) e^{-7}$	0.0
04387-3819	2-1	JCMT	0.05	$0.10_{-0.00}^{+0.00}$	0.0	$1.7\pm 0.2$	-	0.0	14.6	$(7.5\pm 6.7) e^{-7}$	0.0
	3-2	JCMT	0.1	$0.50_{-0.00}^{+0.00}$	0.0	$4.9\pm 0.4$	-	0.0	7.6	$(9.6\pm 10.9) e^{-7}$	0.0
04396+0647	1-0	IRAM	0.02	$0.10_{-0.01}^{+0.01}$	0.0	$1.2\pm 0.1$	0.1	15.2	11.7	$(1.1\pm 1.0) e^{-6}$	14.5
	2-1	IRAM	0.06	$0.20_{-0.02}^{+0.02}$	0.0	$3.7\pm 0.1$	0.0	15.5	11.5	$(6.6\pm 5.8) e^{-7}$	0.0
04573-1452	1-0	SEST	0.04	$0.20_{-0.01}^{+0.01}$	0.0	$5.6\pm 0.2$	0.0	11.8	18.0	$(1.2\pm 1.1) e^{-6}$	0.0
05028+0106	1-0	SEST	0.01	$0.10_{-0.00}^{+0.00}$	0.0	$0.9\pm 0.0$	0.0	18.4	11.6	$(2.0\pm 1.6) e^{-7}$	0.0
05052-8420	3-2	APEX	0.02	$0.10_{-0.01}^{+0.01}$	0.0	$2.0\pm 0.1$	0.1	-6.4	15.9	$(6.3\pm 7.3) e^{-7}$	15.6

05069-3434	2-1	JCMT	-	-	0.0	-	-	0.0	-	-	0.0
	3-2	JCMT	0.09	$0.60^{+0.00}_{-0.00}$	0.0	$3.2\pm 0.2$	0.0	0.0	3.5	$(1.8\pm 2.0) \text{ e-7}$	0.0
05090-1154	1-0	SEST	0.01	$0.00^{+0.01}_{-0.00}$	0.0	$0.3\pm 0.0$	0.0	29.1	6.4	$(8.0\pm 7.1) \text{ e-8}$	0.0
05096-4834	2-1	APEX	0.07	$0.30^{+0.02}_{-0.02}$	0.02	$5.3\pm 0.1$	0.3	-1.4	11.0	$(1.5\pm 1.3) \text{ e-6}$	15.3
	2-1	JCMT	-	-	0.0	-	-	0.0	-	-	0.0
	3-2	APEX	0.03	$0.10^{+0.01}_{-0.01}$	0.0	$1.9\pm 0.1$	0.1	-1.2	11.3	$(3.6\pm 4.2) \text{ e-7}$	15.7
	3-2	JCMT	0.04	$0.30^{+0.00}_{-0.00}$	0.0	$4.6\pm 0.2$	-	0.0	11.2	$(5.3\pm 6.0) \text{ e-7}$	0.0
05131+4530	1-0	IRAM	0.07	$0.30^{+0.03}_{-0.02}$	0.13	$5.7\pm 0.2$	3.0	-31.7	13.7	$(1.7\pm 1.6) \text{ e-5}$	1.9
	2-1	IRAM	0.09	$0.30^{+0.03}_{-0.03}$	0.0	$6.9\pm 0.2$	0.0	-31.6	14.0	$(8.2\pm 7.5) \text{ e-6}$	0.0
05150-4056	2-1	APEX	0.02	$0.10^{+0.01}_{-0.01}$	0.0	$1.3\pm 0.1$	0.2	-17.0	11.8	$(2.0\pm 1.8) \text{ e-6}$	7.7
	3-2	APEX	0.01	$0.00^{+0.00}_{-0.00}$	0.0	$0.2\pm 0.1$	0.0	-15.3	14.4	$(2.6\pm 3.0) \text{ e-7}$	-26.9
05217-3943	2-1	JCMT	-	-	0.0	-	-	0.0	-	-	0.0
	3-2	JCMT	0.08	$0.00^{+0.00}_{-0.00}$	0.0	$0.0\pm 0.3$	0.0	0.0	0.0	-	0.0
05354+2458	1-0	SEST	0.03	$0.40^{+0.41}_{-0.02}$	0.0	$6.1\pm 0.1$	0.0	10.0	7.8	$(3.2\pm 3.0) \text{ e-6}$	0.0
05365-1404	1-0	SEST	0.01	$0.00^{+0.00}_{-0.00}$	0.0	$0.1\pm 0.0$	0.0	36.4	8.3	$(2.1\pm 2.0) \text{ e-7}$	0.0
05367+3736	1-0	IRAM	0.09	$0.30^{+0.03}_{-0.03}$	0.01	$6.3\pm 0.3$	0.2	-35.6	13.2	$(3.6\pm 3.4) \text{ e-6}$	26.5
	2-1	IRAM	0.15	$0.50^{+0.05}_{-0.04}$	0.0	$10.5\pm 0.4$	0.0	-34.6	12.7	$(1.6\pm 1.4) \text{ e-6}$	0.0
05411-8625	2-1	APEX	0.03	$0.10^{+0.01}_{-0.01}$	0.0	$0.8\pm 0.1$	0.1	19.4	7.1	$(2.8\pm 2.4) \text{ e-7}$	5.8
	3-2	APEX	0.01	$0.00^{+0.01}_{-0.01}$	0.0	$0.3\pm 0.1$	-0.1	19.8	6.3	$(6.2\pm 6.9) \text{ e-8}$	-2.0
05450-3142	2-1	APEX	0.01	$0.00^{+0.01}_{-0.00}$	0.0	$0.2\pm 0.0$	0.0	63.1	5.2	$(2.4\pm 2.1) \text{ e-7}$	-9.1
	2-1	JCMT	-	-	0.0	-	-	0.0	-	-	0.0
	3-2	APEX	0.01	$0.00^{+0.00}_{-0.00}$	0.0	$0.1\pm 0.1$	0.0	47.1	15.7	$(1.3\pm 1.5) \text{ e-7}$	-21.0
	3-2	JCMT	0.08	$0.00^{+0.00}_{-0.00}$	0.0	$0.2\pm 0.3$	0.0	0.0	10.0	$(1.1\pm 0.0) \text{ e-7}$	0.0
05534+4530	1-0	OSO	0.04	$0.90^{+1.19}_{-0.92}$	0.0	$0.1\pm 0.2$	0.0	8.0	11.2	$(1.3\pm 1.2) \text{ e-7}$	0.0

06216-0004	1-0	IRAM	0.04	$0.10^{+0.01}_{-0.01}$	0.0	$1.9\pm 0.2$	0.1	35.2	13.3	$(2.0\pm 1.9) e-6$	13.1
	2-1	IRAM	0.06	$0.20^{+0.02}_{-0.02}$	0.0	$3.7\pm 0.2$	0.0	34.0	13.2	$(9.2\pm 8.2) e-7$	0.0
06278+2729	1-0	OSO	0.02	$1.20^{+1.21}_{-1.20}$	0.0	$0.1\pm 0.1$	0.0	13.3	11.2	$(1.7\pm 1.6) e-7$	0.0
06310-6650	2-1	APEX	0.02	$0.10^{+0.01}_{-0.01}$	0.0	$0.6\pm 0.1$	0.0	-12.8	8.2	$(1.2\pm 1.0) e-7$	48.0
	3-2	APEX	0.01	$0.00^{+0.00}_{-0.00}$	0.01	$0.3\pm 0.0$	0.0	-13.1	9.3	$(3.4\pm 3.8) e-8$	-214.4
06333-0520	1-0	SEST	0.02	$0.00^{+0.00}_{-0.00}$	0.0	$0.7\pm 0.1$	0.0	11.9	21.3	$(1.1\pm 1.1) e-6$	0.0
06397-5223	2-1	APEX	0.02	$0.00^{+0.00}_{-0.00}$	0.0	$-0.1\pm 0.1$	0.1	-7.2	15.9	-	-0.6
	3-2	APEX	0.01	$0.00^{+0.00}_{-0.00}$	0.0	$0.1\pm 0.0$	0.0	10.1	5.9	$(3.0\pm 3.3) e-8$	6.6
06434-3628	2-1	APEX	0.04	$0.10^{+0.01}_{-0.01}$	0.01	$1.8\pm 0.1$	0.2	10.1	7.9	$(1.6\pm 1.4) e-6$	8.5
	2-1	JCMT	-	-	0.0	-	-	0.0	-	-	0.0
	3-2	APEX	0.01	$0.00^{+0.01}_{-0.01}$	0.0	$0.3\pm 0.0$	0.1	11.3	6.8	$(2.0\pm 2.3) e-7$	2.1
	3-2	JCMT	0.11	$0.00^{+0.00}_{-0.00}$	0.0	$0.5\pm 0.5$	0.0	0.0	10.0	$(2.2\pm 0.0) e-7$	0.0
06546-2353	1-0	SEST	0.02	$0.00^{+0.01}_{-0.00}$	0.0	$0.4\pm 0.1$	0.0	-39.3	12.1	$(9.0\pm 8.3) e-7$	0.0
07034-3551	2-1	JCMT	-	-	0.0	-	-	0.0	-	-	0.0
	3-2	APEX	0.02	$0.10^{+0.01}_{-0.01}$	0.0	$1.3\pm 0.1$	0.1	-22.9	9.5	$(1.2\pm 1.4) e-7$	14.2
	3-2	JCMT	0.09	$1.00^{+0.00}_{-0.00}$	0.0	$13.0\pm 0.4$	0.0	0.0	9.5	$(6.3\pm 7.1) e-7$	0.0
07065-7256	1-0	SEST	0.07	$0.10^{+0.02}_{-0.02}$	0.0	$4.6\pm 0.2$	0.0	-22.6	18.0	$(2.8\pm 2.4) e-6$	0.0
	2-1	APEX	0.14	$0.50^{+0.04}_{-0.04}$	0.03	$14.6\pm 0.1$	1.0	-10.8	18.0	$(4.5\pm 3.9) e-6$	14.2
07120-4433	1-0	SEST	0.02	$0.00^{+0.01}_{-0.01}$	0.0	$0.2\pm 0.1$	0.0	56.2	10.4	$(6.8\pm 6.4) e-8$	0.0
	2-1	JCMT	0.06	$0.60^{+0.00}_{-0.00}$	0.0	$2.8\pm 0.1$	-	0.0	3.6	$(4.2\pm 3.5) e-8$	0.0
	3-2	JCMT	-	-	0.0	-	-	0.0	-	-	0.0
07152-3444	2-1	JCMT	0.03	$0.20^{+0.00}_{-0.00}$	0.0	$5.3\pm 0.2$	0.0	0.0	16.7	$(1.9\pm 1.8) e-6$	0.0
	3-2	JCMT	-	-	0.0	-	-	0.0	-	-	0.0
07153-3700	2-1	JCMT	0.07	$0.00^{+0.00}_{-0.00}$	0.0	$0.2\pm 0.3$	0.0	0.0	10.0	$(2.2\pm 0.0) e-8$	0.0

	3-2	APEX	0.01	$0.00^{+0.00}_{-0.00}$	0.0	$0.0\pm 0.0$	0.0	-18.8	15.4	-	1.6
	3-2	JCMT	0.1	$0.00^{+0.00}_{-0.00}$	0.0	$0.5\pm 0.5$	0.0	0.0	10.0	$(2.3\pm 0.0) e-8$	0.0
07373-4021	2-1	APEX	0.12	$0.50^{+0.03}_{-0.03}$	0.02	$11.9\pm 0.1$	0.8	18.3	17.8	$(3.5\pm 3.0) e-6$	14.3
	3-2	APEX	0.02	$0.10^{+0.01}_{-0.01}$	0.01	$2.0\pm 0.1$	0.2	18.2	17.3	$(6.7\pm 7.4) e-7$	8.5
07434-3750	2-1	JCMT	0.04	$0.00^{+0.00}_{-0.00}$	0.0	$0.0\pm 0.2$	0.0	0.0	0.0	-	0.0
	3-2	JCMT	0.0	$0.00^{+0.00}_{-0.00}$	0.0	$0.1\pm 0.0$	0.0	0.0	10.0	$(1.4\pm 0.0) e-8$	0.0
08010-4109	2-1	APEX	0.13	$0.80^{+0.12}_{-0.10}$	0.34	$3.5\pm 0.0$	0.7	11.3	1.6	$(5.9\pm 4.9) e-7$	5.3
	3-2	APEX	0.03	$0.30^{+0.08}_{-0.09}$	0.01	$0.6\pm 0.0$	0.0	10.3	1.2	$(7.8\pm 8.5) e-8$	14.5
08078-3801	2-1	JCMT	0.0	$0.00^{+0.00}_{-0.00}$	0.0	$0.0\pm 0.0$	0.0	0.0	0.0	-	0.0
	3-2	APEX	0.01	$0.00^{+0.00}_{-0.00}$	0.0	$0.1\pm 0.1$	0.0	-12.1	16.4	$(1.4\pm 1.6) e-8$	1.1
	3-2	JCMT	-	-	0.0	-	-	0.0	-	-	0.0
08124-4133	2-1	APEX	0.29	$4.60^{+0.56}_{-0.34}$	0.68	$6.9\pm 0.1$	0.8	15.0	1.1	$(2.7\pm 2.3) e-6$	8.6
	3-2	APEX	0.03	$0.50^{+0.07}_{-0.04}$	0.0	$0.8\pm 0.0$	0.0	15.0	1.2	$(3.4\pm 3.8) e-7$	31.5
08189+0507	1-0	OSO	0.04	$0.20^{+0.78}_{-0.21}$	0.0	$0.2\pm 0.1$	0.0	91.8	12.8	$(2.6\pm 2.4) e-7$	0.0
08214-5920	2-1	APEX	0.01	$0.00^{+0.00}_{-0.00}$	0.0	$0.0\pm 0.0$	0.0	68.8	17.2	$(3.1\pm 2.7) e-9$	-1.0
	3-2	APEX	0.01	$0.00^{+0.00}_{-0.00}$	0.0	$0.0\pm 0.1$	0.1	74.9	13.3	$(1.9\pm 25.1) e-11$	0.0
08349-5945	2-1	APEX	0.07	$0.00^{+0.01}_{-0.01}$	0.03	$0.7\pm 0.4$	0.0	-37.0	17.3	$(5.0\pm 4.6) e-7$	99.8
	3-2	APEX	0.01	$0.00^{+0.00}_{-0.00}$	0.0	$0.2\pm 0.0$	0.0	-19.2	8.7	$(7.2\pm 8.1) e-8$	-43.3
08375-1707	1-0	SEST	0.02	$0.00^{+0.01}_{-0.01}$	0.0	$0.3\pm 0.1$	0.0	34.7	5.2	$(7.4\pm 6.5) e-8$	0.0
08510-5743	2-1	APEX	0.07	$0.10^{+0.03}_{-0.03}$	0.01	$1.2\pm 0.2$	0.3	11.4	6.6	$(1.4\pm 1.2) e-6$	4.1
	3-2	APEX	0.01	$0.00^{+0.00}_{-0.00}$	0.0	$0.3\pm 0.0$	0.1	9.9	8.4	$(2.7\pm 3.0) e-7$	3.8
08555+1102	1-0	OSO	0.02	$0.90^{+1.13}_{-0.86}$	0.0	$0.1\pm 0.1$	0.0	-8.0	10.5	$(7.1\pm 6.5) e-8$	0.0
08571-5901	2-1	APEX	0.06	$0.10^{+0.02}_{-0.02}$	0.01	$1.5\pm 0.3$	-0.5	26.0	12.8	$(1.9\pm 1.7) e-6$	-3.3
	3-2	APEX	0.01	$0.00^{+0.00}_{-0.00}$	0.0	$0.3\pm 0.0$	0.0	27.2	9.5	$(2.2\pm 2.5) e-7$	13.0

09057+1325	1-0	OSO	0.02	$0.10^{+0.02}_{-0.08}$	0.0	$1.3\pm 0.1$	0.0	27.0	10.1	$(3.5\pm 3.2) e^{-7}$	0.0
09105-4334	1-0	SEST	0.01	$0.20^{+0.02}_{-0.01}$	0.0	$0.9\pm 0.1$	0.0	15.7	3.0	$(6.6\pm 5.8) e^{-7}$	0.0
	2-1	APEX	0.05	$0.10^{+0.03}_{-0.07}$	0.0	$1.0\pm 0.1$	0.1	12.8	3.3	$(3.1\pm 2.6) e^{-7}$	20.8
	3-2	APEX	0.02	$0.00^{+0.02}_{-0.01}$	0.0	$0.4\pm 0.0$	0.0	13.9	3.8	$(8.2\pm 9.0) e^{-8}$	-13.7
09161-3248	2-1	APEX	0.05	$0.20^{+0.02}_{-0.01}$	0.01	$3.1\pm 0.1$	0.2	10.2	10.6	$(1.3\pm 1.2) e^{-6}$	13.7
	3-2	APEX	0.01	$0.00^{+0.00}_{-0.00}$	0.0	$0.5\pm 0.1$	0.1	11.0	10.4	$(1.6\pm 1.8) e^{-7}$	7.0
09213-5723	3-2	APEX	0.01	$0.00^{+0.00}_{-0.00}$	0.0	$0.4\pm 0.0$	0.1	31.3	8.5	$(2.0\pm 2.3) e^{-7}$	6.4
09235-2347	1-0	IRAM	0.11	$0.40^{+0.04}_{-0.03}$	0.04	$9.3\pm 0.3$	1.1	10.4	14.7	$(5.6\pm 5.3) e^{-6}$	8.2
	2-1	IRAM	0.14	$0.50^{+0.05}_{-0.04}$	0.0	$11.3\pm 0.3$	0.0	10.4	14.1	$(2.0\pm 1.8) e^{-6}$	0.0
09452+1330	1-0	SEST	4.04	$9.50^{+1.28}_{-1.06}$	0.0	$239.1\pm 0.9$	0.0	-27.2	15.7	$(1.4\pm 1.2) e^{-6}$	0.0
09480-4147	1-0	SEST	0.02	$0.10^{+0.01}_{-0.01}$	0.0	$0.6\pm 0.1$	0.0	22.1	7.0	$(4.6\pm 4.1) e^{-7}$	0.0
09521-7508	2-1	APEX	0.28	$1.30^{+0.09}_{-0.08}$	0.08	$22.9\pm 0.3$	2.0	-4.2	12.4	$(5.3\pm 4.4) e^{-6}$	11.5
	3-2	APEX	0.04	$0.20^{+0.01}_{-0.01}$	0.02	$3.3\pm 0.1$	0.4	-4.2	12.6	$(9.4\pm 10.4) e^{-7}$	8.1
09533-4120	1-0	SEST	0.03	$0.10^{+0.01}_{-0.01}$	0.0	$1.4\pm 0.1$	0.0	-17.8	11.3	$(2.8\pm 2.3) e^{-7}$	0.0
09564-5837	1-0	SEST	0.04	$0.10^{+0.01}_{-0.01}$	0.0	$1.6\pm 0.1$	0.0	-9.0	10.8	$(9.1\pm 8.3) e^{-7}$	0.0
10131+3049	1-0	SEST	0.67	$2.00^{+0.17}_{-0.17}$	0.0	$54.8\pm 0.6$	0.0	-1.3	16.9	$(3.2\pm 2.8) e^{-6}$	0.0
10323-4611	2-1	JCMT	0.05	$0.50^{+0.00}_{-0.00}$	0.0	$16.4\pm 0.3$	0.0	0.0	20.2	$(5.6\pm 5.1) e^{-6}$	0.0
	3-2	JCMT	-	-	0.0	-	-	0.0	-	-	0.0
10329-3918	1-0	SEST	0.11	$0.20^{+0.02}_{-0.03}$	0.0	$9.5\pm 0.2$	0.0	13.6	19.4	$(9.7\pm 8.3) e^{-7}$	0.0
	2-1	JCMT	0.04	$0.10^{+0.00}_{-0.00}$	0.0	$7.5\pm 0.3$	0.0	0.0	21.8	$(2.6\pm 2.2) e^{-7}$	0.0
	3-2	JCMT	0.0	$0.00^{+0.00}_{-0.00}$	0.0	$0.0\pm 0.0$	0.0	0.0	0.0	-	0.0
10350-1307	1-0	SEST	0.13	$0.40^{+0.07}_{-0.08}$	0.0	$4.8\pm 0.1$	0.0	-33.0	8.4	$(2.6\pm 2.1) e^{-7}$	0.0
10383-7741	2-1	APEX	0.02	$0.00^{+0.00}_{-0.01}$	0.0	$0.3\pm 0.1$	0.0	-8.3	13.0	$(2.2\pm 2.0) e^{-7}$	124.1
	3-2	APEX	0.01	$0.00^{+0.00}_{-0.00}$	0.0	$0.2\pm 0.1$	0.1	-8.6	15.4	$(7.8\pm 9.0) e^{-8}$	2.3

10403-7612	2-1	APEX	0.03	$0.10^{+0.01}_{-0.01}$	0.01	$1.9 \pm 0.1$	0.2	-22.5	15.8	$(2.9 \pm 2.6) \text{ e-6}$	10.2
	3-2	APEX	0.01	$0.00^{+0.00}_{-0.00}$	0.0	$0.6 \pm 0.1$	0.0	-24.2	16.8	$(7.5 \pm 8.7) \text{ e-7}$	-22.7
10491-2059	1-0	SEST	0.35	$0.90^{+0.10}_{-0.10}$	0.0	$20.5 \pm 0.4$	0.0	-14.2	15.5	$(1.6 \pm 1.4) \text{ e-6}$	0.0
11125+7524	1-0	OSO	0.02	$0.00^{+0.04}_{-0.03}$	0.0	$0.7 \pm 0.1$	0.0	-57.4	12.6	$(8.0 \pm 7.4) \text{ e-7}$	0.0
11445+4344	1-0	OSO	0.02	$0.00^{+0.01}_{-0.04}$	0.0	$0.3 \pm 0.1$	0.0	-49.7	6.8	$(3.2 \pm 2.9) \text{ e-7}$	0.0
11461-3542	2-1	JCMT	0.09	$0.40^{+0.00}_{-0.00}$	0.0	$4.8 \pm 0.3$	0.0	0.0	6.4	$(2.2 \pm 1.9) \text{ e-7}$	0.0
	3-2	JCMT	0.03	$1.40^{+0.00}_{-0.00}$	0.0	$18.0 \pm 0.1$	0.0	0.0	7.5	$(4.9 \pm 5.5) \text{ e-7}$	0.0
12106-3350	2-1	JCMT	0.04	$0.10^{+0.00}_{-0.00}$	0.0	$1.1 \pm 0.2$	-	0.0	8.6	$(1.5 \pm 1.3) \text{ e-7}$	0.0
	3-2	JCMT	0.06	$0.50^{+0.00}_{-0.00}$	0.0	$6.5 \pm 0.3$	0.0	0.0	8.1	$(4.1 \pm 4.7) \text{ e-7}$	0.0
12148-6741	2-1	APEX	0.01	$0.00^{+0.00}_{-0.00}$	0.0	$0.1 \pm 0.1$	0.1	14.5	15.8	$(2.5 \pm 2.1) \text{ e-9}$	0.7
	3-2	APEX	0.01	$0.00^{+0.00}_{-0.00}$	0.0	$0.0 \pm 0.1$	0.0	-0.8	16.3	$(4.6 \pm 5.7) \text{ e-10}$	-1.4
12247-5842	2-1	APEX	0.01	$0.00^{+0.00}_{-0.00}$	0.0	$0.1 \pm 0.0$	0.0	-54.1	16.4	$(3.2 \pm 2.7) \text{ e-9}$	1.9
12274-7647	3-2	APEX	0.01	$0.00^{+0.00}_{-0.00}$	0.0	$0.1 \pm 0.1$	0.1	19.1	16.7	$(5.4 \pm 6.2) \text{ e-8}$	0.9
12283-5650	2-1	APEX	0.03	$0.40^{+0.06}_{-0.03}$	0.0	$0.5 \pm 0.0$	0.0	-17.0	1.1	$(4.8 \pm 3.9) \text{ e-9}$	-112.2
12319-6728	2-1	APEX	0.01	$0.00^{+0.00}_{-0.00}$	0.0	$0.2 \pm 0.1$	-0.1	-2.0	12.6	$(3.3 \pm 2.8) \text{ e-8}$	-2.5
	3-2	APEX	0.01	$0.00^{+0.00}_{-0.00}$	0.0	$0.1 \pm 0.1$	0.1	4.0	17.1	$(1.2 \pm 1.4) \text{ e-8}$	1.2
12377-6102	2-1	APEX	0.38	$0.10^{+0.09}_{-0.12}$	0.03	$4.5 \pm 1.6$	0.9	-20.6	12.3	$(6.3 \pm 5.8) \text{ e-6}$	4.8
	3-2	APEX	0.05	$0.00^{+0.01}_{-0.01}$	0.0	$0.7 \pm 0.2$	0.1	-46.1	17.1	$(1.0 \pm 1.2) \text{ e-6}$	5.5
12384-4536	2-1	JCMT	0.03	$0.20^{+0.00}_{-0.00}$	0.0	$5.0 \pm 0.2$	0.0	0.0	14.0	$(4.6 \pm 4.2) \text{ e-6}$	0.0
	3-2	APEX	0.01	$0.00^{+0.00}_{-0.00}$	0.01	$0.7 \pm 0.0$	0.2	-36.4	14.3	$(1.0 \pm 1.2) \text{ e-6}$	4.3
	3-2	JCMT	-	-	0.0	-	-	0.0	-	-	0.0
12387-3717	2-1	JCMT	-	-	0.0	-	-	0.0	-	-	0.0
	3-2	JCMT	-	-	0.0	-	-	0.0	-	-	0.0
12391-6834	2-1	APEX	0.01	$0.00^{+0.01}_{-0.01}$	0.0	$0.6 \pm 0.1$	0.1	-35.5	8.9	$(7.9 \pm 6.9) \text{ e-7}$	7.5

	3-2	APEX	0.01	$0.00_{-0.00}^{+0.00}$	0.0	$0.2\pm 0.0$	0.0	-33.2	11.7	$(2.1\pm 2.4) e^{-7}$	-13.4
12394-6808	2-1	APEX	0.04	$0.10_{-0.01}^{+0.01}$	0.0	$1.1\pm 0.2$	0.0	-5.6	11.4	$(1.0\pm 0.9) e^{-6}$	-29.4
	3-2	APEX	0.04	$0.00_{-0.01}^{+0.00}$	0.0	$0.4\pm 0.2$	0.0	0.6	16.3	$(2.8\pm 3.2) e^{-7}$	44.5
12447+0425	1-0	IRAM	0.07	$0.20_{-0.02}^{+0.02}$	0.01	$5.8\pm 0.1$	0.3	-0.9	15.1	$(1.1\pm 0.9) e^{-6}$	17.7
	2-1	IRAM	0.11	$0.40_{-0.03}^{+0.03}$	0.0	$9.8\pm 0.2$	0.0	-0.9	14.8	$(7.0\pm 5.8) e^{-7}$	0.0
12454-6659	2-1	APEX	0.02	$0.10_{-0.00}^{+0.00}$	0.01	$1.5\pm 0.1$	0.3	-17.3	19.5	$(2.4\pm 2.2) e^{-6}$	5.3
	3-2	APEX	0.01	$0.00_{-0.00}^{+0.00}$	0.0	$0.5\pm 0.0$	0.0	-15.6	17.5	$(5.1\pm 5.9) e^{-7}$	19.3
12506-6004	2-1	APEX	0.02	$0.00_{-0.00}^{+0.00}$	0.0	$0.1\pm 0.1$	0.0	5.5	16.2	$(1.0\pm 0.9) e^{-7}$	-1.4
	3-2	APEX	0.01	$0.00_{-0.00}^{+0.00}$	0.0	$0.1\pm 0.1$	0.1	8.2	16.2	$(1.1\pm 1.2) e^{-7}$	2.7
12540-6845	2-1	APEX	0.18	$0.60_{-0.04}^{+0.04}$	0.01	$24.6\pm 0.1$	0.5	-34.1	27.6	$(1.0\pm 0.9) e^{-5}$	46.0
	3-2	APEX	0.04	$0.10_{-0.01}^{+0.01}$	0.01	$5.2\pm 0.1$	0.2	-33.7	28.1	$(2.6\pm 3.0) e^{-6}$	20.5
12563-6100	2-1	APEX	0.18	$1.00_{-0.99}^{+0.17}$	0.01	$2.2\pm 0.2$	0.1	-35.1	1.6	$(6.7\pm 5.8) e^{-7}$	35.0
	3-2	APEX	0.05	$0.10_{-0.03}^{+0.03}$	0.0	$1.4\pm 0.1$	0.2	-40.6	5.8	$(5.8\pm 6.5) e^{-7}$	8.4
13114-0232	1-0	OSO	0.07	$0.40_{-0.04}^{+0.03}$	0.0	$5.0\pm 0.2$	0.0	-10.8	7.7	$(3.7\pm 3.3) e^{-7}$	0.0
	1-0	SEST	0.1	$0.20_{-0.03}^{+0.04}$	0.0	$3.2\pm 0.2$	0.0	-15.8	7.7	$(4.1\pm 3.7) e^{-7}$	0.0
13136-4426	2-1	APEX	0.02	$0.00_{-0.00}^{+0.01}$	0.0	$0.7\pm 0.1$	0.0	-25.0	12.6	$(2.2\pm 1.9) e^{-7}$	-77.4
	3-2	APEX	0.01	$0.00_{-0.00}^{+0.00}$	0.01	$0.3\pm 0.1$	0.1	-25.4	13.9	$(6.7\pm 7.5) e^{-8}$	2.9
13150-4124	2-1	APEX	0.02	$0.10_{-0.01}^{+0.01}$	0.01	$1.0\pm 0.0$	0.1	45.5	5.9	$(7.1\pm 6.1) e^{-7}$	8.1
	3-2	APEX	0.01	$0.00_{-0.00}^{+0.00}$	0.0	$0.2\pm 0.0$	0.0	46.2	5.6	$(1.2\pm 1.4) e^{-7}$	10.7
13244-5904	2-1	APEX	0.02	$0.10_{-0.00}^{+0.01}$	0.0	$1.1\pm 0.0$	0.1	-11.4	12.6	$(9.9\pm 8.8) e^{-7}$	16.2
13283-5839	2-1	APEX	0.08	$0.70_{-0.54}^{+0.18}$	0.0	$1.9\pm 0.1$	0.2	-48.4	2.1	$(1.4\pm 1.2) e^{-6}$	12.1
	3-2	APEX	0.02	$0.00_{-0.02}^{+0.04}$	0.0	$0.2\pm 0.1$	-0.1	6.2	7.2	$(2.7\pm 3.1) e^{-7}$	-2.5
13368-4941	2-1	APEX	0.03	$0.20_{-0.01}^{+0.02}$	0.0	$1.4\pm 0.1$	0.1	-14.5	6.0	$(6.3\pm 5.3) e^{-8}$	9.6
	2-1	JCMT	0.03	$0.20_{-0.00}^{+0.00}$	0.0	$1.5\pm 0.1$	-	0.0	5.6	$(4.1\pm 3.4) e^{-8}$	0.0

	3-2	JCMT	0.07	$0.30_{-0.00}^{+0.00}$	0.0	$2.3\pm 0.2$	-	0.0	5.8	$(3.1\pm 3.5) \text{ e-}8$	0.0
13462-2807	1-0	SEST	0.01	$0.10_{-0.00}^{+0.01}$	0.0	$0.7\pm 0.1$	0.0	40.4	7.9	$(9.3\pm 8.3) \text{ e-}8$	0.0
13465-3412	2-1	APEX	0.01	$0.00_{-0.00}^{+0.00}$	0.01	$0.1\pm 0.1$	0.2	-7.1	14.9	$(9.4\pm 8.3) \text{ e-}10$	0.4
	2-1	JCMT	-	-	0.0	-	-	0.0	-	-	0.0
	3-2	APEX	0.01	$0.00_{-0.00}^{+0.00}$	0.0	$0.1\pm 0.0$	0.0	7.6	16.8	$(2.8\pm 3.5) \text{ e-}10$	1.6
	3-2	JCMT	0.06	$0.00_{-0.00}^{+0.00}$	0.0	$0.0\pm 0.2$	0.0	0.0	0.0	-	0.0
13466-3512	2-1	APEX	0.02	$0.10_{-0.01}^{+0.01}$	0.0	$1.3\pm 0.1$	0.0	-9.1	11.5	$(1.7\pm 1.5) \text{ e-}6$	38.0
	3-2	APEX	0.01	$0.00_{-0.00}^{+0.00}$	0.0	$0.3\pm 0.0$	0.0	-8.5	9.6	$(2.5\pm 2.9) \text{ e-}7$	-82.2
13477-6009	2-1	APEX	0.13	$0.10_{-0.04}^{+0.03}$	0.04	$3.9\pm 0.7$	0.8	-42.2	21.3	$(1.0\pm 0.9) \text{ e-}6$	4.5
	3-2	APEX	0.01	$0.10_{-0.01}^{+0.01}$	0.0	$0.2\pm 0.0$	0.0	-62.3	3.3	$(3.0\pm 3.1) \text{ e-}8$	8.8
13517-6515	2-1	APEX	0.04	$0.10_{-0.01}^{+0.01}$	0.01	$3.5\pm 0.1$	0.3	-19.6	18.4	$(8.7\pm 8.0) \text{ e-}6$	9.8
	3-2	APEX	0.01	$0.00_{-0.00}^{+0.00}$	0.0	$0.5\pm 0.0$	0.0	-21.4	12.6	$(9.6\pm 11.1) \text{ e-}7$	11.2
13581-5930	2-1	APEX	0.08	$0.90_{-0.07}^{+0.10}$	0.02	$2.0\pm 0.1$	0.2	-25.7	1.6	$(1.8\pm 1.5) \text{ e-}7$	8.9
	3-2	APEX	0.04	$0.60_{-0.04}^{+0.05}$	0.0	$1.2\pm 0.0$	0.0	-25.6	1.6	$(7.0\pm 7.7) \text{ e-}8$	33.4
13586-4617	2-1	APEX	0.02	$0.10_{-0.01}^{+0.01}$	0.01	$1.1\pm 0.0$	0.2	5.2	6.8	$(8.0\pm 6.9) \text{ e-}7$	6.9
	3-2	APEX	0.01	$0.00_{-0.00}^{+0.00}$	0.0	$0.3\pm 0.0$	0.0	6.0	7.1	$(1.5\pm 1.7) \text{ e-}7$	12.6
14003-7633	1-0	SEST	0.02	$0.10_{-0.01}^{+0.01}$	0.0	$0.7\pm 0.1$	0.0	10.7	7.7	$(1.1\pm 1.0) \text{ e-}7$	0.0
	2-1	APEX	0.06	$0.40_{-0.03}^{+0.04}$	0.01	$2.8\pm 0.1$	0.2	2.2	5.1	$(6.1\pm 5.1) \text{ e-}8$	11.1
14020-3515	2-1	APEX	0.03	$0.20_{-0.01}^{+0.01}$	0.01	$1.9\pm 0.1$	0.2	3.8	8.6	$(1.2\pm 1.1) \text{ e-}6$	8.5
	2-1	JCMT	0.06	$0.10_{-0.00}^{+0.00}$	0.0	$1.9\pm 0.2$	-	0.0	7.8	$(7.1\pm 6.2) \text{ e-}7$	0.0
	3-2	APEX	0.01	$0.00_{-0.00}^{+0.00}$	0.0	$0.4\pm 0.0$	0.0	4.8	8.6	$(2.1\pm 2.4) \text{ e-}7$	-11.7
	3-2	JCMT	0.05	$0.50_{-0.00}^{+0.00}$	0.0	$6.1\pm 0.2$	0.0	0.0	8.6	$(1.5\pm 1.7) \text{ e-}6$	0.0
14103-6311	2-1	APEX	0.02	$0.20_{-0.02}^{+0.03}$	0.0	$0.4\pm 0.0$	0.0	-45.6	1.7	$(1.4\pm 1.2) \text{ e-}6$	-47.9
	3-2	APEX	0.01	$0.10_{-0.01}^{+0.02}$	0.0	$0.2\pm 0.0$	0.0	-45.7	1.7	$(6.5\pm 7.2) \text{ e-}7$	23.0

14119-6453	2-1	APEX	0.03	$0.10_{-0.01}^{+0.01}$	0.03	$3.0\pm 0.1$	0.8	-38.0	15.8	$(1.5\pm 1.4) e^{-5}$	3.5
	3-2	APEX	0.01	$0.00_{-0.00}^{+0.00}$	0.0	$0.6\pm 0.1$	0.1	-37.7	18.5	$(3.1\pm 3.7) e^{-6}$	5.0
14166-3637	2-1	APEX	0.03	$0.00_{-0.00}^{+0.00}$	0.02	$-0.1\pm 0.2$	0.1	-43.3	15.6	-	-0.8
	2-1	JCMT	-	-	0.0	-	-	0.0	-	-	0.0
	3-2	APEX	0.01	$0.00_{-0.00}^{+0.00}$	0.0	$0.0\pm 0.1$	0.1	-51.7	16.9	-	-0.2
14180-7107	3-2	JCMT	0.08	$0.00_{-0.00}^{+0.00}$	0.0	$0.2\pm 0.3$	0.0	0.0	10.0	$(1.2\pm 0.0) e^{-8}$	0.0
	2-1	APEX	0.02	$0.10_{-0.01}^{+0.01}$	0.0	$1.0\pm 0.1$	0.1	-8.8	11.2	$(1.1\pm 1.0) e^{-6}$	11.2
	3-2	APEX	0.01	$0.00_{-0.00}^{+0.00}$	0.0	$0.3\pm 0.0$	0.0	-7.7	10.4	$(2.3\pm 2.6) e^{-7}$	14.2
14286-4706	2-1	APEX	0.02	$0.00_{-0.00}^{+0.00}$	0.0	$1.1\pm 0.1$	0.0	-20.1	17.7	$(9.2\pm 8.5) e^{-6}$	29.2
	3-2	APEX	0.0	$0.00_{-0.00}^{+0.00}$	0.0	$0.2\pm 0.0$	0.0	-17.2	19.8	$(1.4\pm 1.7) e^{-6}$	-5.7
14415-7850	2-1	APEX	0.01	$0.00_{-0.00}^{+0.00}$	0.0	$0.2\pm 0.1$	0.1	-5.0	18.0	$(8.5\pm 7.3) e^{-9}$	2.0
14428-5742	2-1	APEX	0.06	$0.10_{-0.02}^{+0.02}$	0.01	$1.7\pm 0.3$	0.4	-67.2	16.1	$(1.2\pm 1.1) e^{-5}$	4.8
	3-2	APEX	0.05	$0.00_{-0.01}^{+0.00}$	0.0	$0.0\pm 0.2$	0.0	8.0	17.1	-	4.0
14484-6152	3-2	APEX	0.06	$0.20_{-0.02}^{+0.02}$	0.02	$6.6\pm 0.1$	0.8	22.1	18.5	$(1.2\pm 1.4) e^{-6}$	8.4
14531-5337	2-1	APEX	0.06	$0.20_{-0.01}^{+0.02}$	0.02	$5.8\pm 0.1$	0.6	-49.5	20.5	$(1.1\pm 1.0) e^{-5}$	9.2
14559-5446	2-1	APEX	0.02	$0.10_{-0.01}^{+0.01}$	0.0	$1.0\pm 0.1$	0.1	14.4	11.2	$(8.3\pm 7.4) e^{-7}$	9.1
	3-2	APEX	0.02	$0.00_{-0.01}^{+0.02}$	0.0	$0.4\pm 0.1$	0.0	12.8	8.7	$(2.1\pm 2.4) e^{-7}$	-14.5
14562-5406	2-1	APEX	0.05	$0.10_{-0.01}^{+0.01}$	0.03	$6.3\pm 0.1$	1.4	-53.4	32.7	$(6.4\pm 5.8) e^{-6}$	4.4
14591-4438	2-1	APEX	0.1	$0.40_{-0.03}^{+0.03}$	0.04	$8.1\pm 0.2$	1.1	34.8	14.2	$(6.8\pm 6.2) e^{-6}$	7.7
	2-1	JCMT	-	-	0.0	-	-	0.0	-	-	0.0
	3-2	APEX	0.02	$0.10_{-0.01}^{+0.01}$	0.01	$1.2\pm 0.1$	0.2	34.5	13.6	$(8.8\pm 10.1) e^{-7}$	5.9
	3-2	JCMT	0.08	$0.50_{-0.00}^{+0.00}$	0.0	$10.2\pm 0.4$	-	0.0	14.4	$(4.0\pm 4.7) e^{-6}$	0.0
15023-6916	2-1	APEX	0.02	$0.10_{-0.01}^{+0.01}$	0.0	$0.6\pm 0.0$	0.1	-41.0	4.3	$(2.1\pm 1.8) e^{-7}$	6.7
	3-2	APEX	0.01	$0.00_{-0.01}^{+0.01}$	0.0	$0.2\pm 0.0$	0.0	-41.0	4.7	$(4.1\pm 4.5) e^{-8}$	10.0

15027-5959	2-1	APEX	0.52	$5.00^{+0.49}_{-0.38}$	1.55	$19.3\pm 0.2$	3.9	-33.0	2.8	$(8.9\pm 7.8) e-6$	5.0
	3-2	APEX	0.09	$0.80^{+0.09}_{-0.07}$	0.23	$3.4\pm 0.1$	0.6	-32.8	3.1	$(1.8\pm 2.1) e-6$	5.6
15030-5319	2-1	APEX	0.02	$0.10^{+0.01}_{-0.01}$	0.01	$1.1\pm 0.1$	0.2	12.3	11.2	$(1.5\pm 1.3) e-6$	6.2
	3-2	APEX	0.01	$0.00^{+0.00}_{-0.00}$	0.0	$0.3\pm 0.1$	0.0	13.1	14.0	$(3.7\pm 4.2) e-7$	-77.8
15082-4808	2-1	APEX	0.8	$2.90^{+0.21}_{-0.20}$	0.15	$83.8\pm 1.1$	5.3	-3.2	19.4	$(1.0\pm 0.9) e-5$	15.9
	2-1	JCMT	-	-	0.0	-	-	0.0	-	-	0.0
	3-2	JCMT	-	-	0.0	-	-	0.0	-	-	0.0
15094-6953	1-0	SEST	0.05	$0.10^{+0.02}_{-0.02}$	0.0	$2.3\pm 0.1$	0.0	-1.3	9.1	$(3.5\pm 2.9) e-7$	0.0
	2-1	APEX	0.12	$0.60^{+0.04}_{-0.04}$	0.01	$8.2\pm 0.1$	0.2	-1.8	8.5	$(4.8\pm 3.9) e-7$	46.1
15099-5509	2-1	APEX	0.13	$0.30^{+0.03}_{-0.03}$	0.05	$11.2\pm 0.6$	1.7	-19.3	21.1	$(1.1\pm 1.0) e-5$	6.6
15148-4940	2-1	APEX	0.19	$0.30^{+0.05}_{-0.08}$	0.26	$21.4\pm 0.5$	0.8	-37.9	28.8	$(7.3\pm 6.5) e-6$	28.7
	2-1	JCMT	-	-	0.0	-	-	0.0	-	-	0.0
	3-2	APEX	0.03	$0.00^{+0.21}_{-0.02}$	0.0	$3.2\pm 0.1$	0.1	-36.9	28.0	$(1.2\pm 1.4) e-6$	23.8
	3-2	JCMT	-	-	0.0	-	-	0.0	-	-	0.0
15194-5115	2-1	APEX	0.83	$2.90^{+0.21}_{-0.19}$	0.75	$100.2\pm 0.3$	29.4	-15.9	23.9	$(8.2\pm 7.2) e-6$	3.4
	2-1	JCMT	0.08	$2.40^{+0.00}_{-0.00}$	0.0	$83.1\pm 0.5$	20.3	0.0	20.2	$(4.0\pm 3.4) e-6$	4.1
	3-2	JCMT	0.11	$4.80^{+0.00}_{-0.00}$	0.0	$159.2\pm 0.7$	-	0.0	20.3	$(7.4\pm 8.5) e-6$	-0.2
15226-3603	2-1	APEX	0.09	$0.40^{+0.03}_{-0.03}$	0.04	$7.1\pm 0.1$	0.9	-57.8	13.3	$(3.7\pm 3.3) e-6$	7.8
	2-1	JCMT	0.03	$0.10^{+0.00}_{-0.00}$	0.0	$2.3\pm 0.1$	0.0	0.0	13.2	$(8.7\pm 7.7) e-7$	0.0
	3-2	APEX	0.02	$0.10^{+0.01}_{-0.01}$	0.01	$1.2\pm 0.1$	0.2	-57.5	12.7	$(5.3\pm 6.0) e-7$	6.7
	3-2	JCMT	0.08	$0.20^{+0.00}_{-0.00}$	0.0	$3.7\pm 0.4$	-	0.0	14.2	$(9.3\pm 10.7) e-7$	0.0
15287-5811	2-1	APEX	0.18	$0.90^{+0.46}_{-0.28}$	0.02	$2.1\pm 0.2$	0.1	-51.4	1.6	$(7.1\pm 6.0) e-7$	17.8
	3-2	APEX	0.03	$0.00^{+0.00}_{-0.00}$	0.0	$0.0\pm 0.1$	0.0	13.1	16.7	$(1.3\pm 1.5) e-8$	-1.2
15323-4920	3-2	APEX	0.01	$0.00^{+0.00}_{-0.00}$	0.0	$0.1\pm 0.1$	0.0	-10.7	17.3	$(3.0\pm 3.4) e-8$	-4.0

15341+1515	1-0	SEST	0.02	$0.00_{-0.01}^{+0.01}$	0.0	$0.4\pm 0.1$	0.0	-26.7	12.0	$(2.0\pm 1.8) e^{-7}$	0.0
15357-5239	2-1	APEX	0.06	$0.10_{-0.02}^{+0.03}$	0.01	$3.3\pm 0.3$	0.4	-50.6	19.1	$(8.5\pm 7.4) e^{-6}$	8.7
	3-2	APEX	0.02	$0.00_{-0.01}^{+0.01}$	0.0	$0.6\pm 0.1$	0.1	-57.7	14.3	$(1.7\pm 1.9) e^{-6}$	7.0
15373-5308	2-1	APEX	0.33	$0.20_{-0.09}^{+0.08}$	0.03	$8.8\pm 1.9$	1.1	-82.0	21.2	$(4.4\pm 4.3) e^{-5}$	8.3
15380-6545	2-1	APEX	0.03	$0.10_{-0.01}^{+0.01}$	0.0	$1.3\pm 0.1$	0.1	-3.1	7.8	$(5.1\pm 4.4) e^{-7}$	28.9
	3-2	APEX	0.01	$0.00_{-0.00}^{+0.01}$	0.0	$0.3\pm 0.0$	0.0	-3.1	6.0	$(7.1\pm 7.8) e^{-8}$	10.0
15402-3700	2-1	APEX	0.06	$0.30_{-0.02}^{+0.03}$	0.01	$3.3\pm 0.1$	0.0	20.4	7.6	$(8.2\pm 7.1) e^{-7}$	195.6
	3-2	APEX	0.01	$0.10_{-0.01}^{+0.01}$	0.0	$0.7\pm 0.0$	0.0	19.9	7.8	$(1.3\pm 1.4) e^{-7}$	124.5
15432-5200	2-1	APEX	0.14	$1.70_{-1.68}^{+0.14}$	0.02	$3.5\pm 0.1$	0.2	-39.8	1.5	$(5.2\pm 5.5) e^{-6}$	16.9
15468-5018	2-1	APEX	0.07	$0.10_{-0.02}^{+0.02}$	0.01	$2.0\pm 0.3$	0.3	5.4	15.6	$(9.7\pm 8.9) e^{-6}$	6.8
15503-6314	2-1	APEX	0.04	$0.00_{-0.01}^{+0.01}$	0.01	$0.7\pm 0.2$	0.2	-48.0	14.0	$(8.5\pm 7.7) e^{-7}$	3.2
	3-2	APEX	0.01	$0.00_{-0.00}^{+0.00}$	0.0	$0.2\pm 0.0$	0.0	-50.1	12.6	$(1.4\pm 1.6) e^{-7}$	6.0
15568-4513	2-1	APEX	0.04	$0.00_{-0.01}^{+0.01}$	0.01	$0.9\pm 0.2$	0.0	24.1	20.3	$(1.2\pm 1.1) e^{-6}$	-125.7
	3-2	APEX	0.01	$0.00_{-0.00}^{+0.00}$	0.0	$0.3\pm 0.1$	-0.1	19.4	17.1	$(2.2\pm 2.6) e^{-7}$	-2.2
16029-3041	2-1	JCMT	0.05	$0.40_{-0.00}^{+0.00}$	0.0	$8.3\pm 0.3$	2.4	0.0	13.9	$(7.3\pm 6.7) e^{-6}$	3.5
	3-2	JCMT	0.03	$0.60_{-0.00}^{+0.00}$	0.0	$11.7\pm 0.2$	-	0.0	15.0	$(8.5\pm 10.0) e^{-6}$	0.0
16055-4621	2-1	APEX	0.23	$2.50_{-0.33}^{+0.45}$	0.62	$5.1\pm 0.1$	1.0	3.5	1.4	$(2.7\pm 2.1) e^{-6}$	5.2
	3-2	APEX	0.07	$0.20_{-0.16}^{+0.05}$	0.0	$0.8\pm 0.2$	0.0	-29.7	3.8	$(9.5\pm 10.6) e^{-7}$	697.8
16063-4906	2-1	APEX	0.5	$3.10_{-0.24}^{+0.28}$	0.57	$26.6\pm 0.4$	3.0	-38.0	6.0	$(4.4\pm 3.8) e^{-6}$	9.0
	3-2	APEX	0.09	$0.40_{-0.04}^{+0.05}$	0.01	$4.4\pm 0.1$	0.3	-37.5	5.2	$(6.4\pm 7.2) e^{-7}$	13.3
16070-4727	2-1	APEX	0.08	$0.00_{-0.01}^{+0.01}$	0.01	$0.7\pm 0.3$	-0.1	4.0	12.9	$(6.0\pm 5.7) e^{-6}$	-7.6
	3-2	APEX	0.03	$0.30_{-0.07}^{+0.06}$	0.0	$0.6\pm 0.0$	0.0	3.6	1.2	$(1.6\pm 1.8) e^{-6}$	-36.4
16105-4205	2-1	APEX	0.42	$1.80_{-0.12}^{+0.14}$	0.57	$38.4\pm 0.2$	13.3	-82.7	14.4	$(1.4\pm 1.3) e^{-5}$	2.9
	2-1	JCMT	0.03	$1.40_{-0.00}^{+0.00}$	0.0	$29.2\pm 0.2$	8.5	0.0	15.4	$(6.9\pm 6.3) e^{-6}$	3.4

	3-2	JCMT	0.09	$2.10^{+0.00}_{-0.00}$	0.0	$42.9 \pm 0.5$	-	0.0	14.9	$(7.9 \pm 9.3) \text{ e-6}$	0.0
16127-7834	2-1	APEX	0.05	$0.00^{+0.01}_{-0.01}$	0.01	$0.5 \pm 0.2$	-0.4	10.5	14.7	$(3.9 \pm 3.4) \text{ e-8}$	-1.2
	3-2	APEX	0.01	$0.00^{+0.00}_{-0.00}$	0.0	$0.0 \pm 0.1$	-0.1	15.0	15.7	$(2.0 \pm 2.2) \text{ e-9}$	-0.2
16146-4619	2-1	APEX	0.35	$0.10^{+2.01}_{-0.12}$	0.01	$1.3 \pm 0.4$	-1.3	-22.7	10.4	$(5.9 \pm 5.5) \text{ e-7}$	-1.0
	3-2	APEX	0.12	$0.10^{+0.63}_{-0.05}$	0.0	$-0.6 \pm 0.1$	-0.1	-21.0	9.6	-	6.1
16156-4756	2-1	APEX	0.16	$1.00^{+0.20}_{-0.12}$	0.04	$7.0 \pm 0.2$	0.8	-83.9	4.2	$(2.0 \pm 1.8) \text{ e-5}$	9.1
	3-2	APEX	0.03	$0.10^{+0.03}_{-0.02}$	0.0	$1.1 \pm 0.1$	0.0	-84.0	3.7	$(3.4 \pm 3.8) \text{ e-6}$	103.2
16263-5533	2-1	APEX	0.03	$0.10^{+0.01}_{-0.01}$	0.03	$2.8 \pm 0.1$	0.8	45.2	14.9	$(1.1 \pm 1.0) \text{ e-5}$	3.6
16265-5100	2-1	APEX	0.04	$0.10^{+0.01}_{-0.01}$	0.02	$2.3 \pm 0.2$	0.2	-21.5	13.3	$(1.6 \pm 1.5) \text{ e-5}$	11.1
	3-2	APEX	0.02	$0.00^{+0.00}_{-0.01}$	0.0	$0.3 \pm 0.1$	-0.1	-20.1	13.9	$(2.1 \pm 2.4) \text{ e-6}$	-5.6
16279-5342	2-1	APEX	0.04	$0.10^{+0.01}_{-0.01}$	0.01	$1.4 \pm 0.2$	0.3	-56.3	15.9	$(8.4 \pm 7.8) \text{ e-6}$	5.5
16316-5026	2-1	APEX	0.13	$1.40^{+0.33}_{-0.20}$	0.0	$2.9 \pm 0.1$	0.0	2.5	1.4	$(9.3 \pm 7.8) \text{ e-7}$	167.9
	3-2	APEX	0.04	$0.40^{+0.14}_{-0.08}$	0.0	$0.7 \pm 0.0$	0.0	2.5	1.4	$(2.2 \pm 2.4) \text{ e-7}$	20.1
16334-3107	2-1	APEX	0.07	$0.40^{+0.03}_{-0.03}$	0.01	$3.1 \pm 0.1$	0.2	-4.3	6.0	$(4.7 \pm 3.8) \text{ e-7}$	14.3
	2-1	JCMT	-	-	0.0	-	-	0.0	-	-	0.0
	3-2	APEX	0.02	$0.10^{+0.01}_{-0.01}$	0.0	$0.7 \pm 0.0$	0.1	-4.2	6.9	$(9.8 \pm 10.5) \text{ e-8}$	10.2
	3-2	JCMT	0.09	$0.00^{+0.00}_{-0.00}$	0.0	$0.5 \pm 0.4$	0.0	0.0	10.0	$(5.5 \pm 0.0) \text{ e-8}$	0.0
16399-3548	2-1	APEX	0.06	$0.00^{+0.01}_{-0.03}$	0.01	$0.8 \pm 0.3$	0.1	-52.6	15.2	$(6.3 \pm 5.9) \text{ e-6}$	8.7
	2-1	JCMT	-	-	0.0	-	-	0.0	-	-	0.0
	3-2	APEX	0.03	$0.00^{+0.00}_{-0.00}$	0.0	$-0.2 \pm 0.1$	0.0	-15.8	16.6	-	19.5
	3-2	JCMT	0.09	$0.00^{+0.00}_{-0.00}$	0.0	$0.0 \pm 0.4$	0.0	0.0	0.0	-	0.0
16460-4022	2-1	APEX	0.08	$0.20^{+0.03}_{-0.02}$	0.04	$3.2 \pm 0.3$	1.0	-35.6	11.1	$(2.5 \pm 2.2) \text{ e-6}$	3.1
	3-2	APEX	0.01	$0.00^{+0.00}_{-0.00}$	0.01	$0.8 \pm 0.1$	0.2	-29.3	20.2	$(5.9 \pm 6.9) \text{ e-7}$	4.3
16469-3412	2-1	JCMT	0.05	$0.00^{+0.00}_{-0.00}$	0.0	$0.0 \pm 0.2$	0.0	0.0	0.0	-	0.0

	3-2	JCMT	0.0	$0.00^{+0.00}_{-0.00}$	0.0	$0.1\pm 0.0$	0.0	0.0	10.0	$(5.0\pm 0.0) e^{-11}$	0.0
16469-4753	2-1	APEX	0.15	$0.10^{+0.06}_{-0.04}$	0.02	$2.9\pm 0.8$	0.6	-78.5	13.9	$(1.7\pm 1.6) e^{-5}$	5.3
	3-2	APEX	0.03	$0.00^{+0.07}_{-0.02}$	0.0	$0.0\pm 0.1$	-0.1	-42.3	12.5	$(1.6\pm 1.8) e^{-7}$	-0.2
16490-4618	2-1	APEX	0.81	$4.30^{+0.93}_{-0.74}$	1.93	$22.6\pm 1.4$	3.4	-12.0	3.5	$(1.1\pm 1.0) e^{-5}$	6.6
	3-2	APEX	0.25	$2.50^{+0.40}_{-0.29}$	0.39	$5.7\pm 0.2$	0.6	-10.9	1.6	$(2.1\pm 2.4) e^{-6}$	9.0
16534-3030	2-1	JCMT	-	-	0.0	-	-	0.0	-	-	0.0
	3-2	JCMT	0.06	$0.50^{+0.00}_{-0.00}$	0.0	$2.1\pm 0.2$	0.0	0.0	2.9	$(8.3\pm 10.6) e^{-8}$	0.0
16541-4901	2-1	APEX	0.04	$0.10^{+0.02}_{-0.09}$	0.01	$1.6\pm 0.1$	0.3	-50.5	12.3	$(1.0\pm 1.0) e^{-5}$	5.5
	3-2	APEX	0.01	$0.00^{+0.00}_{-0.00}$	0.0	$0.3\pm 0.1$	0.1	-49.3	14.5	$(1.9\pm 2.3) e^{-6}$	4.2
16544-5554	2-1	APEX	0.02	$0.00^{+0.00}_{-0.00}$	0.0	$0.0\pm 0.1$	0.0	-7.7	16.6	-	2.9
16558-3958	3-2	APEX	0.72	$0.10^{+0.05}_{-0.07}$	0.01	$-0.1\pm 3.9$	0.1	24.3	16.9	-	-1.2
16594-4656	2-1	APEX	0.5	$2.00^{+0.17}_{-0.15}$	0.15	$40.3\pm 0.9$	3.8	-24.9	13.4	$(2.8\pm 2.4) e^{-5}$	10.7
	2-1	JCMT	0.06	$1.70^{+0.00}_{-0.00}$	0.0	$35.6\pm 0.3$	-	0.0	14.2	$(1.6\pm 1.4) e^{-5}$	0.0
	3-2	JCMT	0.09	$4.30^{+0.00}_{-0.00}$	0.0	$88.2\pm 0.5$	-	0.0	14.4	$(4.5\pm 5.2) e^{-5}$	-0.1
16596-4736	2-1	APEX	0.03	$0.10^{+0.01}_{-0.01}$	0.01	$1.4\pm 0.1$	0.2	-46.9	14.7	$(1.1\pm 1.0) e^{-5}$	5.8
	3-2	APEX	0.02	$0.00^{+0.00}_{-0.00}$	0.0	$0.4\pm 0.1$	0.1	-35.6	16.9	$(2.6\pm 3.1) e^{-6}$	5.0
17001-3651	2-1	JCMT	-	-	0.0	-	-	0.0	-	-	0.0
	3-2	APEX	0.05	$0.20^{+0.02}_{-0.01}$	0.01	$4.0\pm 0.1$	0.3	-46.4	12.8	$(8.2\pm 9.4) e^{-7}$	13.5
	3-2	JCMT	0.1	$0.20^{+0.00}_{-0.00}$	0.0	$3.1\pm 0.5$	-	0.0	12.1	$(4.0\pm 4.6) e^{-7}$	0.0
17007-4823	2-1	APEX	0.04	$0.10^{+0.03}_{-0.04}$	0.01	$2.6\pm 0.2$	0.2	30.0	13.2	$(2.0\pm 1.8) e^{-6}$	15.8
	3-2	APEX	0.01	$0.00^{+0.00}_{-0.00}$	0.0	$0.5\pm 0.1$	0.1	31.7	14.3	$(2.9\pm 3.3) e^{-7}$	5.7
17010-3840	2-1	APEX	0.49	$0.20^{+4.72}_{-0.18}$	0.0	$9.9\pm 1.0$	0.8	-14.8	10.3	$(2.5\pm 2.3) e^{-5}$	12.2
17043-3145	2-1	APEX	0.03	$0.00^{+0.01}_{-0.01}$	0.01	$0.5\pm 0.2$	-0.4	-4.5	17.8	$(1.1\pm 1.1) e^{-6}$	-1.4
	2-1	JCMT	-	-	0.0	-	-	0.0	-	-	0.0

	3-2	APEX	0.01	$0.00_{-0.00}^{+0.00}$	0.0	$0.1\pm 0.1$	-0.1	-6.0	15.6	$(1.4\pm 1.7) e^{-7}$	-1.8
	3-2	JCMT	0.08	$0.00_{-0.00}^{+0.00}$	0.0	$0.1\pm 0.4$	0.0	0.0	10.0	$(8.1\pm 0.0) e^{-8}$	0.0
17076-4702	2-1	APEX	0.04	$0.10_{-0.01}^{+0.01}$	0.1	$3.0\pm 0.1$	2.6	14.7	15.9	$(6.4\pm 5.5) e^{-6}$	1.1
	3-2	APEX	0.01	$0.00_{-0.00}^{+0.00}$	0.01	$0.3\pm 0.1$	0.3	17.8	13.5	$(8.0\pm 8.9) e^{-7}$	1.1
17079-3243	2-1	APEX	0.13	$0.40_{-0.03}^{+0.03}$	0.01	$17.3\pm 0.3$	0.5	19.6	26.9	$(9.3\pm 8.3) e^{-6}$	33.5
	2-1	JCMT	-	-	0.0	-	-	0.0	-	-	0.0
	3-2	APEX	0.03	$0.10_{-0.01}^{+0.01}$	0.0	$3.6\pm 0.1$	0.1	19.7	28.2	$(2.3\pm 2.6) e^{-6}$	46.3
	3-2	JCMT	0.05	$1.00_{-0.00}^{+0.00}$	0.0	$43.1\pm 0.4$	0.0	0.0	27.2	$(1.4\pm 1.6) e^{-5}$	0.0
17080-3215	2-1	JCMT	0.02	$0.10_{-0.00}^{+0.00}$	0.0	$5.7\pm 0.1$	-	0.0	23.6	$(1.1\pm 1.0) e^{-6}$	0.0
	3-2	JCMT	-	-	0.0	-	-	0.0	-	-	0.0
17088-4221	2-1	APEX	0.26	$2.90_{-0.24}^{+0.28}$	0.08	$7.6\pm 0.1$	0.4	-8.3	1.9	$(9.9\pm 8.5) e^{-6}$	20.4
17104-3146	2-1	APEX	0.05	$0.20_{-0.01}^{+0.02}$	0.03	$4.7\pm 0.2$	0.8	24.0	17.9	$(7.7\pm 7.1) e^{-6}$	5.5
	2-1	JCMT	-	-	0.0	-	-	0.0	-	-	0.0
	3-2	APEX	0.01	$0.00_{-0.00}^{+0.00}$	0.0	$1.0\pm 0.1$	0.1	24.7	18.6	$(1.4\pm 1.6) e^{-6}$	9.5
	3-2	JCMT	0.12	$0.20_{-0.00}^{+0.00}$	0.0	$5.3\pm 0.7$	-	0.0	17.3	$(4.0\pm 4.7) e^{-6}$	0.0
17109-3243	2-1	APEX	0.05	$0.00_{-0.02}^{+0.02}$	0.01	$0.8\pm 0.2$	0.1	-86.9	12.6	$(5.4\pm 5.0) e^{-6}$	9.6
	2-1	JCMT	-	-	0.0	-	-	0.0	-	-	0.0
	3-2	APEX	0.04	$0.00_{-0.00}^{+0.00}$	0.0	$-0.4\pm 0.2$	-0.1	9.9	16.9	-	3.2
	3-2	JCMT	0.1	$0.00_{-0.00}^{+0.00}$	0.0	$0.2\pm 0.5$	0.0	0.0	10.0	$(8.5\pm 0.0) e^{-7}$	0.0
17115-3322	2-1	APEX	0.05	$0.20_{-0.02}^{+0.03}$	0.02	$3.0\pm 0.2$	0.5	-71.1	11.2	$(2.4\pm 2.1) e^{-6}$	5.6
	2-1	JCMT	-	-	0.0	-	-	0.0	-	-	0.0
	3-2	APEX	0.02	$0.10_{-0.01}^{+0.01}$	0.0	$0.7\pm 0.1$	0.0	-70.0	10.3	$(4.4\pm 5.0) e^{-7}$	19.6
	3-2	JCMT	0.13	$0.00_{-0.00}^{+0.00}$	0.0	$0.0\pm 0.6$	0.0	0.0	0.0	-	0.0
17150-3224	2-1	JCMT	0.03	$0.50_{-0.00}^{+0.00}$	0.0	$11.2\pm 0.2$	3.1	0.0	16.8	$(1.4\pm 1.3) e^{-5}$	3.6

	3-2	JCMT	0.05	$1.40^{+0.00}_{-0.00}$	0.0	$35.7\pm 0.3$	-	0.0	21.2	$(3.9\pm 4.7) \text{ e-5}$	0.0
17163-3907	2-1	JCMT	0.04	$0.00^{+0.00}_{-0.00}$	0.0	$2.0\pm 0.2$	0.0	0.0	10.0	$(3.4\pm 0.0) \text{ e-7}$	0.0
	3-2	JCMT	-	-	0.0	-	-	0.0	-	-	0.0
17174-4641	3-2	APEX	0.01	$0.00^{+0.00}_{-0.00}$	0.0	$0.2\pm 0.1$	0.1	-6.2	20.1	$(1.5\pm 1.7) \text{ e-7}$	2.8
17189-6501	3-2	APEX	0.01	$0.00^{+0.00}_{-0.00}$	0.0	$0.2\pm 0.0$	0.0	-46.2	10.0	$(1.3\pm 1.5) \text{ e-6}$	11.2
17201-4613	2-1	APEX	0.12	$0.20^{+0.05}_{-0.04}$	0.0	$3.5\pm 0.4$	0.2	-46.6	9.6	$(1.1\pm 1.0) \text{ e-6}$	20.1
	3-2	APEX	0.02	$0.00^{+0.01}_{-0.01}$	0.0	$0.7\pm 0.1$	0.1	-47.0	9.9	$(1.7\pm 1.9) \text{ e-7}$	8.0
17211-5529	2-1	APEX	0.02	$0.00^{+0.00}_{-0.01}$	0.0	$0.3\pm 0.1$	0.1	-35.5	16.7	$(2.5\pm 2.1) \text{ e-8}$	2.7
	3-2	APEX	0.01	$0.00^{+0.00}_{-0.00}$	0.0	$0.1\pm 0.0$	0.0	35.6	16.6	$(2.8\pm 3.1) \text{ e-9}$	-1.5
17213-2219	1-0	IRAM	0.33	$5.00^{+0.59}_{-0.38}$	1.23	$6.7\pm 0.2$	1.4	6.1	1.1	$(1.2\pm 1.1) \text{ e-6}$	4.8
	2-1	IRAM	0.31	$3.50^{+0.76}_{-3.47}$	0.0	$5.8\pm 0.2$	0.0	6.1	1.1	$(5.1\pm 10.0) \text{ e-7}$	0.0
17215-7114	2-1	APEX	0.03	$0.10^{+0.05}_{-0.03}$	0.0	$0.5\pm 0.1$	0.1	-40.7	2.6	$(4.2\pm 3.5) \text{ e-7}$	6.2
	3-2	APEX	0.01	$0.00^{+0.00}_{-0.00}$	0.0	$0.1\pm 0.1$	0.2	-30.6	13.8	$(2.0\pm 2.2) \text{ e-7}$	0.9
17260-3846	2-1	APEX	0.14	$0.00^{+0.01}_{-0.01}$	0.01	$0.1\pm 0.7$	0.2	17.1	16.8	$(4.2\pm 3.9) \text{ e-7}$	0.8
	3-2	APEX	0.07	$0.00^{+0.01}_{-0.01}$	0.0	$0.1\pm 0.4$	0.1	5.1	16.4	$(9.4\pm 10.8) \text{ e-8}$	0.6
17267-1926	1-0	SEST	0.02	$0.10^{+0.57}_{-0.08}$	0.0	$1.4\pm 0.2$	0.0	33.3	12.7	$(5.3\pm 4.4) \text{ e-7}$	0.0
17277-2356	1-0	IRAM	0.28	$3.60^{+0.53}_{-0.34}$	0.17	$5.0\pm 0.3$	0.3	4.0	1.1	$(4.0\pm 3.5) \text{ e-6}$	19.5
	2-1	IRAM	0.38	$0.50^{+0.22}_{-0.18}$	0.0	$7.1\pm 0.6$	0.0	6.6	2.8	$(4.6\pm 3.9) \text{ e-6}$	0.0
17282-5102	2-1	APEX	0.02	$0.00^{+0.00}_{-0.01}$	0.0	$0.3\pm 0.1$	-0.1	-25.5	13.0	$(2.1\pm 1.9) \text{ e-7}$	-3.3
	3-2	APEX	0.01	$0.00^{+0.00}_{-0.00}$	0.0	$0.0\pm 0.1$	-0.2	39.9	17.4	$(1.3\pm 1.5) \text{ e-8}$	-0.1
17294-4326	2-1	APEX	0.04	$0.10^{+0.01}_{-0.01}$	0.01	$2.5\pm 0.2$	0.2	-28.1	17.8	$(4.0\pm 3.7) \text{ e-6}$	14.5
	3-2	APEX	0.01	$0.00^{+0.00}_{-0.00}$	0.0	$0.7\pm 0.1$	0.1	-25.2	19.0	$(9.4\pm 10.9) \text{ e-7}$	7.8
17319-6234	3-2	APEX	0.03	$0.10^{+0.01}_{-0.01}$	0.03	$2.4\pm 0.1$	0.6	-6.3	16.5	$(2.2\pm 2.6) \text{ e-6}$	3.8
17328-3327	2-1	JCMT	0.03	$0.00^{+0.00}_{-0.00}$	0.0	$0.0\pm 0.1$	0.0	0.0	0.0	-	0.0

	3-2	JCMT	-	-	0.0	-	-	0.0	-	-	0.0
17334+1537	1-0	IRAM	0.16	$0.40^{+0.05}_{-0.04}$	0.02	$10.9 \pm 0.7$	0.7	-51.6	16.3	$(5.7 \pm 5.4) \text{ e-6}$	14.8
	2-1	IRAM	0.21	$0.70^{+0.07}_{-0.06}$	0.0	$15.0 \pm 0.6$	0.0	-51.5	13.3	$(2.1 \pm 1.9) \text{ e-6}$	0.0
17341-3453	2-1	JCMT	0.04	$0.00^{+0.00}_{-0.00}$	0.0	$0.2 \pm 0.2$	0.0	0.0	10.0	$(1.3 \pm 0.0) \text{ e-7}$	0.0
	3-2	JCMT	0.08	$0.00^{+0.00}_{-0.00}$	0.0	$0.8 \pm 0.4$	0.0	0.0	10.0	$(2.1 \pm 0.0) \text{ e-7}$	0.0
17361+5746	1-0	OSO	0.02	$0.00^{+0.38}_{-0.04}$	0.0	$0.6 \pm 0.1$	0.0	-34.4	11.2	$(8.3 \pm 7.6) \text{ e-7}$	0.0
17361-2807	1-0	IRAM	0.18	$0.90^{+0.99}_{-0.30}$	0.03	$-0.3 \pm 0.3$	-0.1	23.5	1.9	-	5.4
	2-1	IRAM	0.8	$10.30^{+2.65}_{-6.92}$	0.0	$15.6 \pm 0.7$	0.0	39.9	1.1	$(5.4 \pm 4.6) \text{ e-6}$	0.0
17363-5213	2-1	APEX	0.03	$0.10^{+0.01}_{-0.01}$	0.01	$0.9 \pm 0.1$	-0.1	36.4	7.2	$(9.3 \pm 8.1) \text{ e-7}$	-14.3
	3-2	APEX	0.01	$0.00^{+0.00}_{-0.01}$	0.0	$0.1 \pm 0.0$	0.0	37.5	10.8	$(8.3 \pm 9.5) \text{ e-8}$	70.2
17389-5742	2-1	APEX	0.13	$0.50^{+0.04}_{-0.04}$	0.02	$12.0 \pm 0.1$	0.5	18.6	14.9	$(8.9 \pm 7.4) \text{ e-7}$	24.4
	3-2	APEX	0.02	$0.10^{+0.01}_{-0.01}$	0.0	$2.1 \pm 0.1$	0.1	18.4	14.9	$(1.5 \pm 1.7) \text{ e-7}$	22.1
17403-3238	2-1	APEX	0.44	$4.00^{+0.72}_{-0.52}$	0.04	$15.0 \pm 0.2$	1.0	1.6	2.6	$(6.8 \pm 5.4) \text{ e-7}$	15.1
	2-1	JCMT	-	-	0.0	-	-	0.0	-	-	0.0
	3-2	APEX	0.02	$0.10^{+0.01}_{-0.01}$	0.0	$2.1 \pm 0.1$	0.0	18.4	14.9	$(2.0 \pm 2.2) \text{ e-7}$	0.0
	3-2	JCMT	0.11	$1.50^{+0.00}_{-0.00}$	0.0	$3.4 \pm 0.2$	-	0.0	1.6	$(1.4 \pm 1.5) \text{ e-7}$	0.0
17411-3154	2-1	JCMT	-	-	0.0	-	-	0.0	-	-	0.0
	3-2	JCMT	0.06	$3.50^{+0.00}_{-0.00}$	0.0	$101.7 \pm 0.4$	-	0.0	20.9	$(9.1 \pm 10.8) \text{ e-6}$	-0.1
17436-1545	1-0	IRAM	0.1	$0.10^{+0.03}_{-0.03}$	0.02	$3.6 \pm 0.5$	0.5	14.3	13.5	$(1.1 \pm 1.1) \text{ e-5}$	7.8
	2-1	IRAM	0.12	$0.20^{+0.03}_{-0.03}$	0.0	$6.4 \pm 0.6$	0.0	13.1	16.5	$(7.5 \pm 6.9) \text{ e-6}$	0.0
17446-4048	2-1	APEX	0.16	$0.60^{+0.05}_{-0.04}$	0.04	$15.6 \pm 0.2$	1.2	-45.6	17.1	$(6.2 \pm 5.3) \text{ e-6}$	12.7
	2-1	JCMT	0.11	$0.40^{+0.00}_{-0.00}$	0.0	$11.3 \pm 0.6$	0.0	0.0	18.8	$(3.0 \pm 2.6) \text{ e-6}$	0.0
	3-2	APEX	0.03	$0.10^{+0.01}_{-0.01}$	0.01	$2.7 \pm 0.1$	0.3	-45.8	17.2	$(1.3 \pm 1.4) \text{ e-6}$	9.0
	3-2	JCMT	-	-	0.0	-	-	0.0	-	-	0.0

17446-7809	3-2	APEX	0.05	$0.20^{+0.02}_{-0.02}$	0.02	$5.0\pm 0.1$	0.5	0.5	15.4	$(1.2\pm 1.4) e^{-6}$	9.6
17484-0800	1-0	IRAM	0.1	$0.20^{+0.03}_{-0.03}$	0.03	$5.5\pm 0.4$	0.7	-26.4	13.6	$(3.3\pm 3.1) e^{-6}$	7.7
	2-1	IRAM	0.2	$0.70^{+0.06}_{-0.06}$	0.0	$15.4\pm 0.5$	0.0	-26.5	14.1	$(2.3\pm 2.0) e^{-6}$	0.0
17485-2209	1-0	IRAM	0.06	$0.00^{+0.01}_{-0.01}$	0.0	$1.0\pm 0.3$	-0.1	16.1	11.6	$(1.5\pm 1.4) e^{-6}$	-8.0
	2-1	IRAM	0.05	$0.10^{+0.01}_{-0.01}$	0.0	$2.1\pm 0.3$	0.0	16.6	17.6	$(8.5\pm 7.8) e^{-7}$	0.0
17505-3143	2-1	JCMT	-	-	0.0	-	-	0.0	-	-	0.0
	3-2	JCMT	-	-	0.0	-	-	0.0	-	-	0.0
17505-7021	2-1	APEX	0.02	$0.10^{+0.01}_{-0.01}$	0.0	$0.6\pm 0.1$	-0.1	9.9	6.9	$(3.0\pm 2.6) e^{-7}$	-6.1
	3-2	APEX	0.03	$0.00^{+0.01}_{-0.01}$	0.01	$0.7\pm 0.1$	0.2	10.8	11.4	$(2.4\pm 2.7) e^{-7}$	2.7
17508-3419	2-1	APEX	0.03	$0.00^{+0.01}_{-0.01}$	0.0	$0.3\pm 0.2$	0.1	-50.1	15.2	$(4.5\pm 4.1) e^{-7}$	3.4
	2-1	JCMT	-	-	0.0	-	-	0.0	-	-	0.0
	3-2	JCMT	0.0	$0.00^{+0.00}_{-0.00}$	0.0	$0.4\pm 0.0$	0.0	0.0	10.0	$(2.0\pm 0.0) e^{-7}$	0.0
17513-2313	1-0	SEST	0.05	$0.00^{+0.02}_{-0.02}$	0.0	$0.0\pm 0.3$	0.0	-1.4	12.2	$(1.3\pm 1.3) e^{-7}$	0.0
17534-3030	2-1	APEX	0.24	$0.40^{+0.08}_{-0.08}$	0.06	$11.3\pm 1.1$	1.7	-11.5	16.0	$(5.3\pm 4.5) e^{-6}$	6.6
	2-1	JCMT	-	-	0.0	-	-	0.0	-	-	0.0
	3-2	APEX	0.15	$1.90^{+0.25}_{-0.20}$	0.19	$3.7\pm 0.0$	0.4	7.5	1.4	$(7.6\pm 8.1) e^{-7}$	9.8
	3-2	JCMT	0.11	$0.00^{+0.00}_{-0.00}$	0.0	$1.6\pm 0.5$	0.0	0.0	10.0	$(4.7\pm 0.0) e^{-7}$	0.0
17566-3555	2-1	APEX	0.04	$0.00^{+0.01}_{-0.01}$	0.01	$0.7\pm 0.2$	-0.4	-27.5	18.3	$(1.2\pm 1.1) e^{-6}$	-1.8
	3-2	APEX	0.01	$0.00^{+0.00}_{-0.00}$	0.0	$0.1\pm 0.1$	0.0	-39.7	15.9	$(1.0\pm 1.2) e^{-7}$	-2.6
17570-3713	2-1	APEX	0.05	$0.10^{+0.02}_{-0.01}$	0.01	$3.9\pm 0.2$	0.3	-11.2	15.8	$(5.1\pm 4.7) e^{-6}$	12.4
	2-1	JCMT	-	-	0.0	-	-	0.0	-	-	0.0
	3-2	APEX	0.01	$0.00^{+0.00}_{-0.00}$	0.0	$0.8\pm 0.1$	0.1	-11.4	15.6	$(9.2\pm 10.6) e^{-7}$	16.8
	3-2	JCMT	0.1	$0.00^{+0.00}_{-0.00}$	0.0	$1.4\pm 0.4$	0.0	0.0	10.0	$(7.5\pm 0.0) e^{-7}$	0.0
18018-2802	1-0	IRAM	0.1	$0.20^{+0.03}_{-0.02}$	0.01	$5.2\pm 0.5$	0.4	28.3	15.6	$(3.3\pm 3.1) e^{-6}$	13.3

	2-1	IRAM	0.16	$0.50^{+0.05}_{-0.04}$	0.0	$12.8 \pm 0.4$	0.0	29.4	14.4	$(1.9 \pm 1.7) \text{ e-6}$	0.0
18039-0813	1-0	IRAM	0.08	$0.10^{+0.03}_{-0.03}$	0.02	$2.6 \pm 0.3$	0.5	21.0	11.9	$(1.9 \pm 1.7) \text{ e-6}$	5.2
	2-1	IRAM	0.16	$0.60^{+0.06}_{-0.05}$	0.0	$11.1 \pm 0.4$	0.0	21.5	13.0	$(1.7 \pm 1.5) \text{ e-6}$	0.0
18096-1003	1-0	IRAM	0.16	$1.30^{+0.19}_{-0.14}$	0.03	$3.0 \pm 0.2$	0.2	5.4	1.6	$(3.4 \pm 3.0) \text{ e-6}$	19.3
	2-1	IRAM	0.54	$7.00^{+1.43}_{-0.85}$	0.0	$10.1 \pm 0.5$	0.0	43.0	1.1	$(3.9 \pm 3.3) \text{ e-6}$	0.0
18112+1227	1-0	IRAM	0.04	$0.00^{+0.01}_{-0.01}$	0.0	$1.4 \pm 0.2$	0.1	-0.3	22.2	$(1.8 \pm 1.7) \text{ e-6}$	11.4
	2-1	IRAM	0.05	$0.20^{+0.03}_{-0.02}$	0.0	$1.8 \pm 0.1$	0.0	16.8	6.1	$(2.6 \pm 2.2) \text{ e-7}$	0.0
18142-3646	2-1	JCMT	0.04	$0.00^{+0.00}_{-0.00}$	0.0	$0.0 \pm 0.2$	0.0	0.0	0.0	-	0.0
	3-2	JCMT	0.08	$0.00^{+0.00}_{-0.00}$	0.0	$0.6 \pm 0.3$	0.0	0.0	10.0	$(1.2 \pm 0.0) \text{ e-9}$	0.0
18157+1757	1-0	OSO	0.03	$1.20^{+1.19}_{-1.20}$	0.0	$0.1 \pm 0.1$	0.0	-88.8	11.4	$(1.4 \pm 1.3) \text{ e-7}$	0.0
18186+3143	1-0	OSO	0.01	$0.00^{+0.95}_{-0.02}$	0.0	$0.3 \pm 0.1$	0.0	-9.9	10.7	$(4.2 \pm 3.9) \text{ e-7}$	0.0
18213+0335	1-0	IRAM	0.04	$0.10^{+0.01}_{-0.01}$	0.01	$1.9 \pm 0.2$	0.2	-25.4	14.0	$(1.8 \pm 1.7) \text{ e-6}$	9.6
	2-1	IRAM	0.09	$0.30^{+0.03}_{-0.03}$	0.0	$6.8 \pm 0.3$	0.0	-23.6	14.6	$(1.3 \pm 1.2) \text{ e-6}$	0.0
18261-1748	1-0	IRAM	0.05	$0.00^{+0.01}_{-0.02}$	0.01	$0.7 \pm 0.3$	0.2	26.9	13.7	$(8.8 \pm 8.4) \text{ e-7}$	2.7
	2-1	IRAM	0.06	$0.20^{+0.03}_{-0.02}$	0.0	$2.1 \pm 0.2$	0.0	-18.4	7.8	$(3.8 \pm 3.3) \text{ e-7}$	0.0
18276-4717	2-1	APEX	0.13	$0.50^{+0.04}_{-0.04}$	0.04	$12.9 \pm 0.1$	1.2	14.2	16.2	$(3.8 \pm 3.3) \text{ e-6}$	10.6
	2-1	JCMT	0.08	$0.50^{+0.00}_{-0.00}$	0.0	$12.4 \pm 0.5$	-	0.0	15.3	$(2.2 \pm 1.9) \text{ e-6}$	0.0
	3-2	APEX	0.03	$0.10^{+0.01}_{-0.01}$	0.01	$2.7 \pm 0.1$	0.2	14.3	15.9	$(8.8 \pm 9.8) \text{ e-7}$	14.6
	3-2	JCMT	-	-	0.0	-	-	0.0	-	-	0.0
18280-5639	2-1	APEX	0.03	$0.10^{+0.01}_{-0.01}$	0.0	$2.2 \pm 0.1$	0.1	3.8	11.0	$(7.3 \pm 6.4) \text{ e-7}$	15.1
	3-2	APEX	0.02	$0.00^{+0.01}_{-0.00}$	0.01	$0.8 \pm 0.1$	0.1	3.3	12.8	$(1.9 \pm 2.2) \text{ e-7}$	10.2
18378-3731	2-1	APEX	0.05	$0.30^{+0.03}_{-0.02}$	0.0	$2.4 \pm 0.1$	0.1	-30.3	6.2	$(6.3 \pm 5.4) \text{ e-7}$	26.2
	2-1	JCMT	-	-	0.0	-	-	0.0	-	-	0.0
	3-2	APEX	0.01	$0.10^{+0.01}_{-0.01}$	0.0	$0.6 \pm 0.0$	0.0	-30.3	6.2	$(1.1 \pm 1.2) \text{ e-7}$	-14.8

	3-2	JCMT	0.05	$0.00_{-0.00}^{+0.00}$	0.0	$0.3\pm 0.2$	0.0	0.0	10.0	$(4.4\pm 0.0) \text{ e-8}$	0.0
18406-4324	2-1	APEX	0.02	$0.00_{-0.01}^{+0.01}$	0.01	$0.9\pm 0.1$	0.2	-24.0	14.0	$(1.4\pm 1.2) \text{ e-6}$	4.3
	3-2	APEX	0.01	$0.00_{-0.00}^{+0.00}$	0.0	$0.2\pm 0.1$	0.1	-26.1	14.8	$(2.3\pm 2.6) \text{ e-7}$	4.1
18413+1354	1-0	IRAM	0.14	$0.40_{-0.04}^{+0.04}$	0.04	$11.1\pm 0.5$	1.1	-17.0	16.8	$(6.0\pm 5.7) \text{ e-6}$	10.0
	2-1	IRAM	0.23	$0.70_{-0.06}^{+0.07}$	0.0	$19.3\pm 0.7$	0.0	-15.9	17.0	$(3.0\pm 2.7) \text{ e-6}$	0.0
18449-0514	1-0	IRAM	0.17	$1.70_{-0.60}^{+0.62}$	0.01	$2.9\pm 0.2$	0.2	19.8	1.2	$(3.0\pm 2.6) \text{ e-6}$	14.2
	2-1	IRAM	0.14	$1.00_{-1.03}^{+0.16}$	0.0	$1.6\pm 0.2$	0.0	20.0	1.1	$(8.9\pm 19.3) \text{ e-7}$	0.0
18467-4802	2-1	JCMT	0.09	$0.40_{-0.00}^{+0.00}$	0.0	$7.4\pm 0.5$	-	0.0	13.8	$(3.9\pm 3.5) \text{ e-6}$	0.0
	3-2	APEX	0.02	$0.10_{-0.01}^{+0.01}$	0.03	$1.9\pm 0.1$	0.5	-47.4	13.3	$(1.4\pm 1.6) \text{ e-6}$	3.5
	3-2	JCMT	-	-	0.0	-	-	0.0	-	-	0.0
18520-1635	1-0	SEST	0.01	$0.00_{-0.01}^{+0.01}$	0.0	$0.2\pm 0.0$	0.0	2.3	4.5	$(2.0\pm 1.8) \text{ e-7}$	0.0
18595-3947	2-1	JCMT	0.06	$1.00_{-0.00}^{+0.00}$	0.0	$32.1\pm 0.4$	-	0.0	18.2	$(3.3\pm 3.0) \text{ e-6}$	0.0
	3-2	APEX	0.06	$0.20_{-0.01}^{+0.02}$	0.03	$6.3\pm 0.1$	1.0	13.7	19.7	$(9.1\pm 10.6) \text{ e-7}$	6.1
	3-2	JCMT	0.1	$1.90_{-0.00}^{+0.00}$	0.0	$59.6\pm 0.6$	-	0.0	19.0	$(4.4\pm 5.1) \text{ e-6}$	-0.1
19007-2247	1-0	SEST	0.01	$0.10_{-0.00}^{+0.01}$	0.0	$1.6\pm 0.1$	0.0	33.5	12.7	$(5.8\pm 5.3) \text{ e-7}$	0.0
19007-3826	2-1	JCMT	0.05	$0.40_{-0.00}^{+0.00}$	0.0	$12.3\pm 0.3$	-	0.0	21.1	$(4.2\pm 3.9) \text{ e-6}$	0.0
	3-2	JCMT	0.09	$1.10_{-0.00}^{+0.00}$	0.0	$33.2\pm 0.6$	0.0	0.0	19.3	$(7.5\pm 8.8) \text{ e-6}$	0.0
19017-0545	1-0	SEST	0.02	$0.20_{-0.19}^{+0.64}$	0.0	$2.6\pm 0.1$	0.0	57.9	10.0	$(5.0\pm 4.2) \text{ e-7}$	0.0
19047-1706	1-0	IRAM	0.05	$0.00_{-0.02}^{+0.02}$	0.0	$0.9\pm 0.2$	0.0	-4.5	12.5	$(9.9\pm 9.5) \text{ e-7}$	28.7
	2-1	IRAM	0.08	$0.30_{-0.03}^{+0.03}$	0.0	$4.7\pm 0.2$	0.0	4.8	10.0	$(7.7\pm 6.7) \text{ e-7}$	0.0
19093-3256	2-1	JCMT	0.04	$0.50_{-0.00}^{+0.00}$	0.0	$10.7\pm 0.2$	-	0.0	13.8	$(1.9\pm 1.7) \text{ e-6}$	0.0
	3-2	JCMT	-	-	0.0	-	-	0.0	-	-	0.0
19098+6601	1-0	OSO	0.01	$0.00_{-0.03}^{+0.66}$	0.0	$0.4\pm 0.1$	0.0	-41.8	10.7	$(1.5\pm 1.4) \text{ e-7}$	0.0
19143-5032	1-0	SEST	0.02	$0.10_{-0.01}^{+0.01}$	0.0	$0.8\pm 0.0$	0.0	-34.5	9.1	$(8.2\pm 7.4) \text{ e-7}$	0.0

	2-1	APEX	0.07	$0.40^{+0.04}_{-0.03}$	0.0	$4.6\pm 0.1$	0.1	-32.4	7.4	$(1.0\pm 0.9) e^{-6}$	70.2
	3-2	APEX	0.02	$0.10^{+0.01}_{-0.01}$	0.0	$1.1\pm 0.0$	0.1	-32.5	7.9	$(1.9\pm 2.1) e^{-7}$	13.4
19267+0345	1-0	IRAM	0.04	$0.10^{+0.02}_{-0.02}$	0.01	$0.8\pm 0.2$	0.0	-1.0	8.7	$(8.0\pm 7.3) e^{-7}$	19.6
	1-0	OSO	0.1	$0.30^{+0.91}_{-0.28}$	0.0	$0.8\pm 0.5$	0.0	-5.2	12.2	$(1.8\pm 1.7) e^{-6}$	0.0
	2-1	IRAM	0.06	$0.20^{+0.02}_{-0.02}$	0.0	$3.0\pm 0.2$	0.0	2.2	10.0	$(5.8\pm 5.1) e^{-7}$	0.0
19287+4602	1-0	OSO	0.01	$0.00^{+0.58}_{-0.04}$	0.0	$0.2\pm 0.0$	0.0	-15.1	4.6	$(5.7\pm 5.4) e^{-8}$	0.0
19309-6252	2-1	APEX	0.02	$0.10^{+0.02}_{-0.01}$	0.0	$0.3\pm 0.0$	0.0	-46.3	3.3	$(9.1\pm 7.6) e^{-8}$	-10.5
	3-2	APEX	0.01	$0.00^{+0.00}_{-0.00}$	0.0	$0.1\pm 0.1$	0.0	-46.7	13.4	$(3.1\pm 3.5) e^{-8}$	-2.3
19321+2757	1-0	IRAM	0.28	$0.80^{+0.06}_{-0.06}$	0.02	$31.8\pm 0.7$	1.0	-11.9	23.8	$(4.5\pm 4.0) e^{-6}$	32.7
	2-1	IRAM	0.3	$0.90^{+0.07}_{-0.07}$	0.0	$32.8\pm 0.7$	0.0	-11.7	23.7	$(2.3\pm 2.0) e^{-6}$	0.0
20038-2722	1-0	SEST	0.03	$0.10^{+0.01}_{-0.01}$	0.0	$0.9\pm 0.1$	0.0	-22.3	7.7	$(2.6\pm 2.4) e^{-7}$	0.0
20042-4241	2-1	APEX	0.07	$0.30^{+0.02}_{-0.02}$	0.03	$5.7\pm 0.1$	0.7	-34.3	12.6	$(4.2\pm 3.8) e^{-6}$	8.2
	2-1	JCMT	0.04	$0.50^{+0.00}_{-0.00}$	0.0	$8.2\pm 0.2$	-	0.0	11.6	$(3.3\pm 3.0) e^{-6}$	0.0
	3-2	APEX	0.03	$0.10^{+0.01}_{-0.01}$	0.01	$2.1\pm 0.0$	0.3	-34.3	12.3	$(1.2\pm 1.4) e^{-6}$	7.2
	3-2	JCMT	-	-	0.0	-	-	0.0	-	-	0.0
20075-6005	1-0	SEST	0.01	$0.00^{+0.00}_{-0.01}$	0.0	$0.1\pm 0.0$	0.0	-74.3	5.9	$(7.8\pm 7.8) e^{-8}$	0.0
20120-4433	2-1	JCMT	0.06	$1.00^{+0.00}_{-0.00}$	0.0	$10.3\pm 0.2$	-	0.0	7.8	$(1.6\pm 1.3) e^{-6}$	0.0
	3-2	JCMT	-	-	0.0	-	-	0.0	-	-	0.0
20135-7152	2-1	APEX	0.06	$0.20^{+0.01}_{-0.02}$	0.01	$4.8\pm 0.2$	0.6	-2.3	16.1	$(5.6\pm 5.1) e^{-6}$	8.1
	3-2	APEX	0.02	$0.10^{+0.01}_{-0.00}$	0.01	$1.1\pm 0.1$	0.2	-1.2	15.6	$(1.1\pm 1.2) e^{-6}$	5.4
20141-2128	1-0	SEST	0.02	$0.00^{+0.01}_{-0.01}$	0.0	$0.6\pm 0.1$	0.0	-38.0	8.8	$(3.7\pm 3.3) e^{-7}$	0.0
20165-5051	1-0	SEST	0.01	$0.00^{+0.00}_{-0.00}$	0.0	$0.2\pm 0.0$	0.0	-0.6	6.6	$(3.5\pm 3.1) e^{-7}$	0.0
	2-1	APEX	0.03	$0.10^{+0.02}_{-0.01}$	0.01	$1.1\pm 0.1$	0.2	-45.5	5.4	$(3.4\pm 2.9) e^{-7}$	6.1
	3-2	APEX	0.02	$0.00^{+0.01}_{-0.01}$	0.0	$0.3\pm 0.1$	0.1	-43.1	10.3	$(8.9\pm 10.1) e^{-8}$	6.0

20248-2825	1-0	SEST	0.01	$0.10_{-0.00}^{+0.01}$	0.0	$0.9\pm 0.1$	0.0	18.5	7.7	$(2.9\pm 2.6) e^{-7}$	0.0
20359-3806	2-1	APEX	0.05	$0.20_{-0.02}^{+0.02}$	0.01	$2.8\pm 0.1$	0.1	-4.7	8.2	$(9.8\pm 8.5) e^{-7}$	48.3
	2-1	JCMT	-	-	0.0	-	-	0.0	-	-	0.0
	3-2	APEX	0.01	$0.10_{-0.01}^{+0.01}$	0.0	$0.7\pm 0.0$	0.1	-4.7	8.7	$(1.9\pm 2.1) e^{-7}$	6.8
	3-2	JCMT	0.11	$0.30_{-0.00}^{+0.00}$	0.0	$3.6\pm 0.4$	-	0.0	7.3	$(4.9\pm 5.6) e^{-7}$	0.0
	1-0	OSO	0.06	$0.10_{-0.03}^{+0.03}$	0.0	$1.2\pm 0.2$	0.0	-22.8	9.2	$(5.5\pm 5.0) e^{-7}$	0.0
20466+2248	1-0	OSO	0.03	$0.60_{-0.61}^{+1.26}$	0.0	$0.3\pm 0.2$	0.0	-46.3	11.3	$(4.2\pm 3.6) e^{-8}$	0.0
20479+0554	1-0	IRAM	0.05	$0.10_{-0.02}^{+0.02}$	0.01	$2.0\pm 0.2$	0.4	17.3	10.5	$(1.4\pm 1.3) e^{-6}$	5.6
	2-1	IRAM	0.07	$0.20_{-0.02}^{+0.03}$	0.0	$3.5\pm 0.2$	0.0	16.3	10.1	$(5.6\pm 4.9) e^{-7}$	0.0
20484-7202	2-1	APEX	0.04	$0.10_{-0.01}^{+0.01}$	0.01	$3.0\pm 0.1$	0.3	-32.3	13.6	$(2.9\pm 2.6) e^{-6}$	8.8
	3-2	APEX	0.01	$0.00_{-0.00}^{+0.00}$	0.01	$0.6\pm 0.1$	0.1	-33.1	12.9	$(4.5\pm 5.1) e^{-7}$	8.9
20541-6549	3-2	APEX	0.02	$0.10_{-0.00}^{+0.01}$	0.01	$1.5\pm 0.1$	0.2	-5.6	17.5	$(9.6\pm 11.2) e^{-7}$	8.8
21069-3843	2-1	APEX	0.07	$0.40_{-0.03}^{+0.03}$	0.05	$5.1\pm 0.1$	0.8	-22.4	9.8	$(4.2\pm 3.8) e^{-6}$	6.0
	2-1	JCMT	0.04	$0.30_{-0.00}^{+0.00}$	0.0	$4.1\pm 0.2$	-	0.0	9.2	$(2.1\pm 1.9) e^{-6}$	0.0
	3-2	APEX	0.02	$0.10_{-0.01}^{+0.01}$	0.02	$1.0\pm 0.1$	0.3	-21.6	9.5	$(6.8\pm 7.8) e^{-7}$	2.9
	3-2	JCMT	0.07	$0.70_{-0.00}^{+0.00}$	0.0	$9.0\pm 0.3$	-	0.0	9.4	$(3.3\pm 4.3) e^{-6}$	0.0
21206-4054	2-1	APEX	0.03	$0.10_{-0.01}^{+0.01}$	0.03	$1.5\pm 0.1$	0.5	2.4	8.2	$(1.9\pm 1.6) e^{-6}$	3.3
	3-2	APEX	0.02	$0.00_{-0.01}^{+0.01}$	0.0	$0.4\pm 0.1$	0.1	1.2	6.8	$(3.8\pm 4.2) e^{-7}$	4.0
21243-6943	3-2	APEX	0.01	$0.00_{-0.00}^{+0.00}$	0.0	$0.0\pm 0.1$	0.1	6.3	15.4	$(5.1\pm 6.1) e^{-10}$	0.5
21270+7135	1-0	IRAM	0.07	$0.10_{-0.02}^{+0.02}$	0.01	$2.9\pm 0.3$	0.2	-32.2	14.8	$(2.5\pm 2.4) e^{-6}$	12.8
	2-1	IRAM	0.07	$0.20_{-0.02}^{+0.02}$	0.0	$4.8\pm 0.3$	0.0	-33.8	15.6	$(1.1\pm 1.0) e^{-6}$	0.0
21368-3812	2-1	APEX	0.04	$0.20_{-0.02}^{+0.02}$	0.01	$2.3\pm 0.1$	0.3	-26.5	8.5	$(9.2\pm 8.1) e^{-7}$	6.8
	2-1	JCMT	-	-	0.0	-	-	0.0	-	-	0.0
	3-2	APEX	0.01	$0.00_{-0.00}^{+0.01}$	0.0	$0.6\pm 0.0$	0.1	-26.6	9.2	$(1.7\pm 1.9) e^{-7}$	8.6

	3-2	JCMT	0.0	$0.00_{-0.00}^{+0.00}$	0.0	$0.2\pm 0.0$	0.0	0.0	10.0	$(4.9\pm 0.0) e-8$	0.0
21389+5405	1-0	OSO	0.06	$0.00_{-0.02}^{+0.04}$	0.0	$0.9\pm 0.9$	0.0	-40.6	15.0	$(6.5\pm 6.1) e-7$	0.0
21414+7609	1-0	IRAM	0.07	$0.00_{-0.01}^{+0.01}$	0.54	$-0.3\pm 0.4$	-0.1	-24.8	19.2	-	2.3
	2-1	IRAM	0.07	$0.10_{-0.03}^{+0.03}$	0.0	$1.8\pm 0.3$	0.0	-50.9	9.0	$(3.2\pm 2.8) e-7$	0.0
21439-0226	1-0	SEST	0.09	$0.20_{-0.03}^{+0.03}$	0.0	$3.8\pm 0.1$	0.0	-33.0	10.7	$(4.2\pm 3.8) e-7$	0.0
21563+5630	1-0	IRAM	0.15	$1.40_{-0.13}^{+0.18}$	0.73	$4.0\pm 0.1$	0.9	-0.6	2.0	$(8.7\pm 7.6) e-7$	4.4
	2-1	IRAM	0.14	$1.10_{-0.12}^{+0.17}$	0.0	$3.4\pm 0.2$	0.0	-0.5	2.2	$(2.9\pm 2.4) e-7$	0.0
22017+2806	1-0	SEST	0.03	$0.10_{-0.01}^{+0.01}$	0.0	$1.2\pm 0.1$	0.0	-23.4	12.2	$(6.8\pm 6.2) e-7$	0.0
22035+3506	1-0	OSO	0.02	$0.10_{-0.01}^{+0.01}$	0.0	$1.8\pm 0.1$	0.0	-7.0	10.6	$(6.9\pm 6.3) e-7$	0.0
22145-8041	3-2	APEX	0.01	$0.00_{-0.00}^{+0.00}$	0.0	$-0.1\pm 0.1$	0.0	-10.2	16.1	-	30.8
22196-4612	2-1	JCMT	0.1	$1.60_{-0.00}^{+0.00}$	0.0	$32.2\pm 0.5$	-	0.0	15.1	$(4.3\pm 3.7) e-7$	0.0
	3-2	JCMT	-	-	0.0	-	-	0.0	-	-	0.0
22230-4841	2-1	APEX	0.05	$0.30_{-0.02}^{+0.02}$	0.0	$2.6\pm 0.1$	0.1	-25.4	6.9	$(7.0\pm 6.0) e-7$	17.8
	3-2	APEX	0.02	$0.10_{-0.01}^{+0.01}$	0.0	$1.0\pm 0.0$	0.0	-24.9	6.5	$(1.8\pm 2.0) e-7$	-23.8
22231-4529	2-1	APEX	0.03	$0.10_{-0.01}^{+0.01}$	0.01	$1.9\pm 0.1$	0.3	-2.2	18.1	$(3.2\pm 2.9) e-6$	6.0
	3-2	APEX	0.01	$0.00_{-0.00}^{+0.00}$	0.0	$0.4\pm 0.1$	0.2	0.7	16.9	$(4.5\pm 5.2) e-7$	2.3
22396-4708	2-1	APEX	0.02	$0.00_{-0.00}^{+0.00}$	0.0	$-0.2\pm 0.1$	-0.1	-10.2	16.3	-	1.6
	3-2	APEX	0.01	$0.00_{-0.00}^{+0.00}$	0.0	$0.2\pm 0.1$	-0.1	-39.1	16.7	$(6.5\pm 7.8) e-10$	-2.7
22476+4047	1-0	OSO	0.03	$0.10_{-0.05}^{+0.04}$	0.0	$0.7\pm 0.1$	0.0	-26.2	5.0	$(1.3\pm 1.1) e-7$	0.0
22540-5740	2-1	APEX	0.04	$0.30_{-0.02}^{+0.02}$	0.0	$2.0\pm 0.1$	0.1	-39.1	5.3	$(1.4\pm 1.2) e-7$	22.3
	3-2	APEX	0.02	$0.10_{-0.01}^{+0.01}$	0.01	$0.6\pm 0.0$	0.2	-39.3	4.7	$(2.7\pm 2.9) e-8$	3.8
23013+3735	1-0	OSO	0.01	$1.10_{-1.14}^{+1.23}$	0.0	$0.1\pm 0.1$	0.0	21.1	10.9	$(2.8\pm 2.6) e-7$	0.0
23063-3024	1-0	SEST	0.01	$0.00_{-0.01}^{+0.01}$	0.0	$0.2\pm 0.0$	0.0	30.6	6.3	$(7.9\pm 7.0) e-8$	0.0
	2-1	APEX	0.03	$0.20_{-0.02}^{+0.02}$	0.01	$1.4\pm 0.1$	0.3	28.8	5.7	$(6.5\pm 5.5) e-8$	5.1

	2-1	JCMT	-	-	0.0	-	-	0.0	-	-	0.0
	3-2	APEX	0.01	$0.10^{+0.01}_{-0.01}$	0.0	$0.4 \pm 0.0$	0.1	28.7	6.0	$(1.1 \pm 1.2) \text{ e-8}$	6.3
	3-2	JCMT	0.07	$0.00^{+0.00}_{-0.00}$	0.0	$0.4 \pm 0.3$	0.0	0.0	10.0	$(9.1 \pm 0.0) \text{ e-9}$	0.0
23134-7031	3-2	APEX	0.01	$0.00^{+0.00}_{-0.00}$	0.0	$0.1 \pm 0.1$	0.1	-14.0	14.6	$(3.1 \pm 3.6) \text{ e-8}$	1.5
23213-4521	2-1	APEX	0.1	$0.40^{+0.03}_{-0.03}$	0.05	$9.6 \pm 0.1$	1.4	0.9	15.2	$(7.3 \pm 6.7) \text{ e-6}$	7.0
	2-1	JCMT	0.04	$0.30^{+0.00}_{-0.00}$	0.0	$7.5 \pm 0.2$	1.0	0.0	14.9	$(3.6 \pm 3.2) \text{ e-6}$	7.3
	3-2	APEX	0.02	$0.10^{+0.01}_{-0.01}$	0.01	$1.8 \pm 0.1$	0.0	1.0	14.4	$(1.2 \pm 1.4) \text{ e-6}$	43.1
	3-2	JCMT	0.09	$0.90^{+0.00}_{-0.00}$	0.0	$20.4 \pm 0.5$	0.0	0.0	14.4	$(6.8 \pm 7.9) \text{ e-6}$	0.0
23425+4338	1-0	IRAM	0.04	$0.10^{+0.01}_{-0.01}$	0.0	$2.1 \pm 0.2$	0.1	-41.3	13.8	$(1.9 \pm 1.8) \text{ e-6}$	32.0
	2-1	IRAM	0.11	$0.40^{+0.04}_{-0.03}$	0.0	$8.3 \pm 0.3$	0.0	-41.3	14.6	$(1.6 \pm 1.4) \text{ e-6}$	0.0
23438+0312	1-0	SEST	0.04	$0.20^{+0.02}_{-0.02}$	0.0	$3.1 \pm 0.2$	0.0	15.2	9.4	$(4.6 \pm 3.9) \text{ e-7}$	0.0
23564-5651	3-2	APEX	0.01	$0.10^{+0.01}_{-0.01}$	0.0	$0.3 \pm 0.0$	0.1	-2.3	5.0	$(1.3 \pm 1.5) \text{ e-7}$	7.0



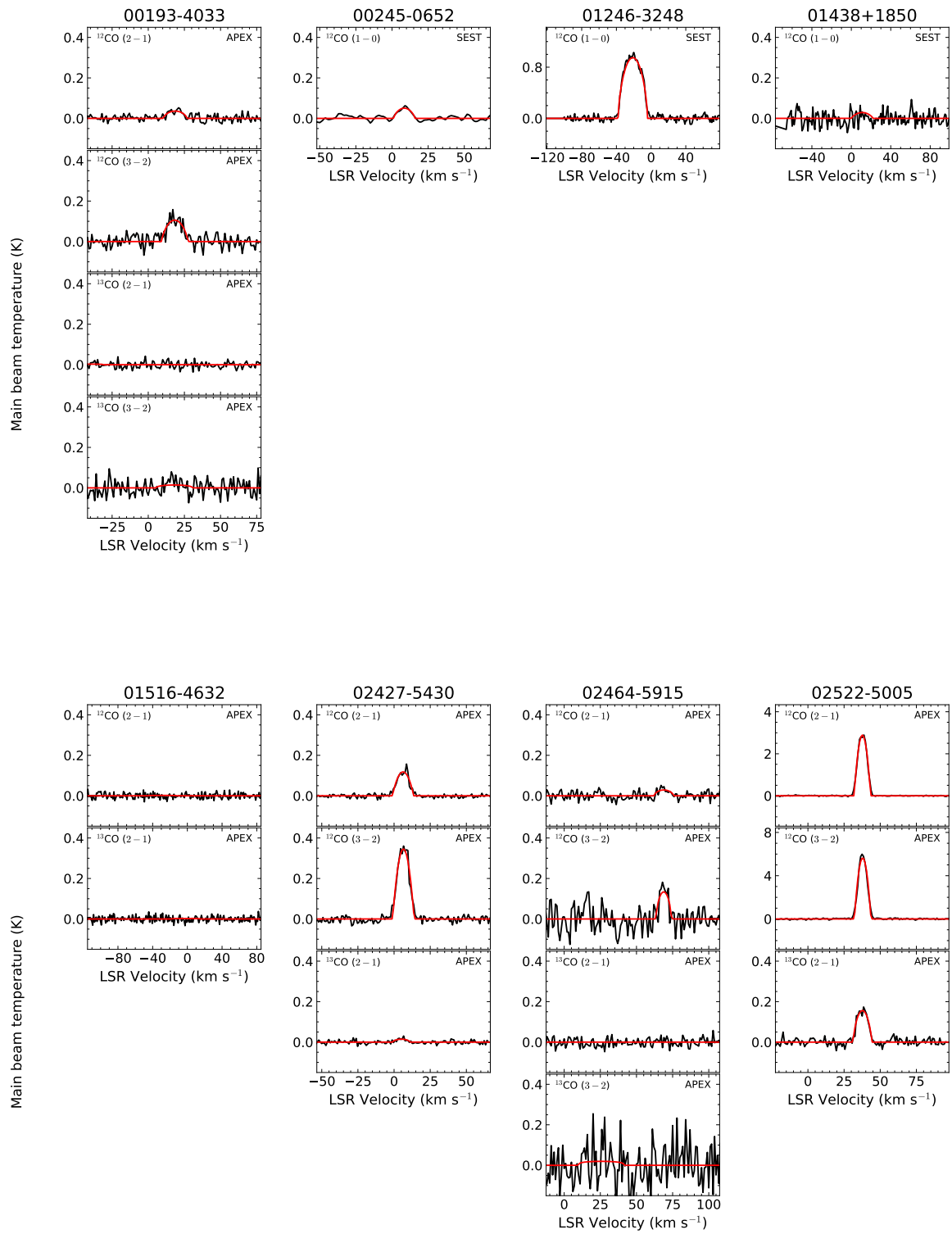
---

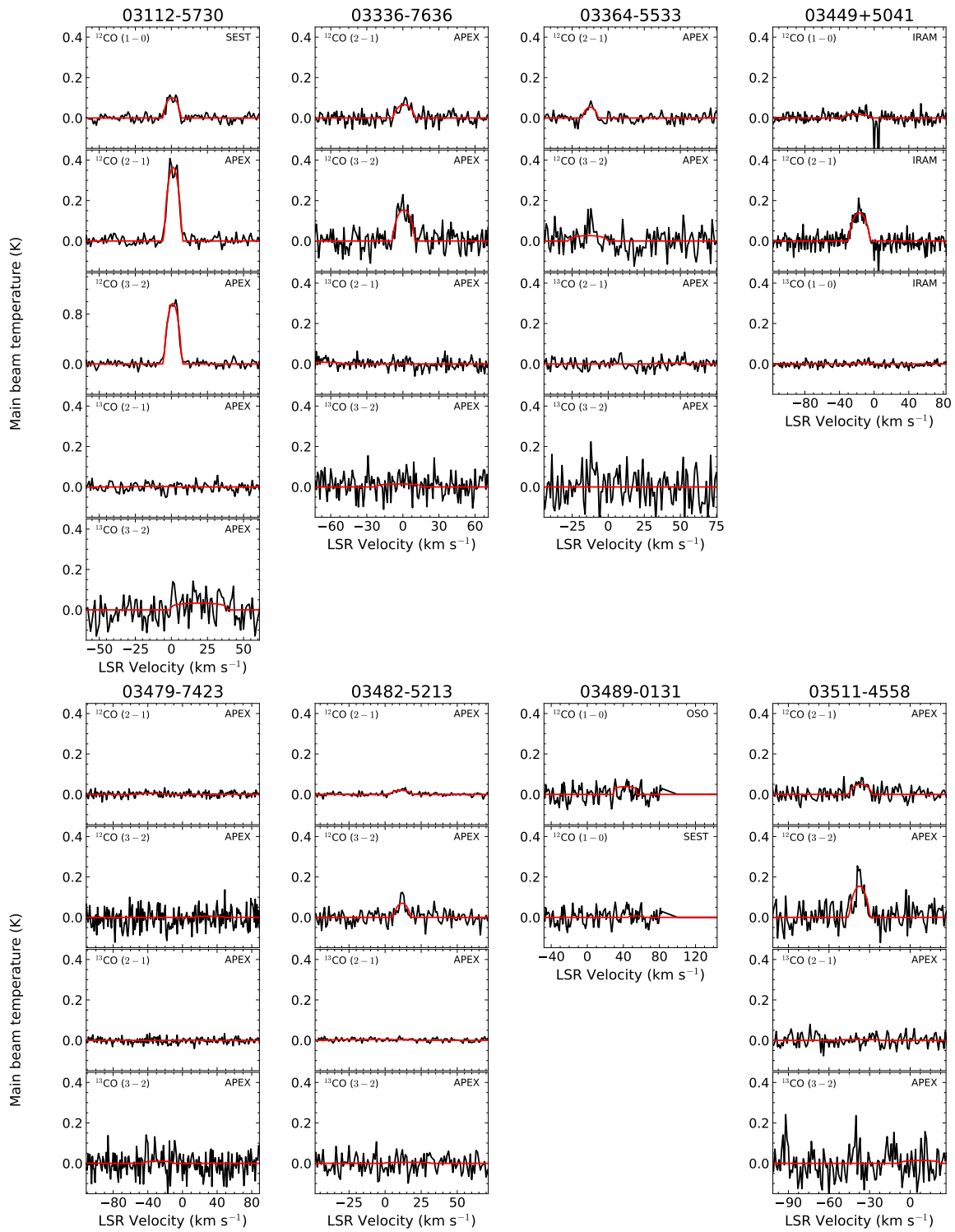
## **NESS: Figures presenting soft-parabola line fitting of the spectra**

---

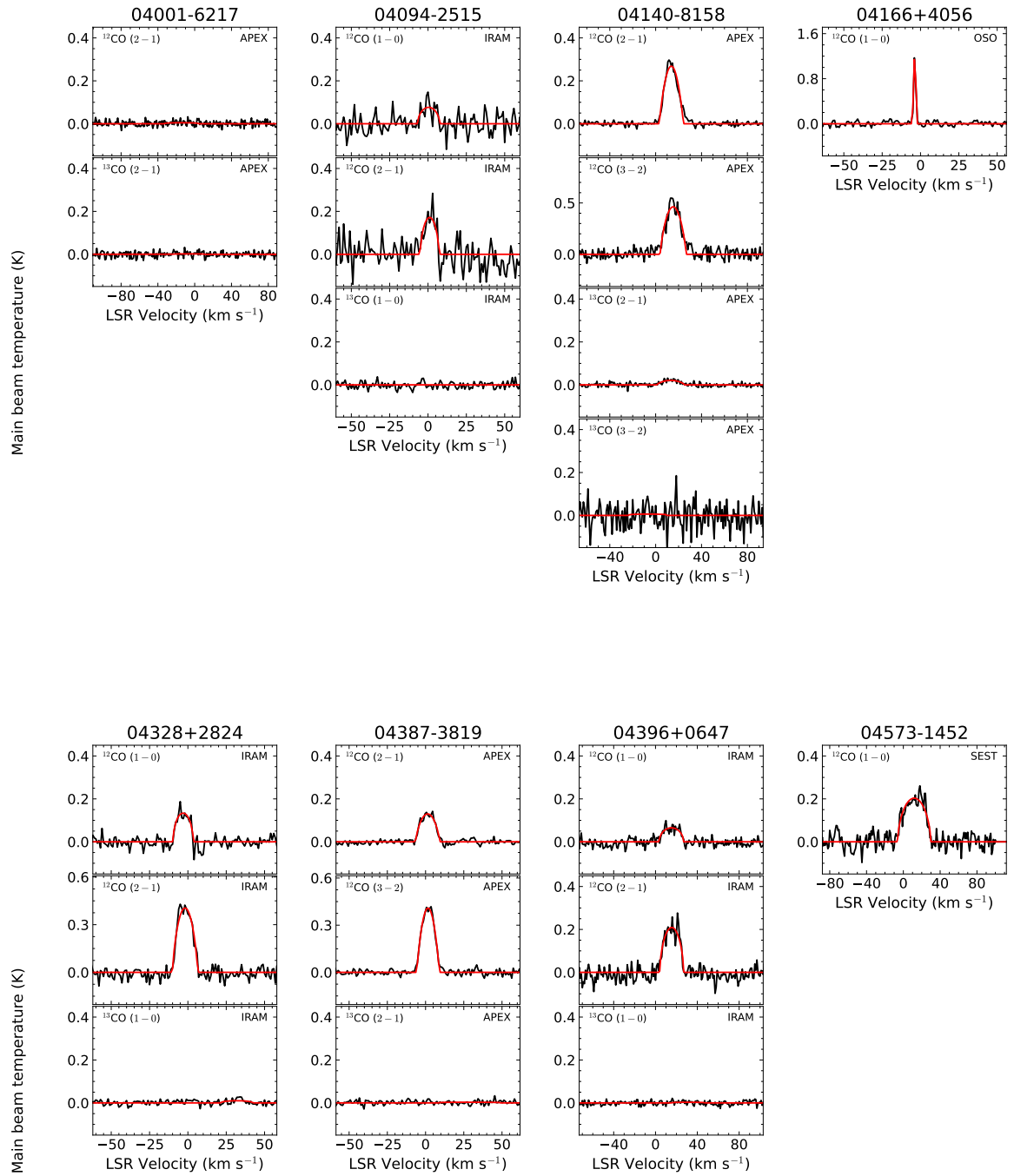
Below are the figures presenting the observed spectra (in black) with a soft-parabola line fitting procedure (in red) used to determine the physical parameters for the NESS sample. The CO transitions are marked on the top left corner of the plot and the telescope used is shown on the top right corner. The star's name is shown at the top of the plot.

Appendix B NESS: Figures presenting soft-parabola line fitting of the spectra

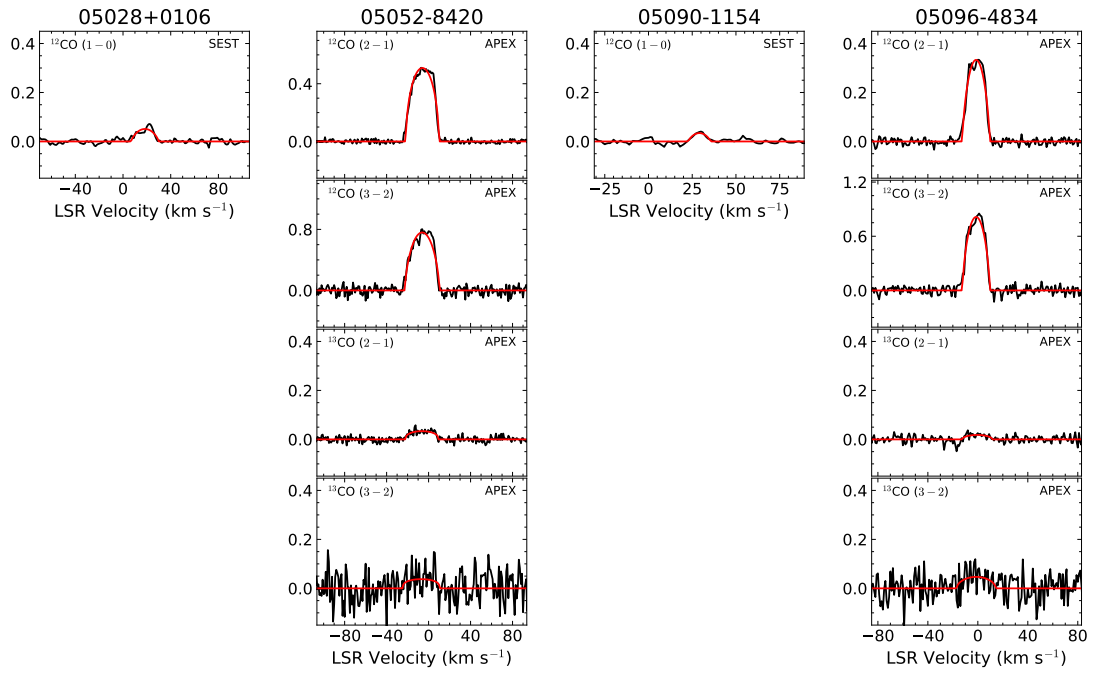




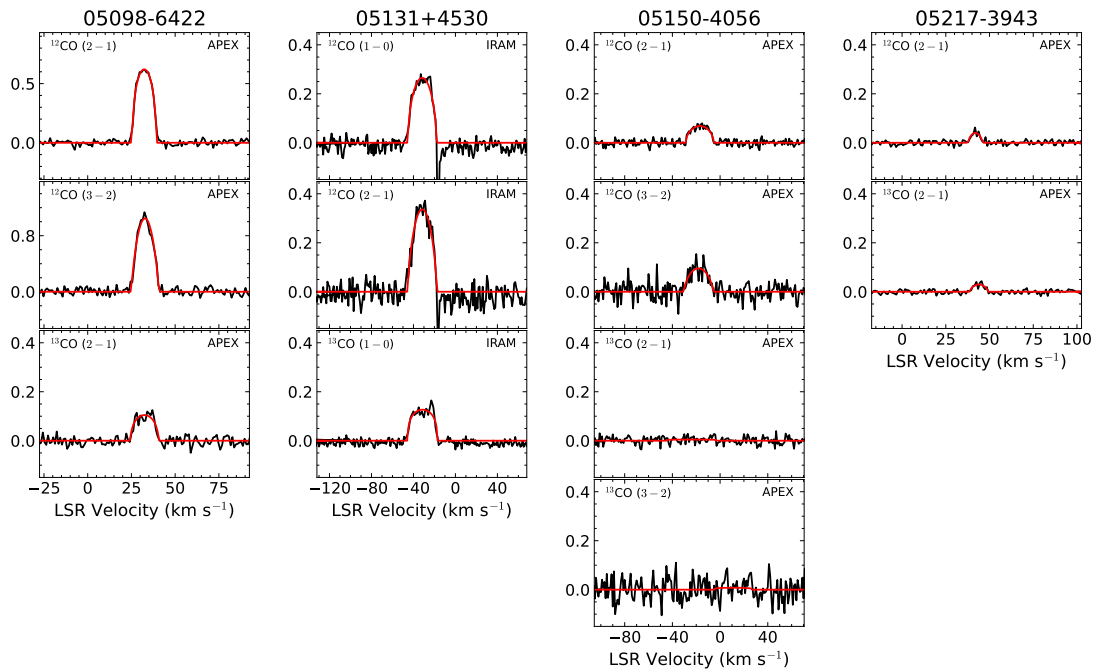
Appendix B NESS: Figures presenting soft-parabola line fitting of the spectra



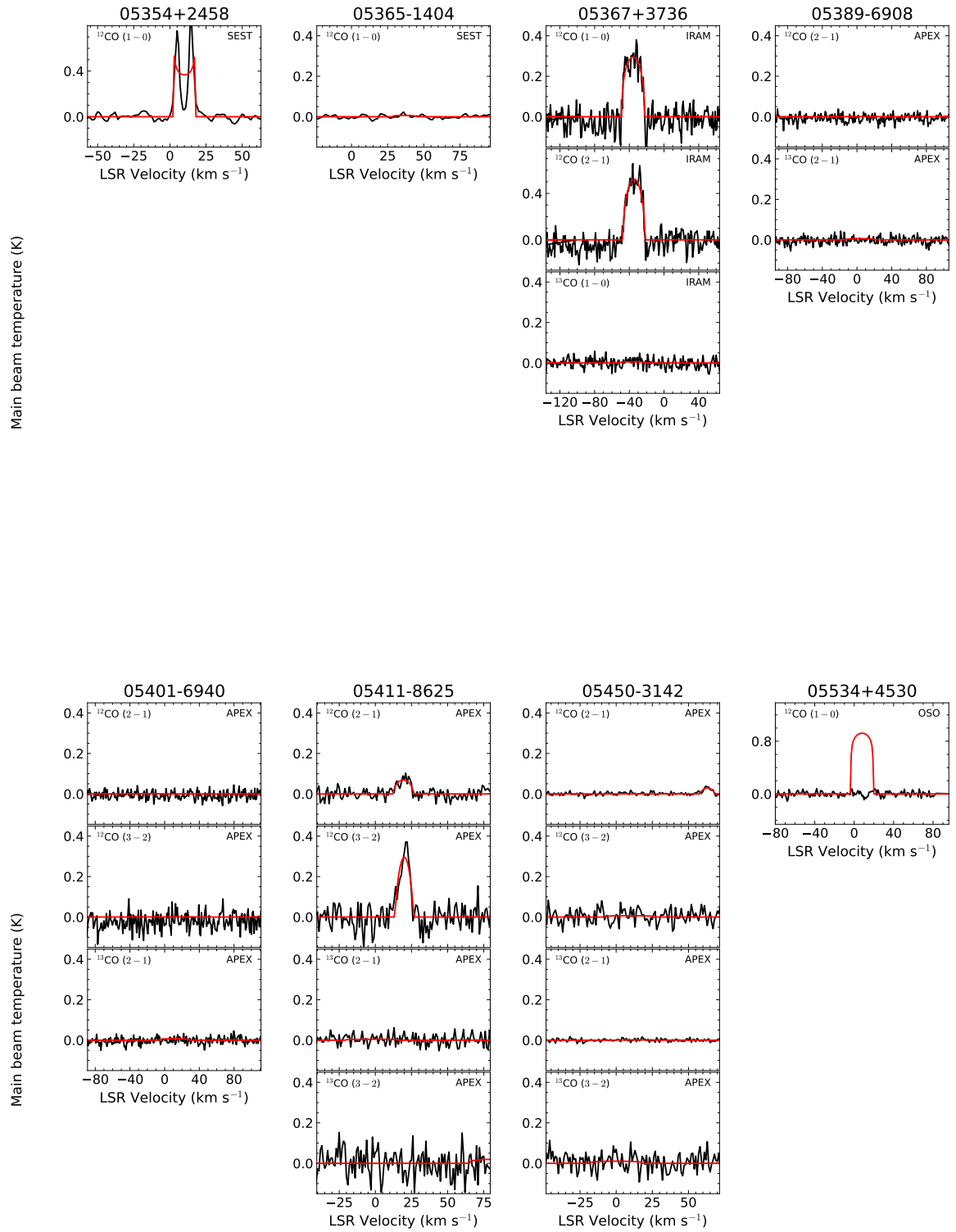
Main beam temperature (K)

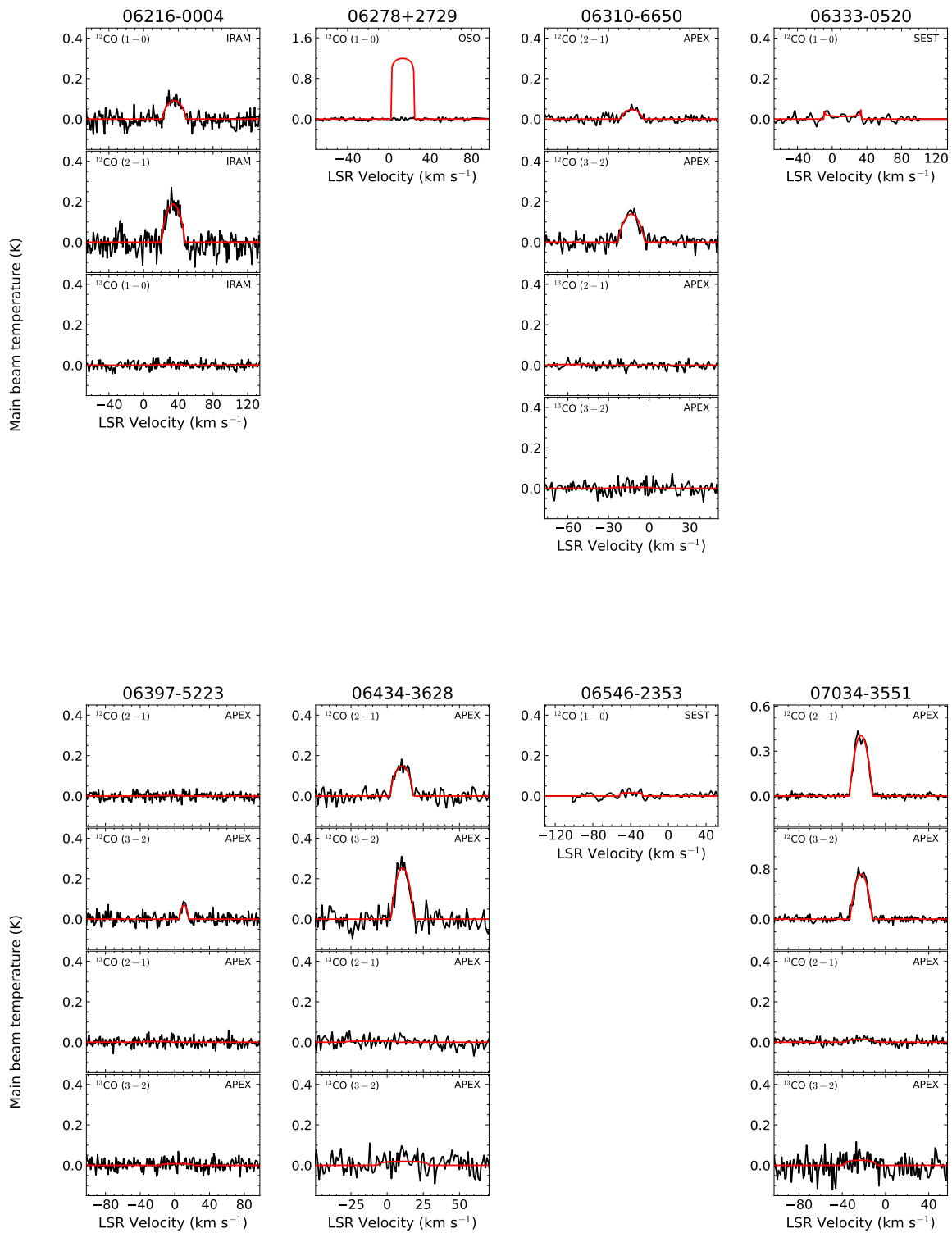


Main beam temperature (K)

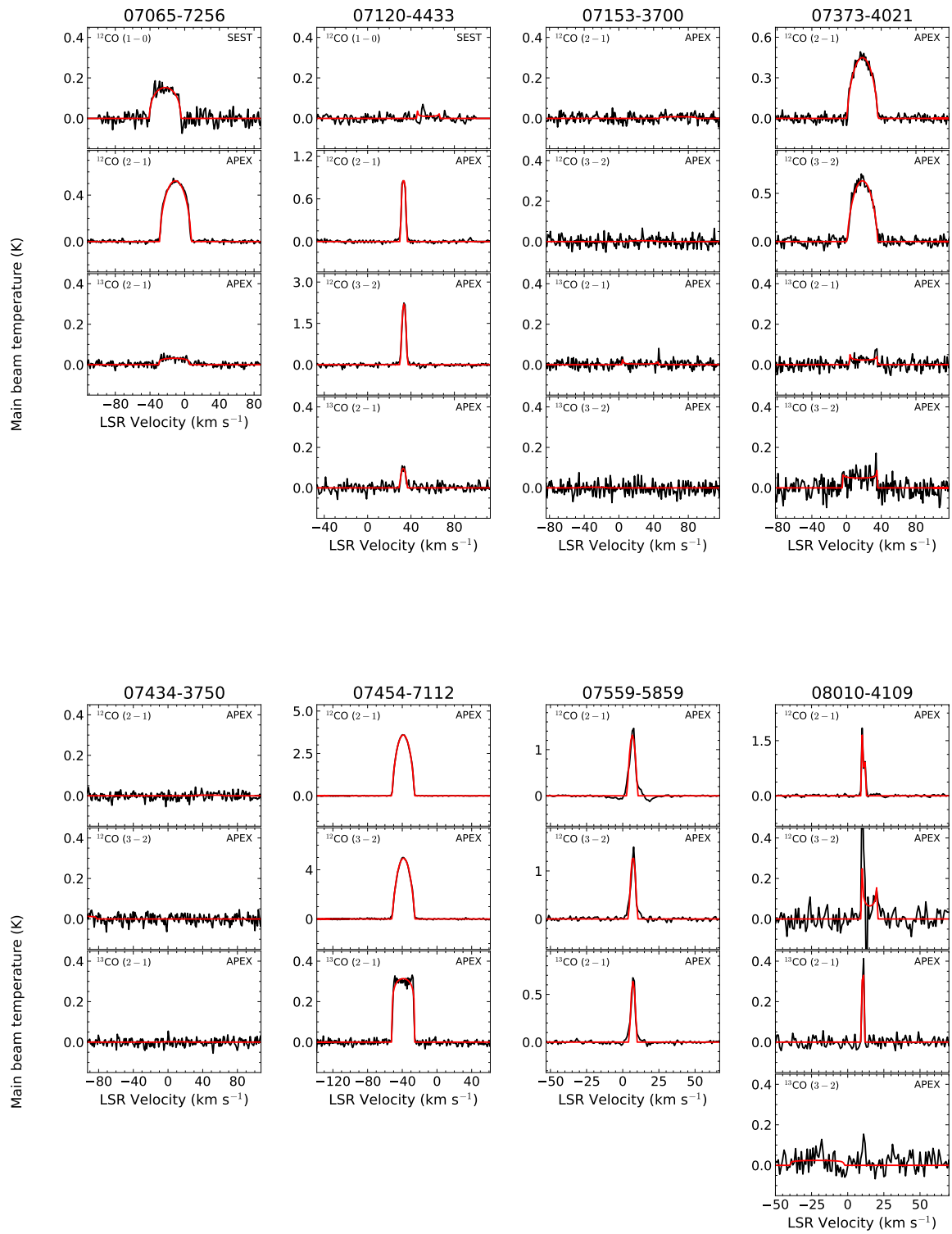


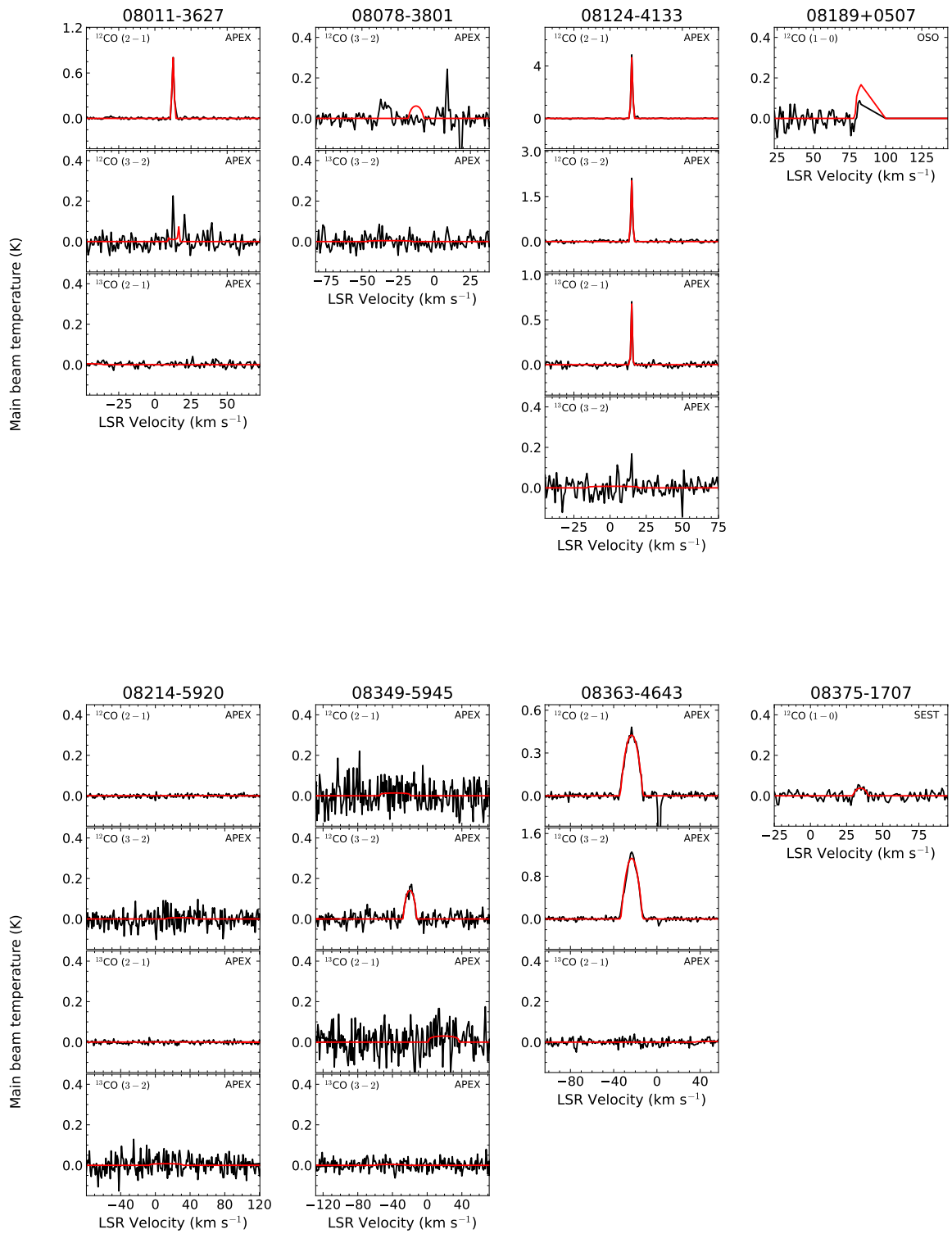
Appendix B NESS: Figures presenting soft-parabola line fitting of the spectra



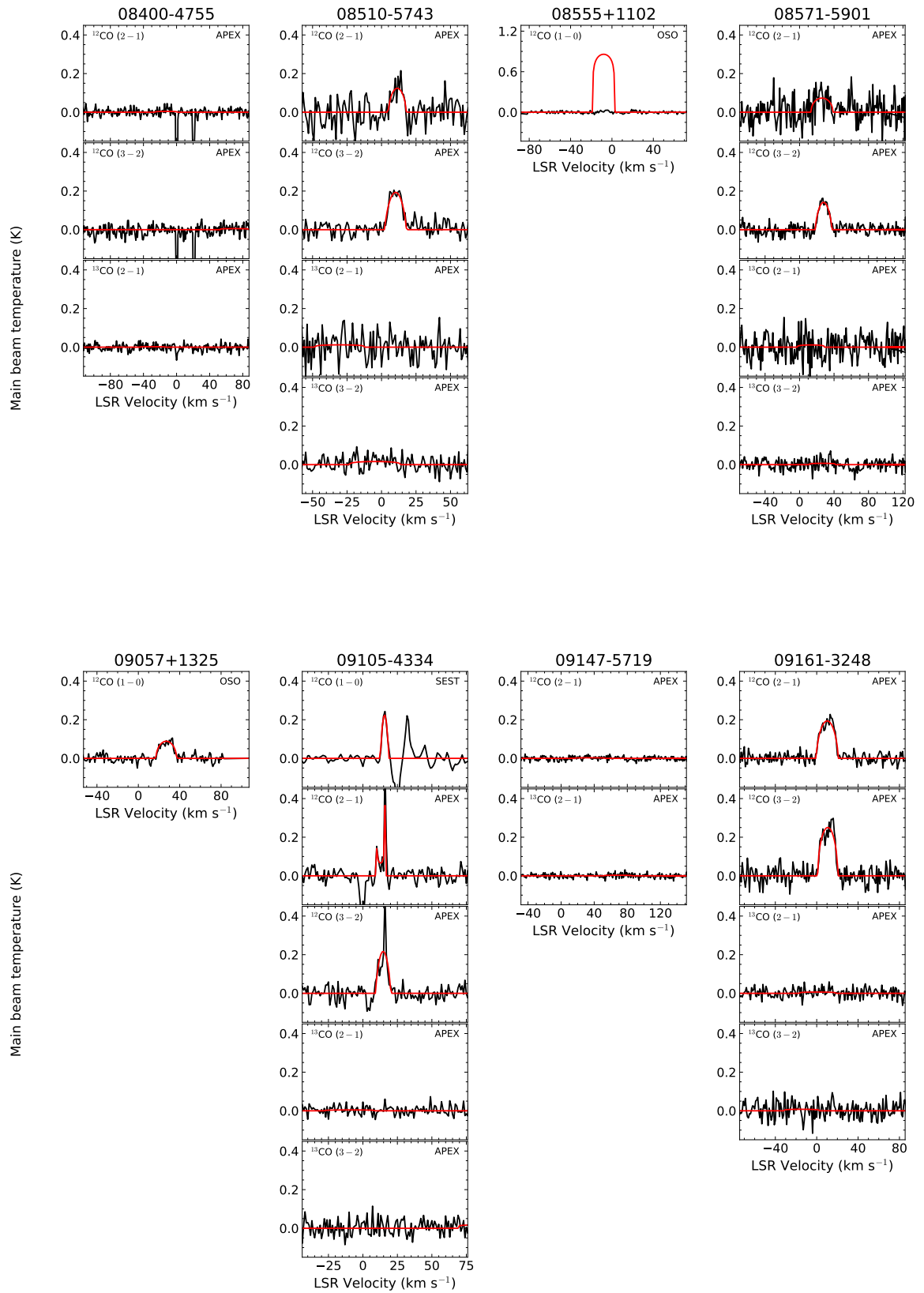


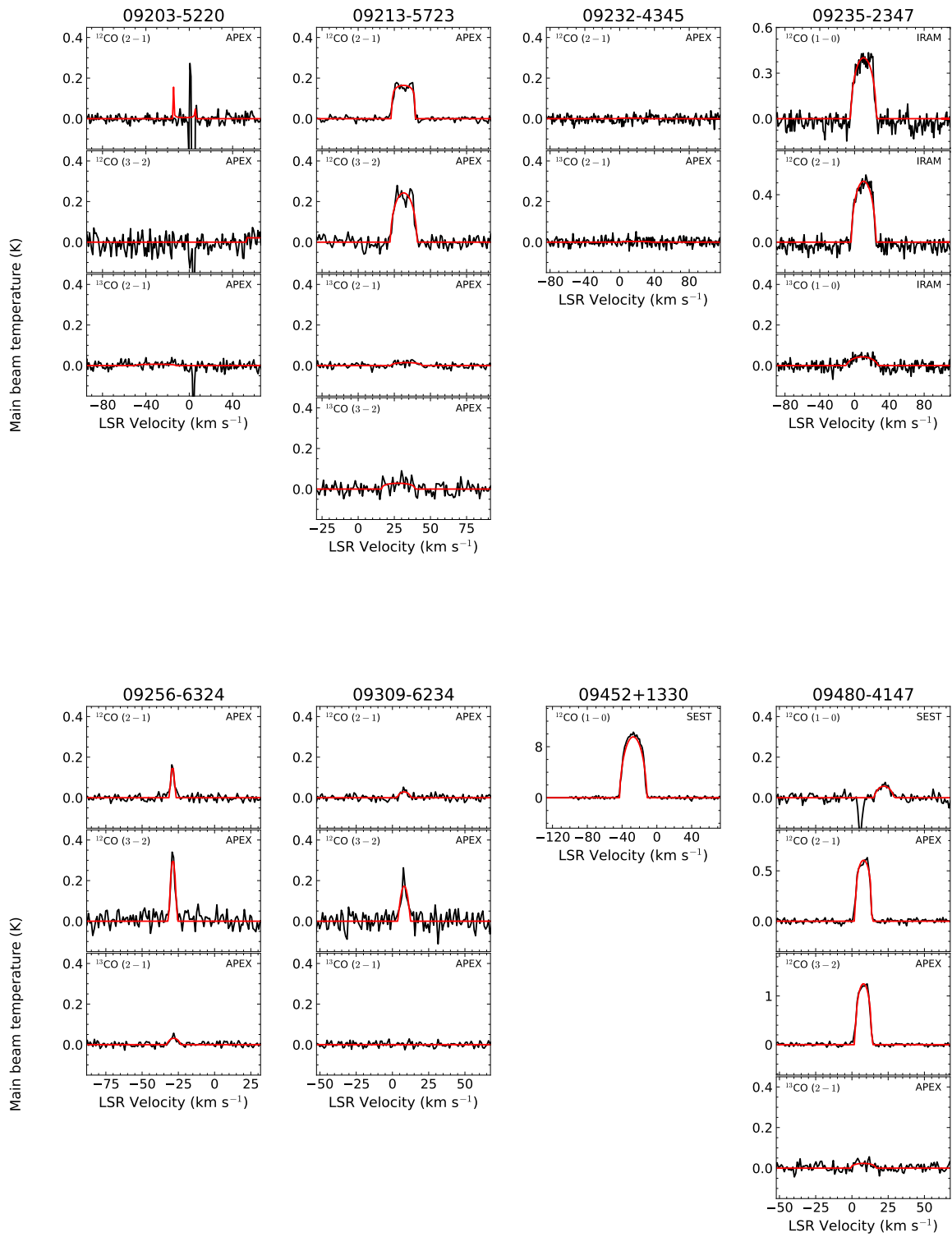
Appendix B NESS: Figures presenting soft-parabola line fitting of the spectra



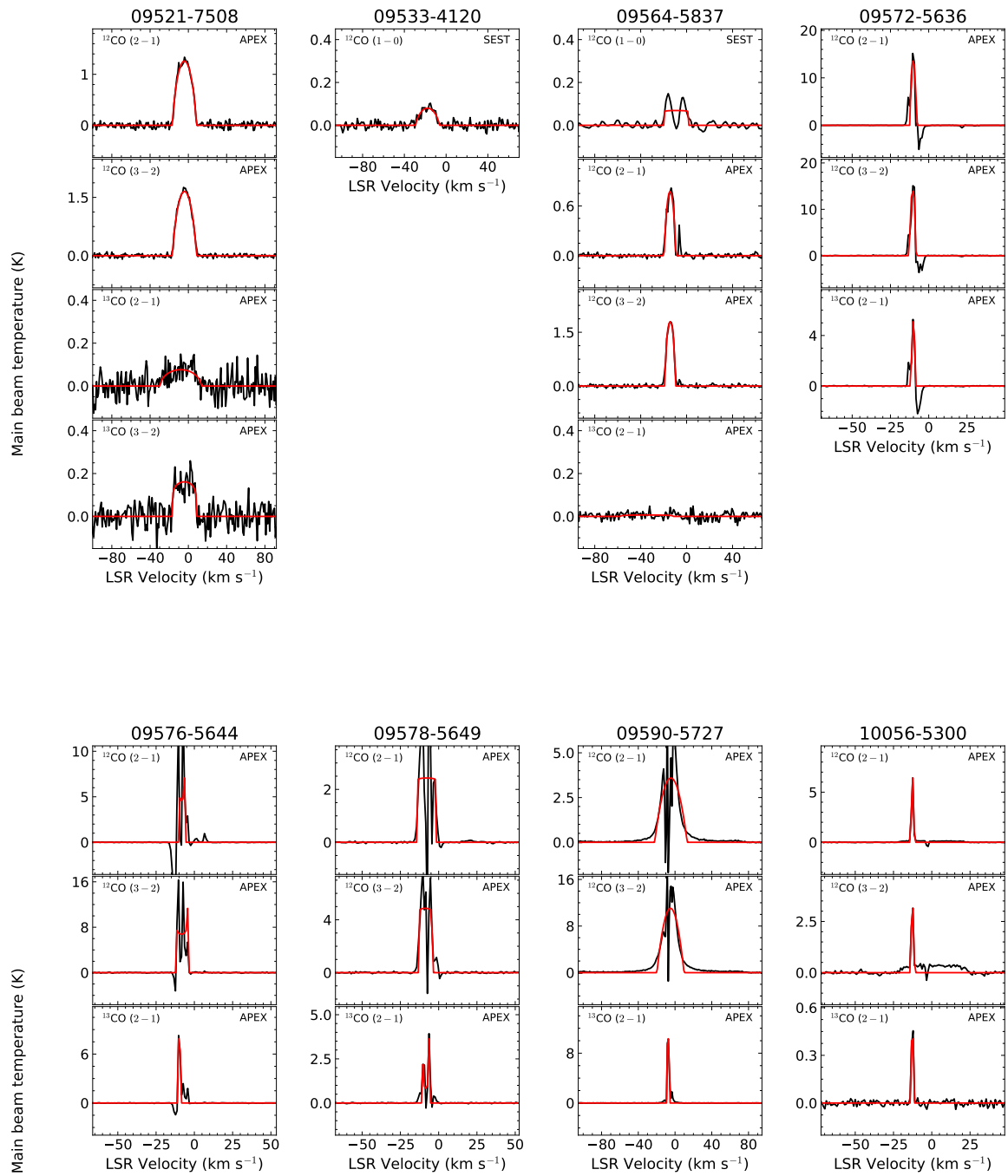


Appendix B NESS: Figures presenting soft-parabola line fitting of the spectra

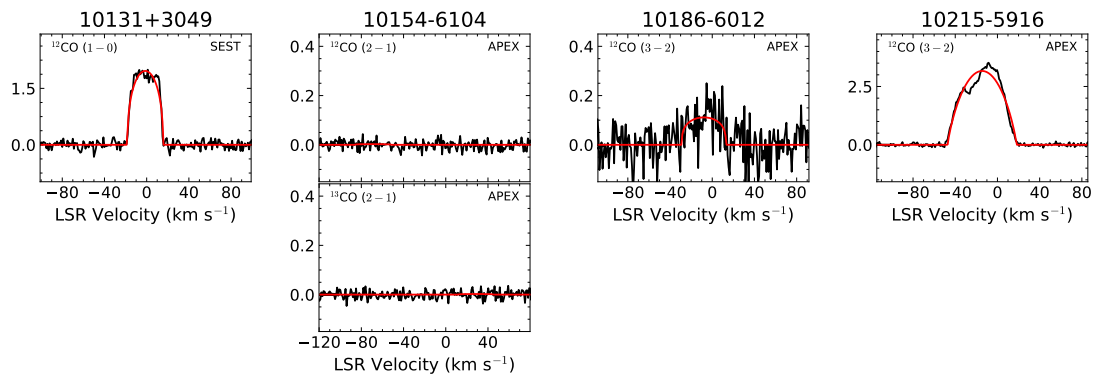




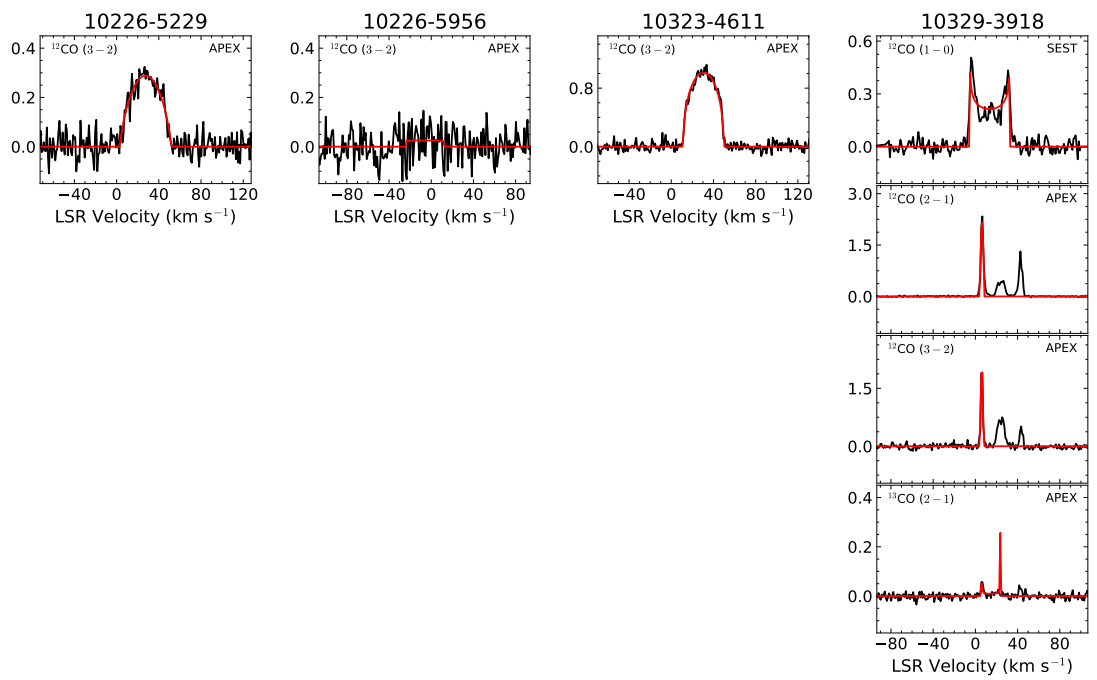
Appendix B NESS: Figures presenting soft-parabola line fitting of the spectra



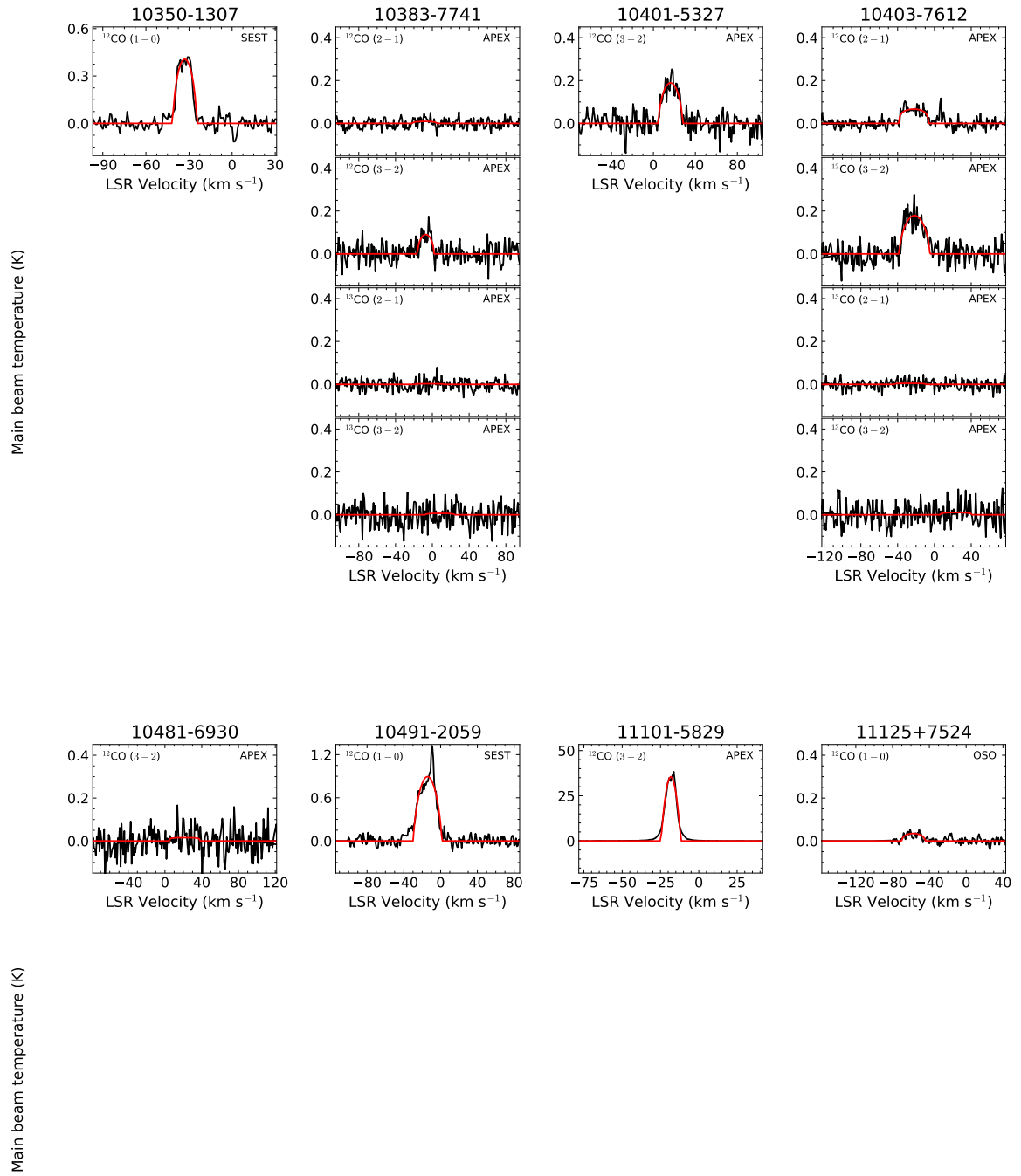
Main beam temperature (K)



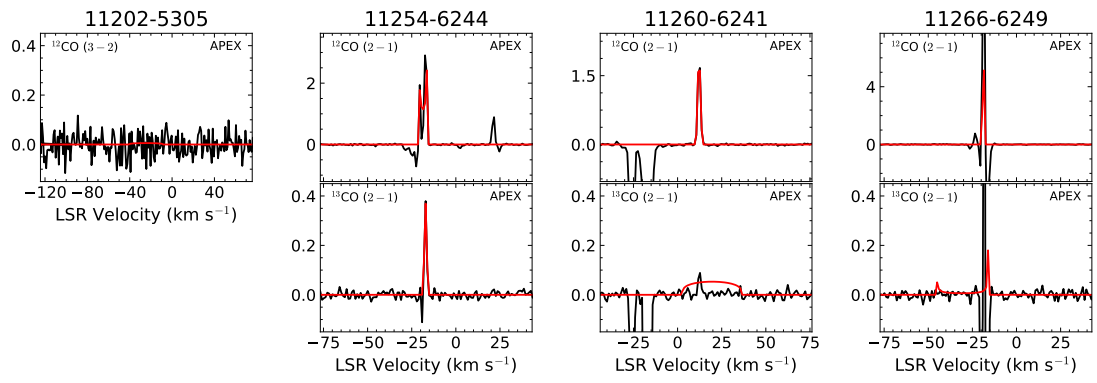
Main beam temperature (K)



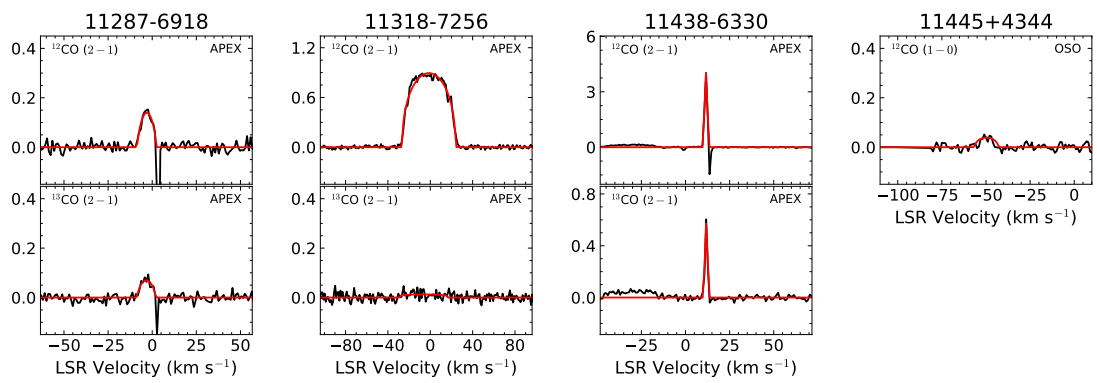
Appendix B NESS: Figures presenting soft-parabola line fitting of the spectra



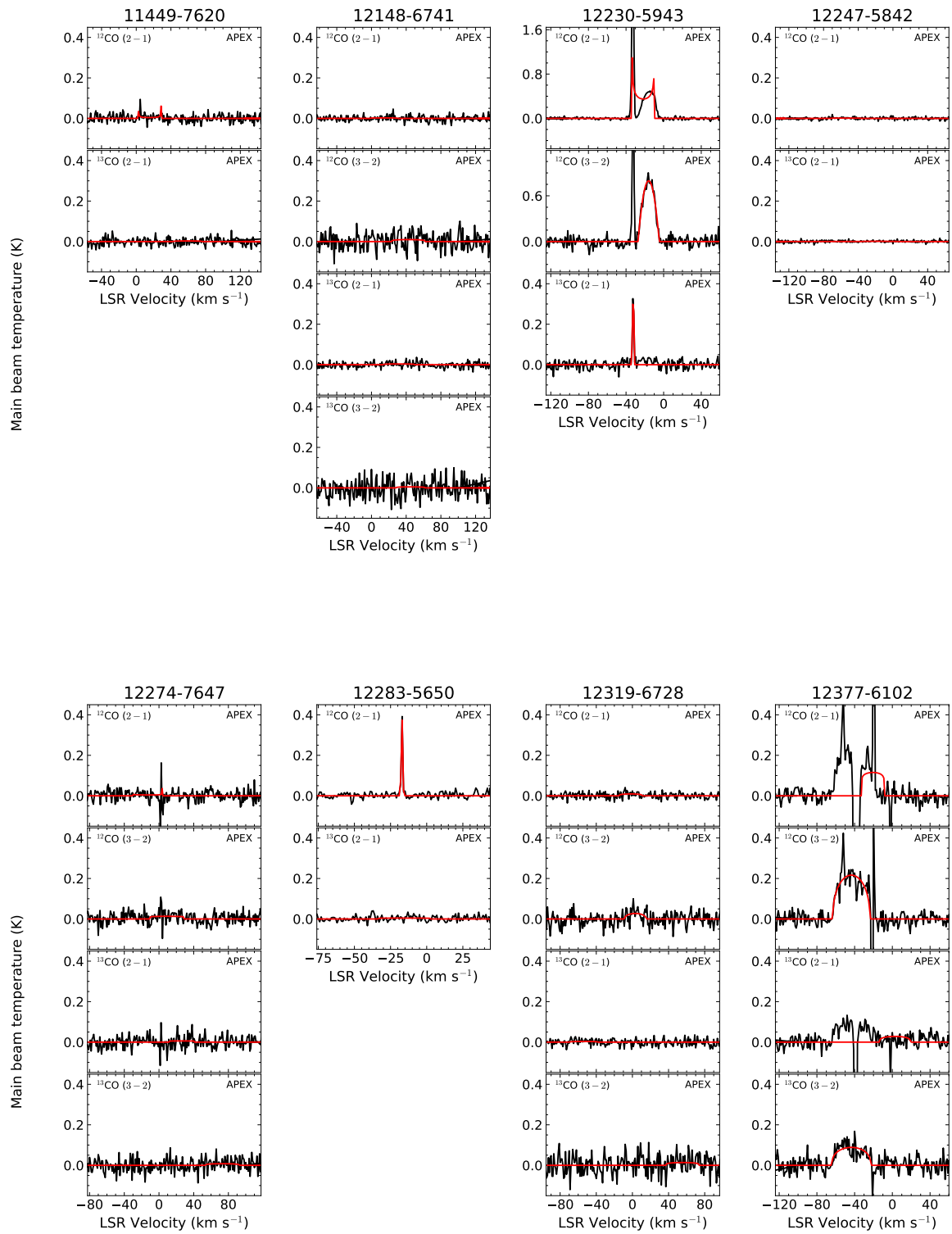
Main beam temperature (K)

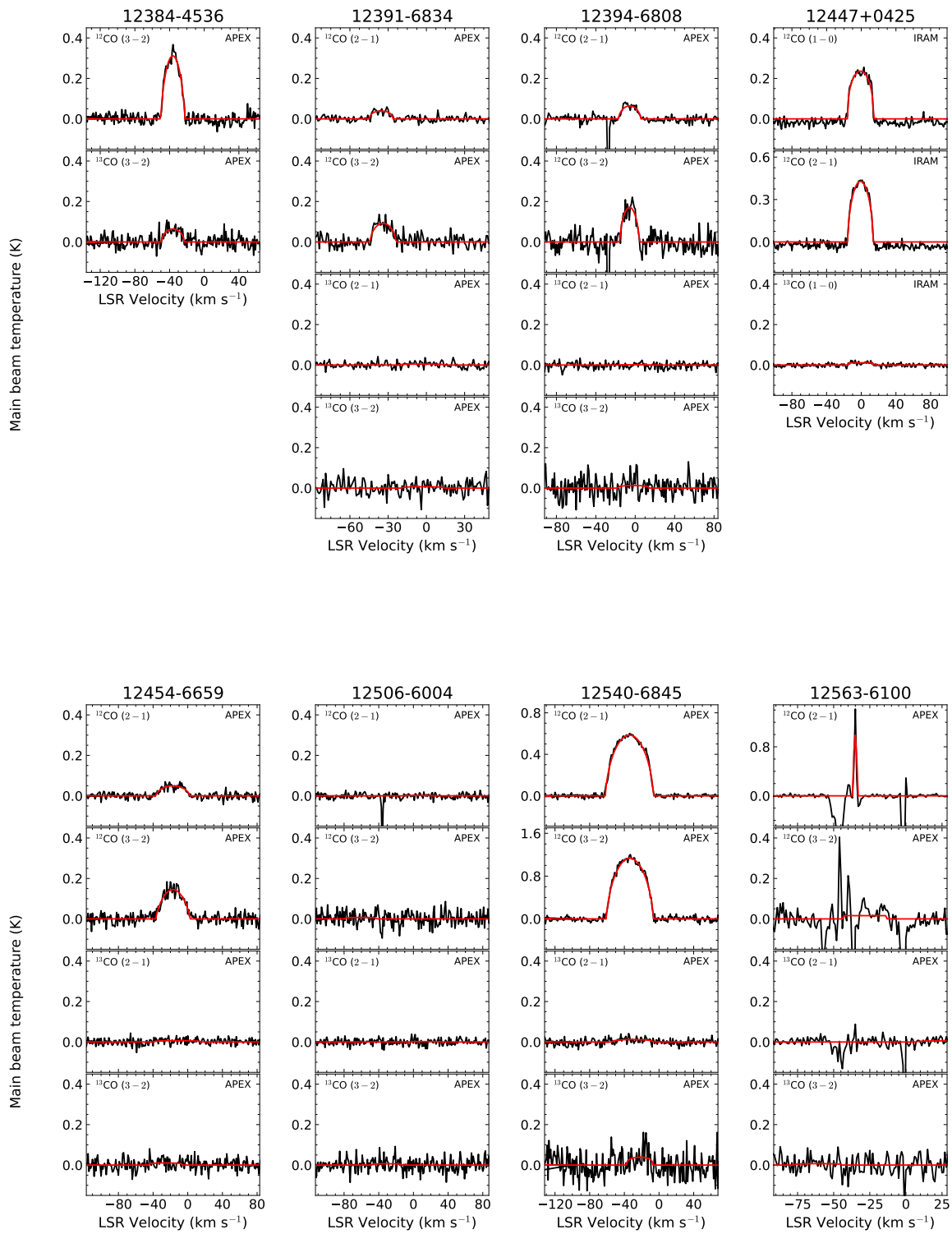


Main beam temperature (K)

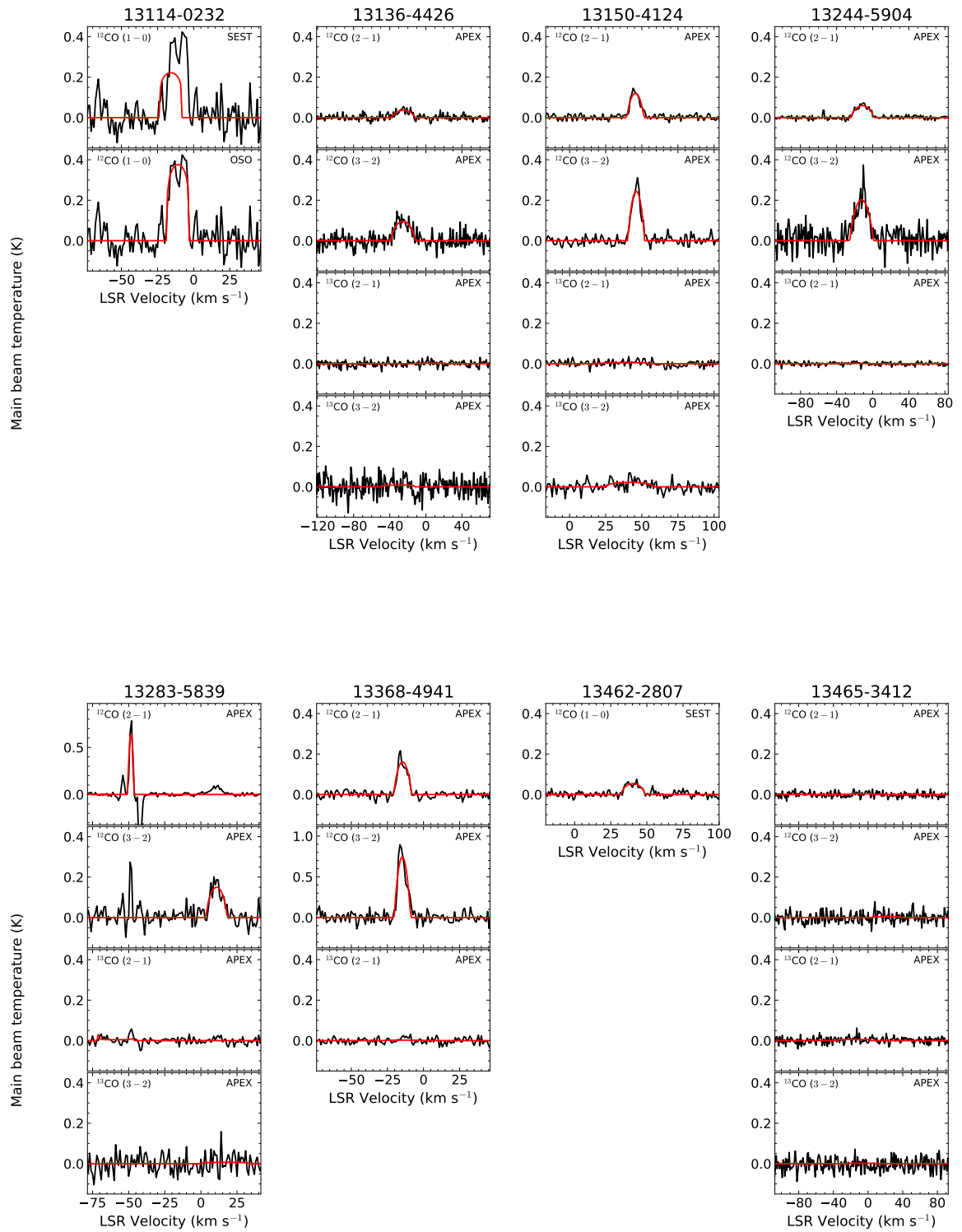


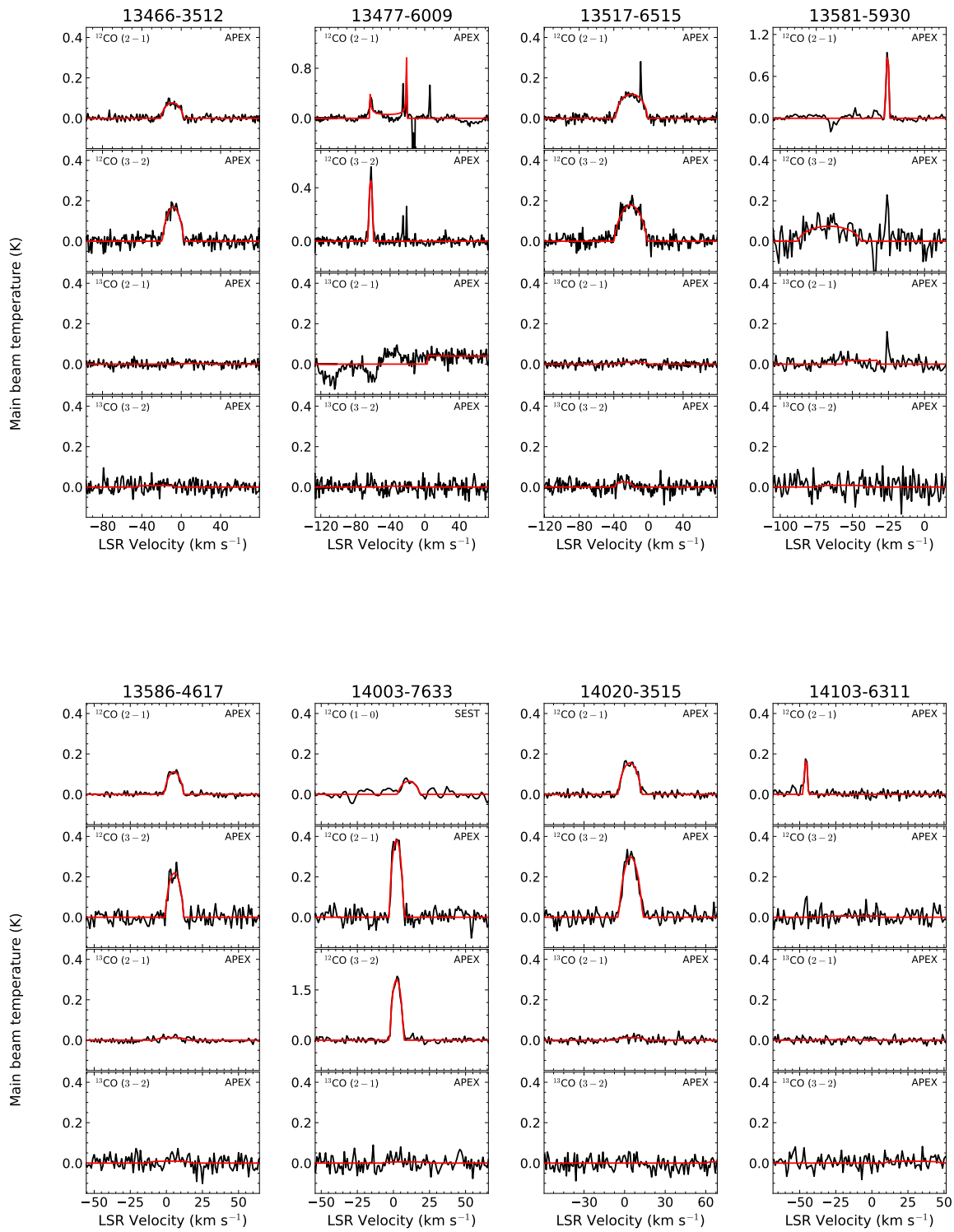
Appendix B NESS: Figures presenting soft-parabola line fitting of the spectra



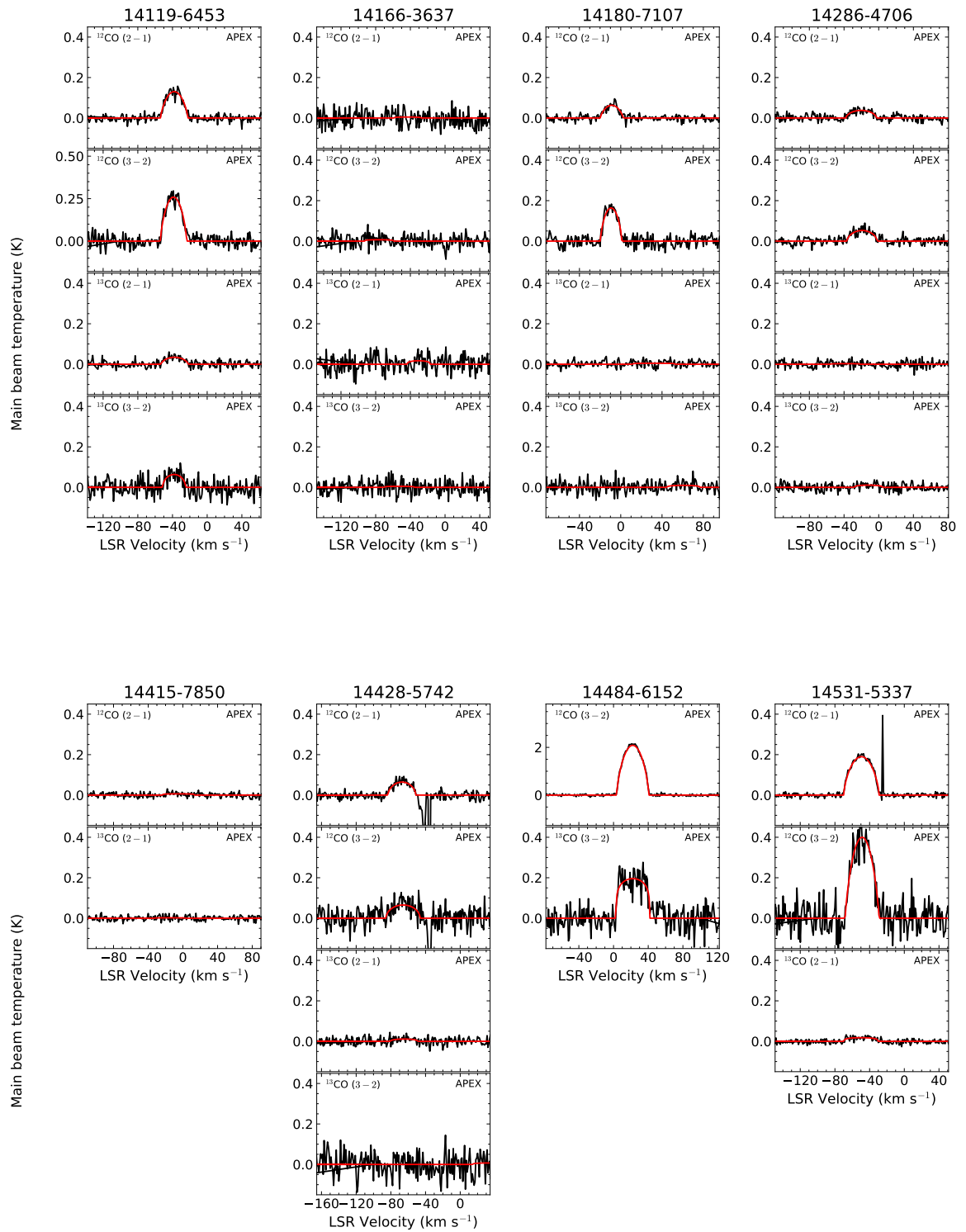


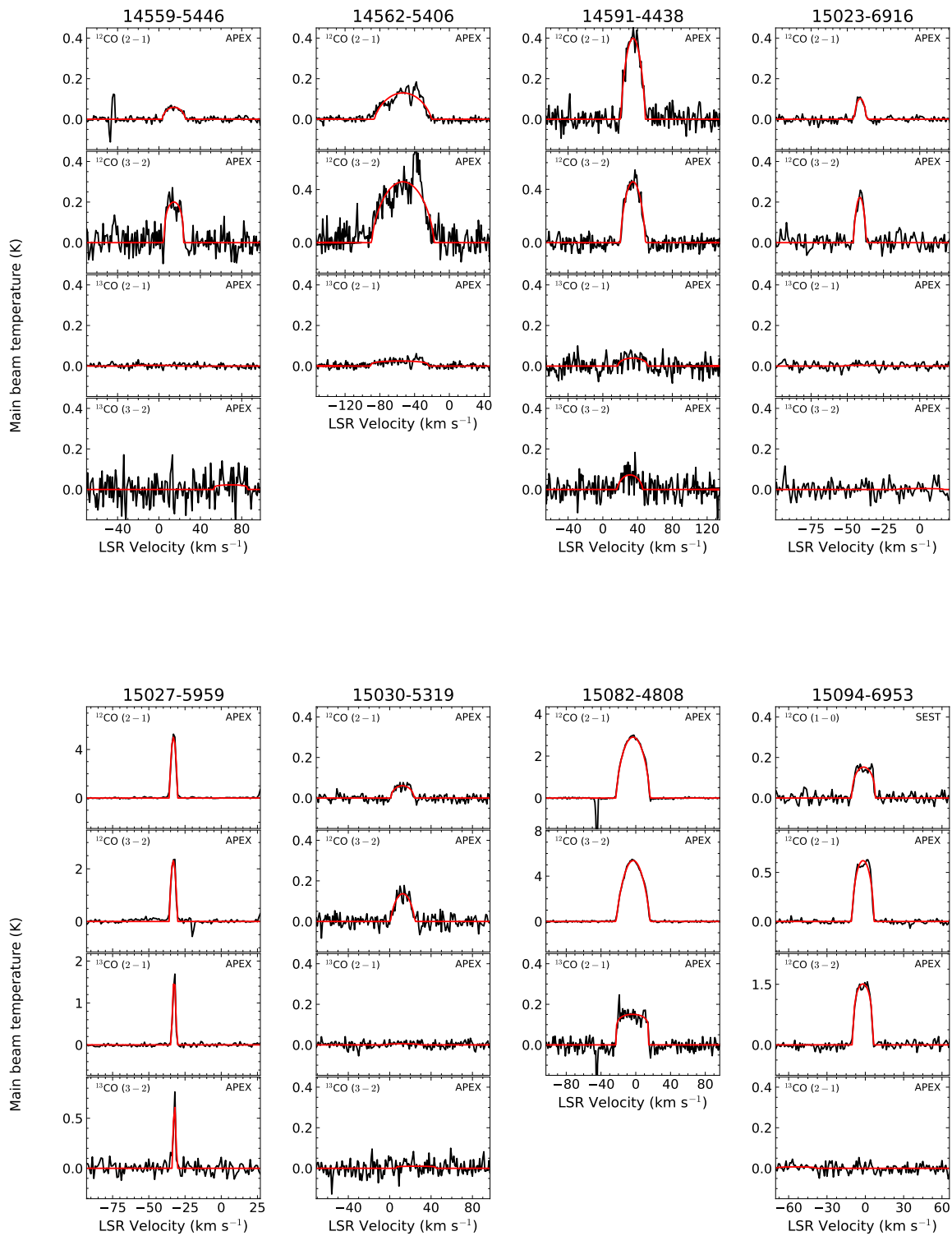
Appendix B NESS: Figures presenting soft-parabola line fitting of the spectra



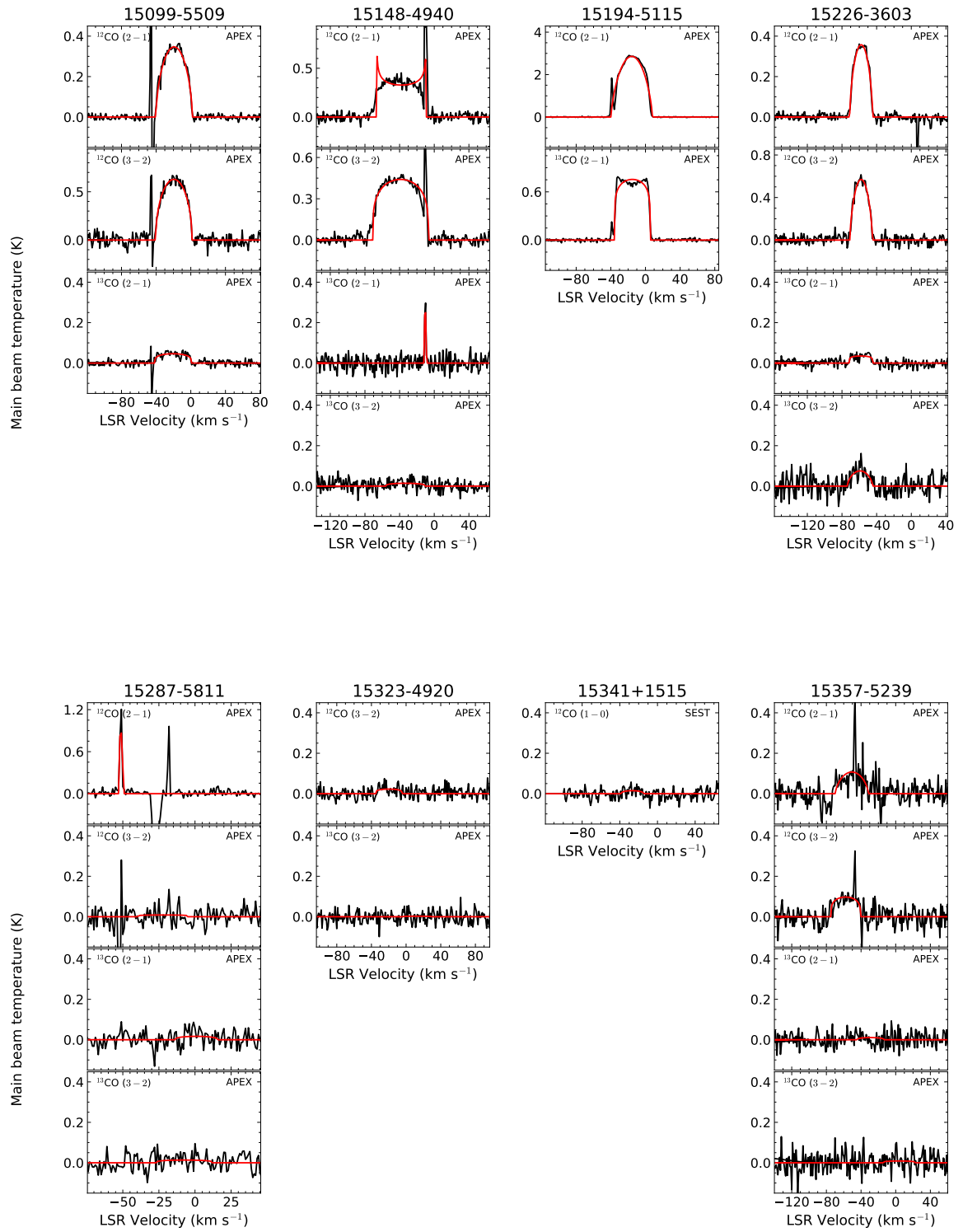


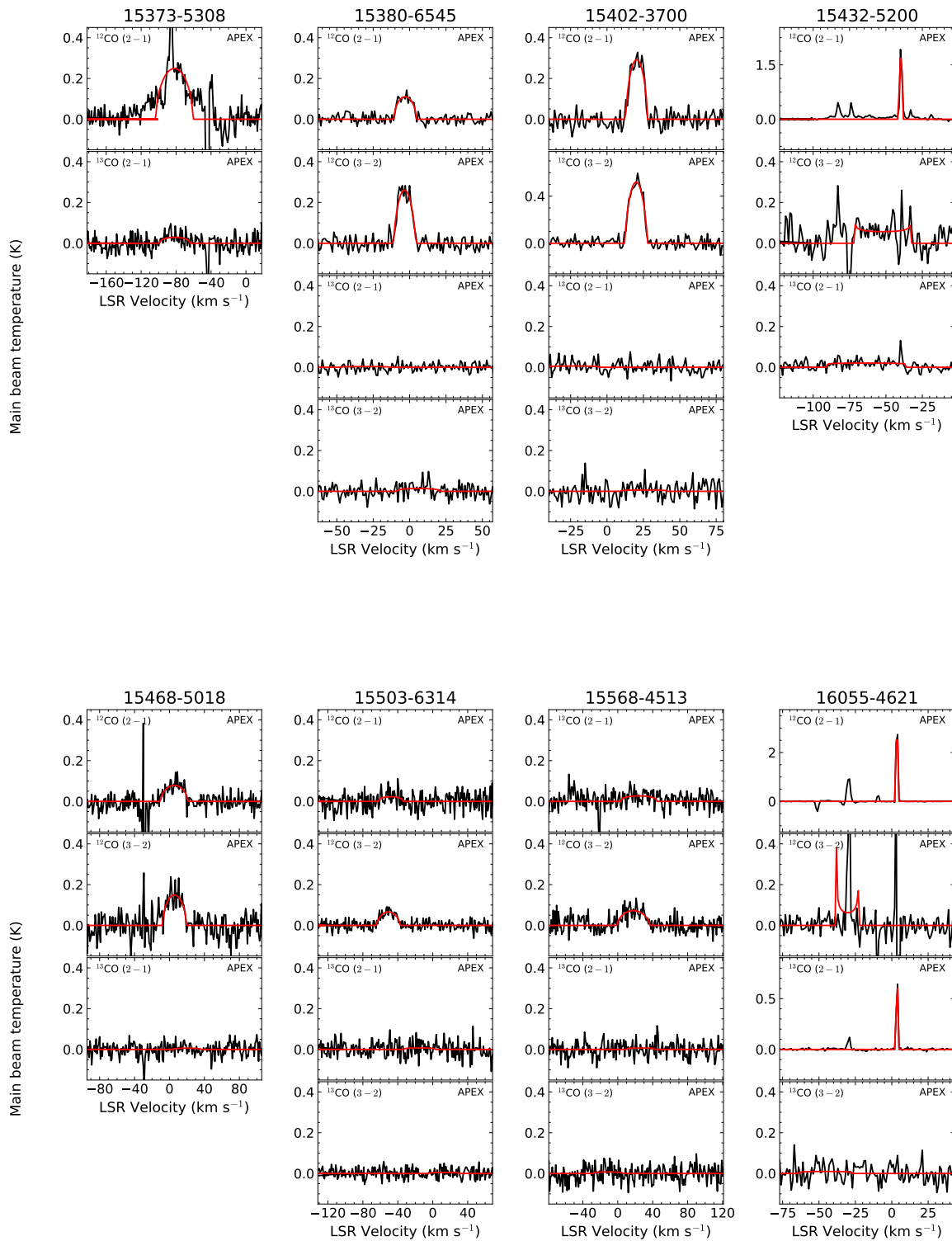
Appendix B NESS: Figures presenting soft-parabola line fitting of the spectra



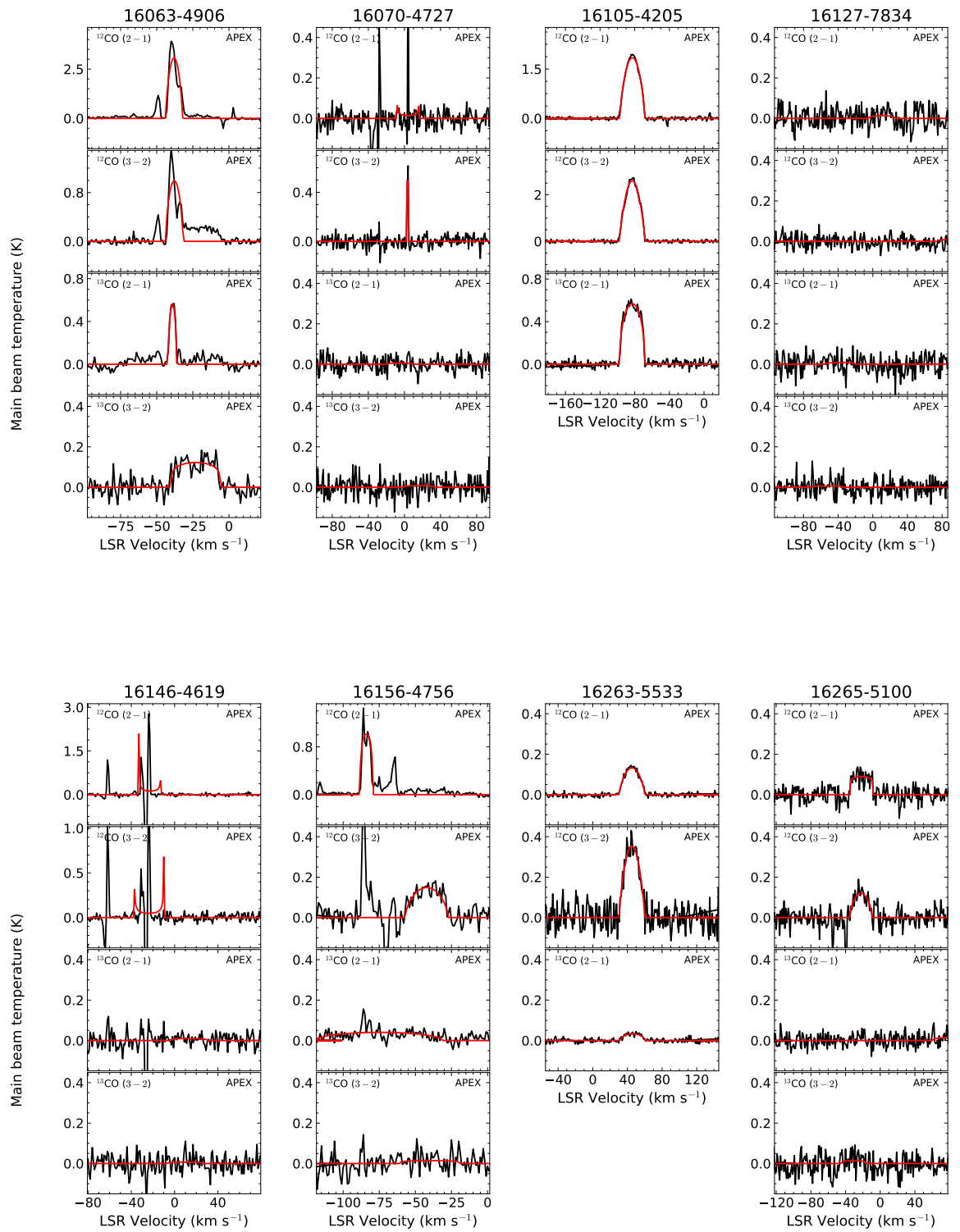


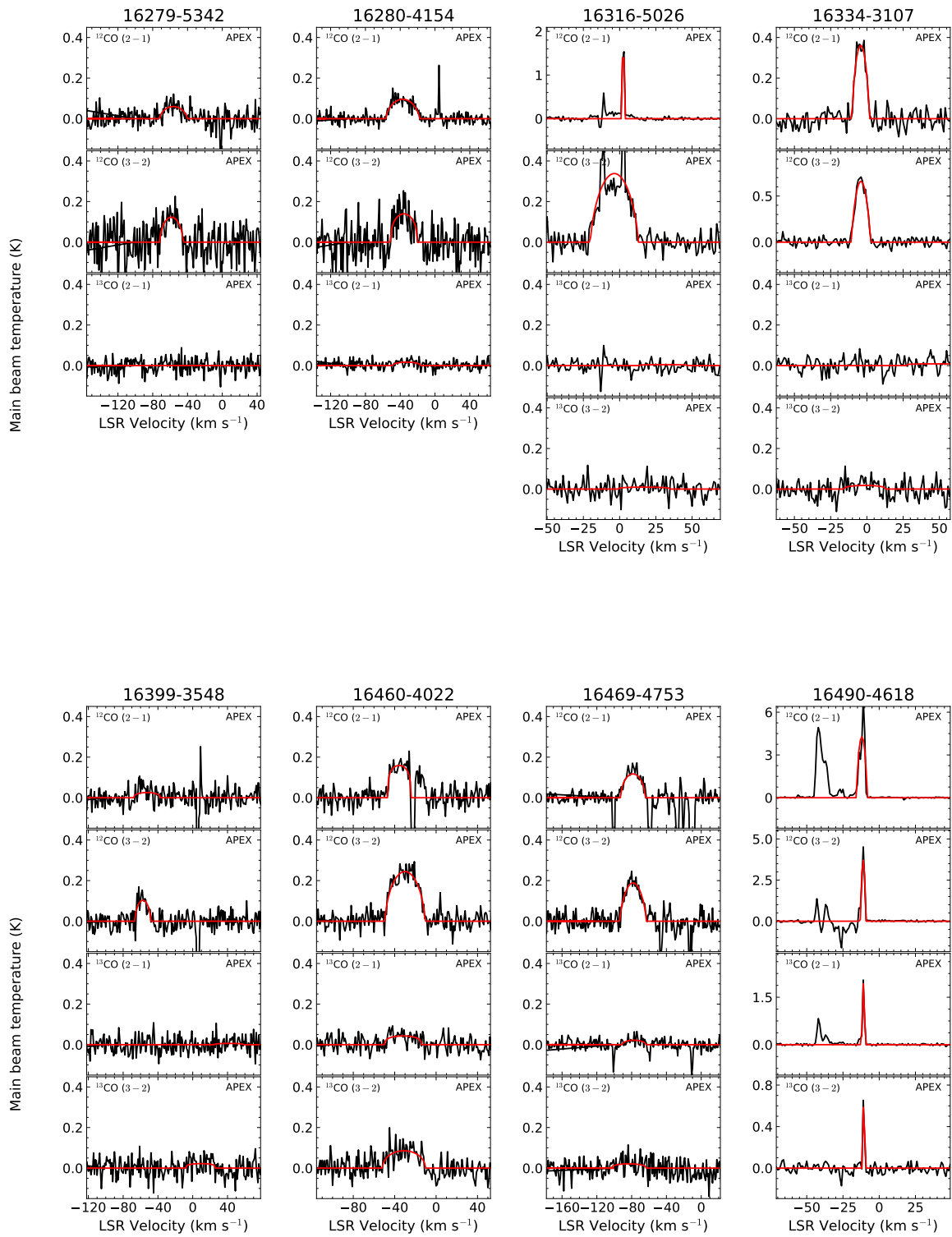
Appendix B NESS: Figures presenting soft-parabola line fitting of the spectra



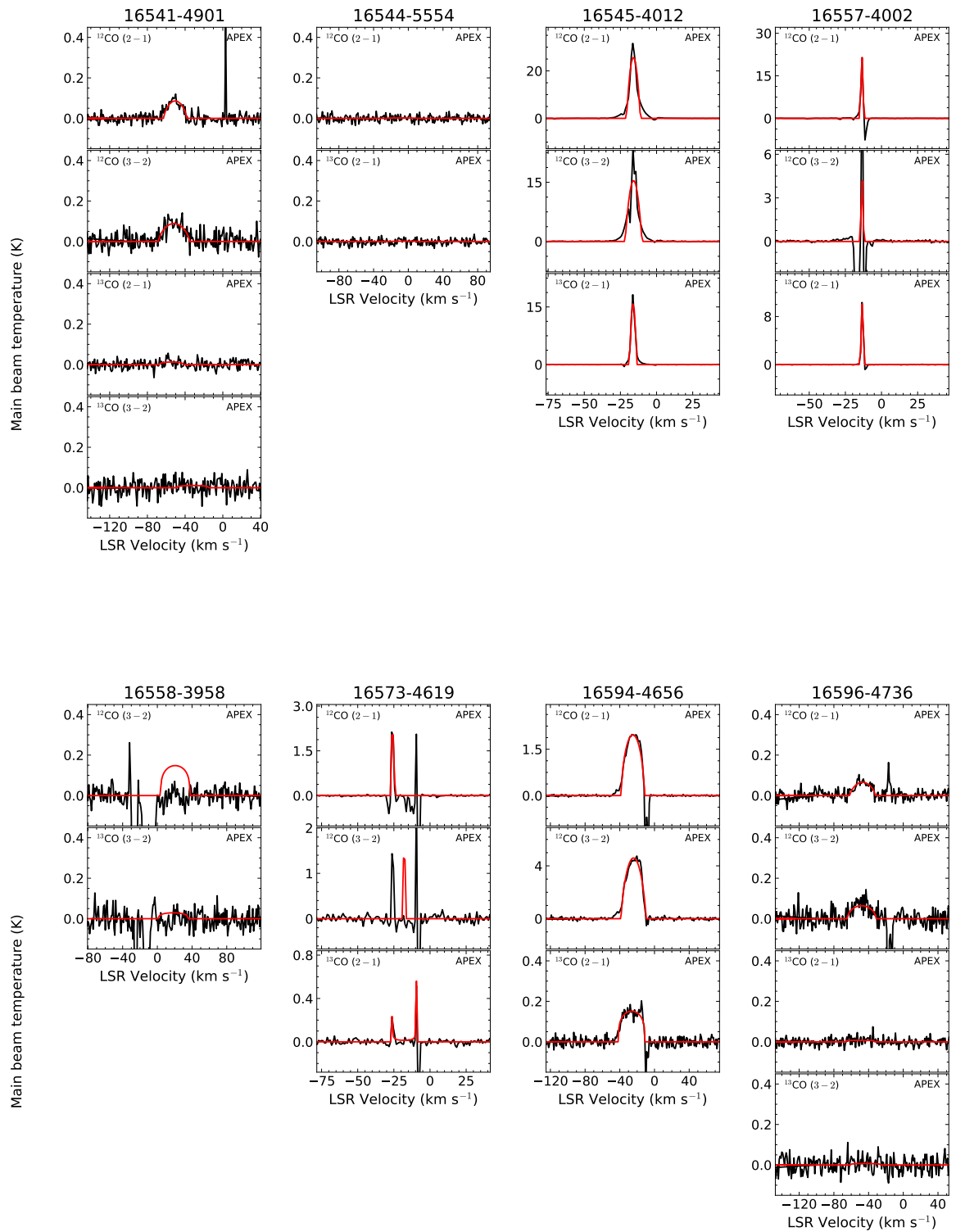


Appendix B NESS: Figures presenting soft-parabola line fitting of the spectra



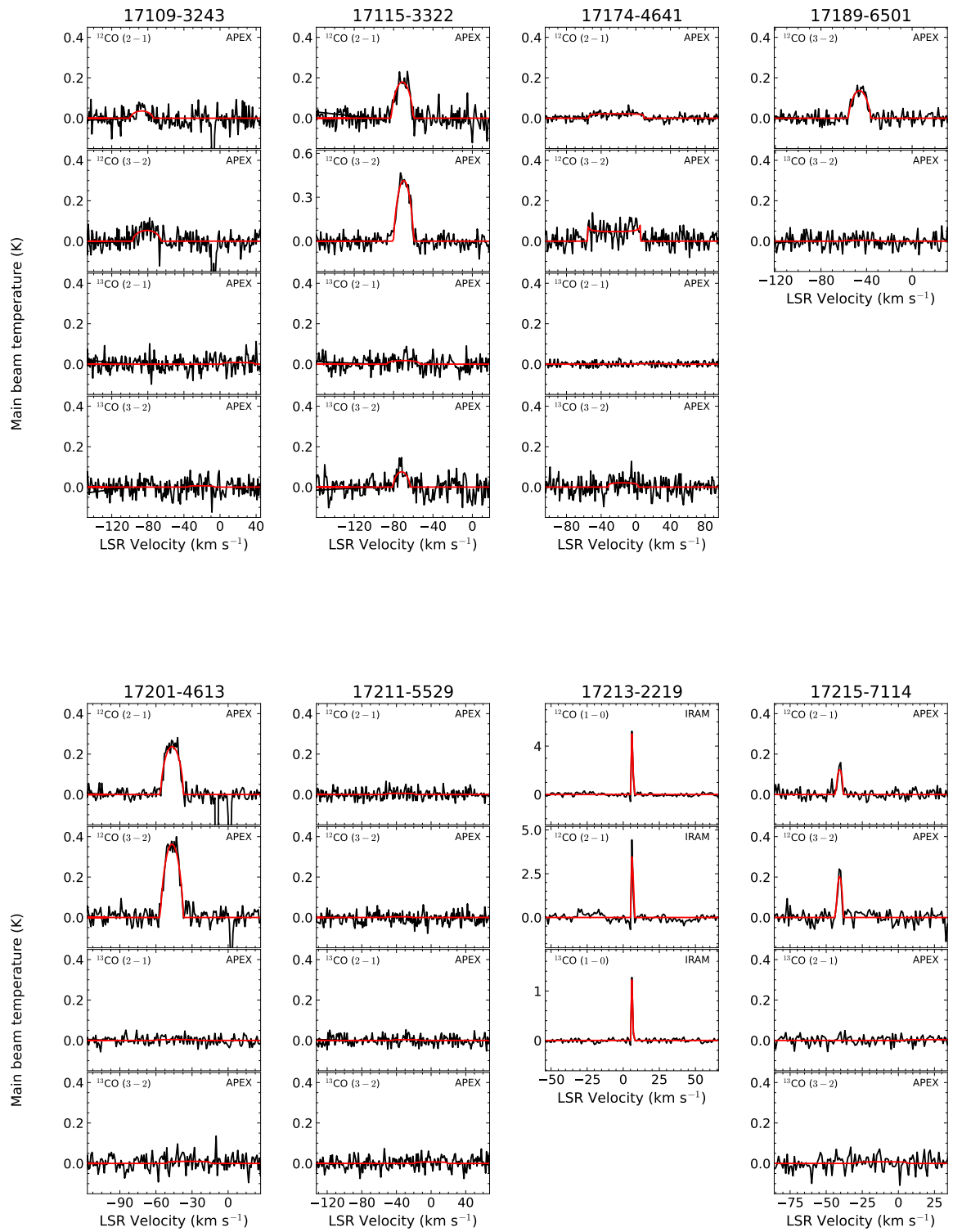


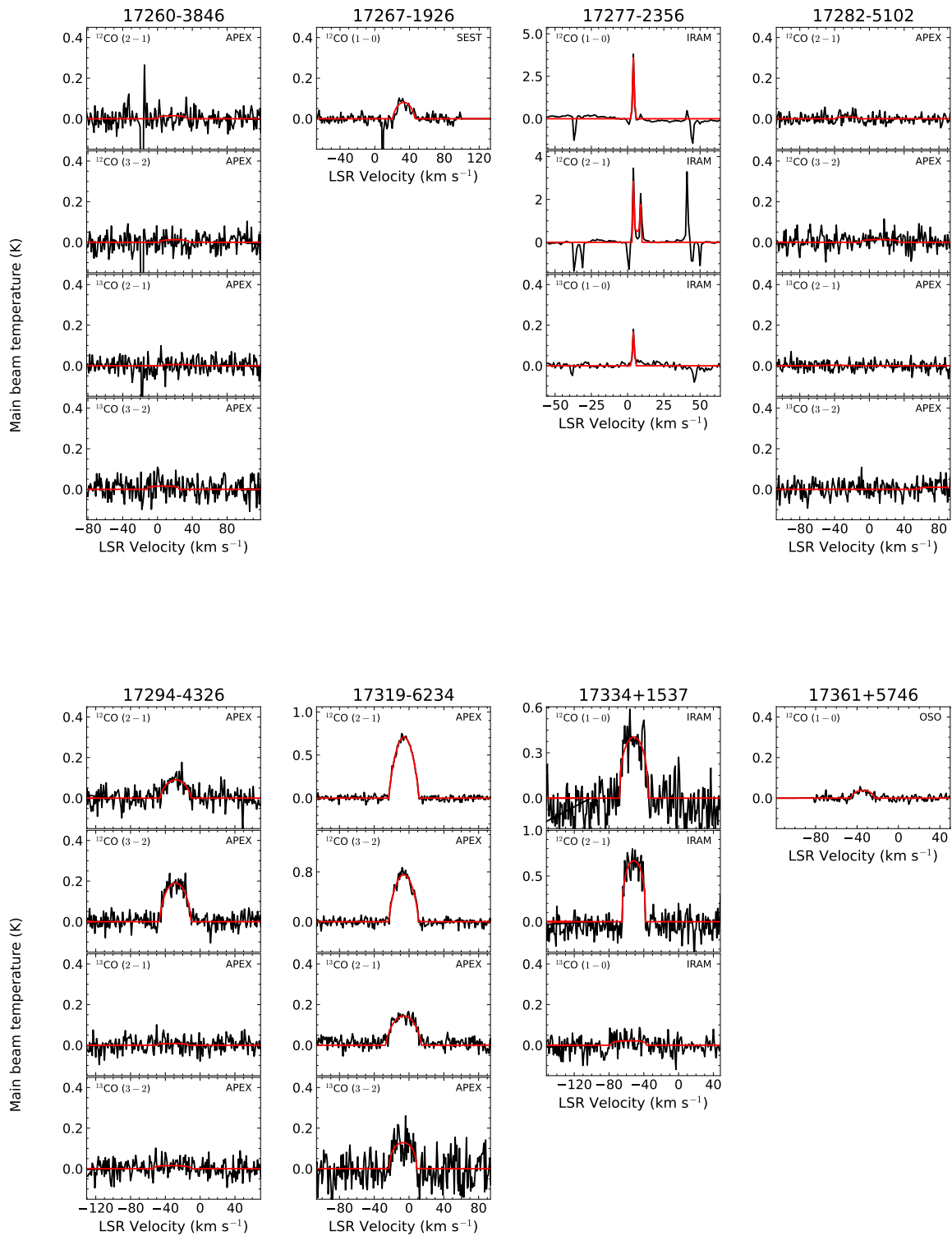
Appendix B NESS: Figures presenting soft-parabola line fitting of the spectra



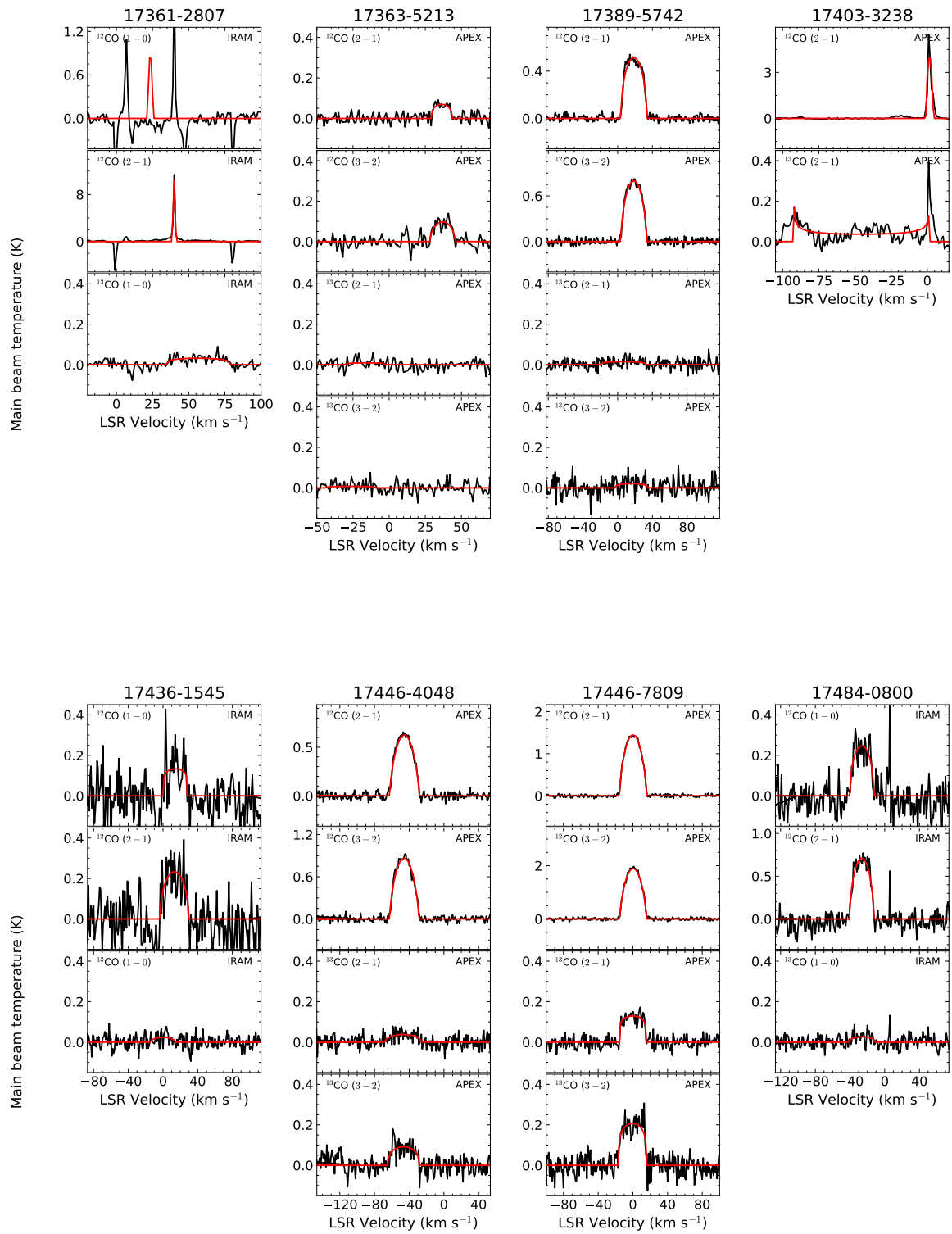


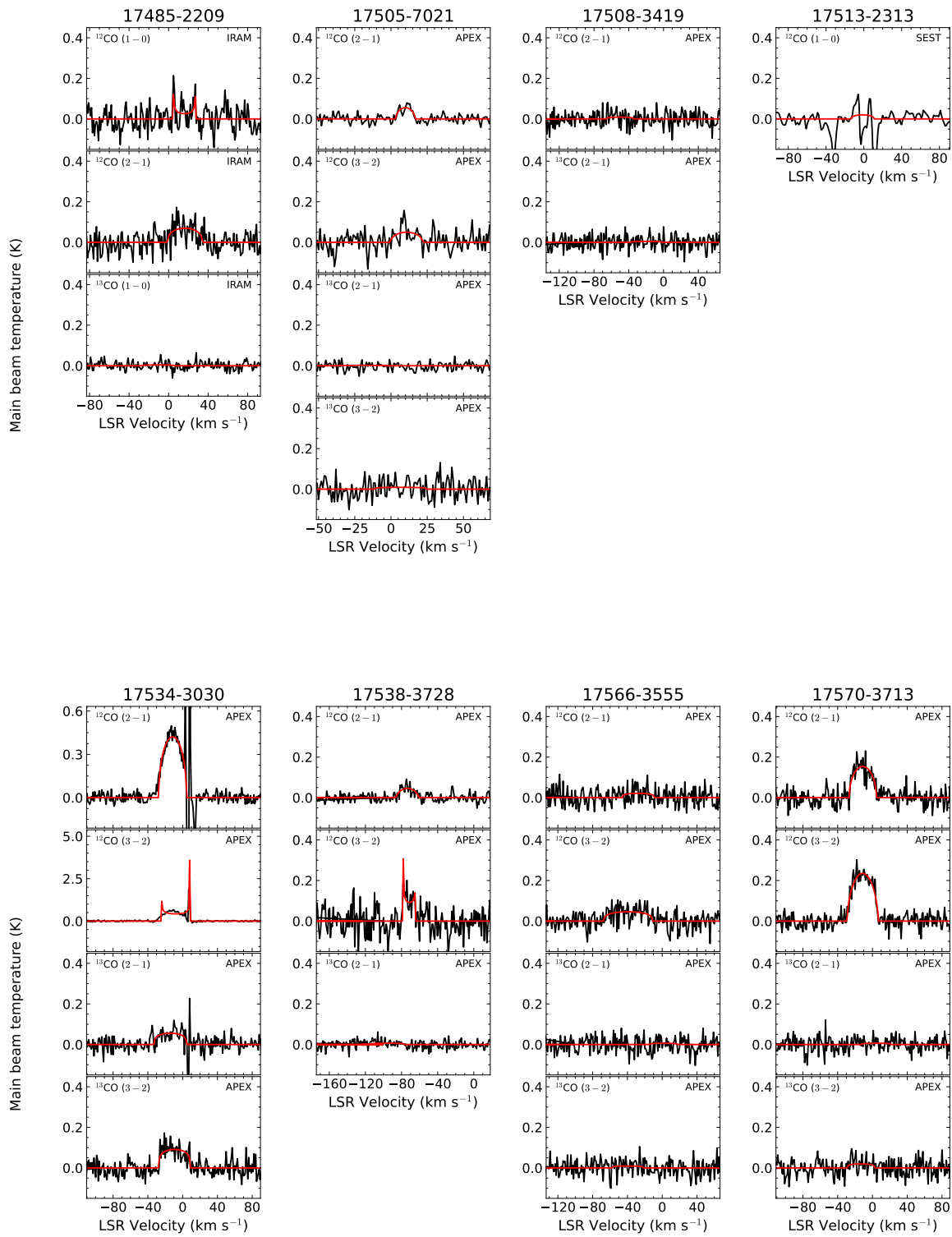
Appendix B NESS: Figures presenting soft-parabola line fitting of the spectra



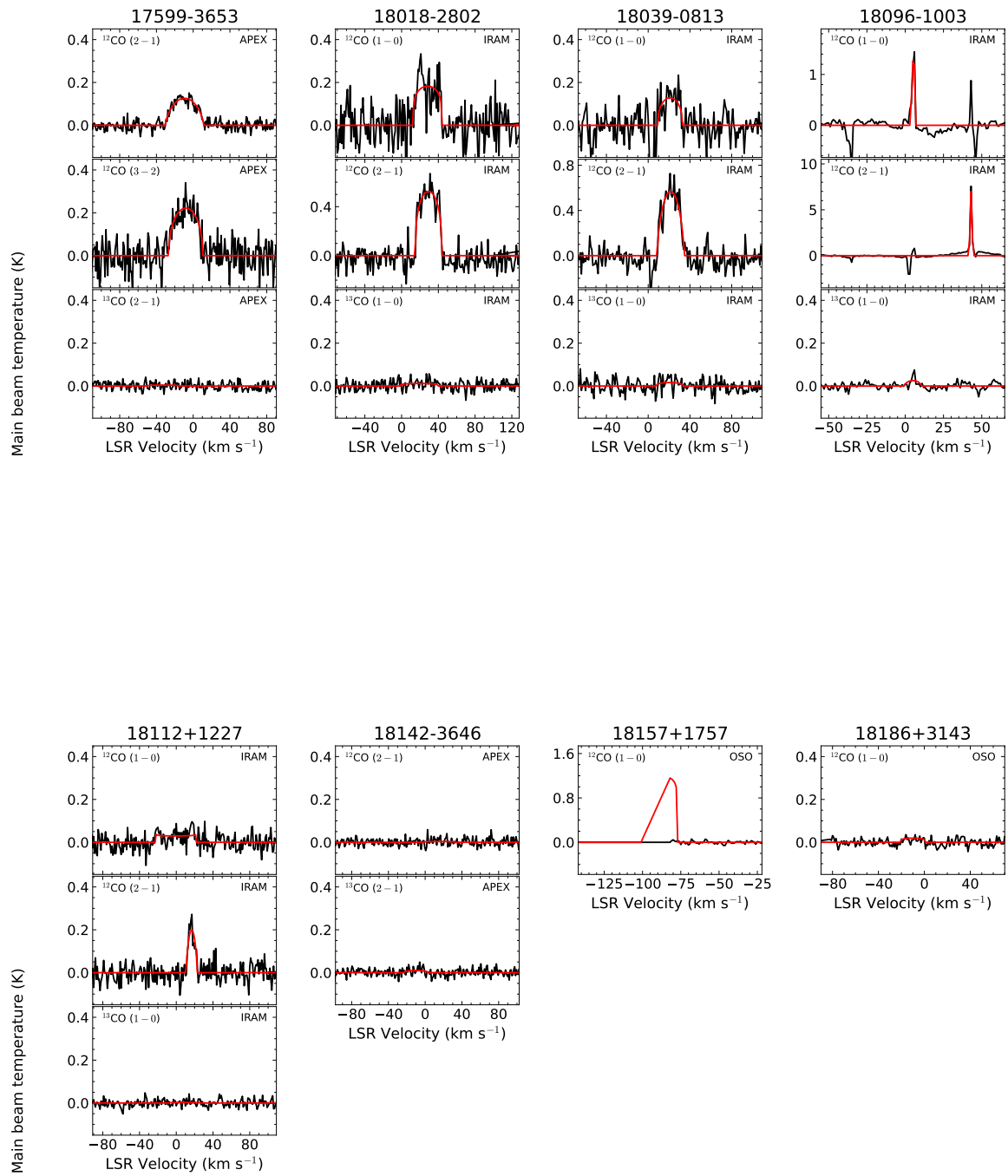


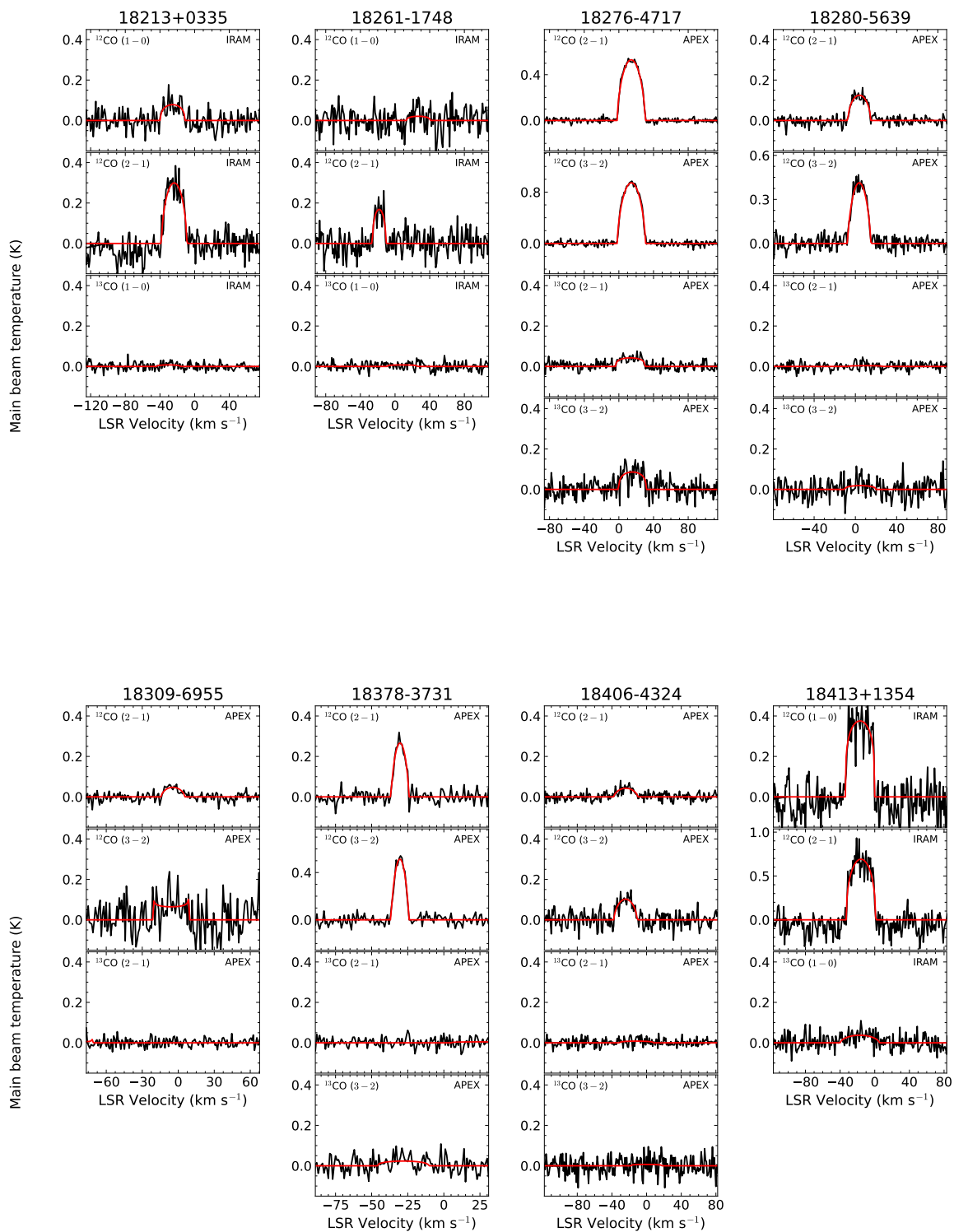
Appendix B NESS: Figures presenting soft-parabola line fitting of the spectra



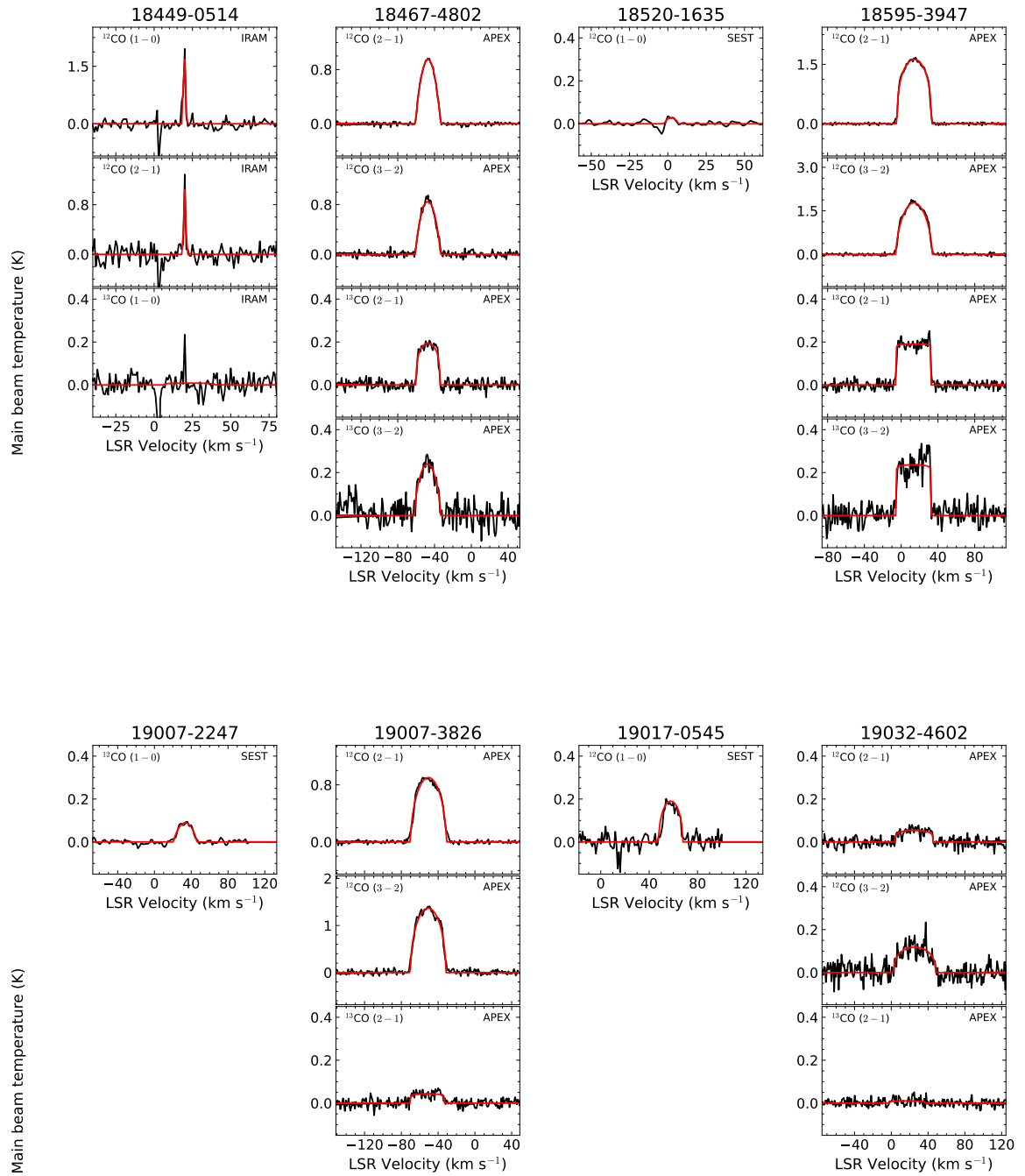


Appendix B NESS: Figures presenting soft-parabola line fitting of the spectra



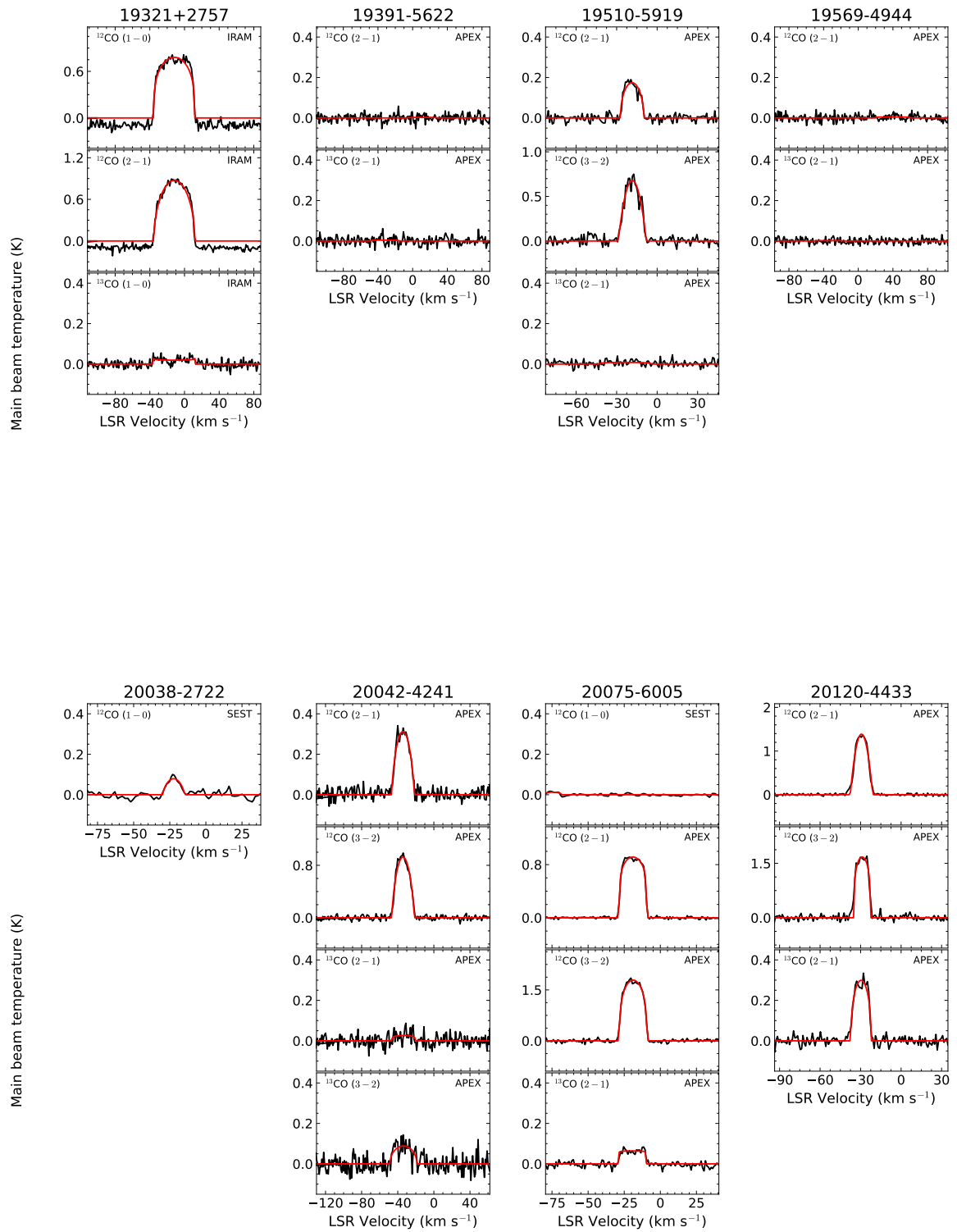


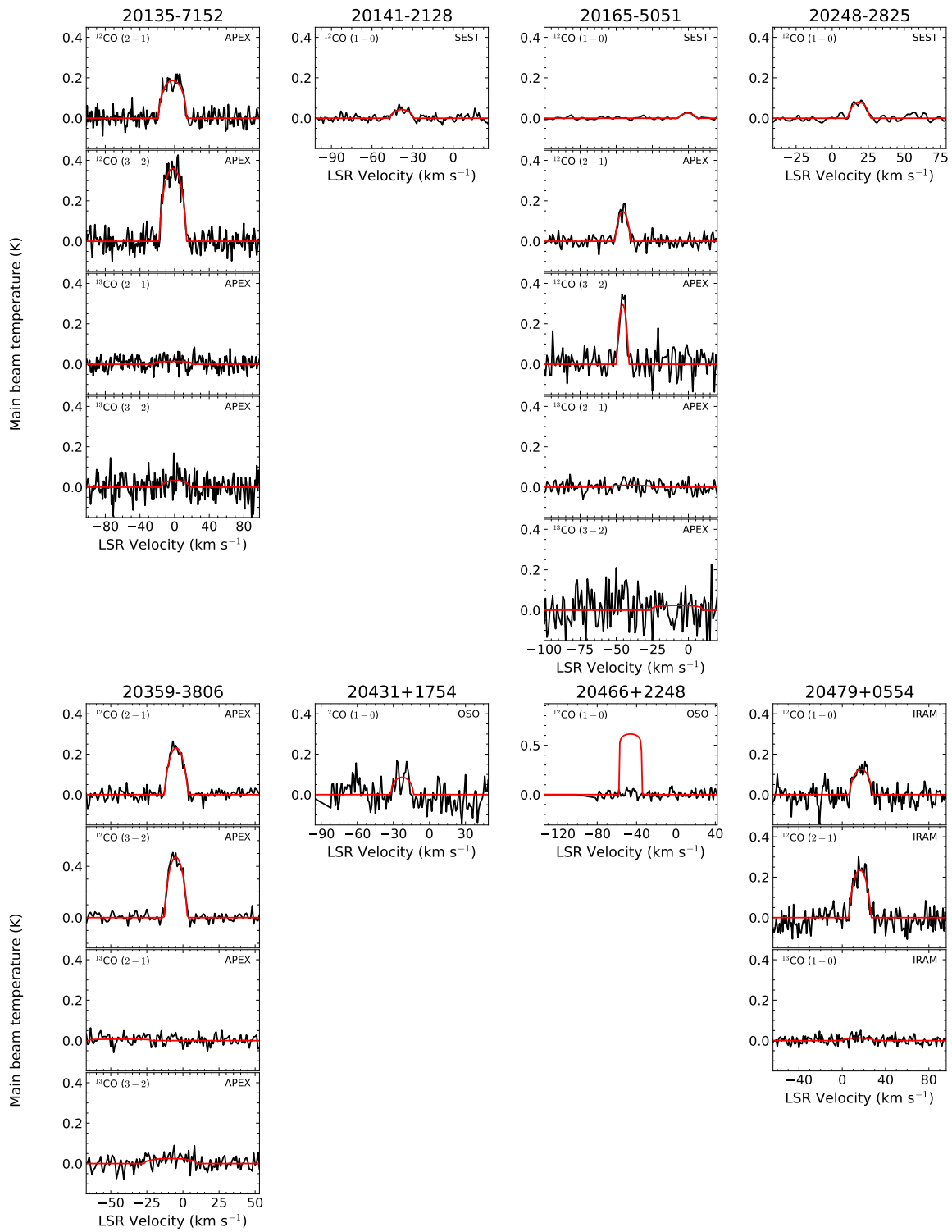
Appendix B NESS: Figures presenting soft-parabola line fitting of the spectra



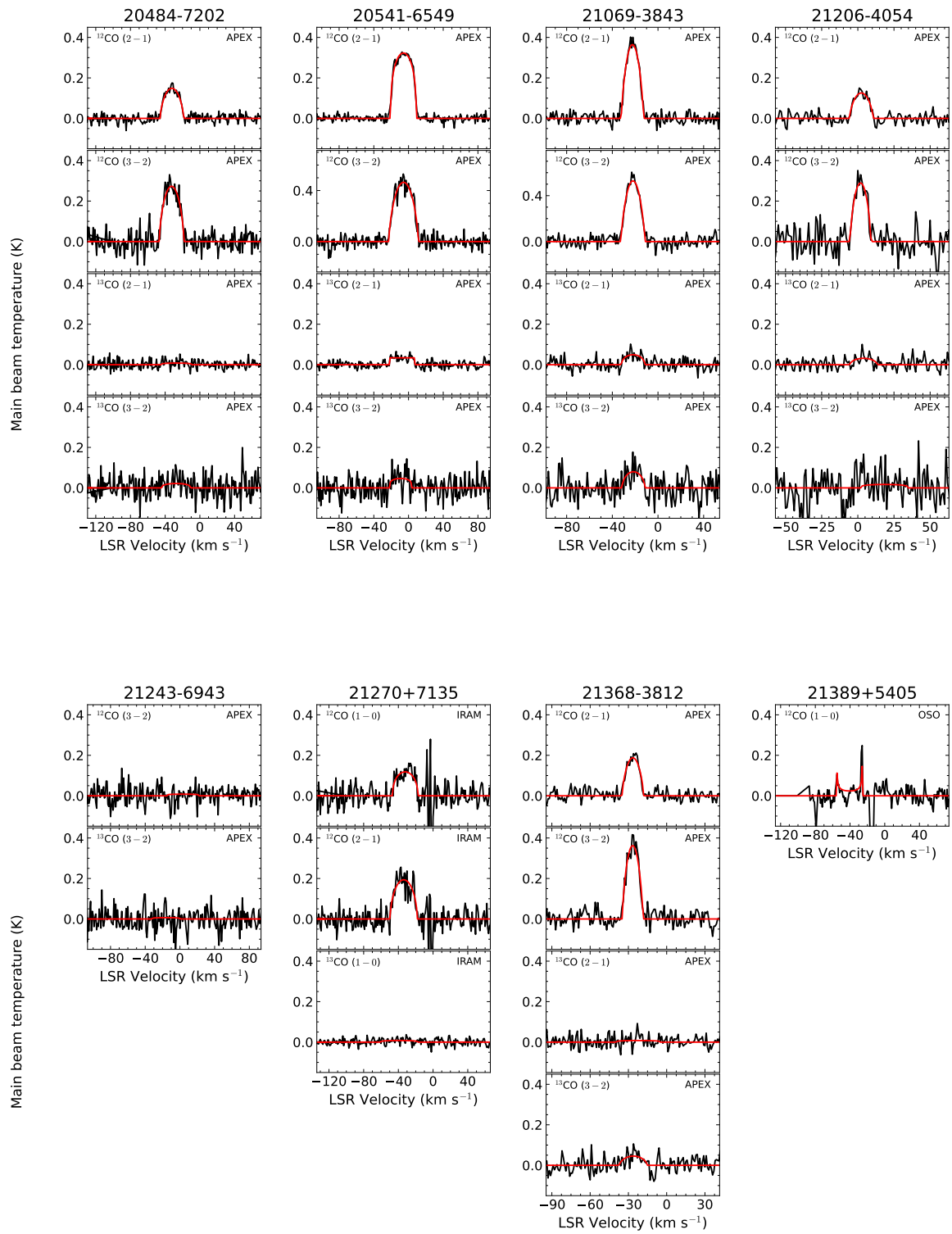


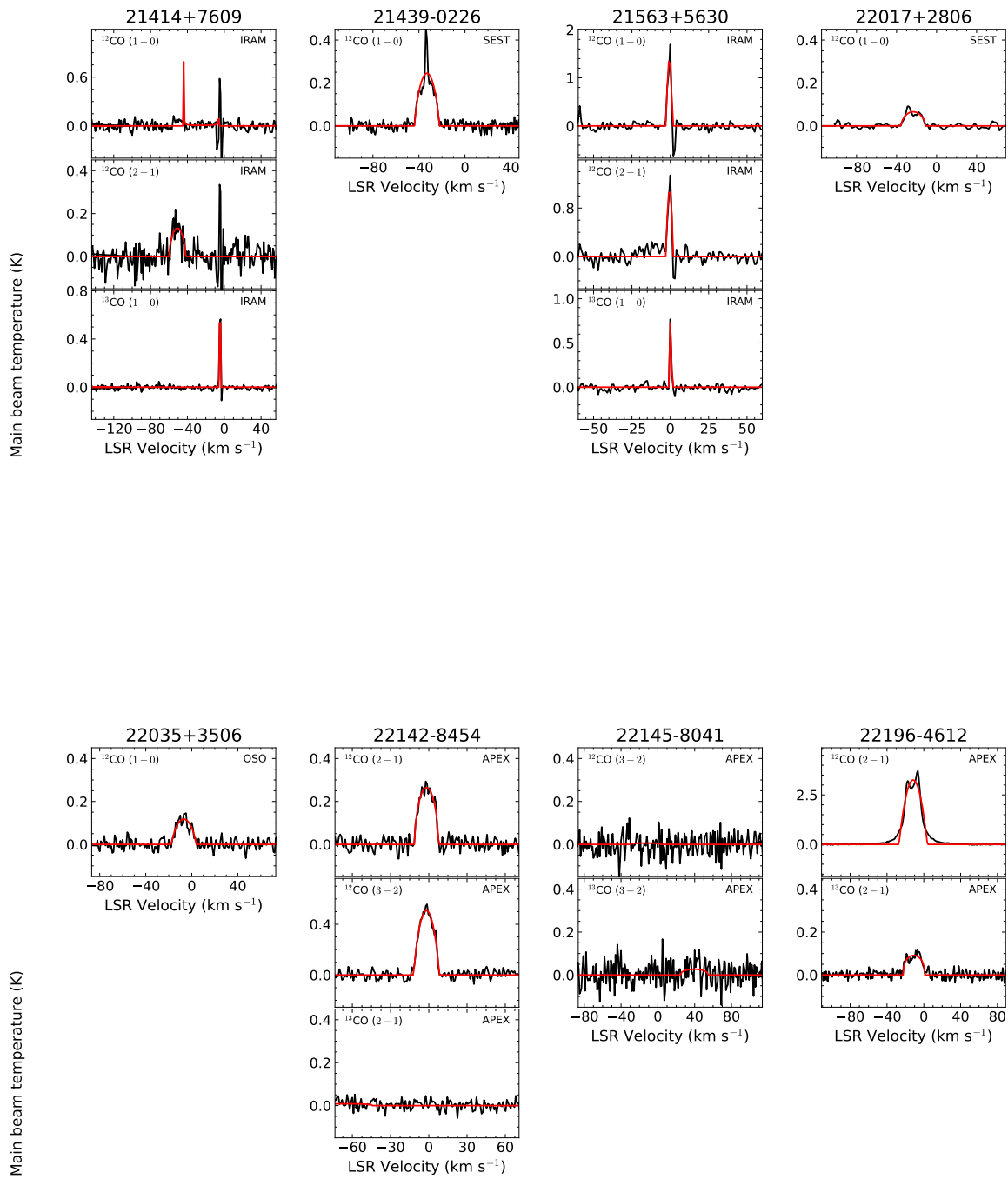
Appendix B NESS: Figures presenting soft-parabola line fitting of the spectra



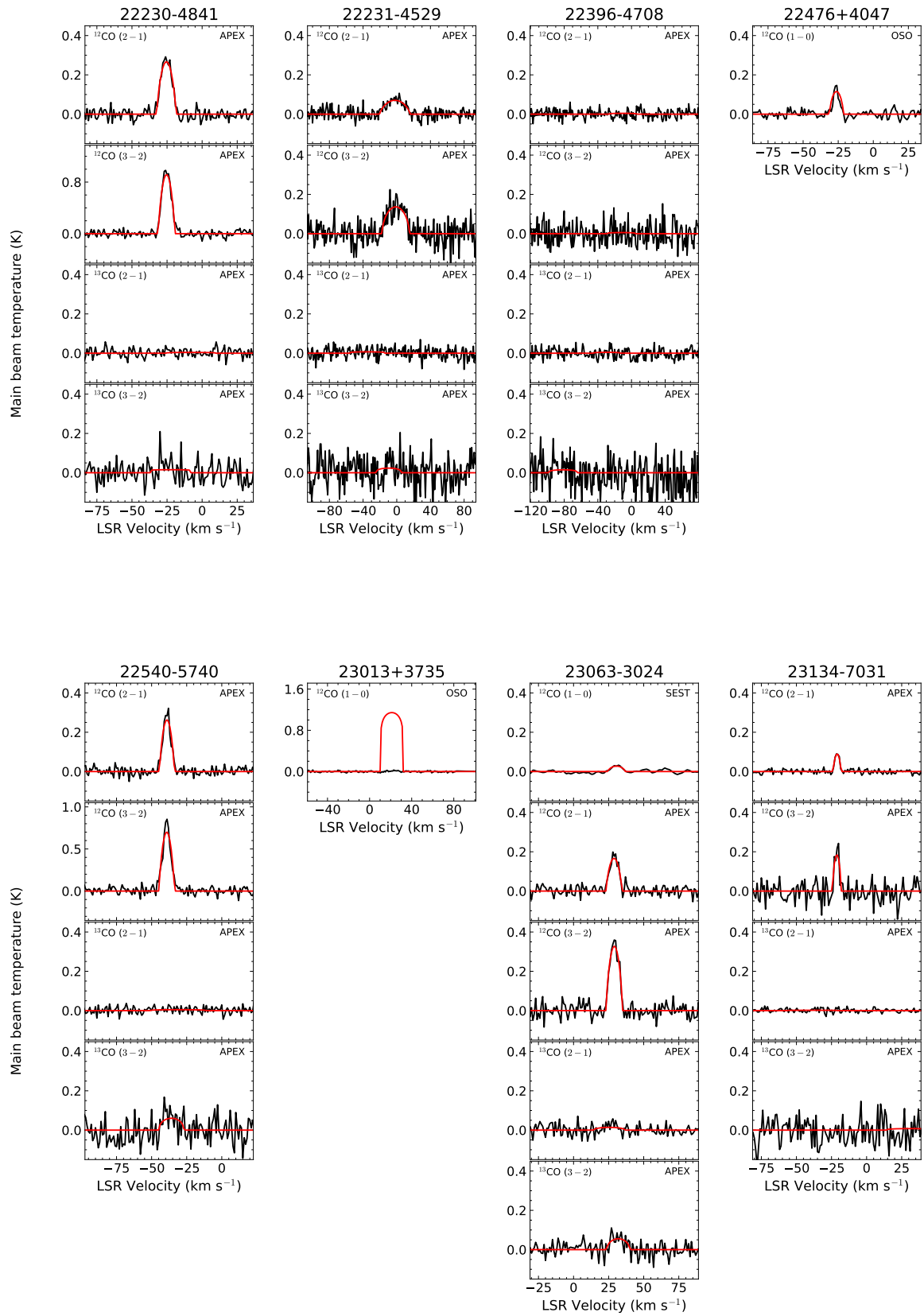


Appendix B NESS: Figures presenting soft-parabola line fitting of the spectra





Appendix B NESS: Figures presenting soft-parabola line fitting of the spectra



---

**Paper I: Vibrationally excited HCN transitions  
in circumstellar envelopes of carbon-rich  
AGB stars**

---

Below the publication Jeste et al. (2022) is presented in the pdf form, which is summarised in Chapter 2.

# Vibrationally excited HCN transitions in circumstellar envelopes of carbon-rich AGB stars

Manali Jeste<sup>1,\*</sup>, Yan Gong<sup>1</sup>, Ka Tat Wong<sup>2</sup>, Karl M. Menten<sup>1</sup>, Tomasz Kamiński<sup>3</sup>, and Friedrich Wyrowski<sup>1</sup>

<sup>1</sup> Max-Planck-Institut für Radioastronomie, Auf dem Hügel 69, 53121 Bonn, Germany  
e-mail: mjeste@mpifr.de

<sup>2</sup> Institut de Radioastronomie Millimétrique, 300 rue de la Piscine, 38406 Saint Martin d'Hères, France

<sup>3</sup> Nicolaus Copernicus Astronomical Center, Polish Academy of Sciences, Rabiańska 8, 87–100 Toruń, Poland

Received 18 February 2022 / Accepted 21 June 2022

## ABSTRACT

**Context.** The most abundant molecule after H<sub>2</sub> and CO in the circumstellar envelopes (CSEs) of carbon-rich asymptotic giant branch (AGB) stars is HCN. Its rotational lines within vibrationally excited states are exceptional tracers of the innermost region of carbon-rich CSEs.

**Aims.** We aim to constrain the physical conditions of CSEs of carbon-rich stars using thermal lines of the HCN molecule. Additionally, we also search for new HCN masers and probe the temporal variations for HCN masers, which should shed light on their pumping mechanisms.

**Methods.** We observed 16 carbon-rich AGB stars in various HCN rotational transitions, within the ground and 12 vibrationally excited states, with the Atacama Pathfinder EXperiment (APEX) 12-metre sub-millimetre telescope.

**Results.** We detect 68 vibrationally excited HCN lines from 13 carbon-rich stars, including 39 thermal transitions and 29 maser lines, suggesting that vibrationally excited HCN lines are ubiquitous in carbon-rich stars. Population diagrams constructed for two objects from the sample, for thermal transitions from different vibrationally excited states, give excitation temperatures around 800–900 K, confirming that they arise from the hot innermost regions of CSEs (i.e.  $r < 20 R_*$ ). Among the detected masers, 23 are newly detected, and the results expand the total number of known HCN masers lines towards carbon-rich stars by 47%. In particular, the  $J = 2-1$  (0, 3<sup>le</sup>, 0),  $J = 3-2$  (0, 2, 0), and  $J = 4-3$  (0, 1<sup>lf</sup>, 0) masers are detected in an astronomical source for the first time. Our observations confirm temporal variations of the  $2-1$  (0, 1<sup>le</sup>, 0) maser on a timescale of a few years. Our analysis of the data suggests that all detected HCN masers are unsaturated. A gas kinetic temperature of  $\geq 700$  K and an H<sub>2</sub> number density of  $> 10^8$  cm<sup>-3</sup> are required to excite the HCN masers. In some ways, HCN masers in carbon-rich stars might be regarded as an analogy of SiO masers in oxygen-rich stars.

**Key words.** stars: AGB and post-AGB – stars: carbon – masers – circumstellar matter

## 1. Introduction

Low- and intermediate-mass stars will reach the asymptotic giant branch (AGB) phase in a late stage of their evolution, during which they will play a crucial role in the cosmic matter cycle (e.g. Kippenhahn et al. 2012; Höfner & Olofsson 2018). Due to the mass-loss processes in this phase, circumstellar envelopes (CSEs) are created around these AGB stars. Depending on the element ratio [C]/[O] in the stellar photosphere, AGB stars can belong to one of three types: oxygen-rich stars (also known as M-type stars, [C]/[O] < 1), S-type stars ([C]/[O]  $\approx$  1), or carbon-rich stars (also known as C-type stars, [C]/[O] > 1) (Habing 1996; Höfner & Olofsson 2018). In light of different chemical compositions for different AGB types (Tsuji 1964; Cherchneff 2006; Schöier et al. 2013), different tracers should be carefully selected to study the physical conditions of CSEs towards different types of AGB stars.

The HCN molecule is of great interest for studying the CSEs of carbon-rich stars because it is one of the parent molecules that is formed in the stellar atmosphere, and is also the most abundant molecule after H<sub>2</sub> and CO in such stars, as suggested by chemical models (e.g. Tsuji 1964; Cherchneff 2006). Observations have

also confirmed that the HCN fractional abundances relative to H<sub>2</sub> are as high as  $\sim 3 \times 10^{-5}$  for carbon-rich stars (e.g. Fonfría et al. 2008; Schöier et al. 2013). The HCN molecule is thus widely used to study the CSEs of carbon-rich stars.

The HCN molecule has three vibrational modes, corresponding to the CH stretching mode,  $\nu_1$ , the doubly degenerate bending mode,  $\nu_2$ , and the CN stretching mode,  $\nu_3$ , together denoted as ( $\nu_1, \nu_2, \nu_3$ ). The wavelengths of the fundamental transitions of these modes are 3.0, 14.0, and 4.8  $\mu$ m, which correspond to excitation temperatures of 4764, 1029, and 3017 K, respectively (e.g. Adel & Barker 1934; Barber et al. 2014; Menten et al. 2018). These infrared ro-vibrational lines are difficult to observe with ground-based telescopes due to the Earth's atmosphere. In contrast, numerous HCN rotational transitions from many vibrational states are easily accessible with ground-based millimetre and sub-millimetre telescopes. Many such HCN transitions have been widely detected in CSEs of carbon-rich stars (Cernicharo et al. 2011; Bieging 2001), the preplanetary nebula CRL 618 (Thorwirth et al. 2003), star-forming regions (Rolffs et al. 2011), and even external galaxies (Sakamoto et al. 2010; Martín et al. 2021). Because of the high extinction and density, the innermost regions of CSEs are difficult to study in lower- $J$  rotational transitions from the vibrational ground state, as they become optically thick; where  $J$  is the angular momentum quantum number. The HCN rotational transitions in vibrationally

\* Member of the International Max Planck Research School (IMPRS) for Astronomy and Astrophysics at the Universities of Bonn and Cologne.

**Table 1.** Relevant parameters of the 16 C-rich stars selected for this study.

Source name	RA J2000	Dec J2000	Distance (pc)	$V_{\text{LSR}}$ (km s <sup>-1</sup> )	$\dot{M}$ ( $M_{\odot}$ yr <sup>-1</sup> )	$2V_{\text{inf}}^*$ (km s <sup>-1</sup> )	Observation time (h)	Period (days)	$L_{\star}$ ( $L_{\odot}$ )
W Ori <sup>(e)</sup>	05:05:23.72	+01:10:39.5	490	-1.0	$3.1 \times 10^{-7}$	22	19.33	212	11600
S Aur <sup>(e)</sup>	05:27:07.45	+34:08:58.6	1099	-17.0	$5.9 \times 10^{-6}$	51	7.08	590.1	24000
V636 Mon <sup>(c)</sup>	06:25:01.43	-09:07:15.9	880	+10.0	$5.8 \times 10^{-6}$	40	11.06	543	8472
R Vol <sup>(b)</sup>	07:05:36.20	-73:00:52.02	$880^{+149}_{-176}$	-11.0	$(2.9 \pm 0.68) \times 10^{-6}$	36	16.02	453	8252
IRC +10216 <sup>(a)</sup>	09:47:57.4	+13:16:44	140	-26.5	$2-4 \times 10^{-5}$	36	3.56	630	$8750^{(c)}$
RAFGL 4211 <sup>(a)</sup>	15:11:41.9	-48:20:01	950	-3.0	$0.93 \times 10^{-5}$	42	14.11	632	
II Lup <sup>(a)</sup>	15:23:05.7	-51:25:59	640	-15.0	$1 \times 10^{-5}$	46	13.21	576	$8900^{(d)}$
IRC +20370 <sup>(c)</sup>	18:41:54.39	+17:41:08.5	600	-0.8	$3.0 \times 10^{-6}$	28	7.07	524	7900
V Aql <sup>(c)</sup>	19:04:24.15	-05:41:05.4	330	+53.5	$1.4 \times 10^{-7}$	16	4.11	407	6500
IRC +30374 <sup>(c)</sup>	19:34:09.87	+28:04:06.3	1200	-12.5	$1.0 \times 10^{-5}$	50	3.37	-	9800
AQ Sgr <sup>(b)</sup>	19:34:18.99	-16:22:27.04	$330^{+95}_{-60}$	+20.0	$2.5 \times 10^{-6}$	25	7.59	199.6	2490
CRL 2477 <sup>(c)</sup>	19:56:48.43	+30:43:59.9	3380	+5.0	$1.1 \times 10^{-4}$	40	2.40	-	13200
CRL 2513 <sup>(c)</sup>	20:09:14.25	+31:25:44.9	1760	+17.5	$2.0 \times 10^{-5}$	51	2.57	706	8300
RV Aqr <sup>(c)</sup>	21:05:51.74	-00:12:42.0	670	+0.5	$2.3 \times 10^{-6}$	30	10.7	453	6800
Y Pav <sup>(b)</sup>	21:24:16.74	-69:44:01.96	$400^{+125}_{-77}$	0.0	$(2.8 \pm 0.96) \times 10^{-6}$	22	12.08	449	5076
CRL 3068 <sup>(c)</sup>	23:19:12.24	+17:11:33.4	1300	-31.5	$2.5 \times 10^{-5}$	29	16.11	696	10900

**Notes.** This table gives information about the parameters of the sample of the carbon-rich stars. <sup>(a)</sup>Menten et al. (2018) – distance considered here is  $D^{\text{PLR}}$ , where the distance is derived from the Mira period-luminosity relation; <sup>(b)</sup>Rau et al. (2017) (Mass-loss rate from Loup et al. 1993); <sup>(c)</sup>Massalkhi et al. (2018). <sup>(d)</sup>Ramstedt & Olofsson (2014); <sup>(e)</sup>Schöier & Olofsson (2001). The distances for W Ori (220 pc) and S Aur (820 pc) were derived from the HIPPARCOS measurements and the period-luminosity relation in Schöier & Olofsson (2001), respectively. The distances are updated by the more accurate *Gaia* parallax measurements (Gaia Collaboration 2018). Their mass-loss rates and luminosities are also updated by scaling the new distances. All periods are from the American Association of Variable Star Observers (AAVSO) (<https://www.aavso.org/>) with the exception of CRL 2513 and IRC+10216 (Kerschbaum et al. 2006; Menten et al. 2012; Pardo et al. 2018).

excited states usually have much lower opacities. These properties, together with their high energy levels and critical densities, make them exceptional tracers for investigating the innermost regions of CSEs around carbon-rich stars, which are still poorly constrained. Similar to the observations of vibrationally excited SiO and H<sub>2</sub>O lines towards oxygen-rich stars (Wong et al. 2016), observations of vibrationally excited HCN lines may pave the way to understanding the acceleration zone and the atmosphere around the photosphere of carbon-rich stars. Furthermore, detections of multiple transitions of HCN will place constraints on the excitation conditions of the maser lines arising in these regions.

Studies of vibrationally excited HCN transitions have been limited. A large number of HCN  $J = 3-2$  rotational transitions from 28 vibrational states have been investigated towards IRC+10216 (Cernicharo et al. 2011). Using *Herschel*/PACS and SPIRE data, Nicolaes et al. (2018) performed a population diagram analysis of HCN vibrationally excited lines for eight carbon-rich stars, but they could not resolve the line profiles due to the coarse spectral resolution of their data. Both studies infer high excitation temperatures, supporting the idea that these transitions arise from the innermost region of CSEs. High spectral resolution observations towards more carbon-rich stars can provide more statistical constraints on the role of vibrationally excited HCN transitions for studying the entire class of carbon-rich AGB stars.

Masers are important tools for studying CSEs (e.g. Habing 1996; Reid & Honma 2014). The OH, SiO, and H<sub>2</sub>O masers are common in CSEs of oxygen-rich stars, but these masers have not yet been detected towards carbon-rich stars (Gray 2012). Instead, HCN and SiS transitions are commonly found to show maser actions towards carbon-rich stars (e.g. Lucas et al. 1988; Bieging 2001; Henkel et al. 1983; Fonfría Expósito et al. 2006; Schilke

et al. 2000; Gong et al. 2017; Fonfría et al. 2018; Menten et al. 2018). Compared with SiS masers, HCN masers are found to be more widespread (Menten et al. 2018). However, previous maser studies have been limited to certain HCN transitions and a low number of targets (see Table A.1). Extending the search for HCN masers to other vibrationally excited HCN transitions and towards more carbon-rich stars may shed light on the pumping mechanism.

With the motivations mentioned above, studies of HCN rotational lines in vibrationally excited states with high spectral resolutions are indispensable in order to investigate the innermost region of carbon-rich CSEs. We therefore undertake new observations of multiple vibrationally excited transitions with different rotational quantum numbers,  $J$ , towards a selected sample of carbon-rich stars. In this paper, we start with an overview of our sample of carbon-rich stars in Sect. 1, followed by the observations and data reduction of the stellar sample in Sects. 2 and 3. We present our results in Sect. 4 and discuss all the sources (some individually) in detail in Sect. 5, followed by a brief discussion on the aspect of summary and outlook of the project in Sect. 6.

## 2. Sample of carbon stars

Table 1 lists the information of the 16 carbon-rich stars in our survey. These sources were selected by applying the following two criteria: (1) the targets should be accessible with the Atacama Pathfinder Experiment<sup>1</sup> telescope (APEX); (2) the carbon-rich

<sup>1</sup> This publication is based on data acquired with the Atacama Pathfinder Experiment (APEX). APEX is a collaboration between the Max-Planck-Institut für Radioastronomie (MPIfR), the European Southern Observatory, and the Onsala Space Observatory.

**Table 2.** Observed HCN lines in ground states and vibrationally excited states with the APEX telescope.

$\Delta J$	$\nu$ (MHz)	$(\nu_1, \nu_2, \nu_3)$	$E_u$ (K)	$S_{ul}\mu^2$ (D <sup>2</sup> )	$\log_{10}(A_{ul})$	
(1)	(2)	(3)	(4)	(5)	(6)	
2–1	176011.260	(1, 0, 0)	4777.1	54.6	–3.64	
	176052.380	(0, 0, 1)	3029.5	53.3	–3.65	
	177238.656	(0, 1 <sup>1e</sup> , 0)	1037.1	38.9	–3.77	
	177261.111	(0, 0, 0)	12.8	53.6	–3.63	
	177698.780	(0, 3 <sup>1e</sup> , 0)	3053.6	36.7	–3.80	
	178136.478	(0, 1 <sup>1f</sup> , 0)	1037.2	38.9	–3.77	
	178170.380	(0, 2 <sup>0</sup> , 0)	2043.5	50.4	–3.66	
	3–2	264011.530	(1, 0, 0)	4789.8	81.9	–3.08
264073.300		(0, 0, 1)	3042.2	79.9	–3.09	
265852.709		(0, 1 <sup>1e</sup> , 0)	1049.9	69.2	–3.14	
265886.434		(0, 0, 0)	25.5	80.5	–3.08	
266540.000		(0, 3 <sup>1e</sup> , 0)	3066.4	65.2	–3.16	
267109.370		(0, 2 <sup>2f</sup> , 0)	2078.1	42.0	–3.35	
267120.020		(0, 2 <sup>2e</sup> , 0)	2078.1	42.0	–3.35	
267199.283		(0, 1 <sup>1f</sup> , 0)	1050.0	69.2	–3.14	
267243.150		(0, 2 <sup>0</sup> , 0)	2056.3	75.6	–3.10	
269312.890		(0, 3 <sup>1f</sup> , 0)	3066.6	65.2	–3.15	
4–3		354460.435	(0, 1 <sup>1e</sup> , 0)	1066.9	97.4	–2.73
		354505.478	(0, 0, 0)	42.5	107.3	–2.69
	355371.690	(0, 3 <sup>1e</sup> , 0)	3083.4	91.8	–2.75	
	356135.460	(0, 2 <sup>2f</sup> , 0)	2095.2	75.6	–2.83	
	356162.770	(0, 2 <sup>2e</sup> , 0)	2095.2	75.6	–2.83	
	356255.568	(0, 1 <sup>1f</sup> , 0)	1067.1	97.4	–2.72	
	356301.178	(0, 2 <sup>0</sup> , 0)	2073.4	100.8	–2.71	
	356839.554	(0, 3 <sup>3e</sup> , 0)	3127.2	42.8	–3.08	
	356839.650	(0, 3 <sup>3f</sup> , 0)	3127.2	42.8	–3.08	

**Notes.** (1) Rotational transition. (2) Rest frequency from the CDMS database (CDMS; Zelinger et al. 2003; Müller et al. 2005). (3) Vibrational state. (4) Upper-level energy. (5) Line strength. (6) Einstein A coefficient.

nature of these stars and the detection of HCN have already been confirmed by previous studies. We ended up with a 16-object sample, three of which were from Menten et al. (2018), where the authors explored 177 GHz HCN maser emission towards a sample of 13 carbon-rich AGB stars, another three from Rau et al. (2017), and the remaining ten from Massalkhi et al. (2018). These stars have mass-loss rates of the order of  $10^{-7}$  to  $10^{-4} M_{\odot} \text{ yr}^{-1}$ , spanning about three orders of magnitude. Additionally, we estimated the pulsation phase of the observed stars for different observational epochs (see Table B.1), which is discussed further in Appendix B.

### 3. Observations and data reduction

We carried out spectral line observations towards the selected 16 carbon-rich stars with the APEX 12-m telescope (Güsten et al. 2006) from 2018 June 8 to 2018 December 20 under the projects M-0101.F-9519A-2018 and M-0102.F-9519B-2018. The total observing time is 185.06 h. We observed a total of 26 rotational transitions of HCN,  $J = 2-1$ ,  $J = 3-2$ , and  $J = 4-3$ , in various vibrationally excited states. Table 2 shows the list of the observed HCN lines. We made use of SEPIA (a Swedish-ESO

**Table 3.** APEX receiver setups of the HCN observations.

Receiver	Tuning $\nu$ (SB) (GHz)	$\Delta J$	IF range (GHz)	$\eta_{mb}$	Jy K <sup>-1</sup>
(1)	(2)	(3)	(4)	(5)	(6)
SEPIA180 <sup>(a)</sup>	177 (USB)	2–1	4–8	0.77	33
PI230 <sup>(b)</sup>	266 (USB)	3–2	4–12	0.62	46
FLASH345 <sup>(c)</sup>	355 (USB)	4–3	4–8	0.66	53

**Notes.** The instrumental information is obtained from the APEX website, <https://www.apex-telescope.org/instruments/>. (1) Receiver name. (2) Tuning frequency (Sideband). The tuning frequency corresponds to an IF frequency of 6 GHz for all of the receivers. (3) Rotational transitions of the covered HCN lines. (4) Intermediate frequency range. (5) Main-beam efficiencies. (6) Jansky to Kelvin conversion factor. <sup>(a)</sup>Belitsky et al. (2018a,b). <sup>(b)</sup><https://www.eso.org/public/teles-instr/apex/pi230/>; also Sect. 2.1 of Brinkmann et al. (2020). <sup>(c)</sup>Klein et al. (2014).

PI receiver; Billade et al. 2012; Immer et al. 2016), PI230, and FLASH<sup>+</sup> (both MPIfR receivers; Klein et al. 2014), as the front-end instruments to observe HCN transitions in  $J = 2-1$ ,  $3-2$ , and  $4-3$ , respectively. Table 3 gives a brief summary of the instrumental setups of our observations. All HCN lines in the same frequency band were observed and calibrated simultaneously in a single setup. The Fast Fourier Transform Spectrometers (FFTSs) were connected as backend instruments to analyse the spectral data (Klein et al. 2006). These FFTS modules provide us with spectral resolutions of 76 kHz (or 0.13 km s<sup>-1</sup>), 61 kHz (or 0.07 km s<sup>-1</sup>), and 38 kHz (or 0.03 km s<sup>-1</sup>) for lines at 177 GHz, 267 GHz, and 355 GHz, respectively.

Additional observations of IRC +10216, II Lup, and RAFGL 4211 (i.e. the three targets from Menten et al. 2018), were observed again with the SEPIA receiver ( $\eta_{mb} = 0.85$ ) in October 2021 under the project M-0108.F-9515B-2021 to study the variability of the vibrationally excited HCN lines in  $J = 2-1$  (Sect. 4.3).

The spectra were obtained with a secondary mirror, wobbling at a rate of 1.5 Hz and a beam throw of  $\pm 60''$  in azimuth. Total integration times for different targets are summarised in Table 1. The chopper-wheel method was used to calibrate the antenna temperature,  $T_A^*$  (Ulich & Haas 1976), and the calibration was done every 8–10 min. We converted the antenna temperatures to main-beam temperatures,  $T_{mb}$ , with the relationship,  $T_{mb} = T_A^* \eta_f / \eta_{mb}$ , where  $\eta_f$  and  $\eta_{mb}$  are the telescope’s forward efficiency and main-beam efficiency, respectively. We obtained the values of  $\eta_f$ ,  $\eta_{mb}$ , and the Jansky to Kelvin (Jy K<sup>-1</sup>) conversion factor for HCN  $J = 3-2$  from the telescope’s report<sup>2</sup>. To get a precise  $\eta_{mb}$  for the  $J = 2-1$  and  $J = 4-3$  transitions of HCN, which was not included in the telescope’s report, we calculated the antenna temperature from the cross scans of Mars taken during the observations and compared it with the modelled brightness temperature of Mars at that time<sup>3</sup>. Table 3 lists the main-beam efficiency and Jy K<sup>-1</sup> factor for each HCN line. The telescope’s focus was checked after sunrise and sunset, while the pointing, based on nearby pointing sources, was accurate to within  $\sim 2''$ . The full width at half maximum (FWHM) beam sizes,  $\theta_b$ , are  $36''$ ,  $24''$ , and  $18''$  at 177 GHz, 267 GHz, and 356 GHz, respectively. Velocities are given with respect to the local standard of rest (LSR). A brief summary of the observed

<sup>2</sup> <https://www.apex-telescope.org/telescope/efficiency/>
<sup>3</sup> <https://lesia.obspm.fr/perso/emmanuel-lellouch/mars/>

HCN rotational lines in various vibrational states is given in Table 2.

Data reduction was performed with the GILDAS<sup>4</sup> software package (Pety 2005). The first-order polynomial baseline was subtracted for all observed spectra. The spectra were smoothed at the expense of velocity resolution to improve the signal-to-noise ratios (S/Ns).

## 4. Results

Figures 1–2, 3, and 4 present the observed spectra towards the three exemplary sources, IRC +10216, RAFGL 4211, and II Lup, respectively, while the spectra of the other 13 sources are presented in Appendix C. In our study, the detection criteria is set to be a S/N of at least three.

### 4.1. Ground-state HCN transitions

HCN  $J = 2-1$ ,  $3-2$ , and  $4-3$  transitions in the ground state are detected towards all 16 sources. These spectral line profiles are parabolic, which is characteristic of a saturated line from an expanding CSE (e.g. Morris 1975; Olofsson et al. 1982). We fit the line profiles in the GILDAS/CLASS software using the SHELL method to obtain line parameters including velocity-integrated intensity ( $\int T_{\text{mb}} dV$ ), systemic LSR velocity ( $V_{\text{LSR}}$ ), and expansion velocity ( $V_{\text{exp}}$ ). The results are given in Table 4. Compared with the integrated HCN  $J = 2-1$  (0, 0, 0) intensities of IRC +10216, II Lup, and RAFGL 4211 in Menten et al. (2018), our values are lower by a factor of  $\sim 50\%$  on the  $T_{\text{mb}}$  scale. Regular measurements of calibration sources with APEX in the HCN  $J = 2-1$  line find a scatter of intensities of about 15%. Given the large spatial extent of the HCN emission (Dayal & Bieging 1995; Menten et al. 2018), variability of the vibrational ground state HCN lines is unlikely. We therefore attribute this difference to calibration uncertainties<sup>5</sup>. Comparing with the published results (see Table 1), we find that our derived  $V_{\text{LSR}}$  are generally higher than the systemic LSR velocities in the literature by  $1-3 \text{ km s}^{-1}$ , except for V636 Mon. As already explained by previous studies (Olofsson et al. 1982; Menten et al. 2018), this velocity difference is attributed to the presence of blueshifted self-absorption caused by low-excitation gas in the outer parts of CSEs. Our observations demonstrate that such HCN blueshifted self-absorption is ubiquitous in carbon-rich stars. Figure 5 presents the distribution of expansion velocities derived from the HCN  $J = 3-2$  ground-state line towards our sample. The median value of the expansion velocity is  $16.1 \text{ km s}^{-1}$ , higher than previously reported medians in carbon-rich stars in Ramstedt et al. (2009) because our sample includes objects with higher mass-loss rates than the Ramstedt et al. study.

### 4.2. Vibrationally excited HCN transitions

HCN rotational transitions in vibrational states with upper energy levels of up to 4789 K (see Table 2) were targeted in our study. We detected HCN rotational lines in the following 11 excited vibrational states: (1, 0, 0), (0, 0, 1), (0, 1<sup>1e</sup>, 0), (0, 1<sup>1f</sup>, 0), (0, 2<sup>2e</sup>, 0), (0, 2<sup>2f</sup>, 0), (0, 2<sup>0</sup>, 0), (0, 3<sup>1e</sup>, 0), (0, 3<sup>1f</sup>, 0), (0, 3<sup>3e</sup>, 0), and (0, 3<sup>3f</sup>, 0). Table 5 summarises the detection

<sup>4</sup> <https://www.iram.fr/IRAMFR/GILDAS/>

<sup>5</sup> During 2017–2018, there had been continuous upgrades of the APEX telescope including the replacements of panels, sub-reflector, and wobbler. The calibration, optics, and position of the SEPIA receiver has also changed.

statuses in each source. Vibrationally excited HCN transitions are found to show more complex line profiles, because both thermal and maser emission may contribute to the observed line profiles. The properties of the thermal emission and the maser emission are discussed in Sect. 4.2.1 and Sect. 4.2.2, respectively.

#### 4.2.1. Thermal emission

We detect 39 vibrationally excited HCN thermal lines towards IRC +10216, II Lup, RAFGL 4211, S Aur, W Ori, RV Aqr, IRC +30374, and CRL 3068, while thermal lines are not detected towards the other sources. Most of these sources have high mass-loss rates of  $\geq 1 \times 10^{-5} M_{\odot} \text{ yr}^{-1}$ , except for RV Aqr and W Ori, which have lower mass-loss rates of  $< 3 \times 10^{-6} M_{\odot} \text{ yr}^{-1}$ . These thermal lines display Gaussian-like profiles. In order to derive the observed parameters of the thermal emissions, we assumed a single Gaussian component to fit the observed line profile. The results are shown in Table 6. The peak intensities are within a range of 0.001–0.5 K for these lines. The fitted velocities are generally in a good agreement with the systemic velocities in the literature, within  $\sim 3\sigma$  (see also Table 1).

All of these lines have FWHM line widths of  $> 8 \text{ km s}^{-1}$ . We also note that the velocity spread of thermal vibrationally excited HCN lines can be as broad as that of the ground-state line (see Figs. 1 and C.4 for example). Because we only detected enough thermal vibrationally excited HCN lines in IRC +10216 and CRL 3068, we investigated the fitted line widths as a function of upper energy levels for these two sources. The results are shown in Fig. 6. The line widths do not have an apparent dependence on either their upper energy levels or their Einstein  $A$  coefficients (see Table 2). Even though a couple of transitions have similar upper energy levels, their line widths can vary by a factor of 1.5. Particularly, the  $\nu_2 = 3$  lines are found to be the narrowest, with expansions of  $\sim 5 \text{ km s}^{-1}$  in IRC +10216 due to their high energy levels and critical densities. The line widths are comparable to those of other high energy transitions from parent molecules (e.g. HCN, CS, SiS; Highberger et al. 2000; He et al. 2008; Patel et al. 2009). Comparing with the models of the velocity structure in IRC +10216 (e.g. Fig. 5 in Decin et al. 2015), we find that the  $\nu_2 = 3$  lines might arise from the wind acceleration zone, which is about 8 to 10  $R_*$  from the star.

The innermost regions of CSEs have high extinctions, volume densities, and temperatures. Such regions are poorly studied because they are not easily probed with the standard dense-gas tracers in the ground-state lines due to effects such as photon trapping and self-absorption. Our observations extend the spectrally resolved detection of the vibrationally excited thermal HCN transitions towards carbon-rich stars beyond IRC +10216, which paves the way towards a better understanding of the innermost regions of carbon-rich CSEs with vibrationally excited HCN thermal transitions.

#### 4.2.2. Maser emission

We identified HCN maser action following the criteria that the line profiles display either higher peak intensities than expected, or strong asymmetry (i.e. narrow spike features) overlaid on a broader line profile. For instance, different intensities of the  $J = 2-1$  (0, 1<sup>1e</sup>, 0) and  $J = 2-1$  (0, 1<sup>1f</sup>, 0) lines can be taken as evidence for maser action. Under local thermodynamic equilibrium (LTE) conditions, these two lines are expected to emit at nearly identical intensities, so the intensity difference of these

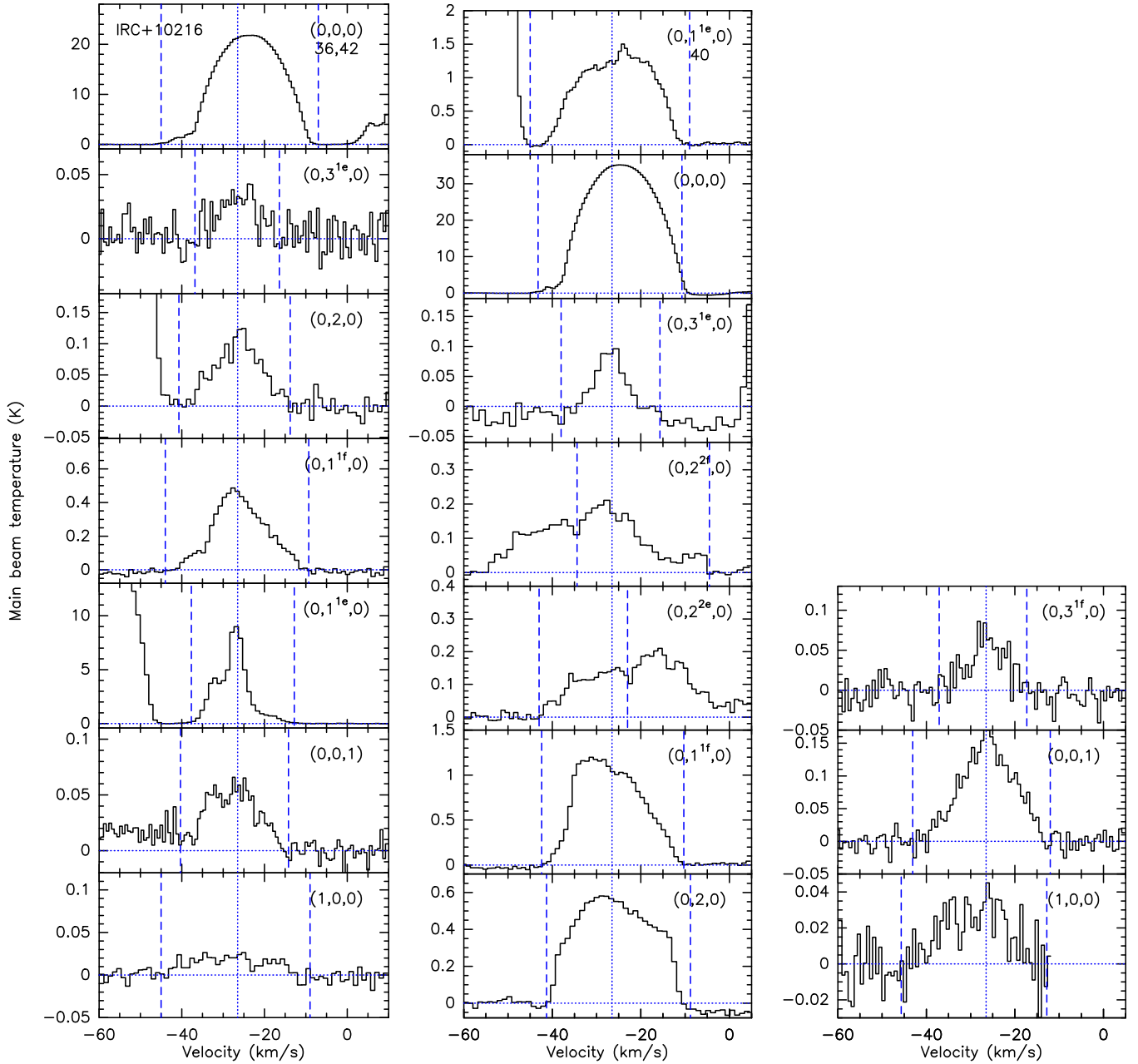


**Fig. 1.** From left to right: Spectra for  $J = 2-1$  (first) and  $3-2$  (second and third) transitions of HCN towards IRC +10216. The vibrational state of each transition is indicated in the top right corner of the respective spectrum. The vertical dashed blue lines denote the range of the emission in  $V_{\text{LSR}}$ , the vertical dotted line shows the systemic  $V_{\text{LSR}}$  of the star, and the horizontal dotted line is the baseline. The number below the vibrational quantum numbers in the panel is a code assigned to the date of observation of the particular transition. The corresponding dates of the codes are listed in the notes of Table 4.

two lines indicates that at least one of them deviates from LTE. In our observations, the  $J = 2-1$   $(0, 1^e, 0)$  line is significantly brighter than the  $J = 2-1$   $(0, 1^f, 0)$  line (see Figs. 1–4), which is suggestive of maser actions. Symmetric profiles are generally expected from thermal emission of typical AGB CSEs and narrow asymmetric spikes are not expected in thermal line profiles by the classic models (e.g. Morris 1975; Olofsson et al. 1982). Previous observations suggested that such asymmetric spikes arise from maser action (e.g. Henkel et al. 1983; Schilke et al. 2000; Fonfría Expósito et al. 2006; Gong et al. 2017; Fonfría et al. 2018), because these masers are only formed at specific regions in CSEs, which correspond to specific velocities

in their line profiles. Hence, the presence of narrow asymmetric spikes are regarded as an indicator of maser action in this work.

In this study, we detect 29 HCN maser lines from 12 carbon-rich stars, whereas HCN masers are not detected towards Y Pav, IRC +30374, CRL 2513, or CRL 2477 in our observations. Except for six maser lines already reported by previous observations (e.g. Menten et al. 2018), 23 transitions are newly discovered HCN masers. Hence, our observations expand the total number of previous known HCN masers towards carbon-rich stars by 47% (see Table A.1). Our results also confirm that HCN masers are common in carbon-rich stars. In particular,

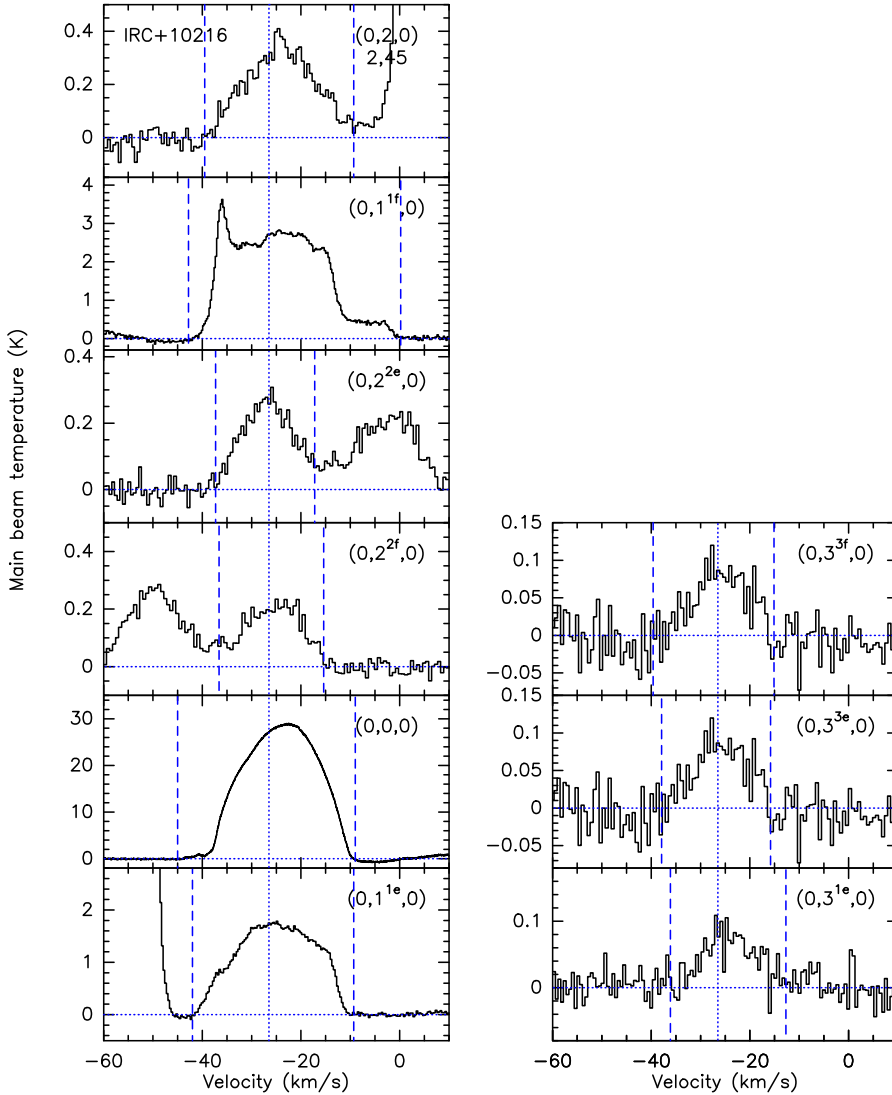


**Fig. 2.** Spectra for  $J = 4-3$  transitions of HCN towards IRC +10216. The description of the figure is the same as in the Fig. 1 caption.

eight CSEs, namely CRL 3068, RV Aqr, R Vol, AQ Sgr, V Aql, V636 Mon, S Aur, and IRC +20370, are newly discovered hosts of HCN masers. The 29 HCN masers arise from eight different transitions, namely  $J = 2-1$  ( $0, 1^{1e}, 0$ ),  $J = 2-1$  ( $0, 1^{1f}, 0$ ),  $J = 3-2$  ( $0, 1^{1e}, 0$ ),  $J = 3-2$  ( $0, 3^{1e}, 0$ ),  $J = 3-2$  ( $0, 2, 0$ ),  $J = 4-3$  ( $0, 1^{1e}, 0$ ), and  $J = 4-3$  ( $0, 1^{1f}, 0$ ). Among them, the  $J = 3-2$  ( $0, 3^{1e}, 0$ ),  $J = 3-2$  ( $0, 2, 0$ ),  $J = 4-3$  ( $0, 1^{1e}, 0$ ), and  $J = 4-3$  ( $0, 1^{1f}, 0$ ) masers are first detected in the interstellar medium.

**IRC +10216.** Five HCN masers, including  $J = 2-1$  ( $0, 1^{1e}, 0$ ),  $J = 2-1$  ( $0, 1^{1f}, 0$ ),  $J = 3-2$  ( $0, 1^{1e}, 0$ ),  $J = 3-2$  ( $0, 1^{1f}, 0$ ), and  $J = 4-3$  ( $0, 1^{1f}, 0$ ), are detected in IRC +10216. The  $J = 2-1$  ( $0, 1^{1e}, 0$ ) maser was reported in previous observations (Lucas & Cernicharo 1989; Menten et al. 2018). Our 2018 observations show at least three peaks at  $-32.2$ ,  $-27.9$ , and  $-26.3$  km s $^{-1}$ , which have peak flux densities of about 145, 295, and 351 Jy, respectively. The intensity of this line is nearly 20 times that of the  $J = 2-1$  ( $0, 1^{1f}, 0$ ) line (see Fig. 1). Comparison with other measurements at different epochs are presented in Sect. 4.3. Furthermore, we find that the flux density is lower for the components with LSR velocities farther from the systemic velocity of  $-26.5$  km s $^{-1}$ . The  $J = 2-1$  ( $0, 1^{1f}, 0$ ) line was believed to show maser actions due to its intensity variation (Menten et al. 2018). This maser peaks close to the systemic velocity and has a

flux density of about 17 Jy. The  $J = 3-2$  ( $0, 1^{1e}, 0$ ) line shows as a narrow spike overlaid on a broad thermal profile, while such a feature is not seen in the  $J = 3-2$  ( $0, 1^{1f}, 0$ ) line. The  $J = 3-2$  ( $0, 1^{1e}, 0$ ) maser peaks at a redshifted LSR velocity of  $-24.0$  km s $^{-1}$ . Subtracting the broad component, we obtained a flux density of 17.5 Jy. We note that this line was observed with NRAO-12 m and IRAM-30 m (Ziurys & Turner 1986; Cernicharo et al. 2011), but they did not detect a spike feature. On the other hand, the  $J = 3-2$  ( $0, 1^{1e}, 0$ ) maser was detected by previous extended Submillimeter Array (eSMA) observations (Shinnaga et al. 2009). We also see a presence of an asymmetrical profile feature in the  $J = 3-2$  ( $0, 1^{1f}, 0$ ) line, which is marked as a maser. He et al. (2017) monitored the line shape of this maser and reported such a variability in its blue-shifted peak. The  $J = 4-3$  ( $0, 1^{1f}, 0$ ) line appears to show a prominent asymmetry narrow spike on the bluishifted side, peaking at an LSR velocity of  $-35.9$  km s $^{-1}$ , while no asymmetric features are found in the  $J = 4-3$  ( $0, 1^{1e}, 0$ ) line. The flux density is estimated to be 68 Jy by subtracting the broad component. The flux densities of our detected HCN masers are at least a factor of two lower than those ( $>800$  Jy) of sub-millimetre HCN lasers (Schilke et al. 2000; Schilke & Menten 2003). Furthermore, we find that the intensity of the  $J = 3-2$  ( $0, 3^{1e}, 0$ ) line may also deviate from the values expected under LTE, because its peak intensity is about 1.4 times that

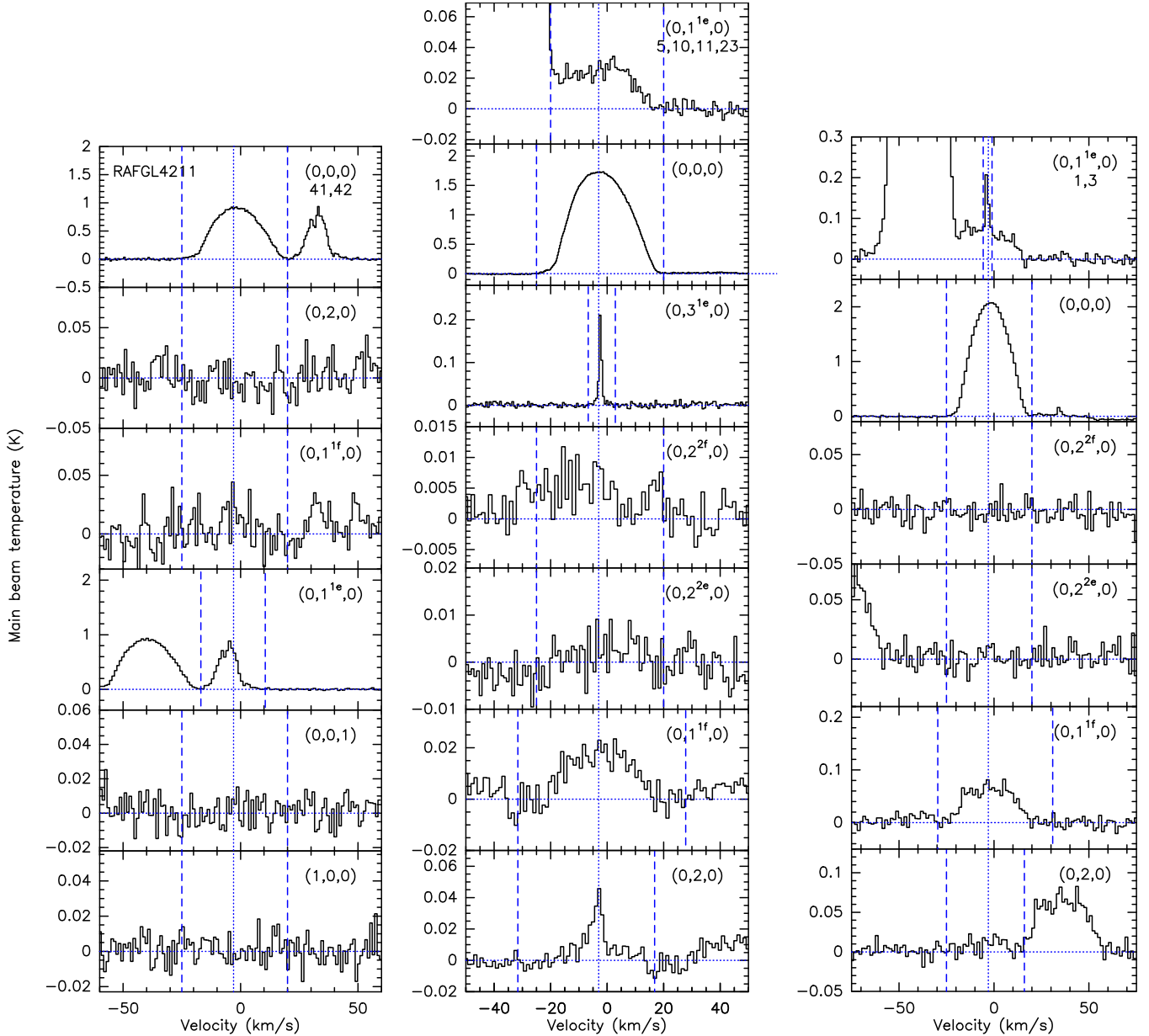


**Fig. 3.** Spectra for  $J = 2-1$  (left),  $3-2$  (centre) and  $4-3$  (right) transitions of HCN towards RAFGL 4211. The description of the figure is the same as in the Fig. 1 caption.

of the  $J = 3-2$  ( $0, 3^{1f}, 0$ ) line. However, the tentative maser nature of the  $J = 3-2$  ( $0, 3^{1e}, 0$ ) line still needs to be confirmed by follow-up observations because the signal-to-noise ratios of the two lines are not good enough for the difference to be significant.

**RAFGL 4211.** We detected four HCN masers. Among them, the  $J = 2-1$  ( $0, 1^{1e}, 0$ ) maser was first reported by Menten et al. (2018). Our  $J = 2-1$  ( $0, 1^{1e}, 0$ ) spectrum shows at least two peaks at  $-8.1 \text{ km s}^{-1}$  and  $-5 \text{ km s}^{-1}$  of flux density of 24.2 Jy and 32.5 Jy, respectively. These peak flux densities are about 20 times that of the  $J = 2-1$  ( $0, 1^{1f}, 0$ ) line (see Fig. 3), strongly supporting its maser nature. The flux density of the  $J = 2-1$  ( $0, 1^{1e}, 0$ ) maser is comparable to that of the  $J = 1-0$  ( $0, 2, 0$ ) maser in this source (see Fig. 1 in Smith et al. 2014). Although the  $J = 3-2$  ( $0, 2, 0$ ) and  $J = 3-2$  ( $0, 3^{1e}, 0$ ) masers only have flux densities of 2.4 Jy and 11.8 Jy, respectively, the detection of the two

masers are exceptional, because these two masers have only been discovered towards RAFGL 4211 so far. Both of the masers peak at  $-2.1 \text{ km s}^{-1}$ , close to the stellar systemic velocity. Unlike the other three masers, the  $J = 4-3$  ( $0, 1^{1e}, 0$ ) profile exhibits a narrow spike overlaid on a broad component, while such a narrow spike does not appear in the  $J = 3-2$  ( $0, 1^{1e}, 0$ ) spectrum. The  $J = 4-3$  ( $0, 1^{1e}, 0$ ) maser peaks at a slightly blueshifted side of  $-3.7 \text{ km s}^{-1}$ , and its flux density is about 18.5 Jy, which is fainter than the  $J = 2-1$  ( $0, 1^{1e}, 0$ ) maser.

**II Lup.** We detected the  $J = 2-1$  ( $0, 1^{1e}, 0$ ) and  $J = 4-3$  ( $0, 1^{1f}, 0$ ) masers in II Lup. The latter one is newly detected in this source. The  $J = 2-1$  ( $0, 1^{1e}, 0$ ) maser shows at least three peaks at  $-22.7$ ,  $-18.1$ , and  $-15.2 \text{ km s}^{-1}$ , which have flux densities of 21.3, 39.3, and 39.3 Jy, respectively. This maser is much brighter than the  $J = 2-1$  ( $0, 1^{1f}, 0$ ) line (see Fig. 4). Two peaks at  $-25.4$  and  $-6.2 \text{ km s}^{-1}$  are also identified in the  $J = 4-3$  ( $0,$

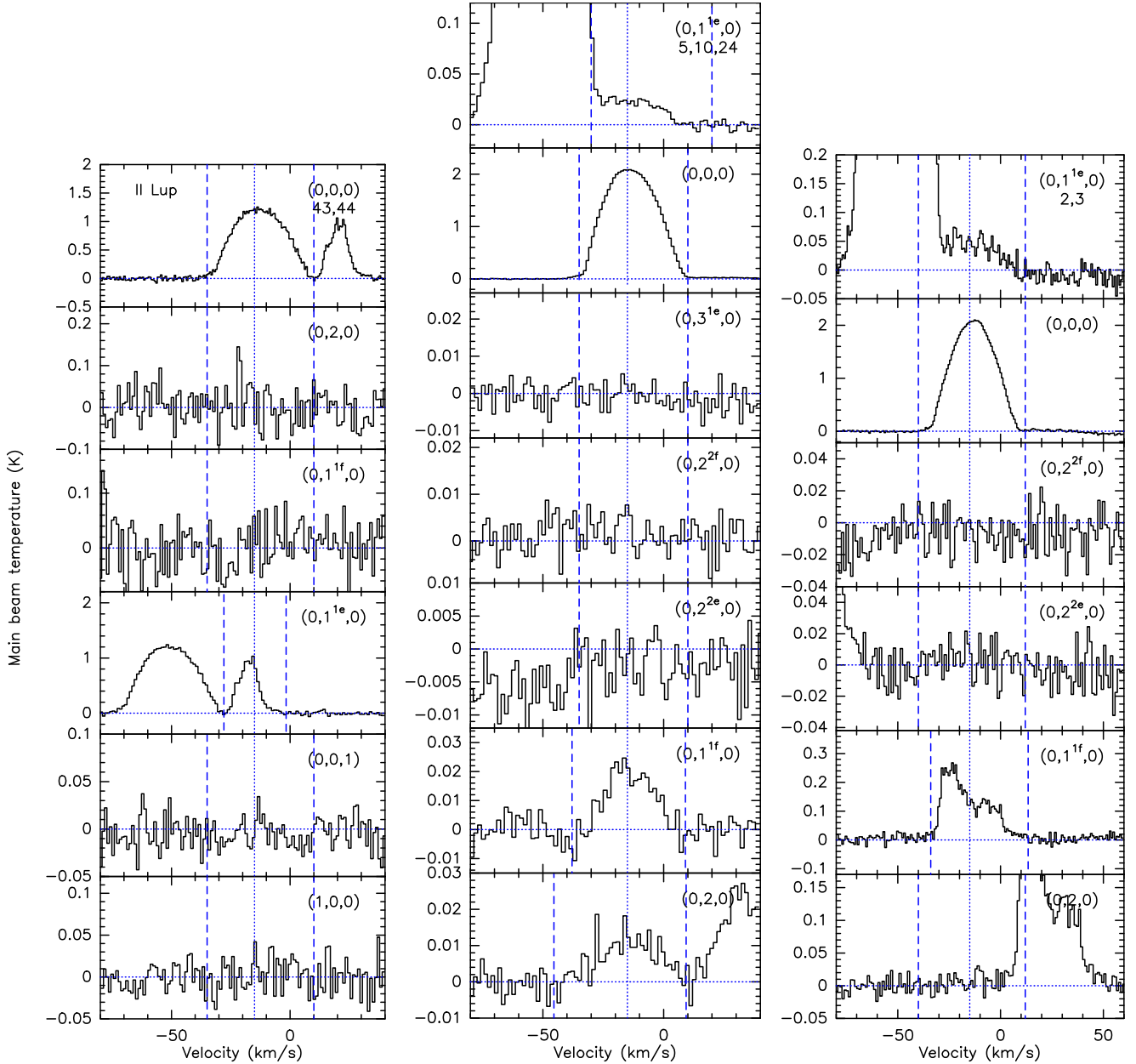


**Fig. 4.** Spectra for  $J = 2-1$  (left),  $3-2$  (centre) and  $4-3$  (right) transitions of HCN towards II Lup. The description of the figure is the same as in the Fig. 1 caption.

$1^{1f}, 0$ ) spectrum. Their corresponding flux densities are 14.3 Jy and 8.2 Jy, which are about four times the peak flux densities at the respective velocity positions of the  $J = 4-3$  ( $0, 1^{1e}, 0$ ) spectrum.

**R Vol.** No HCN masers were reported in this star prior to our observations. In R Vol, our observations result in the first detection of four HCN masers that are the  $J = 2-1$  ( $0, 1^{1e}, 0$ ),  $J = 2-1$  ( $0, 1^{1f}, 0$ ),  $J = 3-2$  ( $0, 1^{1e}, 0$ ), and  $J = 4-3$  ( $0, 1^{1e}, 0$ ) lines. The  $J = 2-1$ ,  $J = 3-2$ , and  $J = 4-3$  lines in the ( $0, 1^{1e}, 0$ ) state have peak flux densities of 8.4 Jy, 3.8 Jy, and 7.5 Jy at  $-12.9$ ,  $-14.5$ ,  $-11$  km s $^{-1}$ , respectively, which are much brighter than their corresponding transitions in the ( $0, 1^{1f}, 0$ ) state (see Fig. C.1). This is suggestive of their maser nature. Although the  $J = 2-1$  ( $0, 1^{1f}, 0$ ) line only has a flux density of 1.9 Jy, this line is still regarded as a maser in this work, because its velocity

coverage is much narrower than the ground state-line and the LSR velocity of its peak is slightly shifted to the blueshifted side at  $-13.2$  km s $^{-1}$ .

**AQ Sgr.** The  $J = 3-2$  ( $0, 1^{1e}, 0$ ) line has peak flux density of 1.2 Jy at 22.6 km s $^{-1}$ . Despite its low flux density, this line is brighter than the  $J = 3-2$  ( $0, 1^{1f}, 0$ ) line, which is not detected by the same sensitivity. Furthermore, the peak velocity is slightly redshifted with respect to the systemic velocity ( $\sim 20$  km s $^{-1}$ , see Fig. C.3). Therefore, the  $J = 3-2$  ( $0, 1^{1e}, 0$ ) line is regarded as a maser in this study, which makes it the first HCN maser towards this source.

**CRL 3068.** Two HCN masers are newly discovered in the source: the  $J = 2-1$  ( $0, 1^{1e}, 0$ ) and  $J = 4-3$  ( $0, 1^{1f}, 0$ ) masers. Asymmetric features indicate that these two transitions show maser actions (see Fig. C.4). The  $J = 2-1$  ( $0, 1^{1e}, 0$ ) maser

**Table 4.** Observed parameters derived from the SHELL method for the HCN rotational transitions in the ground vibrational state.

Source	$\Delta J$	$\int T_{\text{mb}} dV$ (K km s <sup>-1</sup> )	$V_{\text{exp}}$ (km s <sup>-1</sup> )	$V_{\text{LSR}}$ (km s <sup>-1</sup> )	Date obs.
IRC+10216	2–1	437.43 (5.21)	14.8 (1.5)	–23.6 (1.0)	36, 42
	3–2	706.15 (1.7)	14.7 (0.3)	–24.3 (0.2)	40
	4–3	553.62 (0.4)	14.4 (0.08)	–24.06 (0.0)	2, 45
RAFGL4211	2–1	21.89 (0.64)	17.86 (1.6)	–1.36 (3.14)	41, 42
	3–2	41.30 (0.05)	17.82 (0.19)	–1.93 (0.07)	5, 10, 11, 23
	4–3	47.83 (0.22)	17.45 (1.19)	–1.74 (1.02)	1, 3
II Lup	2–1	33.22 (0.8)	20.36 (1)	–12.76 (2.7)	43, 44
	3–2	57.00 (0.08)	20.42 (0.2)	–13.45 (0.0)	5, 10, 24
	4–3	54.58 (0.14)	20.02 (0.7)	–13.21 (0.32)	2, 3
R Vol	2–1	5.41 (0.1)	17.59 (1.2)	–9.06 (2.0)	36, 38, 42
	3–2	9.44 (0.06)	17.5 (0.9)	–9.97 (0.66)	31
	4–3	10.27 (0.04)	16.81 (0.07)	–9.99 (0.06)	12, 14, 27, 30, 45
Y Pav	2–1	0.45 (0.04)	9.1 (1.7)	–2.84 (3.5)	30
	3–2	0.39 (0.2)	7.1 (1.9)	–2.85 (4.6)	5, 7, 9, 24, 29
	4–3	0.39 (0.04)	5.7 (1.6)	–2.49 (0.69)	26–28
AQ Sgr	3–2	0.88 (0.01)	8.3 (1.1)	23.1 (1.1)	5, 6, 17, 21, 24
	4–3	2.9 (0.4)	6.7 (0.2)	24.5 (0.38)	14, 16
	2–1	18.42 (0.39)	13.35 (0.8)	–28.8 (1.6)	30, 36–38
CRL 3068	3–2	27.98 (0.13)	12.87 (0.5)	–29.4 (0.03)	4, 8, 17, 24
	4–3	33.48 (0.06)	12.57 (0.2)	–29.2 (0.05)	14–16, 34
	2–1	12.04 (0.21)	24.2 (3.2)	–10.5 (2.7)	40
IRC+30374	3–2	24.32 (0.13)	23.5 (1)	–10.9 (0.6)	5
	4–3	9.99 (0.12)	21.7 (0.8)	–10.7 (2.5)	25
	2–1	4.88 (0.06)	22.7 (1.6)	998 (1.9)	33, 37
V636 Mon	3–2	6.95 (0.03)	22.8 (0.8)	10.06 (0.7)	28
	4–3	7.92 (0.03)	21.5 (0.06)	10.56 (0.04)	12, 14, 20, 30
	2–1	8.94 (0.14)	13.7 (1.3)	1.36 (2.0)	31
IRC+20370	3–2	14.09 (0.07)	13.4 (0.5)	0.78 (0.45)	5, 10, 23, 24
	4–3	17.79 (0.16)	13.2 (1.7)	0.82 (0.73)	34
	2–1	2.21 (0.14)	11.42 (6.1)	1.10 (4.4)	32, 37
W Ori	3–2	4.67 (0.2)	10.60 (1.0)	0.3 (2.7)	4, 8–10, 21, 31
	4–3	5.55 (0.02)	10.53 (0.27)	0.7 (0.17)	12, 14, 19, 27, 35
	2–1	3.85 (0.29)	24.01 (8.2)	–13.98 (3.9)	37
S Aur	3–2	5.92 (0.13)	21.96 (1.3)	–14.76 (0.82)	24
	4–3	6.56 (0.06)	20.61 (0.3)	–14.64 (1.03)	13, 35
	3–2	4.44 (0.04)	6.9 (0.6)	55.04 (0.5)	5, 8, 22
V Aql	4–3	4.40 (0.03)	7.54 (0.54)	55.06 (0.3)	13, 14
	2–1	4.44 (0.06)	24.6 (2)	19.17 (0.2)	31, 37
	3–2	8.67 (0.11)	26.52 (2.9)	18.77 (2.4)	5, 8
CRL 2513	2–1	3.39 (0.13)	12.5 (1.4)	5.42 (1.35)	41
	3–2	6.88 (0.07)	18.8 (2.5)	6.92 (1.1)	17
	2–1	6.61 (0.1)	14.8 (2.3)	2.94 (1.5)	31, 32
RV Aqr	3–2	8.6 (0.18)	14.6 (0.4)	2.13 (1.8)	8, 9, 18
	4–3	10.8 (0.06)	13.58 (0.02)	2.3 (0.03)	15, 25, 27, 28

**Notes.** The last column refers to the identifier assigned to the date of the observation in 2018 of the corresponding transition towards the source. The dates in 2018 are in the format “DD Month”: 1 = 8 Jun, 2 = 2 Jul, 3 = 3 Jul, 4 = 4 Jul, 5 = 8 Jul, 6 = 11 Jul, 7 = 12 Jul, 8 = 13 Jul, 9 = 14 Jul, 10 = 15 Jul, 11 = 16 Jul, 12 = 3 Sep, 13 = 4 Sep, 14 = 5 Sep, 15 = 6 Sep, 16 = 7 Sep, 17 = 8 Sep, 18 = 9 Sep, 19 = 11 Sep, 20 = 12 Sep, 21 = 13 Sep, 22 = 15 Sep, 23 = 5 Oct, 24 = 6 Oct, 25 = 23 Nov, 26 = 24 Nov, 27 = 25 Nov, 28 = 26 Nov, 29 = 27 Nov, 30 = 28 Nov, 31 = 29 Nov, 32 = 30 Nov, 33 = 2 Dec, 34 = 6 Dec, 35 = 7 Dec, 36 = 9 Dec, 37 = 10 Dec, 38 = 11 Dec, 39 = 13 Dec, 40 = 14 Dec, 41 = 15 Dec, 42 = 16 Dec, 43 = 17 Dec, 44 = 18 Dec, 45 = 20 Dec.

displays five distinct peaks at  $-38.5 \text{ km s}^{-1}$ ,  $-35.3 \text{ km s}^{-1}$ ,  $-33.8 \text{ km s}^{-1}$ ,  $-29.4 \text{ km s}^{-1}$ , and  $-26.8 \text{ km s}^{-1}$ , and their corresponding peak flux densities are 12.9 Jy, 23.8 Jy, 18.2 Jy, 9.9 Jy, and 8.6 Jy, respectively. Stronger peaks are observed on the blueshifted side. They are at least four times higher than the

peak flux density of the  $J = 2-1$  ( $0, 1^{\text{lf}}, 0$ ) line. The  $J = 4-3$  ( $0, 1^{\text{lf}}, 0$ ) maser shows a prominent peak of flux density 70.6 Jy at  $-41.7 \text{ km s}^{-1}$ , which is brighter than any other transitions in the ( $0, 1^{\text{le}}, 0$ ) state, including even the  $J = 2-1$  ( $0, 1^{\text{le}}, 0$ ) maser. The  $J = 4-3$  ( $0, 1^{\text{lf}}, 0$ ) maser is about  $10 \text{ km s}^{-1}$  away from the

**Table 5.** Summary of our HCN line observations and the nature of detection.

(a) $J=2-1$										
$(\nu_1\nu_2\nu_3)$	000	01 <sup>1e</sup> 0	01 <sup>1f</sup> 0	020	001	03 <sup>1e</sup> 0	100			
$E_u$ (K)	13	1037	1037	2044	3030	3054	4777			
IRC +10216	th.	Maser	Maser	th.	th.	th.	n.d.			
RAFGL 4211	th.	Maser	n.d.	n.d.	n.d.	n.d.	n.d.			
II Lup	th.	Maser	n.d.	n.d.	n.d.	n.d.	n.d.			
R Vol	th.	Maser	Maser	n.d.	n.d.	n.d.	n.d.			
Y Pav	th.	n.d.	n.d.	n.d.	n.d.	n.d.	n.d.			
AQ Sgr	–	–	–	–	–	–	–			
CRL 3068	th.	Maser	th.	n.d.	n.d.	n.d.	n.d.			
IRC +30374	th.	bl.	n.d.	n.d.	n.d.	n.d.	n.d.			
V636 Mon	th.	Maser	n.d.	n.d.	n.d.	n.d.	n.d.			
IRC +20370	th.	Maser	n.d.	n.d.	n.d.	n.d.	n.d.			
W Ori	th.	Maser	n.d.	n.d.	n.d.	n.d.	n.d.			
S Aur	th.	Maser	n.d.	n.d.	n.d.	n.d.	n.d.			
V Aql	–	–	–	–	–	–	–			
CRL 2513	th.	n.d.	n.d.	n.d.	n.d.	n.d.	n.d.			
CRL 2477	th.	n.d.	n.d.	n.d.	n.d.	n.d.	n.d.			
RV Aqr	th.	Maser	Maser	n.d.	n.d.	n.d.	n.d.			
#sources det.	14	11	4	1	1	1	0			

(b) $J=3-2$										
$(\nu_1\nu_2\nu_3)$	000	01 <sup>1e</sup> 0	01 <sup>1f</sup> 0	020	02 <sup>2e</sup> 0	02 <sup>2f</sup> 0	001	03 <sup>1e</sup> 0	03 <sup>1f</sup> 0	100
$E_u$ (K)	26	1050	1050	2056	2078	2078	3042	3066	3067	4790
IRC +10216	th.	Maser+th.	Maser+th.	bl.	bl.	bl.	th.	th.	th.	bl.
RAFGL 4211	th.	bl.	th.	Maser	n.d.	n.d.	n.d.	Maser	n.d.	n.d.
II Lup	th.	bl.	th.	bl.	n.d.	n.d.	n.d.	n.d.	n.d.	n.d.
R Vol	th.	Maser	n.d.	n.d.	n.d.	n.d.	n.d.	n.d.	n.d.	n.d.
Y Pav	th.	n.d.	n.d.	n.d.	n.d.	n.d.	n.d.	n.d.	n.d.	n.d.
AQ Sgr	th.	Maser	n.d.	n.d.	n.d.	n.d.	n.d.	n.d.	n.d.	n.d.
CRL 3068	th.	th.	th.	th.	n.d.	n.d.	th.	n.d.	n.d.	n.d.
IRC +30374	th.	n.d.	n.d.	n.d.	n.d.	n.d.	n.d.	n.d.	n.d.	n.d.
V636 Mon	th.	n.d.	n.d.	n.d.	n.d.	n.d.	n.d.	n.d.	n.d.	n.d.
IRC +20370	th.	Maser	n.d.	n.d.	n.d.	n.d.	n.d.	n.d.	n.d.	n.d.
W Ori	th.	Maser	th.	n.d.	n.d.	n.d.	n.d.	n.d.	n.d.	n.d.
S Aur	th.	th.	n.d.	n.d.	n.d.	n.d.	th.	n.d.	n.d.	n.d.
V Aql	th.	Maser	n.d.	n.d.	n.d.	n.d.	n.d.	n.d.	n.d.	n.d.
CRL 2513	th.	n.d.	n.d.	n.d.	n.d.	n.d.	n.d.	n.d.	n.d.	n.d.
CRL 2477	th.	n.d.	n.d.	n.d.	n.d.	n.d.	n.d.	n.d.	n.d.	n.d.
RV Aqr	th.	Maser	n.d.	n.d.	n.d.	n.d.	n.d.	n.d.	n.d.	n.d.
#sources det.	16	11	5	4	1	1	3	2	1	1

(c) $J=4-3$										
$(\nu_1\nu_2\nu_3)$	000	01 <sup>1e</sup> 0	01 <sup>1f</sup> 0	020	02 <sup>2e</sup> 0	02 <sup>2f</sup> 0	03 <sup>1e</sup> 0	03 <sup>3e</sup> 0	03 <sup>3f</sup> 0	
$E_u$ (K)	43	1067	1067	2074	2095	2095	3083	3127	3127	
IRC +10216	th.	th.	Maser+th.	th.	bl.	bl.	th.	bl.	bl.	
RAFGL 4211	th.	Maser+th.	bl.	n.d.	n.d.	n.d.	n.d.	n.d.	n.d.	
II Lup	th.	bl.	Maser+th.	n.d.	n.d.	n.d.	n.d.	n.d.	n.d.	
R Vol	th.	Maser	n.d.	n.d.	n.d.	n.d.	n.d.	n.d.	n.d.	
Y Pav	th.	n.d.	n.d.	n.d.	n.d.	n.d.	n.d.	n.d.	n.d.	
AQ Sgr	th.	n.d.	n.d.	n.d.	n.d.	n.d.	n.d.	n.d.	n.d.	
CRL 3068	th.	th.	Maser+th.	th.	bl.	bl.	n.d.	n.d.	n.d.	
IRC +30374	th.	n.d.	n.d.	n.d.	n.d.	n.d.	n.d.	n.d.	n.d.	
V636 Mon	th.	n.d.	n.d.	n.d.	n.d.	n.d.	n.d.	n.d.	n.d.	
IRC +20370	th.	n.d.	n.d.	n.d.	n.d.	n.d.	n.d.	n.d.	n.d.	
W Ori	th.	Maser	th.	n.d.	n.d.	n.d.	n.d.	n.d.	n.d.	
S Aur	th.	n.d.	n.d.	n.d.	n.d.	n.d.	n.d.	n.d.	n.d.	
V Aql	th.	n.d.	n.d.	n.d.	n.d.	n.d.	n.d.	n.d.	n.d.	
CRL 2513	–	–	–	–	–	–	–	–	–	
CRL 2477	–	–	–	–	–	–	–	–	–	
RV Aqr	th.	th.	n.d.	n.d.	n.d.	n.d.	n.d.	n.d.	n.d.	
#sources det.	14	7	5	2	2	2	1	1	1	

**Notes.** “Maser”: maser emission, “th.”: thermal emission, “bl.”: blended line profile, “n.d.”: non-detection, “–”: transition not observed.

**Table 6.** Observed properties of detected HCN transitions in vibrationally excited states.

Source name	$J$	$(\nu_1, \nu_2, \nu_3)$	$\int T_{\text{mb}} dV$ (K km s <sup>-1</sup> )	$\Delta V$ (km s <sup>-1</sup> )	$V_{\text{LSR}}$ (km s <sup>-1</sup> )	$V_{\text{LSR}}$ range (km s <sup>-1</sup> )	Comments
IRC+10216	2–1	(0, 0, 1)	0.85 (0.03)	18.4 (2.5)	-28.7 (0.8)	[-37.3, -14.2]	maser
		(0, 1 <sup>1e</sup> , 0)	66.54 (0.06)	8.0 (0.0)	-27.6 (0.0)	[-37.7, -12.8]	
		(0, 3 <sup>1e</sup> , 0)	0.39 (0.05)	10.8 (1.6)	-26.3 (0.7)	[-36.8, -16.4]	
	3–2	(0, 1 <sup>1f</sup> , 0)	7.36 (0.06)	15.0 (0.1)	-26.2 (0.0)	[-44.0, -9.3]	maser
		(0, 2, 0)	1.42 (0.05)	12.6 (0.5)	-26.3 (0.2)	[-40.7, -13.8]	
		(1, 0, 0)	0.51 (0.06)	–	–	[-45.7, -12.8]	
	4–3	(0, 0, 1)	2.6 (0.03)	15.7 (0.5)	-26.4 (0.2)	[-40.7, -9.3]	maser + c
		(0, 1 <sup>1e</sup> , 0)	23.84 (0.3)	17.8 (0.6)	-25.04 (0.3)	[-42.7, -7.3]	
		(0, 3 <sup>1e</sup> , 0)	1.16 (0.05)	9.4 (0.6)	-26.9 (0.2)	[-38.0, -15.7]	
		(0, 2 <sup>2f</sup> , 0)	2.95 (0.05)	17.91 (1.2)	-28.3 (0.4)	[-34.4, -4.5]	blended <sup>(b)</sup>
		(0, 2 <sup>2e</sup> , 0)	2.05 (0.05)	18.43 (0.8)	-27.7 (0.4)	[-43.0, -23.0]	
		(0, 1 <sup>1f</sup> , 0)	20.24 (0.1)	16.52 (0.2)	-27.53 (0.08)	[-41.5, -8.5]	maser + c
		(0, 2, 0)	13.5 (0.07)	–	–	[-41.3, -8.8]	
		(0, 3 <sup>1f</sup> , 0)	0.65 (0.06)	9.3 (1.0)	-26.2 (0.5)	[-37.1, -17.3]	blended <sup>(d)</sup>
		(0, 1 <sup>1e</sup> , 0)	36.45 (0.08)	19.0 (0.05)	-24.8 (0.02)	[-42.0, -9.3]	
	(0, 3 <sup>1e</sup> , 0)	1.06 (0.07)	13.6 (1.4)	-24.12 (0.5)	[-36.1, -12.7]	blended <sup>(d)</sup>	
	(0, 2 <sup>2f</sup> , 0)	3.23 (0.09)	14.35 (0.6)	-25.6 (0.2)	[-36.6, -15.4]		
	(0, 2 <sup>2e</sup> , 0)	3.5 (0.08)	13.5 (0.5)	-26.5 (0.2)	[-37.3, -17.2]	maser + c	
(0, 1 <sup>1f</sup> , 0)	70.41 (0.12)	22.5 (0.04)	-25.4 (0.0)	[-42.8, 0.2]			
(0, 2, 0)	5.8 (0.09)	16.5 (0.4)	-23.9 (0.1)	[-39.5, -9.3]	blended <sup>(d)</sup>		
(0, 3 <sup>3e</sup> , 0)	1.10 (0.09)	11.6 (1.1)	-25.8 (0.5)	[-37.9, -15.8]			
(0, 3 <sup>3f</sup> , 0)	1.09 (0.1)	11.6 (1.1)	-25.8 (0.5)	[-39.6, -15.1]	blended <sup>(d)</sup>		
RAFGL4211	2–1	(0, 1 <sup>1e</sup> , 0)	7.66 (0.09)	8.97 (0.07)	-5.42 (0.03)	[-16.9, 10.5]	maser
	3–2	(0, 1 <sup>1e</sup> , 0)	0.62 (0.02)	–	–	[-20.0, 20.0]	blended <sup>(e)</sup>
		(0, 3 <sup>1e</sup> , 0)	0.28 (0.01)	0.89 (0.02)	-2.37 (0.01)	[-6.7, 2.9]	
	4–3	(0, 1 <sup>1f</sup> , 0)	0.51 (0.03)	24.30 (1.4)	-2 (0.7)	[-21.6, 27.8]	maser
		(0, 2, 0)	0.5 (0.02)	14.9 (1.7)	-3.4 (0.4)	[-31.6, 16.8]	
		(0, 1 <sup>1e</sup> , 0)	0.62 (0.02)	24.41 (0.9)	-5.83 (0.4)	[-5.7, -1.0]	maser + c
(0, 1 <sup>1f</sup> , 0)		1.82 (0.08)	26.7 (1.3)	-2.5 (0.6)	[-29.6, 30.9]		
II Lup	2–1	(0, 1 <sup>1e</sup> , 0)	9.71 (0.3)	9.3 (0.13)	-17.51 (0.06)	[-27.9, -1.7]	maser
	3–2	(0, 1 <sup>1e</sup> , 0)	0.82 (0.03)	–	–	[-30.0, 20.0]	blended <sup>(e)</sup>
		(0, 1 <sup>1f</sup> , 0)	0.43 (0.03)	20.06 (1.2)	-14.0 (0.6)	[-37.9, 9.0]	
	4–3	(0, 2, 0)	0.35 (0.03)	–	–	[-45.4, 9.3]	blended <sup>(c)</sup>
		(0, 1 <sup>1e</sup> , 0)	1.48 (0.07)	–	–	[-30.0, 12.0]	
		(0, 1 <sup>1f</sup> , 0)	5.27 (0.08)	25.6 (0.59)	-19.03 (0.25)	[-34.0, 13.4]	maser + c
R Vol	2–1	(0, 1 <sup>1e</sup> , 0)	0.86 (0.03)	3.85 (0.11)	-12.99 (0.05)	[-22.7, -1.4]	maser
		(0, 1 <sup>1f</sup> , 0)	0.19 (0.06)	5.06 (1.6)	-12.87 (0.49)	[-32.7, 0.0]	maser
	3–2	(0, 1 <sup>1e</sup> , 0)	0.25 (0.03)	4.8 (0.5)	-14.3 (0.23)	[-21.1, -8.7]	maser
	4–3	(0, 1 <sup>1e</sup> , 0)	0.25 (0.03)	4.2 (0.9)	-11.9 (0.3)	[-18.2, -6.2]	maser
AQ Sgr	3–2	(0, 1 <sup>1e</sup> , 0)	0.09 (0.01)	7.7 (1.3)	21.5 (0.5)	[13.4, 30.1]	maser
CRL 3068	2–1	(0, 1 <sup>1e</sup> , 0)	5.84 (0.02)	10.1 (0.04)	-34.1 (0.02)	[-46.6, -16.2]	maser
		(0, 1 <sup>1f</sup> , 0)	0.45 (0.03)	12.1 (0.9)	-29.4 (0.4)	[-40.3, -19.8]	
	3–2	(0, 0, 1)	0.19 (0.01)	16.1 (1.7)	-30.18 (0.8)	[-48.2, -14.8]	maser
		(0, 1 <sup>1e</sup> , 0)	1.31 (0.02)	15.5 (0.7)	-29.6 (0.4)	[-47.0, -16.0]	
		(0, 1 <sup>1f</sup> , 0)	1.25 (0.01)	14.36 (0.4)	-31.4 (0.03)	[-45.9, -17.1]	
	4–3	(0, 2, 0)	0.59 (0.02)	17.3 (0.8)	-30.7 (0.3)	[-45.5, -15.8]	blended <sup>(d)</sup>
		(0, 1 <sup>1e</sup> , 0)	3.0 (0.04)	15.9 (0.3)	-30.6 (0.1)	[-46.3, -15.5]	
		(0, 2 <sup>2f</sup> , 0)	0.44 (0.04)	13.8 (1.6)	-30.2 (0.7)	[-40.1, -20.6]	blended <sup>(d)</sup>
		(0, 2 <sup>2e</sup> , 0)	0.56 (0.04)	14.6 (1.3)	-31.0 (0.6)	[-40.1, -21.1]	
		(0, 1 <sup>1f</sup> , 0)	10.23 (0.03)	19.8 (0.1)	-34.8 (0.04)	[-45.9, -16.9]	maser + c
(0, 2, 0)	0.63 (0.05)	15.3 (1.2)	-31.1 (0.5)	[-50.0, -10.0]			
IRC+30374	2–1	(0, 1 <sup>1e</sup> , 0)	1.01 (0.1)	14.4 (2.4)	-15.8 (1.1)	[-24.4, -7.5]	blended <sup>(e)</sup>
V636 Mon	2–1	(0, 1 <sup>1e</sup> , 0)	0.2 (0.02)	5.1 (1.5)	6.2 (0.4)	[2.7, 12.7]	maser
IRC+20370	2–1	(0, 1 <sup>1e</sup> , 0)	1.14 (0.04)	5.7 (0.2)	-1.9 (0.08)	[-7.1, 5.08]	maser
	3–2	(0, 1 <sup>1e</sup> , 0)	0.86 (0.03)	8.3 (0.4)	-2.5 (0.15)	[-9.9, 6.1]	maser
W Ori	2–1	(0, 1 <sup>1e</sup> , 0)	1.84 (0.04)	4.25 (0.08)	-0.08 (0.03)	[-10.3, 8.3]	maser
	3–2	(0, 1 <sup>1e</sup> , 0)	2.03 (0.01)	6.04 (0.04)	-1.15 (0.01)	[-12.0, 9.6]	maser
		(0, 1 <sup>1f</sup> , 0)	0.13 (0.01)	5.71 (0.7)	-1.51 (0.23)	[-9.3, 7.6]	
	4–3	(0, 1 <sup>1e</sup> , 0)	0.53 (0.02)	6.19 (0.28)	-1.18 (0.12)	[-7.9, 8.3]	maser
(0, 1 <sup>1f</sup> , 0)	0.25 (0.03)	8.7 (1.0)	-1.25 (0.43)	[-10.3, 10.7]			
S Aur	2–1	(0, 1 <sup>1e</sup> , 0)	1.42 (0.07)	5.21 (0.2)	-16.61 (0.09)	[-25.0, -3.9]	maser
	3–2	(0, 1 <sup>1e</sup> , 0)	0.55 (0.07)	7.7 (2.3)	-16.88 (0.62)	[-25.9, -8.4]	
	(0, 0, 1)	0.024 (0.003)	0.19 (0.04)	-17.15 (0.02)	[-19.5, -15.1]		
V Aql	3–2	(0, 1 <sup>1e</sup> , 0)	0.4 (0.03)	5.0 (0.51)	55.31 (0.19)	[41.8, 62.0]	maser
RV Aqr	2–1	(0, 1 <sup>1e</sup> , 0)	1.11 (0.01)	4.02 (0.05)	-1.0 (0.02)	[-5.2, 7.6]	maser
		(0, 1 <sup>1f</sup> , 0)	0.17 (0.03)	3.1 (0.4)	-1.1 (0.2)	[-6.2, 5.5]	maser
	3–2	(0, 1 <sup>1e</sup> , 0)	1.09 (0.02)	3.63 (0.09)	-1.0 (0.03)	[-7.4, 4.8]	maser
	4–3	(0, 1 <sup>1e</sup> , 0)	0.53 (0.1)	7.3 (1.0)	-0.16 (0.4)	[-5.7, 4.0]	

**Notes.** The integrated intensities ( $\int T_{\text{mb}} dV$ ) are calculated by integrating over the intensities within the LSR velocity range of the detection, whereas the line widths ( $\Delta V$ ) and velocity centroids ( $V_{\text{LSR}}$ ) are obtained from a Gaussian fit. The last column gives our interpretation on the properties of the emission: ‘maser’ indicates that the line profile is dominated by maser emission; ‘maser + c’ indicates that the maser is contaminated with a thermal component; and ‘blended’ indicates that the line may be blended with another line. <sup>(a)</sup> $J = 3-2$  (1,0,0): potentially blended with another unspecified line (IRC +10216; Cernicharo et al. 2011). <sup>(b)</sup> $J = 3-2$  (0,2<sup>2e</sup>,0) and (0,2<sup>2f</sup>,0): two  $l$ -type doublet components blended with each other and multiple lines of C<sub>4</sub>H, C<sub>3</sub>N, and <sup>13</sup>CCCN (IRC +10216; He et al. 2017). <sup>(c)</sup> $J = 3-2$  (0,2,0): potentially blended with <sup>29</sup>SiS (15–14) at 267242.2178 MHz (IRC +10216 and II Lup; Cernicharo et al. 2011; He et al. 2017). <sup>(d)</sup>Two  $l$ -type doublet components blended with each other. <sup>(e)</sup> $\nu_2 = 1^{1e}$  line blended with the corresponding ground-state emission. <sup>(f)</sup> $J = 4-3$  (0, 1<sup>1f</sup>, 0): potentially blended with <sup>29</sup>SiS (20–19) at 356242.4290 MHz (RAFGL 4211 only).

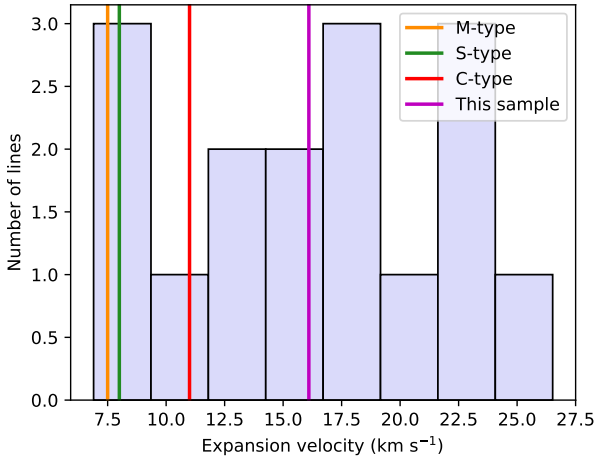


**Fig. 5.** Histogram distribution of expansion velocities derived from  $J = 3-2$  ground-state HCN lines. The magenta line marks the median for HCN  $J = 3-2$  from this work. The median values calculated by Ramstedt et al. (2009) towards M-type, S-type, and C-type stars are marked in orange, green, and red, respectively.

systemic velocity of  $-31.5 \text{ km s}^{-1}$ , but still does not reach its terminal velocity of  $14.5 \text{ km s}^{-1}$ .

**V636 Mon.** The  $J = 2-1 (0, 1^{1e}, 0)$  line is the only vibrationally excited HCN maser detected in V636 Mon. Its spectrum exhibits a narrow spike at  $5.7 \text{ km s}^{-1}$ , and its peak flux density is  $2.2 \text{ Jy}$  (see Fig. C.6). This line is at least three times the peak flux density of the  $J = 2-1 (0, 1^{1f}, 0)$  line. Furthermore, the narrow spike is about  $4 \text{ km s}^{-1}$  away from the systemic velocity. These two features support that the  $J = 2-1 (0, 1^{1e}, 0)$  line is a maser, which make it the first maser to be detected in V636 Mon.

**IRC +20370.** Two HCN masers from the  $J = 2-1 (0, 1^{1e}, 0)$  and  $J = 3-2 (0, 1^{1e}, 0)$  transitions are detected towards this source. Our results are the first maser detection towards this source. Both maser transitions are brighter than their corresponding lines in the  $(0, 1^{1f}, 0)$  state by a factor of roughly ten (see Fig. C.7). The  $J = 2-1 (0, 1^{1e}, 0)$  maser hosts two peaks at  $-4.6 \text{ km s}^{-1}$  and  $-2 \text{ km s}^{-1}$ , and their corresponding flux densities are  $6.7$  and  $7.3 \text{ Jy}$ . The  $J = 3-2 (0, 1^{1e}, 0)$  maser exhibits at least one peak at  $-4 \text{ km s}^{-1}$  with a flux density of  $7.1 \text{ Jy}$ , which is slightly weaker than the  $J = 2-1 (0, 1^{1e}, 0)$  maser. These velocity components are slightly blueshifted from the systemic velocity of  $-0.8 \text{ km s}^{-1}$ . The peak flux density at  $-4.6 \text{ km s}^{-1}$  is lower than that at  $-1.7 \text{ km s}^{-1}$  in the  $J = 2-1 (0, 1^{1e}, 0)$  maser, which is in stark contrast to the  $J = 3-2 (0, 1^{1e}, 0)$  maser. The different velocities indicate that these masers could arise from different zones or different pumping mechanisms.

**W Ori.** In this study, we report three new HCN masers from the  $J = 2-1 (0, 1^{1e}, 0)$ ,  $J = 3-2 (0, 1^{1e}, 0)$ , and  $J = 4-3 (0, 1^{1e}, 0)$  transitions that display single-peak profiles. Their maser nature is strongly supported by the fact that these three transitions have peak intensities about 20 times those of their corresponding  $(0, 1^{1f}, 0)$  transitions (see Fig. C.8). The respective LSR velocities of the three masers are around  $0.13 \text{ km s}^{-1}$ ,  $-1.1 \text{ km s}^{-1}$ , and  $-2.5 \text{ km s}^{-1}$ , while the corresponding flux densities are  $14.5 \text{ Jy}$ ,  $16 \text{ Jy}$ , and  $6.5 \text{ Jy}$ . All of these maser peaks are within  $3 \text{ km s}^{-1}$  away from the systemic velocity of  $-1.0 \text{ km s}^{-1}$ . W Ori has been found to host the HCN  $J = 1-0 (0, 0, 0)$  maser by spike emission at an LSR velocity of  $\sim 8 \text{ km s}^{-1}$  and shows

temporal variations in this maser (Olofsson et al. 1993; Izumiura et al. 1995). The LSR velocities indicate that our newly detected masers arise from the regions closer to the star when compared with the ground-state  $J = 1-0$  maser. Furthermore, the  $J = 2-1 (0, 1^{1e}, 0)$  maser is more luminous than the HCN  $J = 1-0 (0, 0, 0)$  maser.

**S Aur.** In this source, the  $J = 2-1 (0, 1^{1e}, 0)$  transition exhibits a narrow component with a high flux density of  $9.1 \text{ Jy}$  at  $-17.0 \text{ km s}^{-1}$  (see Fig. C.9). Its peak intensity is at least 30 times that of the  $J = 2-1 (0, 1^{1f}, 0)$  transition, and is even twice the peak intensity of the  $J = 2-1 (0, 0, 0)$  transitions. Furthermore, its line width is much narrower than that of the  $J = 3-2 (0, 1^{1e}, 0)$  transition. These facts support that the  $J = 2-1 (0, 1^{1e}, 0)$  transition is a maser, which is the first maser reported towards this source. We also tentatively detect the  $J = 3-2 (0, 0, 1)$  line exhibiting a peak intensity of  $8.5 \text{ Jy}$  with a very narrow line width of  $0.19 \text{ km s}^{-1}$ . The emission feature peaks close to the systematic velocity of  $-17 \text{ km s}^{-1}$ . Since this emission feature is only detected in two native spectral channels above the noise level, we conservatively do not identify it as a maser.

**V Aql.** The  $J = 3-2 (0, 1^{1e}, 0)$  transition is the only vibrationally excited HCN line detected in V Aql. This transition displays a single-peaked spectrum with a peak flux density of  $\sim 4.9 \text{ Jy}$  at  $55.4 \text{ km s}^{-1}$  (see Fig. C.10). The peak flux density is at least three times that of the  $J = 3-2 (0, 1^{1f}, 0)$  transition. Furthermore, the LSR velocity appears to be slightly redshifted with respect to the systemic velocity of  $53.5 \text{ km s}^{-1}$ . These facts support that the  $J = 3-2 (0, 1^{1e}, 0)$  transition is a maser, which is the first maser detected in V Aql.

**RV Aqr.** In this study, we report three new HCN masers from the  $J = 2-1 (0, 1^{1e}, 0)$ ,  $(0, 1^{1f}, 0)$ , and  $J = 3-2 (0, 1^{1e}, 0)$  transitions. Figure C.13 shows that the  $J = 2-1 (0, 1^{1e}, 0)$  and  $J = 3-2 (0, 1^{1e}, 0)$  transitions are at least ten times brighter than their corresponding  $(0, 1^{1f}, 0)$  transitions. Compared with the vibrationally ground-state lines, the  $J = 2-1 (0, 1^{1f}, 0)$  line, and also the two detected  $(0, 1^{1e}, 0)$  lines, have much narrower velocity spreads. Furthermore, their peak velocities are about  $-1 \text{ km s}^{-1}$ , which are blueshifted with respect to the systemic velocity of  $0.5 \text{ km s}^{-1}$ . Therefore, all three transitions are identified as masers in this work, which are the first maser detection in RV Aqr. Their flux densities are  $9.5 \text{ Jy}$ ,  $1.9 \text{ Jy}$ , and  $14.7 \text{ Jy}$  for the  $J = 2-1 (0, 1^{1e}, 0)$ ,  $(0, 1^{1f}, 0)$ , and  $J = 3-2 (0, 1^{1e}, 0)$  masers, respectively. On the other hand, the  $J = 4-3 (0, 1^{1e}, 0)$  transition is only slightly brighter than the  $J = 4-3 (0, 1^{1f}, 0)$  transition; the latter has a S/N of approximately two at the peak channel and does not formally meet our detection criteria. We conservatively do not identify the  $J = 4-3 (0, 1^{1e}, 0)$  transition as a maser in this work.

**Non-detection.** HCN masers are not detected towards Y Pav, IRC +30374, CRL 2513, or CRL 2477 in our observations. Hence, we are only able to give a  $3\sigma$  upper limit of  $0.9 \text{ Jy}$ ,  $1.8 \text{ Jy}$ ,  $0.8 \text{ Jy}$ , and  $2.6 \text{ Jy}$  for the  $J = 2-1 (0, 1^{1e}, 0)$  transitions towards Y Pav, IRC +30374, CRL 2513, and CRL 2477, respectively. Among these sources, we note that the HCN  $J = 1-0 (0, 2, 0)$  maser was detected towards CRL 2513 by Lucas et al. (1988), but the higher rotational transitions ( $J = 2-1$  and  $J = 3-2$ ) in the  $(0, 2, 0)$  state are not detected in this work (see Fig. C.11).

In summary, the  $J = 2-1 (0, 1^{1e}, 0)$  maser is detected towards 12 out of 16 sources. The detection rate of 75% is similar to that of the previous  $J = 2-1 (0, 1^{1e}, 0)$  maser study (85%; Menten et al. 2018) and is much higher than that of the

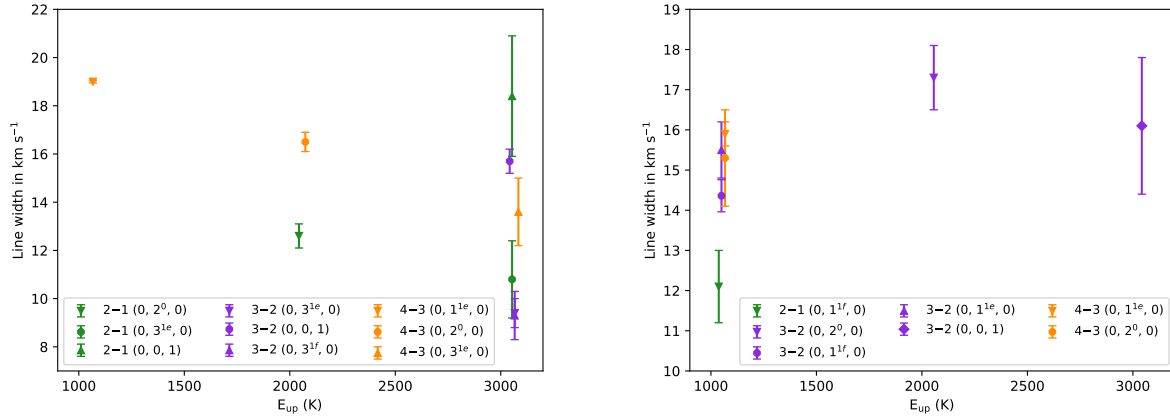


**Fig. 6.** FWHM line widths as a function of upper energy levels for IRC +10216 (left) and CRL 3068 (right). The colours represent the rotational transitions and the symbols represent the various thermal vibrationally excited lines, as indicated in the legends.

$J = 1-0 (0, 2, 0)$  maser in carbon-rich stars (7%; Lucas et al. 1988). This suggests that the  $J = 2-1 (0, 1^{1e}, 0)$  maser is more common than the  $J = 1-0 (0, 2, 0)$  maser in carbon-rich stars.

The peak flux density of the  $J = 2-1 (0, 1^{1e}, 0)$  maser is brighter than that of the  $J = 2-1 (0, 0, 0)$  line in W Ori and S Aur, while the peak flux densities of these two lines are comparable in RAFGL 4211, R Vol, and RV Aqr. In contrast, the  $J = 2-1 (0, 1^{1f}, 0)$  masers are much weaker and are only detected in three sources. The  $J = 3-2 (0, 1^{1e}, 0)$  maser is detected towards seven sources. The flux density of the  $J = 3-2 (0, 1^{1e}, 0)$  maser is much lower than that of the  $J = 2-1 (0, 1^{1e}, 0)$  maser towards IRC +10216 and R Vol, but is roughly comparable to that of the  $J = 2-1 (0, 1^{1e}, 0)$  maser towards IRC +20370, W Ori, and RV Aqr. The  $J = 4-3 (0, 1^{1f}, 0)$  masers are only detected in IRC +10216, CRL 3068, and II Lup, and all are found to show a prominent blueshifted component with a peak at  $\sim 10 \text{ km s}^{-1}$  from their systemic LSR velocities.

Moreover, we find that none of the detected HCN maser peaks reach the terminal velocities, suggesting that these HCN masers arise from shells that are not yet fully accelerated. This supports the notion that these masers can be used to investigate the wind acceleration of carbon-rich stars. Furthermore, most of the bright HCN maser components appear on the blueshifted side with respect to their respective systemic LSR velocities, which may be attributed to their underlying pumping mechanisms (see Sect. 5.2).

#### 4.3. Time variability of HCN masers

Three of our targets, IRC +10216, II Lup, and RAFGL 4211, have been observed in the  $J = 2-1 (0, 1^{1e}, 0)$  and  $J = 2-1 (0, 1^{1f}, 0)$  lines at least twice in previous works (Lucas & Cernicharo 1989; Menten et al. 2018), allowing us to study the time variability of the HCN masers. Figure 7 presents the HCN masers obtained at different epochs on a flux density scale. It can be seen that the line shape of the  $J = 2-1 (0, 1^{1e}, 0)$  line has changed significantly over time. For IRC +10216, the spectra of the  $(0, 1^{1e}, 0)$  line show four peaks at  $-32.6 \text{ km s}^{-1}$ ,  $-29.8 \text{ km s}^{-1}$ ,  $-25.1 \text{ km s}^{-1}$ , and  $-22.6 \text{ km s}^{-1}$  in 1989, two peaks at  $-33 \text{ km s}^{-1}$ , and  $-27.2 \text{ km s}^{-1}$  in 2015, three peaks at about  $-32.2 \text{ km s}^{-1}$ ,  $-26.3 \text{ km s}^{-1}$ , and  $-27.9 \text{ km s}^{-1}$  in 2018, and five peaks at  $-33.5 \text{ km s}^{-1}$ ,  $-32.1 \text{ km s}^{-1}$ ,  $-29.7 \text{ km s}^{-1}$ ,  $-26.7 \text{ km s}^{-1}$ , and  $-24.1 \text{ km s}^{-1}$  in 2021 (see the top left panel in Fig. 7).

Towards II Lup, this line shows two peaks at  $-23.6 \text{ km s}^{-1}$  and  $-15.9 \text{ km s}^{-1}$  in 2015, three peaks at  $-22.6 \text{ km s}^{-1}$ ,  $-18.3 \text{ km s}^{-1}$ , and  $-15.1 \text{ km s}^{-1}$  in 2018, and two peaks again in 2021 at  $-25.1 \text{ km s}^{-1}$  and  $-15.3 \text{ km s}^{-1}$  (see the bottom left panel in Fig. 7). Similarly, RAFGL 4211 shows three peaks at  $-8.2 \text{ km s}^{-1}$ ,  $-5.1 \text{ km s}^{-1}$ , and  $-3.7 \text{ km s}^{-1}$  in 2018, two peaks at  $-5.1 \text{ km s}^{-1}$  and  $-2.9 \text{ km s}^{-1}$  in 2015, and three peaks in 2021 at  $-9.7 \text{ km s}^{-1}$ ,  $-3.7 \text{ km s}^{-1}$ , and  $-2.6 \text{ km s}^{-1}$  (see the bottom right panel in Fig. 7).

Based on the measurements of the ground-state HCN lines, we note that there might be about a 50% uncertainty in flux calibration. In order to minimise the effect of calibration uncertainty, we used the integrated intensity *ratio* between the maser line and the ground-state  $J = 2-1 (0, 0, 0)$  line to assess the temporal variation between the three epochs of APEX observations (2015–2021). For IRC +10216, the ratio changes from 0.16  $\rightarrow$  0.15  $\rightarrow$  0.28, suggesting that the flux density significantly increased between 2018 and 2021 ( $\approx 86\%$ ). For II Lup, the ratio changes from 0.28  $\rightarrow$  0.35  $\rightarrow$  0.20, indicative of a 25% increase in the flux density of the  $(0, 1^{1e}, 0)$  maser between 2015 and 2018, but a 42% decrease between 2018 and 2021. For RAFGL 4211, the ratio increases from 0.16  $\rightarrow$  0.25  $\rightarrow$  0.36, indicating that the flux density of the  $(0, 1^{1e}, 0)$  maser increased by 63% in the first two epochs and by 44% in the last two. These suggest that the HCN  $J = 2-1 (0, 1^{1e}, 0)$  masers are variable in the three sources over a timescale of a few years. In contrast, as shown in the top right panel in Fig. 7, the weaker HCN  $J = 2-1 (0, 1^{1f}, 0)$  maser is not quite as variable over the 3 yr in IRC +10216. The spectral profiles are comparable between the three epochs and the intensity ratio between the  $(0, 1^{1f}, 0)$  and  $(0, 0, 0)$  lines only changes by  $\leq 10\%$ . However, it is worth noting that the most significant variation in the  $J = 2-1 (0, 1^{1e}, 0)$  transition happened over a longer period in time, from 1989 to 2015 (see Sect. 6.3.4 in Menten et al. 2018).

Although the time variability of HCN masers is confirmed by our study, observations are too sparse to allow for a search for periodic variations or for association with stellar pulsation periods. Previous monitoring observations of the HCN  $J = 3-2 (0, 1^{1f}, 0)$  maser in IRC +10216 indicate a period of  $\sim 730$  days (He et al. 2017), which is at least 100–200 days longer than the periods in the infrared ( $\sim 630 \pm 3$  days; Le Bertre 1992; Menten et al. 2012) and centimetre bands ( $535 \pm 50$  days; Menten et al. 2006). An anti-correlation between HCN maser luminosity and infrared luminosity was found in their single-dish observations (He et al. 2017), but was not confirmed by the

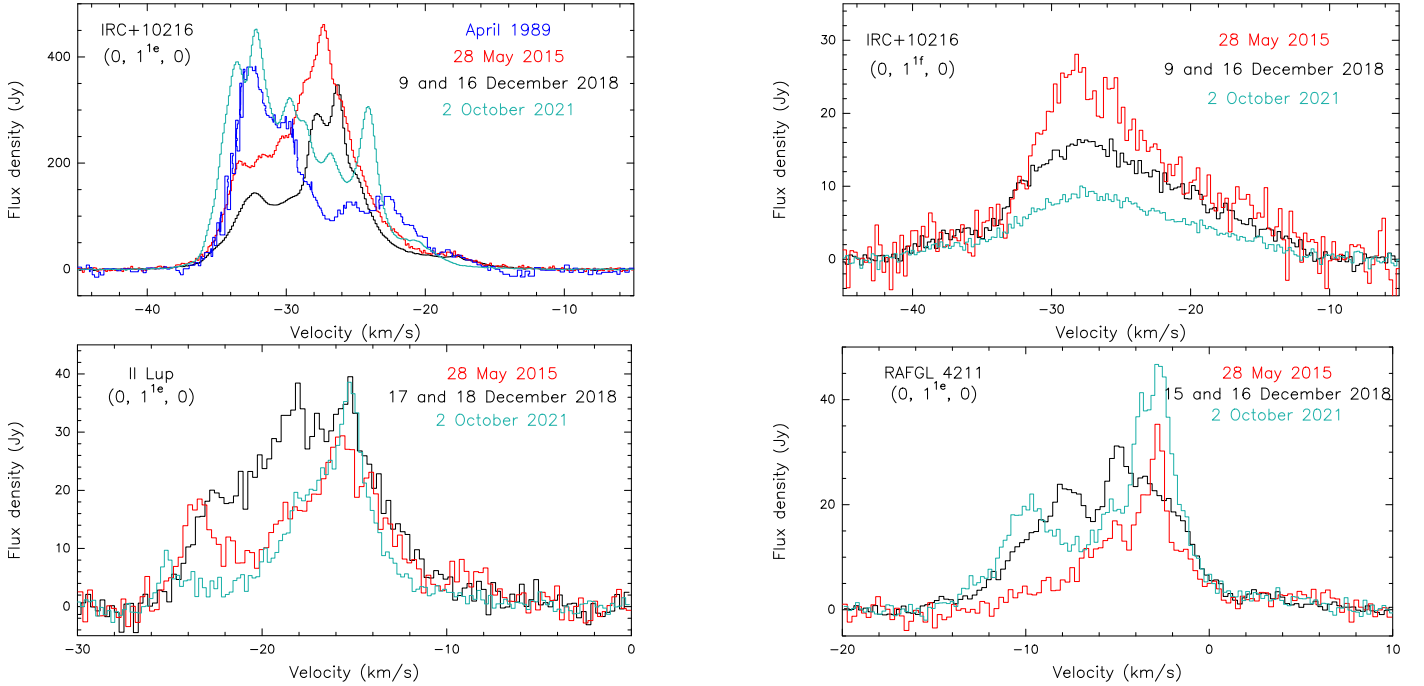


**Fig. 7.** Variability of HCN (2–1) masers seen towards IRC+10216 (top two panels) in  $(0, 1^{1e}, 0)$  and  $(0, 1^{1f}, 0)$ , II Lup (*bottom left*) and RAFGL 4211 (*bottom right*) in  $(0, 1^{1e}, 0)$  vibrationally excited lines. The black spectra are from observations in 2018, cyan spectra are from 2021, red spectra are from Menten et al. (2018), and blue spectra are from Lucas & Cernicharo (1989) with the date of observations indicated in the legend.

follow-up monitoring observations with the Atacama Compact Array (He et al. 2019). Previous observations towards RAFGL 4211 indicate that the variability of the HCN  $J = 1-0$   $(0, 2, 0)$  maser may be unrelated to stellar pulsation, although the observations consisted of only three epochs (Smith et al. 2014). Menten et al. (2018) suggest that the apparent absence of correlation between the vibrationally excited HCN lines emission cycle and the stellar cycle may arise from the additional contribution of collisional pumping. Further long-term monitoring observations with higher cadences and consistent flux calibration are needed to identify the exact cause(s) of the time variability of HCN masers, such as inhomogeneity in the outflowing wind or a highly anisotropic infrared field.

## 5. Discussion

### 5.1. Population diagram

The vibrationally excited HCN lines detected in our observations occupy energy levels above 1000 K (see Table 2). Their spectra, including those of the thermal lines, cover narrow velocity ranges (see Table 6), suggesting that they most likely arise from a hot region where the stellar outflow has not reached its terminal velocity (i.e. close to the stellar surface; Menten et al. 2018). In order to better constrain the properties of the region traced by these transitions, we take advantage of the population-diagram method to estimate the HCN excitation temperature and column density. Assuming LTE conditions and low opacities for the thermal emission of vibrationally excited HCN, we can use the standard formula to derive HCN column density and excitation temperature (e.g. Goldsmith & Langer 1999):

$$N_u/g_u = \frac{N_{\text{tot}}}{Q(T_e)} e^{-E_u/T_e} = \frac{3k \int T_{\text{mb}} dV}{8\pi^3 \nu \mu^2 S_{\text{ul}}}, \quad (1)$$

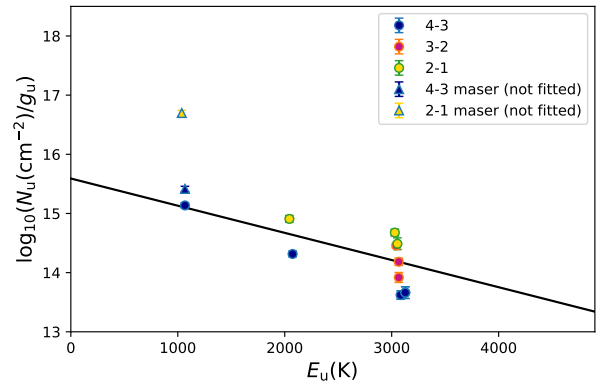


**Fig. 8.** Rotation diagram of IRC+10216 constructed from vibrationally excited HCN lines. Some masers are also plotted in the diagram, shown by triangles, but are excluded from the linear least-square fit.

where  $N_{\text{tot}}$  is the HCN column density,  $Q(T_e)$  is the partition function at the excitation temperature  $T_e$ ,  $\int T_{\text{mb}} dV$  is the velocity-integrated intensity,  $k$  is the Boltzmann constant,  $\nu$  is the transition's rest frequency,  $\mu$  is the permanent dipole moment of HCN, and  $S_{\text{ul}}$  is the line strength. We obtained the values of  $Q$ ,  $\nu$ , and  $S_{\text{ul}}\mu^2$  from CDMS (Müller et al. 2005) via Splatalogue<sup>6</sup> (see also Table 2). Since the emitting size of vibrationally excited HCN lines should be small, we should correct the observed integrated intensities by dividing by the beam dilution factor,  $\frac{\theta_s^2}{\theta_s^2 + \theta_b^2}$ , where  $\theta_s$  and  $\theta_b$  are the source size and FWHM beam size, respectively. However, the source size is still not well constrained. The eSMA observations suggest that the vibrationally excited HCN  $J = 3-2$   $(0, 1^{1e}, 0)$  emission can be as extended as

<sup>6</sup> <https://splatalogue.online/advanced.php>

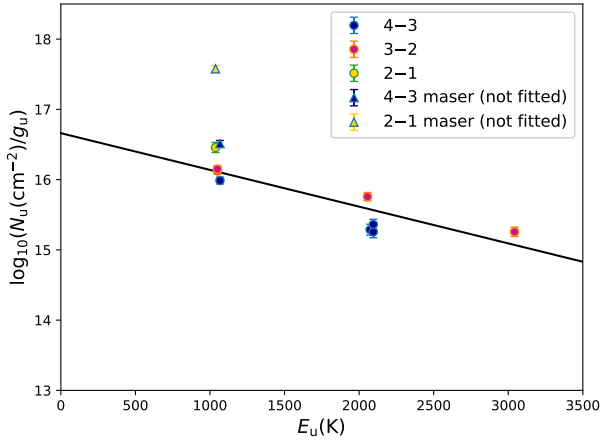


**Fig. 9.** Rotation diagram of CRL 3068. The description of the figure is the same as in the caption of Fig. 8.

**Table 7.** Column densities and excitation temperatures derived from the population diagram method.

Source	$\theta_s$ (")	$T_e$ (K)	$N_{\text{tot}}$ ( $\text{cm}^{-2}$ )
(1)	(2)	(3)	(4)
IRC +10216	0.20	$946 \pm 282$	$(1.2 \pm 0.9) \times 10^{19}$
CRL 3068	0.02	$830 \pm 163$	$(10.8 \pm 4.3) \times 10^{19}$
II Lup	0.04	700	$(1.7 \pm 0.1) \times 10^{19}$
W Ori	0.06	700	$(1.8 \pm 0.1) \times 10^{18}$
S Aur	0.02	700	$(3.3 \pm 0.4) \times 10^{19}$
RAFGL 4211	0.03	700	$(5.2 \pm 0.1) \times 10^{19}$

**Notes.** (1) Source name. (2) Assumed source size. (3) Excitation temperature. The excitation temperature is fitted for IRC +10216 and CRL 3068, while the excitation temperature assumed to be 700 K for the other sources. (4) Source-averaged HCN column density.

1'' in IRC +10216 (see Fig. 7 in Shinnaga et al. 2009) but with double peaks. Our assumption was to adopt a Gaussian FWHM source size of  $\theta_s = 0.2''$  ( $\sim 28$  au) towards IRC +10216. Assuming the physical size to be the same as that of IRC +10216, we can estimate the source sizes for the other sources according to their distances in Table 1. The assumed angular source sizes are given in Table 7.

In order to fit the population diagrams, at least two transitions covering a large enough energy range are needed to meaningfully derive the excitation temperature and column density. Because a large number of vibrationally excited HCN transitions are found to show maser action for which LTE conditions do not hold (see Sect. 4.2.2), linear least-square fits can only be applied to two sources: IRC +10216 and CRL 3068. In the case of IRC +10216, we included lines that are blended with each other:  $(0, 3^{3e}, 0)$  and  $(0, 3^{3f}, 0)$ . Assuming LTE conditions, these two lines are expected to show nearly identical integrated intensities. We therefore used half the intensities integrated over the velocity range covered by the two lines for our analysis. Excluding the maser lines and other blended lines, we performed the linear least-square fits to the two sources. The results are shown in Figs. 8–9. In each of these plots, we display, without fitting, the data points of two masers,  $J = 2-1$  ( $0, 1^{1e}, 0$ ) and  $J = 4-3$  ( $0, 1^{1f}, 0$ ). The  $J = 2-1$  ( $0, 1^{1e}, 0$ ) maser lies above the fitted lines in both plots, indicating the highly non-thermal nature of its emission. The  $J = 4-3$  ( $0, 1^{1f}, 0$ ) maser is weaker than the

$J = 2-1$  ( $0, 1^{1e}, 0$ ) maser because its maser component only contributes a small fraction to the total integrated intensity of the transition (see Fig. 1 and Sect. 4.2.2 for more information). The fitted excitation temperatures and HCN column densities from the population diagrams are given in Table 7.

In the range of  $\theta_s = 0.1''-1''$ , we note that the derived HCN column densities are largely dependent on the assumed source size with a relationship of  $N_{\text{tot}} \propto 1/\theta_s^2$ , that is, the derived HCN column densities can vary by at most a factor of 100. On the other hand, the excitation temperature is not sensitive to the adopted value of  $\theta_s$ . The excitation temperatures of the two sources are consistent, within uncertainties, with the  $T_{\text{ex}}$  range of 452–753 K as derived from *Herschel* observations of eight other carbon-rich stars (Nicolae et al. 2018) and the  $T_{\text{ex}}$  values of IRC +10216 ( $T_{\text{ex}} = 1000$  K, Schilke et al. 2000;  $T_{\text{ex}} = 410-2465$  K, Cernicharo et al. 2011). We also note that Cernicharo et al. (2011) defined three different zones in their population diagram of IRC +10216, based on the upper energy levels of HCN lines. The  $T_{\text{ex}}$  value in IRC +10216 derived by our single-component fitting is higher than that of Zone III ( $410 \pm 60$  K;  $E_u \leq 2000$  K), but slightly lower than that of Zone II ( $1240 \pm 210$  K;  $2000 < E_u \leq 5000$  K), probably because we fit HCN lines from both zones. Some of our identified thermal lines might in fact show (weak) maser actions because their column densities tend to deviate from other transitions of similar energies in the population diagrams (Figs. 8–9). However, they are not easily identified from their line profiles alone. This may lead to an overestimation of the HCN excitation temperature. Comparing the kinetic temperature model in IRC +10216 (e.g. Fig. 1 in Agúndez et al. 2012), we infer that the vibrationally excited HCN line-emitting regions have a size of  $< 20R_*$  ( $0''.4$ ), where the stellar radius,  $R_*$ , is 22 mas (Monnier et al. 2000). Our assumed source size of  $0''.2$  for IRC +10216 is consistent with this inferred size.

For the other four stars with vibrationally excited HCN lines but without a broad coverage of line excitation energy, we derived their HCN column densities by fixing the excitation temperature to be 700 K, which is a representative value among the results from *Herschel* data (452–753 K; Nicolae et al. 2018) and our fitting. The associated uncertainties in column density were derived by Monte Carlo analysis with 10 000 simulations. A Gaussian function was used to fit the resulted distribution, and the standard deviation of the Gaussian distribution was regarded as the  $1\sigma$  error. The results are shown in Table 7. The derived source-averaged HCN column densities range from  $0.18-10.8 \times 10^{19} \text{ cm}^{-2}$ . Among these sources, W Ori has the lowest source-averaged column density, likely due to its lowest mass-loss rate of  $\sim 3.1 \times 10^{-7}$ . We note that the uncertainties in the adopted source sizes can lead to even larger uncertainties than those shown in Table 7.

Based on the model of IRC +10216 (e.g. Fig. 1 in Agúndez et al. 2012), the  $\text{H}_2$  number density is about  $2 \times 10^8 \text{ cm}^{-3}$  at the radius of  $0.2''$  (i.e.  $4 \times 10^{14} \text{ cm}$ ), corresponding to a  $\text{H}_2$  column density of  $1.6 \times 10^{23} \text{ cm}^{-2}$ . The HCN abundance with respect to  $\text{H}_2$  is thus determined to be  $(7.4 \pm 5.5) \times 10^{-5}$ . The HCN abundance is roughly consistent with previous estimates of HCN abundances in carbon-rich stars (Fonfría et al. 2008; Schöier et al. 2013), but it seems to be much higher than the prediction ( $< 3 \times 10^{-6}$  at  $r > 5R_*$ ) in the non-equilibrium chemical model (Cherchneff 2006). However, we also note that the derived HCN abundance largely relies on the assumptions, such as the emission source size, which can result in large uncertainties in the estimated HCN column density and, therefore, its abundance.

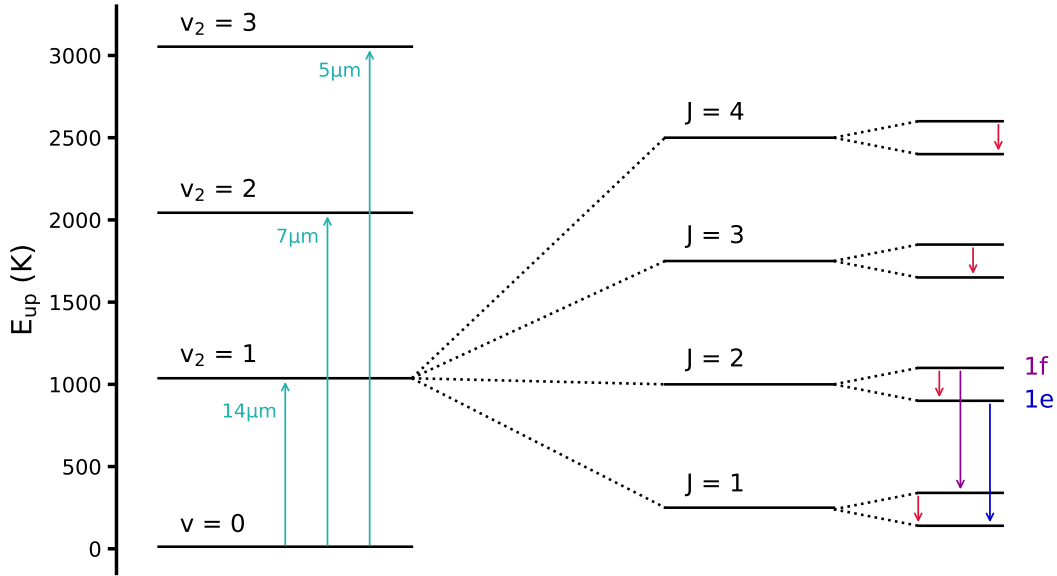


**Fig. 10.** Energy diagram of HCN. The quantum numbers,  $v$  and  $J$ , indicate the vibrational state and rotational state, respectively.  $l$ -type doubling causes the splitting of every rotational level into two sub-levels,  $1e$  and  $1f$ , which are also denoted in this figure. Pumping photons from the ground state to highly vibrationally excited states are indicated by cyan arrows. The  $J = 2-1$  ( $0, 1^{1e}, 0$ ) and  $J = 2-1$  ( $0, 1^{1f}, 0$ ) transitions are indicated by the blue and purple arrows, respectively. The direct  $l$ -type transitions are marked by red arrows. We note that the separations of the  $l$ -type doublets are not drawn to scale.

## 5.2. Pumping mechanism of HCN masers

Vibrationally excited HCN masers are generally thought to be explained by pumping through infrared radiations (e.g. Lucas & Cernicharo 1989; Menten et al. 2018). Our detected HCN masers are found in the excited states of the bending mode:  $v_2 = 1^{1e}$  or  $1^{1f}$ ,  $v_2 = 2$ , and  $v_2 = 3^{1e}$  (Sect. 4.2.2). As illustrated in the energy level diagram in Fig. 10, pumping HCN molecules from the ground state to these excited states requires infrared photons at  $14 \mu\text{m}$ ,  $7 \mu\text{m}$ , and  $5 \mu\text{m}$ , respectively (see Fig. 10). Following Menten et al. (2018), we extended the comparison between the isotropic maser luminosities,  $L_M$ , and the corresponding infrared luminosities,  $L_{\text{IR}}$ , towards all detected HCN masers, as shown in Table 8. Their luminosity ratios,  $L_{\text{IR}}/L_M$ , should be more reliable than their luminosities because the ratios are independent of the assumed distances. We find that the luminosity ratios are much greater than 50 for all the detected HCN masers. The infrared flux densities are based on the WISE and IRAS measurements at  $4.6 \mu\text{m}$  and  $12 \mu\text{m}$  (Abrahamyan et al. 2015), but not at the exact wavelengths of HCN vibrational excitation of  $14 \mu\text{m}$ ,  $7 \mu\text{m}$ , and  $5 \mu\text{m}$ . While this adds to the uncertainties in the derived luminosity ratios  $L_{\text{IR}}/L_M$ , Menten et al. (2018) suggest that the flux densities at  $7 \mu\text{m}$  and  $14 \mu\text{m}$  are within a factor of two of the  $12\text{-}\mu\text{m}$  flux density based on the SED towards IRC +10216. Hence, our conclusion is still robust because the luminosity ratios are much higher than two.

The fact that the amount of IR pumping photons is much more than adequate to account for HCN masers indicates that all these masers are unsaturated. The unsaturated nature of detected HCN masers is also supported by their brightness temperature estimates. Assuming a typical maser emission size of  $28 \text{ au}$  ( $\sim 0''.2$  for IRC +10216; Sect. 5.1), the brightness temperatures of these masers are roughly  $1000\text{--}300\,000 \text{ K}$ . The map of the HCN  $J = 3-2$  ( $0, 1^{1e}, 0$ ) emission indicates that the maser can have a smaller emission size of  $<0''.2$  towards IRC+10216 (Shinnaga et al. 2009), which would lead to a higher estimate in

brightness temperature. Accounting for the fact that the brightness temperature increases quadratically with decreasing source size and that the emission size may vary in other sources or transitions, the maser brightness temperatures are still too low to reach their saturation levels, even if we assume a source size that is ten times smaller. Unsaturated masers tend to vary on much shorter timescales than saturated masers due to their exponential amplification behaviour. This may explain the observed temporal variability on a relative short timescale of a few years (Sect. 4.3).

Most of the bright HCN maser components appear on the blueshifted side of their spectra with respect to their systemic LSR velocities. This may be explained by having the maser-emitting regions in the front of the stars, assuming an expanding outflow. The observed blueshifted maser may arise from the ‘radial’ amplification of background photospheric emission. This scenario has been invoked to account for the observed blueshifted SiS ( $1-0$ ) maser in IRC +10216 (Gong et al. 2017). Stellar occultation may cause maser emission arising from the far side of the star to be partially blocked. Alternatively, the blueshift velocities of certain narrow maser profiles are not really significant and the maser spikes appear to peak very close to the systemic velocity. Prominent examples include RAFGL 4211, W Ori, and S Aur. These masers may be better interpreted as ‘tangential’ amplification, where the emission region is on the plane of sky beside the central star. This scenario requires an outward-accelerating velocity field and has been proposed to explain the detection of strong SiO masers near the systemic velocity in oxygen-rich stars (Bujarrabal & Nguyen-Q-Rieu 1981).

The  $J = 2-1$  ( $0, 1^{1e}, 0$ ) transition is the brightest HCN maser in our observations (see Sect. 4.2.2). This could arise from the fact that the Einstein  $A$  coefficient strongly depends on the rotational quantum number  $J$ . The HCN molecules rapidly decay to the lower- $J$  levels, and are likely to accumulate at the lowest- $J$  levels. Direct  $l$ -type transitions have been detected in emission towards different carbon-rich stars (e.g. Thorwirth et al. 2003; Cernicharo et al. 2011). Emission from direct  $l$ -type transitions

**Table 8.** Comparison of detected HCN masers and corresponding infrared photon luminosities.

Source	$J$	$(\nu_1, \nu_2, \nu_3)$	$S_{\text{IR}}$ (Jy)	$L_{\text{IR}}$ ( $\text{s}^{-1}$ )	$L_{\text{M}}$ ( $\text{s}^{-1}$ )	$L_{\text{IR}}/L_{\text{M}}$
(1)	(2)	(3)	(4)	(5)	(6)	(7)
IR = 12 $\mu\text{m}$ vs. 14 $\mu\text{m}$						
IRC +10216	2–1	(0, 1 <sup>1e</sup> , 0)	$4.75 \times 10^4$	$1.4 \times 10^{46}$	$2.6 \times 10^{43}$	531
	2–1	(0, 1 <sup>1f</sup> , 0)	$4.75 \times 10^4$	$1.9 \times 10^{46}$	$2.9 \times 10^{42}$	6745
	3–2	(0, 1 <sup>1e</sup> , 0)	$4.75 \times 10^4$	$1.8 \times 10^{46}$	$9.3 \times 10^{42}$	1950
RAFGL 4211	4–3	(0, 1 <sup>1f</sup> , 0)	$4.75 \times 10^4$	$2.4 \times 10^{46}$	$2.8 \times 10^{43}$	874
	2–1	(0, 1 <sup>1e</sup> , 0)	$7.93 \times 10^2$	$1.2 \times 10^{46}$	$1.4 \times 10^{44}$	85
	4–3	(0, 1 <sup>1e</sup> , 0)	$7.93 \times 10^2$	$2.0 \times 10^{45}$	$1.1 \times 10^{43}$	181
II Lup	2–1	(0, 1 <sup>1e</sup> , 0)	$1.32 \times 10^3$	$8.5 \times 10^{45}$	$8.0 \times 10^{43}$	107
	4–3	(0, 1 <sup>1f</sup> , 0)	$1.32 \times 10^3$	$1.2 \times 10^{46}$	$4.3 \times 10^{43}$	282
R Vol	2–1	(0, 1 <sup>1e</sup> , 0)	$2.03 \times 10^2$	$2.0 \times 10^{45}$	$1.3 \times 10^{43}$	151
	2–1	(0, 1 <sup>1f</sup> , 0)	$2.03 \times 10^2$	$3.0 \times 10^{45}$	$2.9 \times 10^{42}$	1052
	3–2	(0, 1 <sup>1e</sup> , 0)	$2.03 \times 10^2$	$1.2 \times 10^{45}$	$3.9 \times 10^{42}$	303
AQ Sgr	4–3	(0, 1 <sup>1e</sup> , 0)	$2.03 \times 10^2$	$1.1 \times 10^{45}$	$3.9 \times 10^{42}$	293
	3–2	(0, 1 <sup>1e</sup> , 0)	56.6	$9.9 \times 10^{43}$	$2.0 \times 10^{41}$	506
	CRL 3068	2–1	(0, 1 <sup>1e</sup> , 0)	$7.07 \times 10^2$	$2.2 \times 10^{46}$	$2.0 \times 10^{44}$
V636 Mon	4–3	(0, 1 <sup>1f</sup> , 0)	$7.07 \times 10^2$	$2.1 \times 10^{46}$	$3.5 \times 10^{44}$	60
	2–1	(0, 1 <sup>1e</sup> , 0)	$1.25 \times 10^2$	$5.8 \times 10^{44}$	$3.1 \times 10^{42}$	188
IRC +20370	2–1	(0, 1 <sup>1e</sup> , 0)	$5.34 \times 10^2$	$5.6 \times 10^{45}$	$3.3 \times 10^{43}$	172
	3–2	(0, 1 <sup>1e</sup> , 0)	$5.34 \times 10^2$	$7.4 \times 10^{45}$	$2.5 \times 10^{43}$	299
W Ori	2–1	(0, 1 <sup>1e</sup> , 0)	$1.84 \times 10^2$	$1.0 \times 10^{44}$	$1.8 \times 10^{42}$	56
	3–2	(0, 1 <sup>1e</sup> , 0)	$1.84 \times 10^2$	$1.2 \times 10^{44}$	$2.0 \times 10^{42}$	59
	4–3	(0, 1 <sup>1e</sup> , 0)	$1.84 \times 10^2$	$8.7 \times 10^{43}$	$5.1 \times 10^{41}$	169
S Aur	2–1	(0, 1 <sup>1e</sup> , 0)	$1.62 \times 10^2$	$1.9 \times 10^{44}$	$2.6 \times 10^{42}$	73
V Aql	3–2	(0, 1 <sup>1e</sup> , 0)	$1.50 \times 10^2$	$2.0 \times 10^{44}$	$8.7 \times 10^{41}$	228
RV Aqr	2–1	(0, 1 <sup>1e</sup> , 0)	$3.08 \times 10^2$	$1.1 \times 10^{45}$	$1.0 \times 10^{43}$	107
	2–1	(0, 1 <sup>1f</sup> , 0)	$3.08 \times 10^2$	$9.7 \times 10^{44}$	$1.5 \times 10^{42}$	638
	3–2	(0, 1 <sup>1e</sup> , 0)	$3.08 \times 10^2$	$1.0 \times 10^{45}$	$9.8 \times 10^{42}$	133
IR = 4.6 $\mu\text{m}$ vs. 5 $\mu\text{m}$						
RAFGL 4211	3–2	(0, 3 <sup>1e</sup> , 0)	42.6	$1.1 \times 10^{45}$	$3.8 \times 10^{42}$	289
IR = 12 $\mu\text{m}$ vs. 7 $\mu\text{m}$						
RAFGL 4211	3–2	(0, 2, 0)	$7.93 \times 10^2$	$4.1 \times 10^{45}$	$7.8 \times 10^{42}$	533

**Notes.** (1) Source name. (2) Rotational levels. (3) Vibrational states. (4) Flux density at corresponding infrared wavelength. (5) Photon rates at a wavelength range according to the velocity range given by maser line (see Table 6). (6) Photon rates in the corresponding maser line. (7) Ratios between the infrared photon and HCN maser luminosities.

can cause molecules to cascade down from the (0, 1<sup>1f</sup>, 0) level to (0, 1<sup>1e</sup>, 0) level. Furthermore, the rotational transitions in the  $\nu_2 = 1$  state do not change the parity due to the selection rule. The net effects result in more HCN molecules in the (0, 1<sup>1e</sup>, 0) state than in the (0, 1<sup>1f</sup>, 0) state. The gain of masers is directly proportional to molecular column densities at their corresponding energy levels, which makes the  $J = 2-1$  (0, 1<sup>1e</sup>, 0) transition the brightest HCN masers in the  $\nu_2=1$  state. This may explain why HCN masers in the (0, 1<sup>1e</sup>, 0) state are typically stronger or more readily detectable than the (0, 1<sup>1f</sup>, 0) state, as shown in Figs. 11, 12, and D.1, which compare the (0, 1<sup>1e</sup>, 0) and (0, 1<sup>1f</sup>, 0) spectra in the same rotation transition at different  $J$  levels and in different sources.

The above pumping scenario is only consistent with our results for the  $J = 2-1$  and  $J = 3-2$  masers. For the  $J = 4-3$  transition, it is also consistent with the results in RAFGL 4211, R Vol, W Ori (Fig. 11), and perhaps RV Aqr (Fig. D.1), but fails to

explain the fact that (0, 1<sup>1f</sup>, 0) maser is brighter than the (0, 1<sup>1e</sup>, 0) masers in IRC +10216, II Lup, and CRL 3068 (Fig. 12). There are two common features in these sources showing the brighter (0, 1<sup>1f</sup>, 0) maser in  $J = 4-3$ . First, the peak velocities of these  $J = 4-3$  (0, 1<sup>1f</sup>, 0) masers are all blueshifted by about  $10 \text{ km s}^{-1}$  from their systemic LSR velocities, regardless of their discrepant ground-state or excited-state line widths (Tables 4 and 6). The peak velocities are different from those of the  $J = 2-1$  (0, 1<sup>1e</sup>, 0) masers of the same sources or the  $J = 4-3$  (0, 1<sup>1e</sup>, 0) masers of different sources, indicating a different pumping mechanism of this maser in these three sources. Second, all three sources show a broad emission profile in (0, 1<sup>1f</sup>, 0), which is roughly a factor of two brighter than the corresponding, apparently thermal, (0, 1<sup>1e</sup>, 0) profile. This indicates weak maser activities in the (0, 1<sup>1f</sup>, 0) line. The  $J = 4-3$  (0, 1<sup>1f</sup>, 0) masers may stem from (a combination of) infrared line overlap, anisotropic infrared radiation fields, and/or non-negligible collisional pumping. Observations

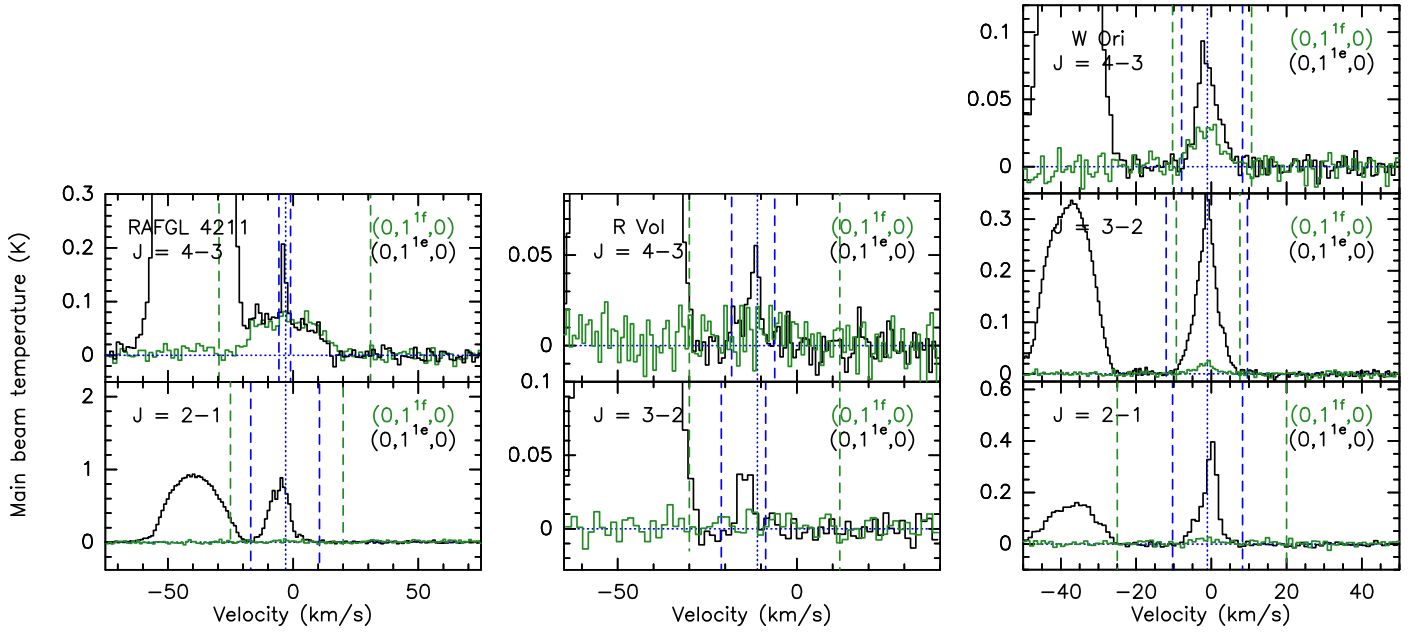


**Fig. 11.** Overlaid spectra for HCN  $(0, 1^e, 0)$  (in black) and  $(0, 1^f, 0)$  (in green) transitions in different rotational transitions towards RAFGL 4211 (*left*), R Vol (*middle*), and W Ori (*right*). These sources show brighter  $J = 4-3$   $(0, 1^e, 0)$  emission than  $J = 4-3$   $(0, 1^f, 0)$ . The vertical lines are labelled in the same way as for Fig. 1.

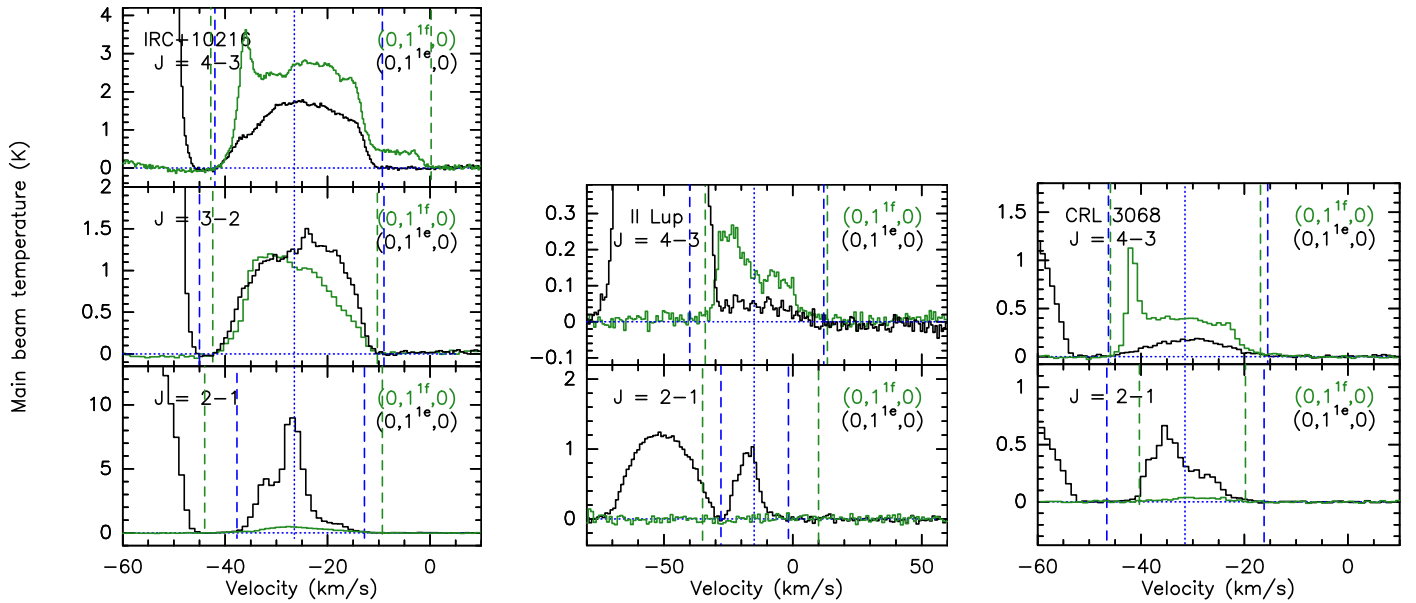


**Fig. 12.** Same as Fig. 11 towards IRC+10216 (*left*), II Lup (*middle*), and CRL 3068 (*right*). These sources show brighter  $J = 4-3$   $(0, 1^f, 0)$  emission than  $J = 4-3$   $(0, 1^e, 0)$ .

have shown a large amount of ro-vibrational HCN and  $C_2H_2$  transitions at  $\sim 14 \mu\text{m}$ , and a large fraction of them are overlapped (Fonfría et al. 2008). The ro-vibrational HCN and  $C_2H_2$  lines at  $14 \mu\text{m}$  could partially contribute to the pumping of HCN masers in the  $v_2=1$  state. Such an infrared line overlap has been invoked to explain the observed high- $J$  SiS masers (Fonfría Expósito et al. 2006). Because the HCN and  $C_2H_2$  lines are displaced in frequency, the overlap should give rise to the line asymmetries in the maser profiles. Furthermore, such a mechanism would lead to the presence of masers at nearly the same velocity shift with respect to their systemic velocities for different sources. This is

in agreement with our observations, where the most prominent component of the  $J = 4-3$   $(0, 1^f, 0)$  maser in these three sources peaks at about  $10 \text{ km s}^{-1}$ , blueshifted from the respective systemic velocities. Alternatively, the asymmetries in the maser profiles can arise from a highly anisotropic infrared radiation field, caused by substructures in the circumstellar envelope such as spirals or broken shells. Anisotropic infrared radiation field has been indicated by the non-spherical infrared morphology towards II Lup (Lykou et al. 2018). Thirdly, collisional pumping might not be negligible, although the vibrationally excited transitions are thought to be dominated by radiative pumping.

As pointed out in previous studies (Smith et al. 2014; Menten et al. 2018), the time variability does not appear to correlate with stellar cycles, indicating that collisional pumping may also contribute to part of the population inversion. This may explain the second feature where the  $J = 4-3$  ( $0, 1^{1f}, 0$ ) line exhibits a weak maser over a broad velocity range in these three sources. Inhomogeneous density structures driven by stellar pulsating shocks may result in the diverse line shapes among the HCN masers.

The HCN  $J = 3-2$  ( $0, 2, 0$ ) and  $J = 3-2$  ( $0, 3^{1e}, 0$ ) masers are only detected in RAFGL 4211 among carbon stars as of today (Table A.1). The uniqueness of these two masers could stem from the peculiar geometry of RAFGL 4211. For instance, the relatively long coherent length of maser amplification along the line of sight may result in a uniquely high gain for this maser. Both  $J = 2-1$  and  $J = 4-3$  ( $0, 1^{1e}, 0$ ) masers are detected, with the latter showing a narrow spike on top of a broad component. The higher- $J$  maser lines ( $3-2$  and  $4-3$ ) could partly arise from a region closer to the star, where the temperature and  $H_2$  number density are higher than in the region producing the  $J = 2-1$  ( $0, 1^{1e}, 0$ ) maser.

The physical conditions to excite the detected HCN masers can be roughly constrained. Based on the population diagram analysis (see Sect. 5.1), the excitation temperature is found to be around 800–900 K for the vibrationally excited HCN emitting regions. These masers have to be formed in these regions, which should have a kinetic temperature of  $\geq 700$  K. Furthermore, the velocity widths of the maser profiles indicate that the masers form in the wind acceleration zones. Comparing with the physical model in IRC +10216 (e.g. Agúndez et al. 2012), the expected gas temperature and velocity correspond to a  $H_2$  number density of  $> 10^8 \text{ cm}^{-3}$ . This gives a loose constraint on the physical conditions.

### 5.3. Comparison with masers in oxygen-rich stars

It is known that OH, SiO, and  $H_2O$  masers are common in oxygen-rich stars. SiO masers are formed in the dust formation zone, OH masers are formed farther out, and  $H_2O$  masers lie between (e.g. Habing 1996). As discussed above, HCN masers should be formed in the innermost regions (i.e.  $r < 20 R_*$ ), similar to the formation regions of SiO masers in oxygen-rich stars. Furthermore, both HCN and SiO are linear molecules that show maser actions in their ground vibrational states towards respective classes of stars (see Table A.1 for HCN ground-state masers towards carbon-rich stars, and see Boboltz & Claussen 2004; Dike et al. 2021 for SiO ground-state masers towards oxygen-rich stars). High-excitation masers with lower energy levels above 4000 K are detected in both SiO and HCN, with SiO masers in vibrational states up to  $v = 4$  detected in VY CMa (Cernicharo et al. 1993) and up to  $v = 7$  detected in Betelgeuse (Kervella et al. 2018); and HCN masers in the ( $0, 4^0, 0$ ) state were reported towards IRC +10216, CIT 6, and Y CVn (Schilke et al. 2000; Schilke & Menten 2003). These similar properties suggest that HCN masers in carbon-rich stars may be an analogue of SiO masers in oxygen-rich stars. If confirmed, HCN masers can be regarded as a powerful tool for measuring the accurate proper motions and parallaxes of carbon-rich stars as performed towards oxygen-rich stars with SiO masers (e.g. Zhang et al. 2012), especially towards the high mass-loss carbon-rich stars, which cannot be determined by optical and infrared telescopes due to their high extinctions. Very long baseline interferometry measurements of HCN masers might be the only way to determine their proper motions and parallaxes.

## 6. Summary and outlook

We performed APEX observations of multiple vibrationally excited HCN transitions towards a sample of 16 carbon-rich stars. The main results are summarised as follows:

1. Our observations resulted in the detection of 68 vibrationally excited HCN transitions from 13 stars, suggesting that vibrationally excited HCN lines are ubiquitous in carbon-rich stars. Among the detected transitions, 39 of them tend to be thermal, while 29 of them show maser actions. Our observations extend the spectrally resolved detection of the vibrationally excited thermal HCN transitions in carbon-rich stars beyond IRC +10216. Among the detected masers, 23 are new detections. The results expand the total number of HCN masers towards carbon-rich stars by 47%. The masers arise from 12 different transitions, and the  $J = 3-2$  ( $0, 3^{1e}, 0$ ),  $J = 3-2$  ( $0, 2, 0$ ),  $J = 4-3$  ( $0, 1^{1f}, 0$ ) masers are detected in the interstellar medium for the first time.
2. Temporal variations of the  $J = 2-1$  ( $0, 1^{1e}, 0$ ) maser on a timescale of a few years have been confirmed by the dramatic change of maser line profiles. However, the cause of the time variability of HCN masers is still unclear.
3. Population diagrams of vibrationally excited thermal HCN transitions suggest an excitation temperature of about 800 K for IRC+10216 and CRL 3068, consistent with the previous studies. Assuming a typical size of 28 au for the regions showing the vibrationally excited HCN transitions, we derived the source-average HCN column densities of  $(0.18-10.8) \times 10^{19} \text{ cm}^{-2}$  for six carbon-rich stars. The corresponding HCN abundance with respect to  $H_2$  is roughly  $\sim 7.4 \pm 5.5 \times 10^{-5}$ .
4. The ratios between HCN masers and corresponding infrared luminosities suggest that HCN masers are unsaturated. The unsaturated nature is supported by the temporal variation and relatively low brightness temperatures of these HCN masers. The spontaneous decay of rotational transitions and direct  $l$ -type transitions in the  $v_2=1$  state may explain the fact that the  $J = 2-1$  ( $0, 1^{1e}, 0$ ) transition is the brightest maser in the  $v_2=1$  state. Comparing with the physical model of IRC+10216, we infer that a gas kinetic temperature of  $\geq 700$  K and an  $H_2$  number density of  $> 10^8 \text{ cm}^{-3}$  are required to excite the HCN masers. A comparison between masers in carbon-rich and oxygen-rich stars suggests that HCN masers in carbon-rich stars may be an analogue of SiO masers in oxygen-rich stars.

Our observations suggest that both vibrationally excited HCN thermal and maser line emission are rich in the CSEs of carbon-rich stars and have quite high flux densities. This indicates that these transitions are suitable for follow-up high-resolution observations in order to study the entire class of carbon-rich stars. With the very long baselines, the Atacama Large Millimeter/submillimeter Array observations of these vibrationally excited HCN lines can achieve an angular resolution of  $\lesssim 30$  mas (e.g. Wong et al. 2016), which should be able to constrain the physical conditions of the extended atmospheres and inner winds of carbon-rich stars.

*Acknowledgements.* This publication is based on data acquired with the Atacama Pathfinder EXperiment (APEX). APEX is a collaboration between the Max-Planck-Institut für Radioastronomie, the European Southern Observatory, and the Onsala Space Observatory. This research has made use of NASA's Astrophysics Data System. We thank A. V. Lapinov and the Editor-in-chief of the *Astronomicheskii Tsirkulyar* for kindly providing the scanned copies of Lapinov et al. (1994) and Zinchenko et al. (1988), respectively. We acknowledge with thanks the variable star observations from the AAVSO International Database contributed by observers worldwide and used in this research. This work has

made use of Python libraries including NumPy (<https://www.numpy.org/>) (van der Walt et al. 2011), SciPy (<https://www.scipy.org/>) (Jones et al. 2001), Matplotlib (<https://matplotlib.org/>) (Hunter 2007). We thank the anonymous referee for their useful comments.

## References

- Abrahamyan, H. V., Mickaelian, A. M., & Knyazyan, A. V. 2015, *Astron. Comput.*, **10**, 99
- Adel, A., & Barker, E. F. 1934, *Phys. Rev.*, **45**, 277
- Agúndez, M., Fonfría, J. P., Cernicharo, J., et al. 2012, *A&A*, **543**, A48
- Barber, R. J., Strange, J. K., Hill, C., et al. 2014, *MNRAS*, **437**, 1828
- Belitsky, V., Bylund, M., Desmaris, V., et al. 2018a, *A&A*, **611**, A98
- Belitsky, V., Lapkin, I., Fredrixon, M., et al. 2018b, *A&A*, **612**, A23
- Biegging, J. H. 2001, *ApJ*, **549**, L125
- Biegging, J. H., Shaked, S., & Gensheimer, P. 2000, *ApJ*, **543**, 897
- Billade, B., Nystrom, O., Meledin, D., et al. 2012, *IEEE Trans. Terahertz Sci. Technol.*, **2**, 208
- Boboltz, D. A., & Claussen, M. J. 2004, *ApJ*, **608**, 480
- Brinkmann, N., Wyrowski, F., Kauffmann, J., et al. 2020, *A&A*, **636**, A39
- Bujarrabal, V., & Nguyen-Q-Rieu. 1981, *A&A*, **102**, 65
- Cernicharo, J., Bujarrabal, V., & Santaren, J. L. 1993, *ApJ*, **407**, L33
- Cernicharo, J., Agúndez, M., Kahane, C., et al. 2011, *A&A*, **529**, L3
- Cherchneff, I. 2006, *A&A*, **456**, 1001
- Dayal, A., & Biegging, J. H. 1995, *ApJ*, **439**, 996
- Decin, L., Richards, A. M. S., Neufeld, D., et al. 2015, *A&A*, **574**, A5
- Dike, V., Morris, M. R., Rich, R. M., et al. 2021, *AJ*, **161**, 111
- Feast, M. W., Whitelock, P. A., & Marang, F. 2003, *MNRAS*, **346**, 878
- Fonfría, J. P., Cernicharo, J., Richter, M. J., & Lacy, J. H. 2008, *ApJ*, **673**, 445
- Fonfría, J. P., Fernández-López, M., Pardo, J. R., et al. 2018, *ApJ*, **860**, 162
- Fonfría, J. P., Montiel, E. J., Cernicharo, J., et al. 2021, *A&A*, **651**, A8
- Fonfría Expósito, J. P., Agúndez, M., Tercero, B., Pardo, J. R., & Cernicharo, J. 2006, *ApJ*, **646**, L127
- Gaia Collaboration (Brown, A. G. A., et al.) 2018, *A&A*, **616**, A1
- Goldsmith, P. F., & Langer, W. D. 1999, *ApJ*, **517**, 209
- Gong, Y., Henkel, C., Ott, J., et al. 2017, *ApJ*, **843**, 54
- Gray, M. 2012, Maser Sources in Astrophysics
- Guilloteau, S., Omont, A., & Lucas, R. 1987, *A&A*, **176**, L24
- Güsten, R., Nyman, L. Å., Schilke, P., et al. 2006, *A&A*, **454**, L13
- Habing, H. J. 1996, *A&ARv*, **7**, 97
- He, J. H., Dinh-V-Trung, Kwok, S., et al. 2008, *ApJS*, **177**, 275
- He, J. H., Dinh-V-Trung, & Hasegawa, T. I. 2017, *ApJ*, **845**, 38
- He, J. H., Kamiński, T., Mennickent, R. E., et al. 2019, *ApJ*, **883**, 165
- Henkel, C., Matthews, H. E., & Morris, M. 1983, *ApJ*, **267**, 184
- Highberger, J. L., Apponi, A. J., Biegging, J. H., Ziurys, L. M., & Mangum, J. G. 2000, *ApJ*, **544**, 881
- Höfner, S., & Olofsson, H. 2018, *A&ARv*, **26**, 1
- Hunter, J. D. 2007, *Comput. Sci. Eng.*, **9**, 90
- Immer, K., Belitsky, V., Olberg, M., et al. 2016, *The Messenger*, **165**, 13
- Izumiura, H., Ukita, N., Kawabe, R., et al. 1987, *ApJ*, **323**, L81
- Izumiura, H., Ukita, N., & Tsuji, T. 1995, *ApJ*, **440**, 728
- Jones, E., Oliphant, T., Peterson, P., et al. 2001, SciPy: Open source scientific tools for Python
- Kerschbaum, F., Groenewegen, M. A. T., & Lazaro, C. 2006, *A&A*, **460**, 539
- Kervella, P., Decin, L., Richards, A. M. S., et al. 2018, *A&A*, **609**, A67
- Kippenhahn, R., Weigert, A., & Weiss, A. 2012, Stellar Structure and Evolution
- Klein, B., Philipp, S. D., Krämer, I., et al. 2006, *A&A*, **454**, L29
- Klein, T., Ciechanowicz, M., Leinz, C., et al. 2014, *IEEE Trans. Terahertz Sci. Technol.*, **4**, 588
- Lapinov, A. V., Zinchenko, I. I., Krasil'nikov, A. A., & Pirogov, L. E. 1994, in *Molecular Opacities in the Stellar Environment, Poster Session*, eds. P. Thejll, & U. G. Jorgensen, 66
- Le Bertre, T. 1992, *A&AS*, **94**, 377
- Loup, C., Forveille, T., Omont, A., & Paul, J. F. 1993, *A&AS*, **99**, 291
- Lucas, R., & Cernicharo, J. 1989, *A&A*, **218**, L20
- Lucas, R., Omont, A., Guilloteau, S., et al. 1986, *A&A*, **154**, L12
- Lucas, R., Guilloteau, S., & Omont, A. 1988, *A&A*, **194**, 230
- Lykou, F., Zijlstra, A. A., Kluska, J., et al. 2018, *MNRAS*, **480**, 1006
- Martín, S., Mangum, J. G., Harada, N., et al. 2021, *A&A*, **656**, A46
- Massalkhi, S., Agúndez, M., Cernicharo, J., et al. 2018, *A&A*, **611**, A29
- Menten, K. M., Reid, M. J., Krügel, E., Claussen, M. J., & Sahai, R. 2006, *A&A*, **453**, 301
- Menten, K. M., Reid, M. J., Kamiński, T., & Claussen, M. J. 2012, *A&A*, **543**, A73
- Menten, K. M., Wyrowski, F., Keller, D., & Kamiński, T. 2018, *A&A*, **613**, A49
- Menzies, J. W., Feast, M. W., & Whitelock, P. A. 2006, *MNRAS*, **369**, 783
- Monnier, J. D., Danchi, W. C., Hale, D. S., Tuthill, P. G., & Townes, C. H. 2000, *ApJ*, **543**, 868
- Morris, M. 1975, *ApJ*, **197**, 603
- Müller, H. S. P., Schöder, F., Stutzki, J., & Winnewisser, G. 2005, *J. Mol. Struct.*, **742**, 215
- Nicolaes, D., Groenewegen, M. A. T., Royer, P., et al. 2018, *A&A*, **618**, A143
- Olofsson, H., Johansson, L. E. B., Hjalmarson, A., & Nguyen-Quang-Rieu. 1982, *A&A*, **107**, 128
- Olofsson, H., Eriksson, K., Gustafsson, B., & Carlström, U. 1993, *ApJS*, **87**, 305
- Pardo, J. R., Cernicharo, J., Velilla Prieto, L., et al. 2018, *A&A*, **615**, A4
- Patel, N. A., Young, K. H., Brünken, S., et al. 2009, *ApJ*, **692**, 1205
- Pety, J. 2005, in *SF2A-2005: Semaine de l'Astrophysique Française*, eds. F. Casoli, T. Contini, J. M. Hameury, & L. Paganí, 721
- Ramstedt, S., & Olofsson, H. 2014, *A&A*, **566**, A145
- Ramstedt, S., Schöier, F. L., & Olofsson, H. 2009, *A&A*, **499**, 515
- Rau, G., Hron, J., Paladini, C., et al. 2017, *A&A*, **600**, A92
- Reid, M. J., & Honma, M. 2014, *ARA&A*, **52**, 339
- Rolfs, R., Schilke, P., Wyrowski, F., et al. 2011, *A&A*, **529**, A76
- Sakamoto, K., Aalto, S., Evans, A. S., Wiedner, M. C., & Wilner, D. J. 2010, *ApJ*, **725**, L228
- Schilke, P., & Menten, K. M. 2003, *ApJ*, **583**, 446
- Schilke, P., Mehringer, D. M., & Menten, K. M. 2000, *ApJ*, **528**, L37
- Schöier, F. L., & Olofsson, H. 2001, *A&A*, **368**, 969
- Schöier, F. L., Ramstedt, S., Olofsson, H., et al. 2013, *A&A*, **550**, A78
- Shinnaga, H., Young, K. H., Tilanus, R. P. J., et al. 2009, *ApJ*, **698**, 1924
- Smith, C. L., Zijlstra, A. A., & Fuller, G. A. 2014, *MNRAS*, **440**, 172
- Thorwirth, S., Wyrowski, F., Schilke, P., et al. 2003, *ApJ*, **586**, 338
- Tsuji, T. 1964, *Ann. Tokyo Astron. Observ.*, **9**, 1
- Ulich, B. L., & Haas, R. W. 1976, *ApJS*, **30**, 247
- van der Walt, S., Colbert, S. C., & Varoquaux, G. 2011, *Comput. Sci. Eng.*, **13**, 22
- Whitelock, P. A., Feast, M. W., Marang, F., & Groenewegen, M. A. T. 2006, *MNRAS*, **369**, 751
- Wong, K. T., Kamiński, T., Menten, K. M., & Wyrowski, F. 2016, *A&A*, **590**, A127
- Zelinger, Z., Amano, T., Ahrens, V., et al. 2003, *J. Mol. Spectrosc.*, **220**, 223
- Zhang, B., Reid, M. J., Menten, K. M., & Zheng, X. W. 2012, *ApJ*, **744**, 23
- Zinchenko, I. I., Krasilnikov, A. A., Koukina, E. P., Lapinov, A. V., & Pirogov, L. E. 1988, *Astronomicheskij Tsirkulyar*, **1525**, 13
- Ziurys, L. M., & Turner, B. E. 1986, *ApJ*, **300**, L19

## Appendix A: Catalogue of known HCN masers towards carbon-rich stars

Based on our new detections and those in the literature, we have compiled the largest catalogue of HCN masers towards carbon-rich stars, and the results are listed in Table A.1. These masers are assigned to 36 different carbon-rich stars, and these HCN masers can be assigned to ten different vibrational states. Our observations led to the discovery of 23 new HCN masers, increasing the total number to 75.

## Appendix B: Estimates of the stellar variability phase

The phases of stellar variability on the dates of our 2018 observations were calculated for a number of sources in Table B.1, primarily using the information compiled by the AAVSO. In the used convention, phase zero is at the maximum light. While pulsation periods are available for the majority of sources (cf. Table 1), the epochs of maxima are scarce in the literature, limiting the number of stars with known phases at the epochs of our observations. In addition to AAVSO records, we used data from Menten et al. (2012, for IRC+10216), Feast et al. (2003, for II Lup), Whitelock et al. (2006, for IRC+30374), and Menzies et al. (2006, for CRL-2513).

Table A.1: Catalogue of HCN maser detections in the CSEs of 36 stars to date.

Source name (1)	$\nu$ (MHz) (2)	$J$ (3)	$(\nu_1, \nu_2, \nu_3)$ (4)	Source name (1)	$\nu$ (MHz) (2)	$J$ (3)	$(\nu_1, \nu_2, \nu_3)$ (4)
IRC +10216 <sup>a</sup>	89087.7	1–0	(0, 2, 0)	CIT 6 <sup>k</sup>	88006.7	1–0	(1, 0, 0)
IRC +10216 <sup>b</sup>	177238.710	2–1	(0, 1 <sup>e</sup> , 0)	CIT 6 <sup>k</sup>	88027.3	1–0	(0, 0, 1)
IRC +10216 <sup>c</sup>	177238.655	2–1	(0, 1 <sup>f</sup> , 0)	CIT 6 <sup>l</sup>	89087.7	1–0	(0, 2, 0)
IRC +10216 <sup>d</sup>	267199.283	3–2	(0, 1 <sup>f</sup> , 0)	CIT 6 <sup>c</sup>	177238.655	2–1	(0, 1 <sup>e</sup> , 0)
IRC +10216 <sup>e</sup>	356255.568	4–3	(0, 1 <sup>f</sup> , 0)	CIT 6 <sup>c</sup>	178136.477	2–1	(0, 1 <sup>f</sup> , 0)
IRC +10216 <sup>f</sup>	804750.9	9–8	(0, 4, 0)	CIT 6 <sup>g</sup>	804750.9	9–8	(0, 4, 0)
IRC +10216 <sup>g</sup>	890761.0	10–9	(1, 1 <sup>1</sup> , 0)–(0, 4, 0)	CIT 6 <sup>g</sup>	890761.0	10–9	(1, 1 <sup>1</sup> , 0)–(0, 4, 0)
RAFGL 4211 <sup>h</sup>	89087.7	1–0	(0, 2, 0)	CRL 2688 <sup>m</sup>	89087.7	1–0	(0, 2, 0)
RAFGL 4211 <sup>c</sup>	177238.655	2–1	(0, 1 <sup>e</sup> , 0)	CRL 618 <sup>n</sup>	20181.3862	9–9	(0, 1 <sup>f</sup> , 0)–(0, 1 <sup>e</sup> , 0)
RAFGL 4211 <sup>e</sup>	266539.980	3–2	(0, 3 <sup>e</sup> , 0)	CQ Pyx <sup>c</sup>	177238.655	2–1	(0, 1 <sup>e</sup> , 0)
RAFGL 4211 <sup>e</sup>	267243.150	3–2	(0, 2, 0)	CQ Pyx <sup>c</sup>	178136.477	2–1	(0, 1 <sup>f</sup> , 0)
RAFGL 4211 <sup>e</sup>	354460.435	4–3	(0, 1 <sup>e</sup> , 0)	FX Ser <sup>i</sup>	89087.7	1–0	(0, 2, 0)
II Lup <sup>c</sup>	177238.655	2–1	(0, 1 <sup>e</sup> , 0)	RAFGL 2047 <sup>i</sup>	89087.7	1–0	(0, 2, 0)
II Lup <sup>e</sup>	356255.568	4–3	(0, 1 <sup>f</sup> , 0)	IRC +50096 <sup>i</sup>	89087.7	1–0	(0, 2, 0)
R Vol <sup>e</sup>	177238.656	2–1	(0, 1 <sup>e</sup> , 0)	R For <sup>c</sup>	177238.655	2–1	(0, 1 <sup>e</sup> , 0)
R Vol <sup>e</sup>	178136.478	2–1	(0, 1 <sup>f</sup> , 0)	R Lep <sup>c</sup>	177238.655	2–1	(0, 1 <sup>e</sup> , 0)
R Vol <sup>e</sup>	265852.709	3–2	(0, 1 <sup>e</sup> , 0)	R Lep <sup>o</sup>	265852.709	3–2	(0, 1 <sup>e</sup> , 0)
R Vol <sup>e</sup>	354460.435	4–3	(0, 1 <sup>e</sup> , 0)	R Lep <sup>o</sup>	354460.435	4–3	(0, 1 <sup>e</sup> , 0)
AQ Sgr <sup>e</sup>	177238.656	2–1	(0, 1 <sup>e</sup> , 0)	R Scl <sup>o</sup>	265852.709	3–2	(0, 1 <sup>e</sup> , 0)
CRL 3068 <sup>e</sup>	177238.656	2–1	(0, 1 <sup>e</sup> , 0)	R Scl <sup>o</sup>	354460.435	4–3	(0, 1 <sup>e</sup> , 0)
CRL 3068 <sup>e</sup>	356255.568	4–3	(0, 1 <sup>f</sup> , 0)	S Cep <sup>i</sup>	89087.7	1–0	(0, 2, 0)
IRC +30374 <sup>i</sup>	89087.7	1–0	(0, 2, 0)	T Dra <sup>i</sup>	89087.7	1–0	(0, 2, 0)
V636 Mon <sup>e</sup>	177238.656	2–1	(0, 1 <sup>e</sup> , 0)	TU Gem <sup>p</sup>	88631.847	1–0	(0, 0, 0)
IRC +20370 <sup>e</sup>	177238.656	2–1	(0, 1 <sup>e</sup> , 0)	UU Aur <sup>p</sup>	88631.847	1–0	(0, 0, 0)
IRC +20370 <sup>e</sup>	265852.709	3–2	(0, 1 <sup>e</sup> , 0)	V384 Per <sup>o</sup>	265852.709	3–2	(0, 1 <sup>e</sup> , 0)
W Ori <sup>j</sup>	88631.847	1–0	(0, 0, 0)	V384 Per <sup>o</sup>	354460.435	4–3	(0, 1 <sup>e</sup> , 0)
W Ori <sup>e</sup>	177238.656	2–1	(0, 1 <sup>e</sup> , 0)	V Cyg <sup>q</sup>	265852.709	3–2	(0, 1 <sup>e</sup> , 0)
W Ori <sup>e</sup>	265852.709	3–2	(0, 1 <sup>e</sup> , 0)	V Cyg <sup>q</sup>	354460.435	4–3	(0, 1 <sup>e</sup> , 0)
W Ori <sup>e</sup>	354460.435	4–3	(0, 1 <sup>e</sup> , 0)	V Hya <sup>c</sup>	177238.655	2–1	(0, 1 <sup>e</sup> , 0)
S Aur <sup>e</sup>	177238.656	2–1	(0, 1 <sup>e</sup> , 0)	X Vel <sup>j</sup>	88631.847	1–0	(0, 0, 0)
V Aql <sup>e</sup>	265852.709	3–2	(0, 1 <sup>e</sup> , 0)	X Vel <sup>c</sup>	177238.655	2–1	(0, 1 <sup>e</sup> , 0)
RV Aqr <sup>e</sup>	177238.656	2–1	(0, 1 <sup>e</sup> , 0)	X TrA <sup>j</sup>	88631.847	1–0	(0, 0, 0)
RV Aqr <sup>e</sup>	178136.478	2–1	(0, 1 <sup>f</sup> , 0)	X TrA <sup>c</sup>	177238.655	2–1	(0, 1 <sup>e</sup> , 0)
RV Aqr <sup>e</sup>	265852.709	3–2	(0, 1 <sup>e</sup> , 0)	Y CVn <sup>r</sup>	88631.847	1–0	(0, 0, 0)
AFGL 2513 <sup>i</sup>	89087.7	1–0	(0, 2, 0)	Y CVn <sup>o</sup>	265852.709	3–2	(0, 1 <sup>e</sup> , 0)
Al Vol <sup>c</sup>	177238.655	2–1	(0, 1 <sup>e</sup> , 0)	Y CVn <sup>s</sup>	267199.283	3–2	(0, 1 <sup>f</sup> , 0)
Al Vol <sup>c</sup>	178136.477	2–1	(0, 1 <sup>f</sup> , 0)	Y CVn <sup>g</sup>	890761.0	10–9	(1, 1 <sup>1</sup> , 0)–(0, 4, 0)
				Y Tau <sup>p</sup>	88631.847	1–0	(0, 0, 0)

**References.** <sup>(a)</sup>Lucas et al. (1986). <sup>(b)</sup>Lucas & Cernicharo (1989). <sup>(c)</sup>Menten et al. (2018). <sup>(d)</sup>He et al. (2017). <sup>(e)</sup>This work. <sup>(f)</sup>Schilke et al. (2000). <sup>(g)</sup>Schilke & Menten (2003). <sup>(h)</sup>Smith et al. (2014). <sup>(i)</sup>Lucas et al. (1988). <sup>(j)</sup>Olofsson et al. (1993). <sup>(k)</sup>Lapinov et al. (1994). <sup>(l)</sup>Guilloteau et al. (1987). <sup>(m)</sup>Zinchenko et al. (1988). <sup>(n)</sup>Thorwirth et al. (2003). <sup>(o)</sup>Bieging (2001). <sup>(p)</sup>Izumiura et al. (1995). <sup>(q)</sup>Bieging et al. (2000). <sup>(r)</sup>Izumiura et al. (1987). <sup>(s)</sup>Fonfria et al. (2021).

Table B.1: Pulsation phase at the time of the observation.

Source	$\Delta J$	JD	$\phi$	MM/DD	
IRC+10216	4-3	2458302	0.95	07/02	
	2-1	2458462	0.20	12/09	
	3-2	2458467	0.21	12/14	
	2-1	2458469	0.21	12/16	
	4-3	2458473	0.22	12/20	
RAFGL4211	4-3	2458278	–	06/08	
	4-3	2458303	–	07/03	
	3-2	2458308	–	07/08	
	3-2	2458315	–	07/15	
	3-2	2458316	–	07/16	
	3-2	2458397	–	10/05	
	2-1	2458468	–	12/15	
	2-1	2458469	–	12/16	
II Lup	2-1	2458470	0.70	12/17	
	2-1	2458471	0.70	12/18	
	3-2	2458308	0.41	07/08	
	3-2	2458315	0.43	07/15	
	3-2	2458398	0.57	10/06	
	4-3	2458302	0.40	07/02	
	4-3	2458303	0.41	07/03	
	R Vol	4-3	2458365	0.8	09/03
4-3		2458367	0.8	09/05	
4-3		2458448	0.9	11/25	
4-3		2458451	0.9	11/28	
3-2		2458452	0.9	11/29	
2-1		2458462	1.0	12/09	
2-1		2458464	1.0	12/11	
2-1		2458469	1.0	12/16	
4-3		2458473	1.0	12/20	
Y Pav		3-2	2458308	0.03	07/08
		3-2	2458312	0.04	07/12
	3-2	2458314	0.04	07/14	
	3-2	2458398	0.23	10/06	
	4-3	2458447	0.34	11/24	
	4-3	2458448	0.34	11/25	
	4-3	2458449	0.34	11/26	
	3-2	2458450	0.34	11/27	
	2-1	2458451	0.35	11/28	
AQ Sgr	3-2	2458308	–	07/08	
	3-2	2458311	–	07/11	
	4-3	2458367	–	09/05	
	4-3	2458369	–	09/07	
	3-2	2458370	–	09/08	
	3-2	2458375	–	09/13	
	3-2	2458398	–	10/06	
	CRL 3068	2-1	2458451	–	11/28
2-1		2458462	–	12/09	
2-1		2458463	–	12/10	
2-1		2458464	–	12/11	
3-2		2458304	–	07/04	
3-2		2458313	–	07/13	
3-2		2458370	–	09/08	
3-2		2458398	–	10/06	
4-3		2458367	–	09/05	
4-3		2458368	–	09/06	
4-3		2458369	–	09/07	
4-3		2458459	–	12/06	
IRC+30374		2-1	2458467	–	12/14
	3-2	2458308	–	07/08	
	4-3	2458446	–	11/23	
	V636 Mon	2-1	2458455	–	12/02
		2-1	2458463	–	12/10
		3-2	2458449	–	11/26
		4-3	2458365	–	09/03
		4-3	2458367	–	09/05
		4-3	2458374	–	09/12
	IRC+20370	4-3	2458451	–	11/28
		3-2	2458308	0.45	07/08
		3-2	2458315	0.46	07/15
		3-2	2458397	0.62	10/05
3-2		2458398	0.62	10/06	
2-1		2458452	0.73	11/29	
W Ori	4-3	2458459	0.74	12/06	
	3-2	2458304	0.92	07/04	
	3-2	2458313	0.96	07/13	
S Aur	3-2	2458314	0.96	07/14	
	3-2	2458315	0.97	07/15	
	4-3	2458365	0.20	09/03	
	4-3	2458367	0.21	09/05	
	4-3	2458373	0.24	09/11	
	3-2	2458375	0.25	09/13	
	4-3	2458448	0.59	11/25	
	3-2	2458452	0.61	11/29	
	2-1	2458453	0.62	11/30	
	4-3	2458460	0.65	12/07	
	2-1	2458463	0.67	12/10	
V Aql	4-3	2458366	0.73	09/04	
	3-2	2458398	0.79	10/06	
	4-3	2458460	0.89	12/07	
	2-1	2458463	0.90	12/10	
CRL 2513	3-2	2458308	0.91	07/08	
	3-2	2458313	0.92	07/13	
	4-3	2458366	0.05	09/04	
	4-3	2458367	0.05	09/05	
	3-2	2458377	0.08	09/15	
CRL 2477	2-1	2458452	–	11/29	
	2-1	2458463	–	12/10	
	3-2	2458308	–	07/08	
	3-2	2458313	–	07/13	
RV Aqr	2-1	2458468	–	12/15	
	3-2	2458370	–	09/08	
	3-2	2458313	0.74	07/13	
	3-2	2458314	0.74	07/14	
	4-3	2458368	0.86	09/06	
	3-2	2458371	0.87	09/09	
	4-3	2458446	0.04	11/23	
	4-3	2458448	0.04	11/25	
	4-3	2458449	0.04	11/26	
	2-1	2458452	0.05	11/29	
2-1	2458453	0.05	11/30		

### Appendix C: Vibrationally excited HCN lines in other sources

In addition to the HCN spectra of IRC +10216, CRL 3068, and II Lup (see Figs. 1–4), the observed APEX HCN spectra in the other 13 sources are presented in Figs. C.1–C.13.

### Appendix D: Comparison of HCN emission in $(0, 1^e, 0)$ and $(0, 1^f, 0)$ vibrational states

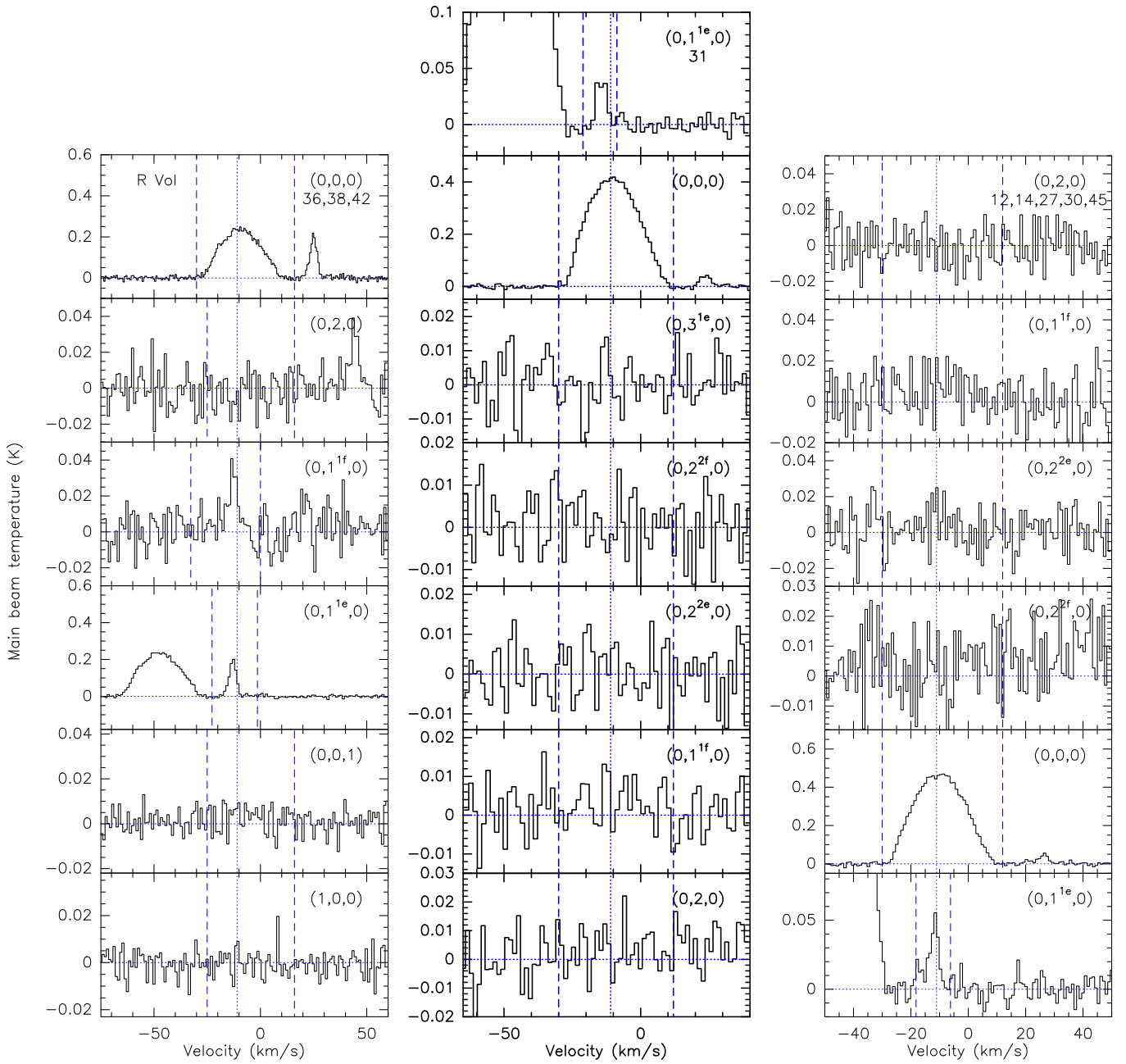


Fig. C.1: Spectra for  $J=2-1$  (left),  $3-2$  (centre) and  $4-3$  (right) transitions of HCN towards R Vol. The description of the figure is the same as in the Fig. 1 caption.

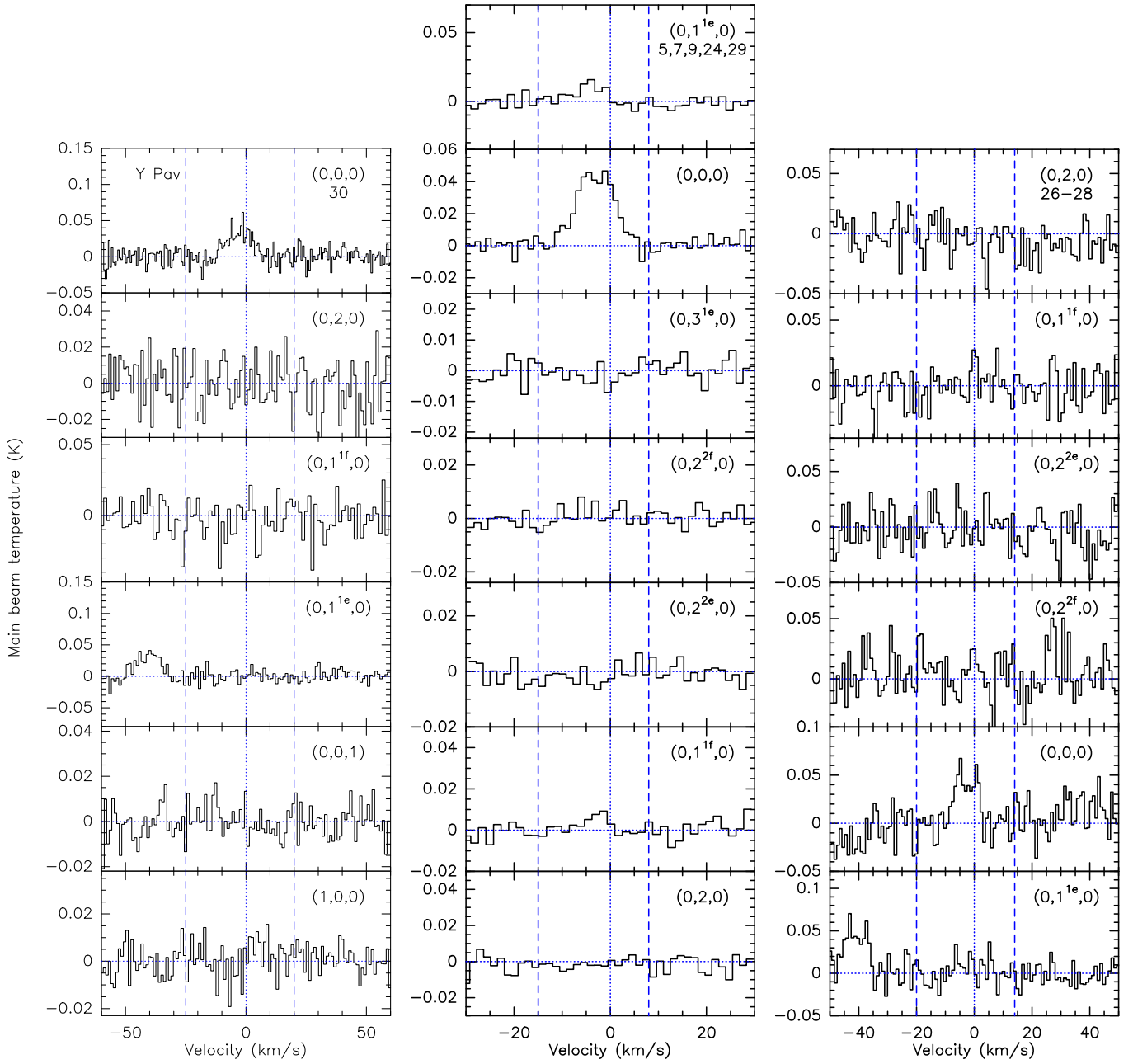


Fig. C.2: Spectra for  $J = 2-1$  (left),  $3-2$  (centre) and  $4-3$  (right) transitions of HCN towards Y Pav. The description of the figure is the same as in the Fig. 1 caption.

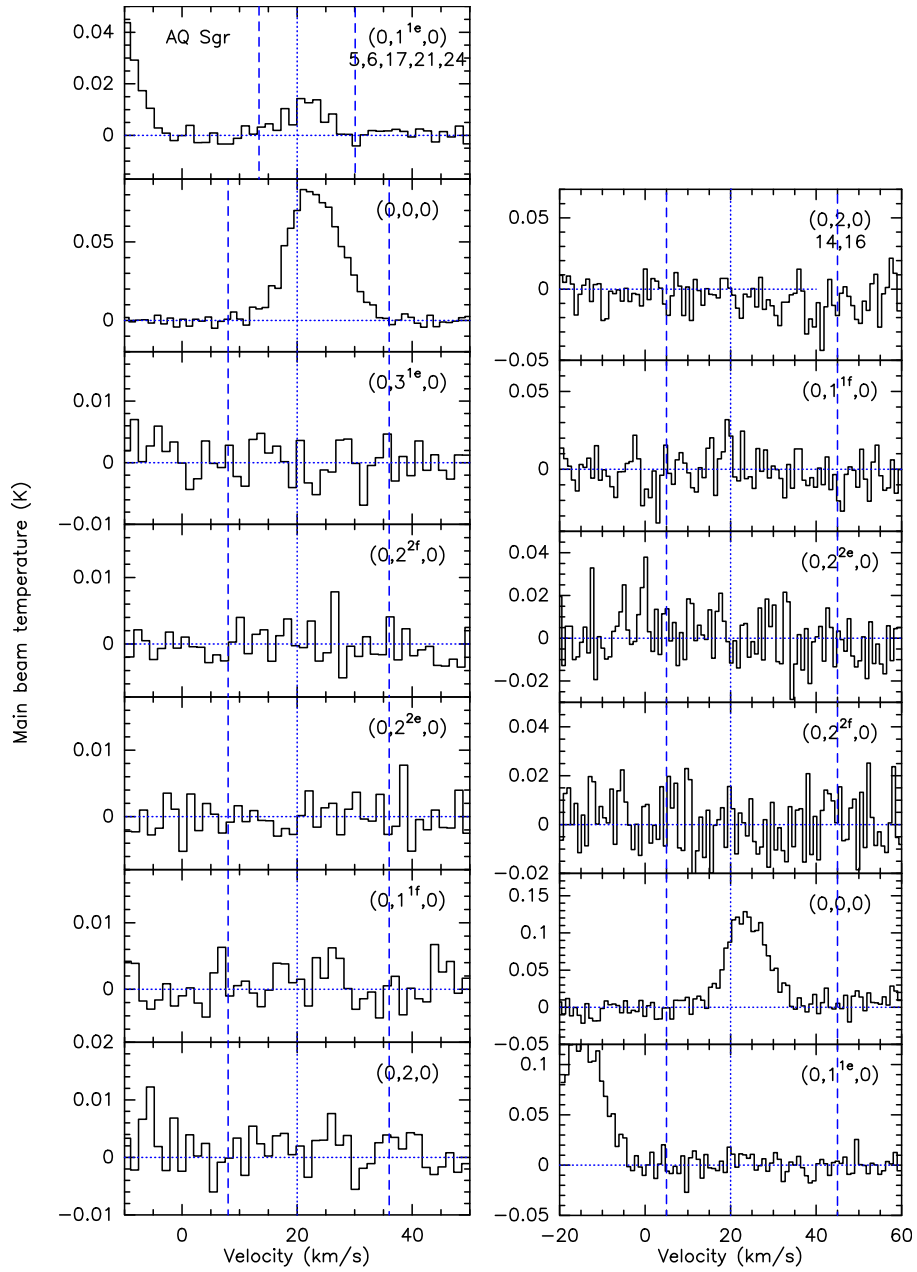


Fig. C.3: Spectra for  $J = 3-2$  (left) and  $4-3$  (right) transitions of HCN towards AQ Sgr. The description of the figure is the same as in the Fig. 1 caption.

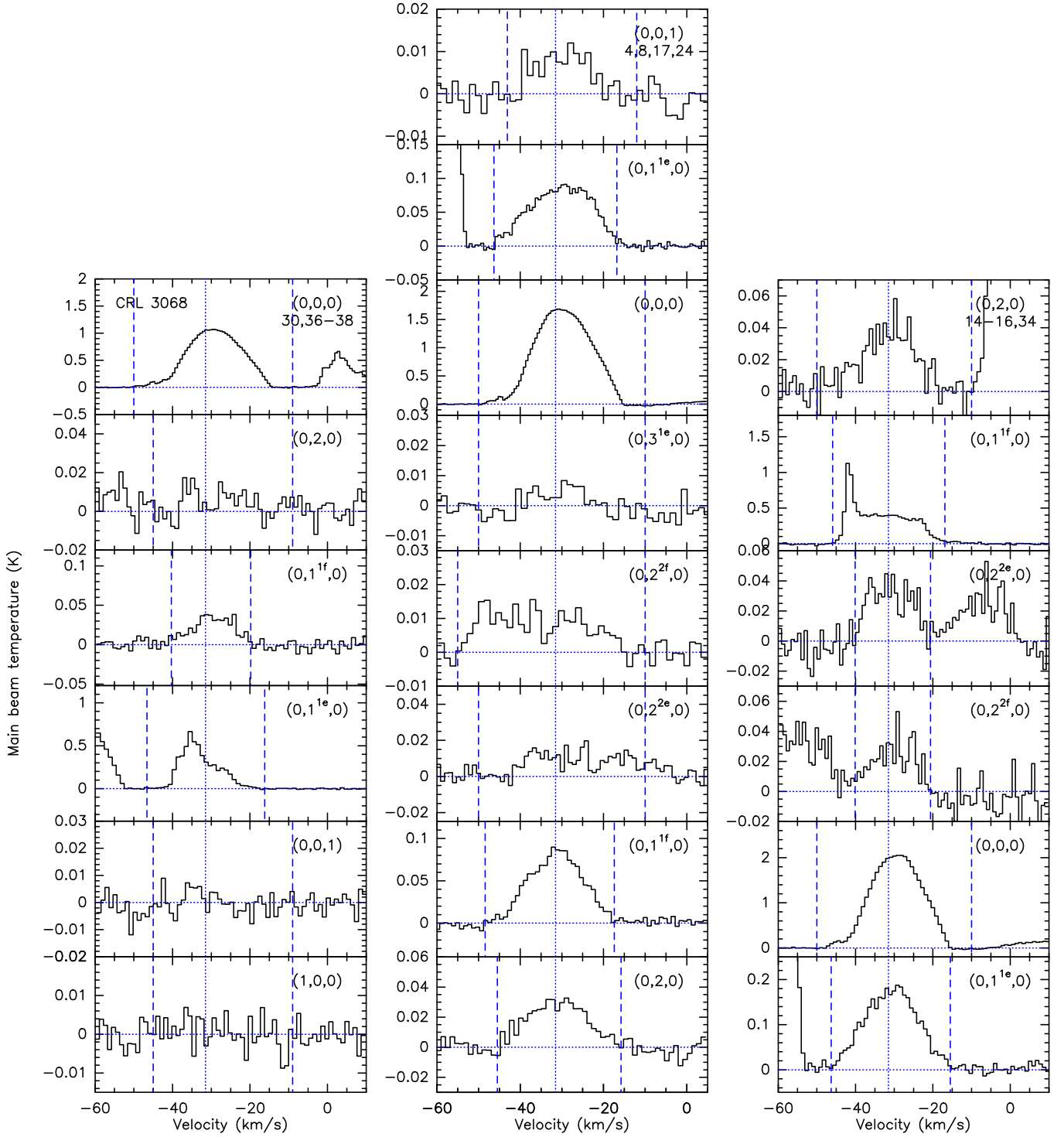


Fig. C.4: Spectra for  $J = 2-1$  (left),  $3-2$  (centre) and  $4-3$  (right) transitions of HCN towards CRL 3068. The description of the figure is the same as in the Fig. 1 caption.

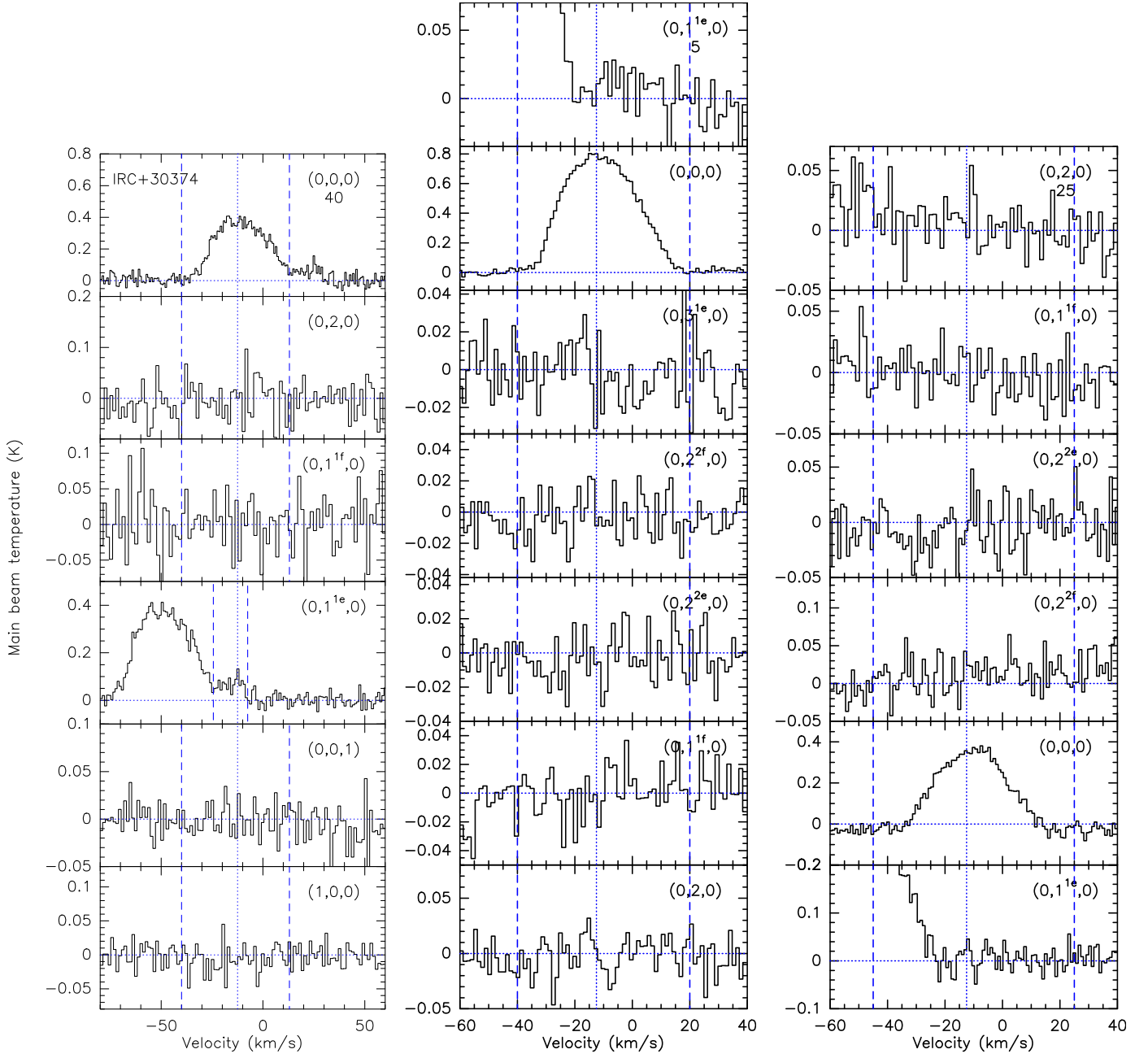


Fig. C.5: Spectra for  $J = 2-1$  (left),  $3-2$  (centre) and  $4-3$  (right) transitions of HCN towards IRC +30374. The description of the figure is the same as in the Fig. 1 caption.

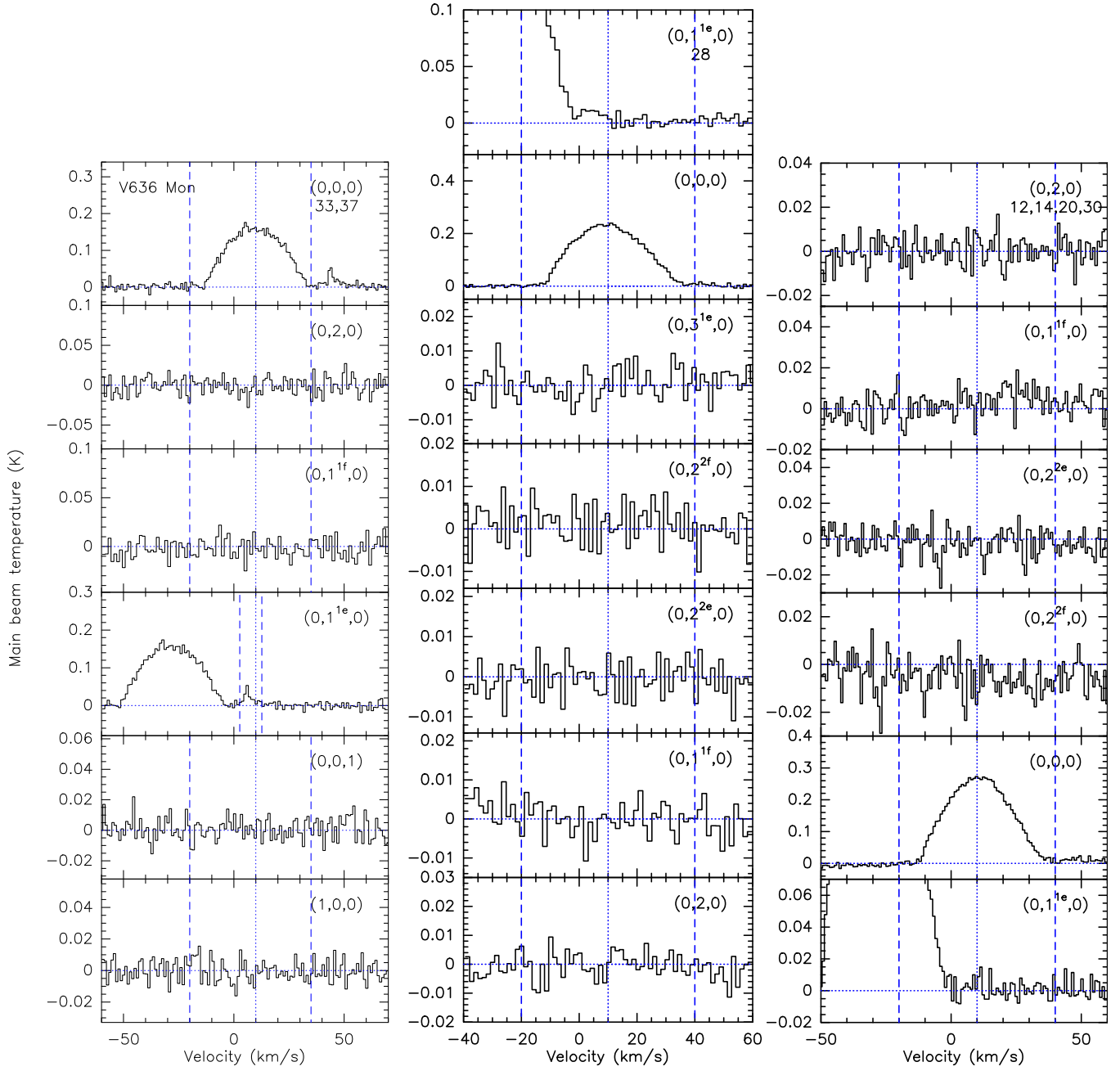


Fig. C.6: Spectra for  $J = 2-1$  (left),  $3-2$  (centre) and  $4-3$  (right) transitions of HCN towards V636 Mon. The description of the figure is the same as in the Fig. 1 caption.

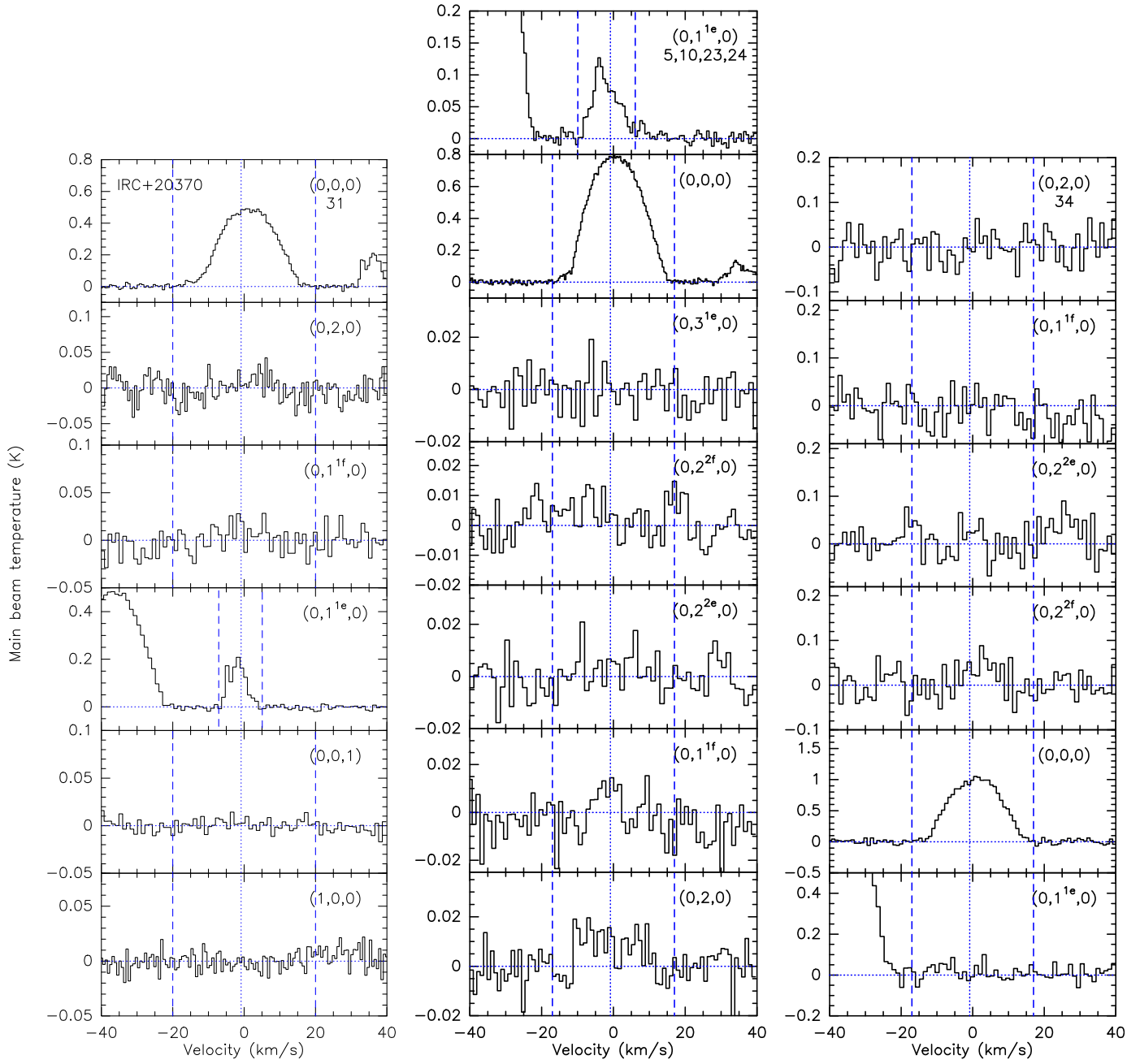


Fig. C.7: Spectra for  $J = 2-1$  (left),  $3-2$  (centre) and  $4-3$  (right) transitions of HCN towards IRC +20370. The description of the figure is the same as in the Fig. 1 caption.

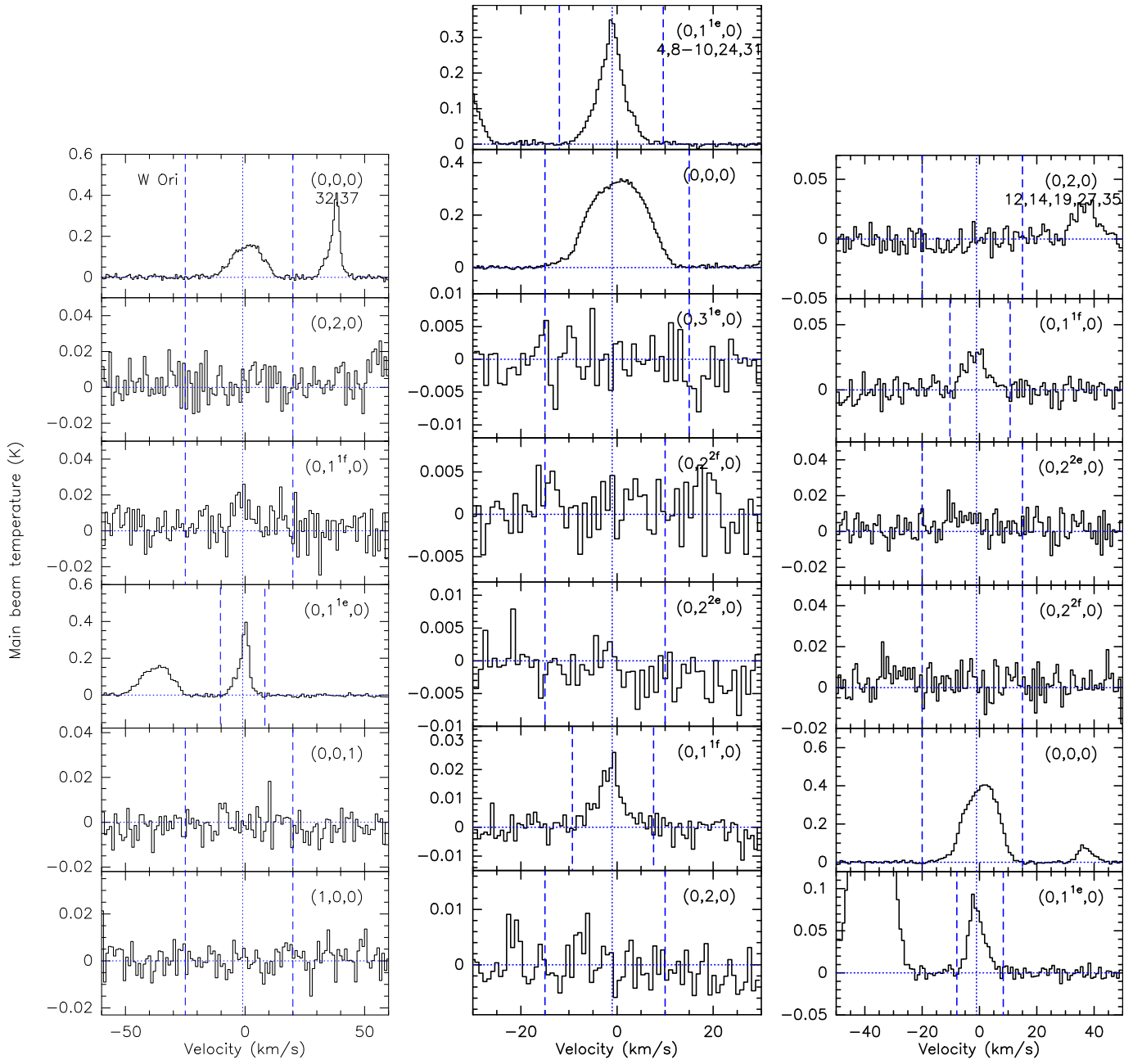


Fig. C.8: Spectra for  $J = 2-1$  (left),  $3-2$  (centre) and  $4-3$  (right) transitions of HCN towards W Ori. The description of the figure is the same as in the Fig. 1 caption.

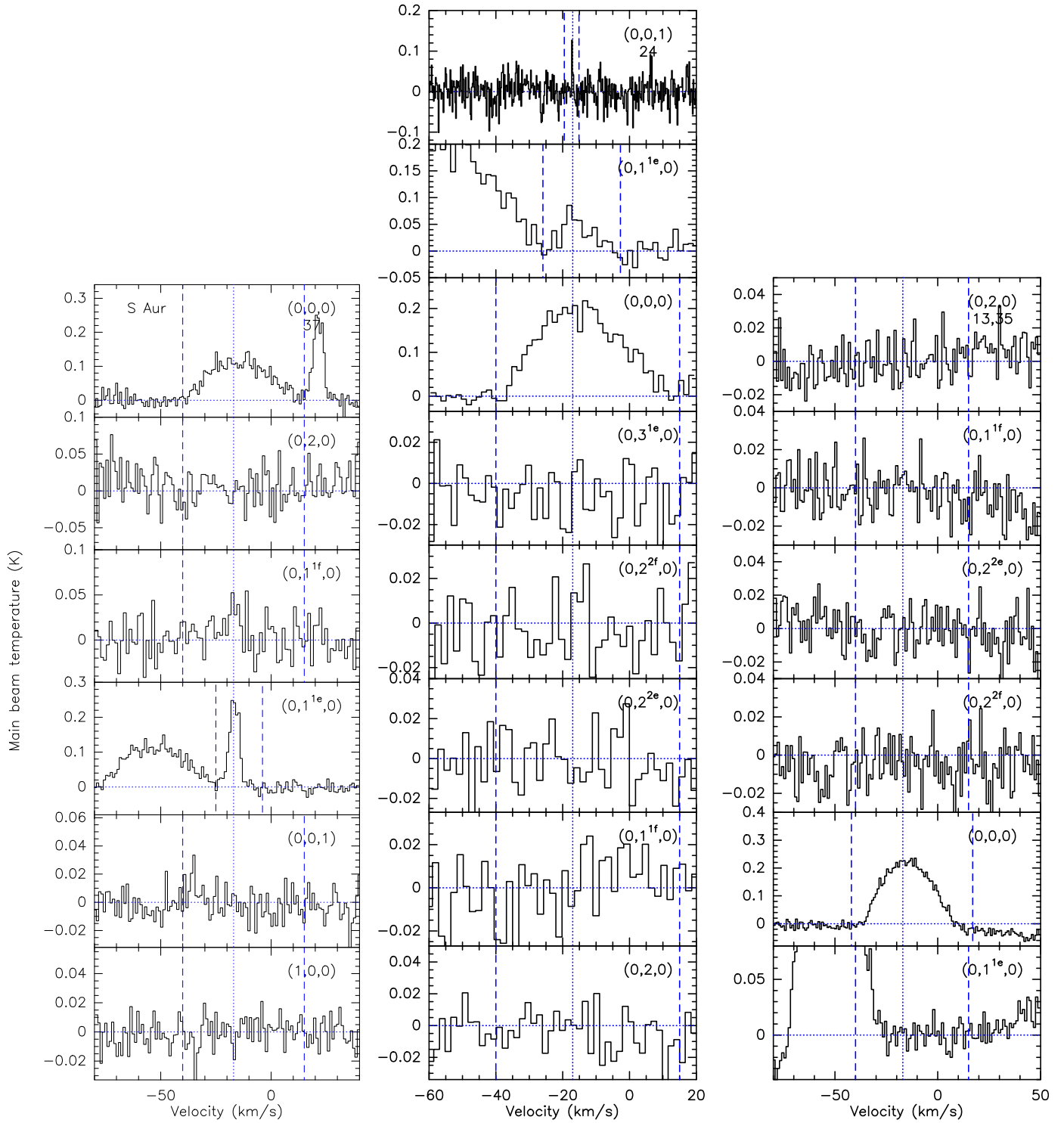


Fig. C.9: Spectra for  $J = 2-1$  (left),  $3-2$  (centre) and  $4-3$  (right) transitions of HCN towards S Aur. The description of the figure is the same as in the Fig. 1 caption.

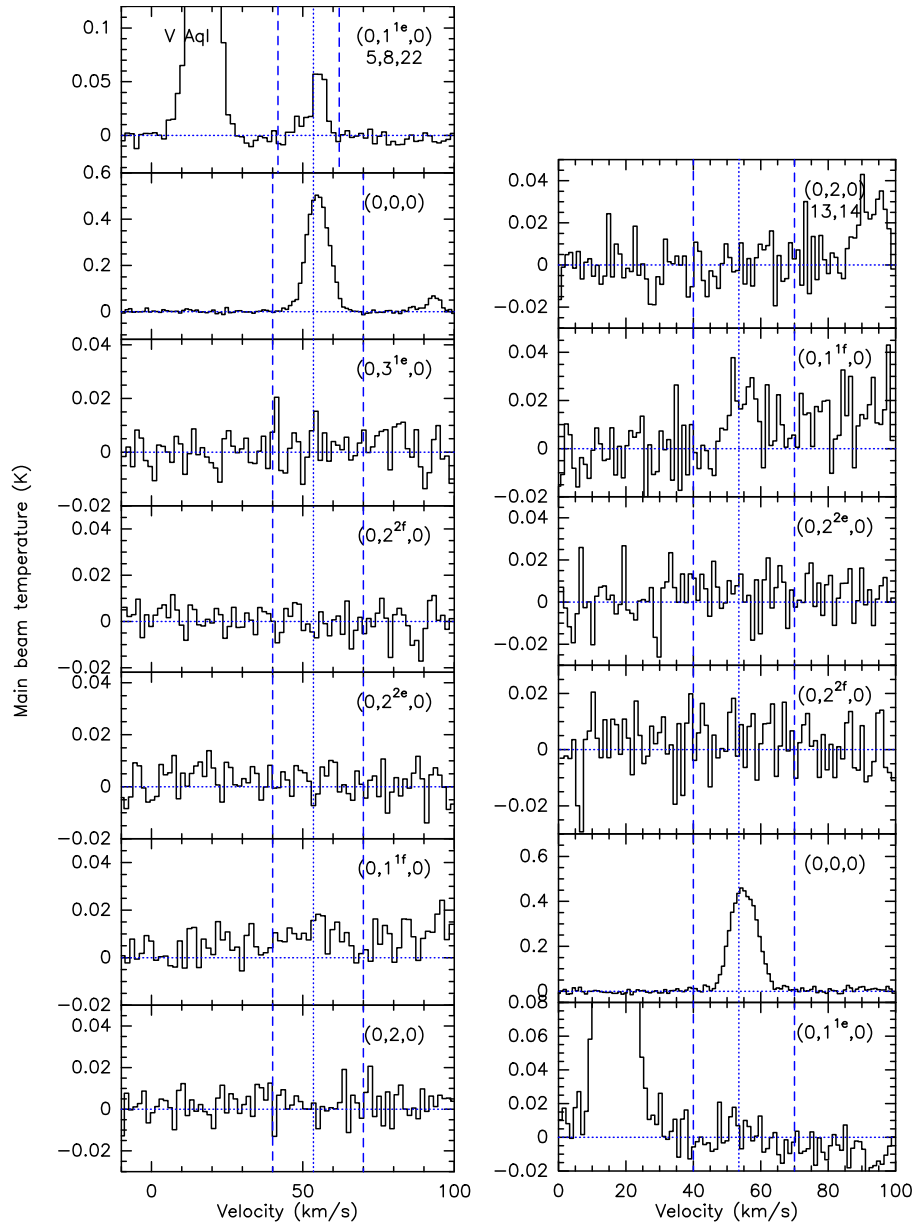


Fig. C.10: Spectra for  $J = 3-2$  (left) and  $4-3$  (right) transitions of HCN towards V Aql. The description of the figure is the same as in the Fig. 1 caption.

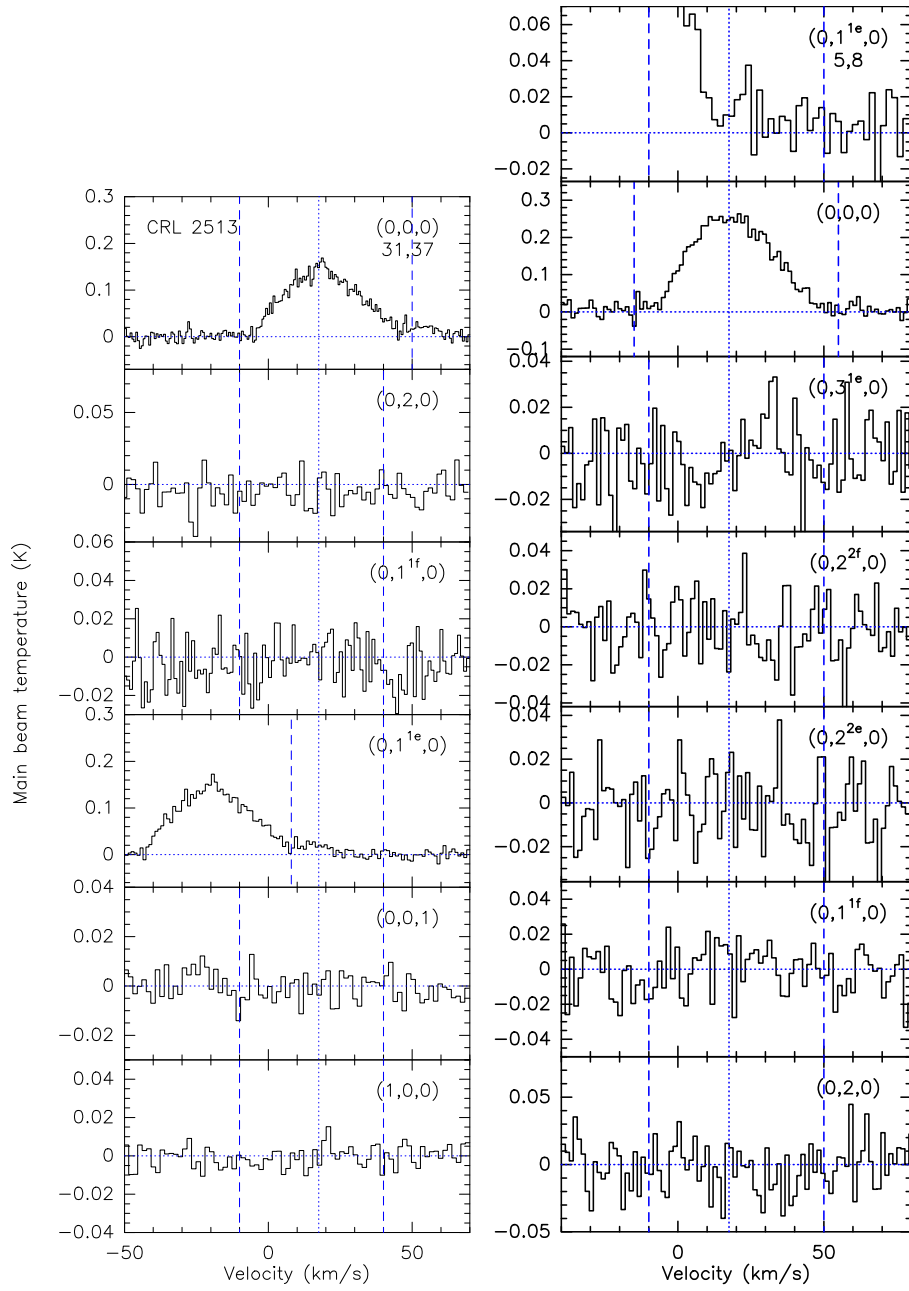


Fig. C.11: Spectra for  $J = 2-1$  (left) and  $3-2$  (right) transitions of HCN towards CRL 2513. The description of the figure is the same as in the Fig. 1 caption.

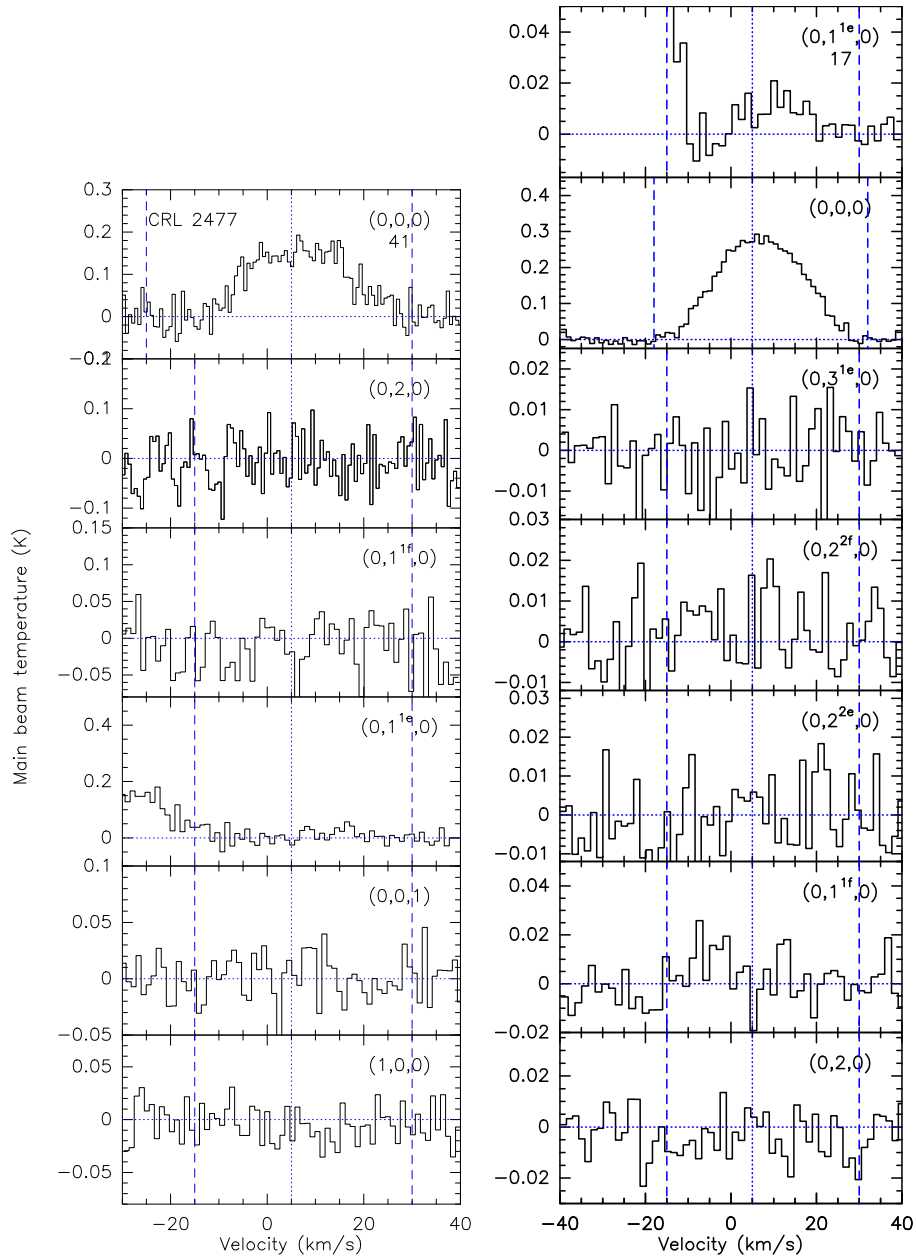


Fig. C.12: Spectra for  $J = 2-1$  (left) and  $3-2$  (right) transitions of HCN towards CRL 2477. The description of the figure is the same as in the Fig. 1 caption.



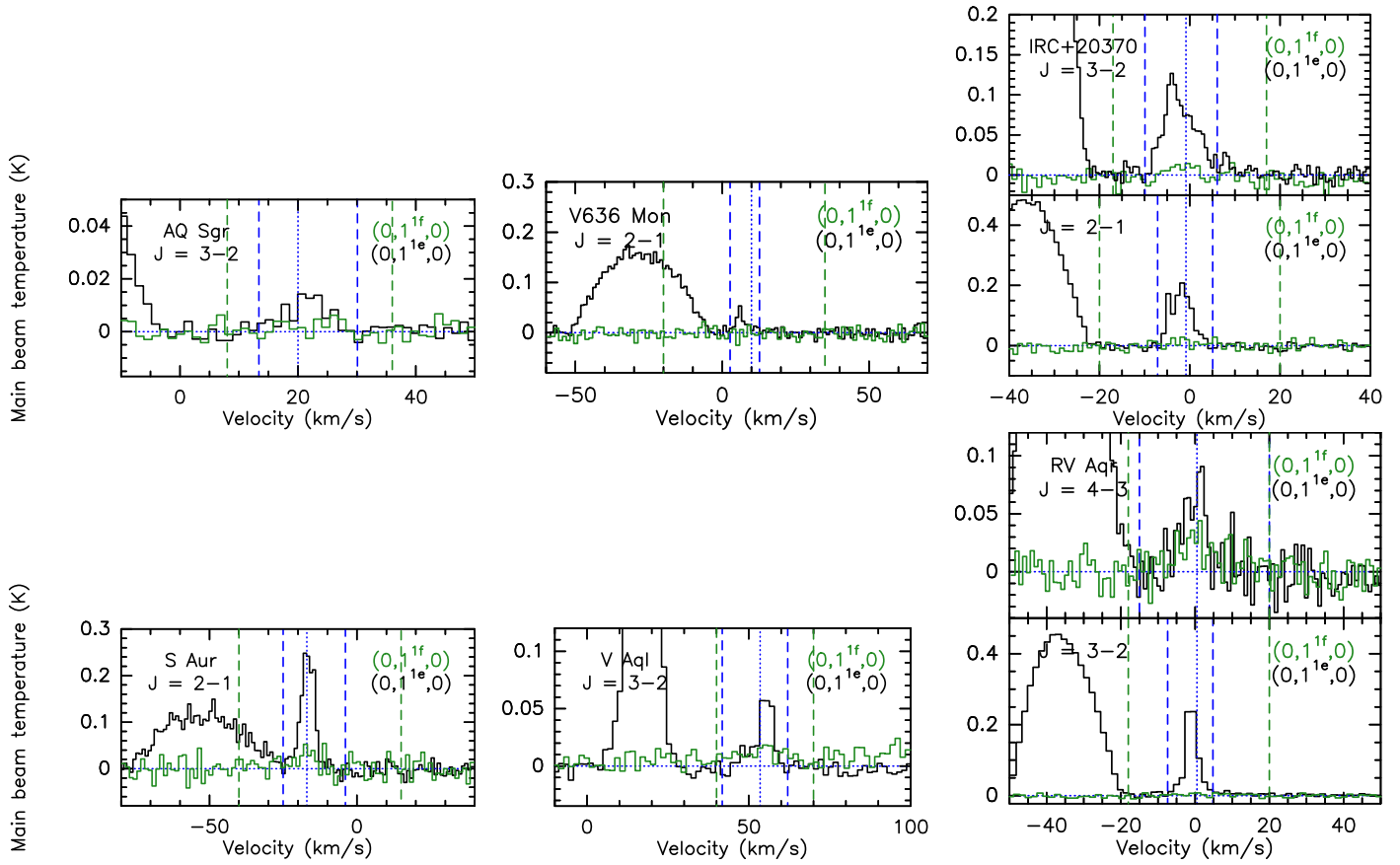


Fig. D.1: Same as for Figs. 11 and 12 towards AQ Sgr, V636 Mon, IRC+20370, S Aur, V Aql, and RV Aqr.



**Paper II: [C I] and [C II] emission in the  
circumstellar envelope of IRC +10216  
I. Observational data and NLTE modelling of  
the [C I] emission**

---

Below the publication Jeste et al. (2023) is presented in the pdf form, which is summarised in Chapter 3.

# [C I] and [C II] emission in the circumstellar envelope of IRC +10216

## I. Observational data and NLTE modelling of the [C I] emission<sup>★</sup>

M. Jeste<sup>★</sup><sup>✉</sup>, H. Wiesemeyer<sup>✉</sup>, K. M. Menten, and F. Wyrowski

Max-Planck-Institut für Radioastronomie, Auf dem Hügel 69, 53121 Bonn, Germany  
e-mail: mjeste@mpi.fr.de

Received 31 January 2023 / Accepted 22 May 2023

### ABSTRACT

**Context.** The envelopes of evolved late-type stars on the asymptotic giant branch are characterised by a complex chemistry that is close to thermochemical equilibrium near the stellar surface; however, in the outer envelope, it is dominated by radical reactions, assisted by a photo-chemistry driven by the interstellar radiation field.

**Aims.** The study at hand aims to describe the distribution of atomic carbon, C<sup>0</sup>, throughout the envelope, in support of an improved understanding of its photo-chemistry. Additionally, we also briefly discuss the observation of [C II] emission towards the star.

**Methods.** We obtain spectra of the [C I] <sup>3</sup>P<sub>1</sub> → <sup>3</sup>P<sub>0</sub> fine structure line (at 492.160700 GHz) at projected distances of up to 78'' from the star. The line profiles are characterised by both direct fitting of Gaussian components, and by modelling the observed line of the [C I] triplet. We also report the detection of the <sup>2</sup>P<sub>3/2</sub> → <sup>2</sup>P<sub>1/2</sub> line (at 1900.5369 GHz) from the C<sup>+</sup> fine structure singlet at the central position and its non-detection at 32'' from the star.

**Results.** The overall picture of the [C I] emission from IRC +10216 agrees with more limited previous studies. The satisfying agreement between the observed and modelled line profiles, with emission at the systemic velocity appearing beyond one beam (13'' HPBW) from the star, rules out that the C<sup>0</sup> is located in a thin shell. Given that the bond energy of CO falls only 0.1 eV below the ionisation threshold of C<sup>0</sup>, the absence of observable [C II] emission from sightlines beyond a projected distance of ~10<sup>17</sup> cm (≳20''–30'') from the star (adopting a distance of 130 pc) does not contradict a scenario where the majority of C<sup>0</sup> is located between that of CO and C<sup>+</sup>, as expected for an external far-ultraviolet radiation field. This conjecture is also corroborated by a model in which the C<sup>0</sup> shell is located farther outside, failing to reproduce the [C I] line profiles at intermediate sky-plane distances from the star. Comparing a photo-chemical model adopted from literature with the simplifying assumption of a constant C<sup>0</sup> abundance with respect to the H<sub>2</sub> density (with the 1/r<sup>2</sup> fall-off of a mass-conserving expansion flow), we constrain the inner boundary of the [C I] emitting shell, located at ~10<sup>16</sup> cm from the star.

**Key words.** stars: AGB and post-AGB – stars: carbon – circumstellar matter

## 1. Introduction

Low- to intermediate-mass stars (0.8–8 M<sub>⊙</sub>) evolve to the asymptotic giant branch (AGB) when they are close to the end of their lives. These objects go through intense mass loss forming a circumstellar envelope (CSE) around them that contains dust and molecules (Höfner & Olofsson 2018). Many of the 241 molecules that so far have been identified in astronomical sources were detected in the CSEs of AGB or red supergiant stars (McGuire 2022), which therefore efficiently enrich the interstellar medium (ISM).

The abundances of carbon and oxygen at the stellar surface reflect the interplay of nucleosynthesis and convection in the stellar interior. Stars with C/O > 1 are defined as carbon-rich, those with C/O < 1 as oxygen-rich, and those with C/O ≈ 1 are the S-type stars. The abundance of these atoms is mainly due to the third dredge-up, where the material is brought up to the

stellar surface and subsequently ejected into the envelope thanks to thermal pulses (TPs) forming in response to instabilities in the helium-burning shell. The third dredge-up occurs after each TP (except for a few initial ones, depending on the model, e.g. Weiss & Ferguson 2009), influencing the C/O ratio in the envelope (Karakas & Lattanzio 2014, further references therein), while the number of TPs depends on the mass loss experienced by the star before it leaves the AGB.

IRC+10216 (= CW Leonis) is the archetypal carbon-rich AGB star located close to us at a distance between 120 and 140 pc (Crosas & Menten 1997; Groenewegen et al. 2012) and losing its mass at a high rate of 2–4 × 10<sup>-5</sup> M<sub>⊙</sub> yr<sup>-1</sup> (Crosas & Menten 1997; De Beck & Olofsson 2018; Fonfría et al. 2022). The star has a luminosity of 8600 L<sub>⊙</sub> determined from the Very Large Array (VLA) imaging of the optically thick radio photosphere (Menten et al. 2012) that, for a photospheric effective temperature of 2750 K (assumed from spectral energy distribution (SED) modelling, Men'shchikov et al. 2001), entails an optical photospheric diameter of 3.8 AU, while measurements of lunar occultations in the H and K bands estimate a near-infrared diameter of 7.1 AU (Richichi et al. 2003).

The star has a very extended molecular envelope moving through the ISM. Mauron & Huggins (1999) and Dharmawardena et al. (2018) also show that the dust

<sup>★</sup> A copy of the reduced spectra is only available at the CDS via anonymous ftp to [cdsarc.cds.unistra.fr](https://cdsarc.cds.unistra.fr) (130.79.128.5) or via <https://cdsarc.cds.unistra.fr/viz-bin/cat/J/A+A/675/A139>

<sup>\*\*</sup> Member of the International Max Planck Research School (IMPRS) for Astronomy and Astrophysics at the Universities of Bonn and Cologne.

continuum emission extends out to  $\sim 200''$  or more from the central star. The interphase between the envelope and the ISM is seen in the ultraviolet images taken with the Galaxy Evolution Explorer (GALEX) satellite (Sahai & Chronopoulos 2010), and at far-infrared wavelengths with the Photodetector Array Camera and Spectrometer (PACS) and Spectral and Photometric Imaging Receiver (SPIRE) instruments aboard *Herschel* (Ladjal et al. 2010). A similar interaction between the two environments is also seen in Mira A as the star shows a bow-shock feature in the southward direction, and a tail extending in the north. The star has a space velocity of  $130 \text{ km s}^{-1}$  (Martin et al. 2007), which is larger than what is seen in IRC +10216 ( $\sim 91 \text{ km s}^{-1}$  in Sahai & Chronopoulos 2010). More than 80 molecular species have been detected in the CSE of IRC +10216 so far (see Cernicharo et al. 2000; Agúndez et al. 2014; De Beck & Olofsson 2018; Pardo et al. 2022, and many other publications cited therein). These molecules are important probes of the chemical processes at work in the envelope as different molecules at various levels of excitation trace distinct regions in the CSE: parent molecules such as HCN and  $\text{C}_2\text{H}_2$  form in the inner, hotter part of the envelope (e.g. Cernicharo et al. 2015; Agúndez et al. 2020, further references therein), whereas the daughter species (i.e. mainly photodissociation products of the former) are found to be present in the outer parts (see Fig. 1 in Li et al. 2014; Millar & Herbst 1994; Millar et al. 2000; Van de Sande et al. 2018 for a further understanding of the circumstellar chemistry).

The distribution of the CO molecule, which is an important tracer of the history of mass loss, is quite widespread in the star's CSE: Observations with the Institut de radioastronomie millimétrique (IRAM) 30 m telescope (Cernicharo et al. 2015) and with the Submillimeter Array (SMA) and Atacama Large Millimeter Array (ALMA) interferometers (Guélin et al. 2018) show almost concentric shells, with strong CO emission up to the photodissociation radius of  $180''$  after which there is a sudden drop (best discernible in the single-dish maps, Cernicharo et al. 2015) owing to the molecule's photodissociation yielding atomic carbon which is further ionised to form  $\text{C}^+$  (Morris & Jura 1983; Mamon et al. 1988; Schöier & Olofsson 2001; Groenewegen 2017; Saberi et al. 2019).

Emission in the two fine-structure lines of neutral atomic carbon,  $\text{C}^0$ , from the  $^3\text{P}_1 \rightarrow ^3\text{P}_0$  and  $^3\text{P}_2 \rightarrow ^3\text{P}_1$  transitions near 492 and 809 GHz, respectively, was first detected in molecular clouds by Phillips et al. (1980) and Jaffe et al. (1985). [C I] emission<sup>1</sup> is recognised as a valuable tracer for environments characterised by a range of molecular gas fractions occurring in photo-dissociation regions, while either  $\text{C}^+$  or CO trace them only partially (Papadopoulos et al. 2004, further references therein). However, for circumstellar envelopes, very few studies exist of these [C I] lines. IRC +10216 has been targeted in the  $^3\text{P}_1\text{--}^3\text{P}_0$  line with the Caltech Submillimeter Observatory (CSO) 10.4 telescope and the *James Clerk Maxwell* 15 m Telescope (JCMT; Keene et al. 1993; van der Veen et al. 1998). As suggested by Keene et al. (1993), another important carrier of carbon in C-rich circumstellar envelopes is acetylene ( $\text{C}_2\text{H}_2$ ), contributing to the shielding against interstellar UV radiation, and acting as a precursor molecule for the subsequent photo-chemistry (Santoro et al. 2020; Siebert et al. 2022).

Thanks to the triple bond between carbon and oxygen, CO has a high bond energy,  $11\,109.2 \pm 4.1 \text{ meV}$  (Darwent 1970) that is slightly below the ionisation energy of  $\text{C}^0$ ,

$11\,260.2880 \pm 0.0011 \text{ meV}$  (Glab et al. 2018). In an environment characterised by internal or external radiation fields and by gas density gradients, the production of free carbon by photodissociation of CO is therefore accompanied by the production of  $\text{C}^+$  (of which minor amounts might arise already before, from the photolysis of carbon-bearing species that dissociate easier than CO). Since the ionisation threshold of carbon falls significantly below that of hydrogen (13.598 eV; Jentschura et al. 2005), the  $^2\text{P}_{3/2} \rightarrow ^2\text{P}_{1/2}$  transition from the  $\text{C}^+$  fine-structure singlet originates from both the warm ionised gas phase of the interstellar medium and from cold, neutral, and partially molecular gas ( $T \sim 10\,000 \text{ K}$  and  $\sim 100 \text{ K}$ , respectively; Wolfire et al. 2003, with further references therein). Its emission from diffuse gas is therefore widespread. However, despite the interest in the  $\text{C}^+$  emission for the analysis of the carbon budget in circumstellar environments, detections of the [C II] line were restricted to post-AGB stars (e.g. Cerrigone et al. 2012; Bujarrabal et al. 2016), before it was found in IRC +10216 (Reach et al. 2022).

Given the importance of atomic and ionised carbon in the circumstellar envelope of IRC +10216, we want to constrain the spatial distribution of the atom. In this publication, we discuss the observations we conducted and the data reduction methods in Sect. 2, followed by the presentation of the obtained spectra and their analysis (Sect. 3). We then discuss the physical constraints we obtained and contextualise them in view of the existing literature in Sect. 4 and conclude our work in Sect. 5. A more detailed model, including dedicated photo-chemical network and radiative transfer calculations, will be presented in a follow-up study (Wiesemeyer et al., in prep., hereafter Paper II), along with the analysis of the variable [C II] emission.

## 2. Observations and data reduction

### 2.1. Observations of the [C I] line

We performed observations towards IRC+10216 in the  $^3\text{P}_1 \rightarrow ^3\text{P}_0$  fine structure line of atomic carbon with the Atacama Pathfinder Experiment (APEX) 12 m sub-millimetre telescope<sup>2</sup>. The star was observed under the project ID M-0108.F-9515C-2021 between 2021 November 15 and 30 with the nFLASH460 receiver, a new facility frontend built by the Max-Planck-Institut für Radioastronomie (MPIfR) for APEX, while a fast Fourier transform spectrometer (FFTS; Klein et al. 2006) was used as the backend, providing a spectral resolution of 61 kHz. nFLASH460 is a dual sideband receiver with two polarisations and covers an intermediate frequency (IF) range from 4–8 GHz. We tuned the lower sideband (LSB) to the studied [C I] line at a frequency of 492.160700 GHz (Haris & Kramida 2017). The observations took place in good weather with a precipitable water vapour level below 0.6 mm, translating to sightline system temperatures ranging from 400 to 1200 K. We adopted a forward efficiency ( $\eta_f$ ) of 0.95 and a main beam efficiency ( $\eta_{\text{mb}}$ ) of 0.48<sup>3</sup> to calibrate the spectra to the main-beam brightness temperature scale ( $T_{\text{mb}}$ ). At the frequency of 492 GHz, the telescope has a beamwidth of  $12.7''$  full width at half maximum (FWHM). The integrations were carried out in a cross along right-ascension and declination offsets, comprising 33 positions, for a total of 9 h equally shared between the target and a reference  $1000''$  away, safely outside of the astrosphere. The observed

<sup>1</sup> We denote neutral and ionised carbon as  $\text{C}^0$  and  $\text{C}^+$ , respectively, while their fine-structure line emission is labelled [C I] and [C II], respectively.

<sup>2</sup> This publication is based on data acquired with APEX, which is a collaboration between the MPIfR, the European Southern Observatory, and the Onsala Space Observatory.

<sup>3</sup> <https://www.apex-telescope.org/telescope/efficiency/>

sky-plane positions are spaced by 6.5'' out to 26'' from the star, and by 13'' beyond, up to a maximum distance of 78''. Frequent line pointings were performed on the CO(4–3) line, with the secondary wobbling with a throw of 120'' at a frequency of 1.5 Hz.

We used the CLASS software from the GILDAS<sup>4</sup> package (Pety 2005) to reduce and further analyse the data. The individual steps consist of masking irrelevant parts of the spectra, subtracting linear baseline fits (with baseline noise figures ranging from 38 mK to 120 mK on  $T_{\text{mb}}$  scale), and averaging adjacent spectral channels, so as to increase the signal-to-noise ratio while preserving an appropriate velocity resolution of 0.2 km s<sup>-1</sup>, corresponding to five spectral channels in the unprocessed data. Spectra from equivalent positions (or distances from the centre) are averaged with  $1/\sigma^2$  weighting (i.e. the inverse of the squared baseline noise).

## 2.2. Observations of the [C II] line

The  $^2P_{3/2} \rightarrow ^2P_{1/2}$  fine-structure line of ionised carbon, [C II], at 1900.5369 GHz was observed with the upGREAT 7-pixel, dual polarisation receiver array for THz spectroscopy (Risacher et al. 2018) aboard the Stratospheric Observatory For Infrared Astronomy (SOFIA). The [C II] line was tuned to the upper sideband, so as to avoid a contamination by telluric features from the image band of the mixer (operation at THz frequencies precludes sideband separation). The data were acquired on a total of twelve SOFIA flights, spanning 1.4 cycles of the stellar surface pulsation of 630 days (Menten et al. 2012). Two more flights targeting IRC +10216 were conducted in 2021 and 2022. The typical (median) on-sky observing time was 1 h (including calibrations and updates of the gyroscope settings), of which typically 40 min were used for integrating towards the target, equally shared between the on-position and the off-positions on either side (chop-and-nod method, with a throw of 2'). The data were taken on subscan granularity (40 s including both chop phases) at elevations ranging from 23° to 52°. Median water vapour columns of 10  $\mu\text{m}$  (as referred to zenith) and single-sideband receiver temperatures of 1770 K resulted in a median single-sideband system temperature of 1870 K.

The spectroscopic analysis was performed with fast Fourier transform spectrometers (XFFTSs, Klein et al. 2012), covering the instantaneous 4 GHz wide bandpass with 16384 channels, resulting in a channel separation of 244 kHz. Data processing followed steps similar to those applied to the [C I] data; here we removed second-order spectral baselines and averaged them to a spectral resolution of 1.5 km s<sup>-1</sup>, resulting in a baseline noise of 16 mK (rms value, in Rayleigh-Jeans equivalent main-beam brightness temperature). The conversion from backend count rates to forward-beam antenna temperatures was done using calibration loads at ambient and cold temperature (typically around 295 and 100 K, respectively), and adopting a forward efficiency of 0.97. The beam efficiency was calibrated by frequent observations of Mars, and determined to a coupling ranging from  $\eta_{\text{mb}} = 0.65$  to 0.70 (i.e. to the physically possible limit set by the design of the telescope's optics). This interval reflects the inherent calibration uncertainty. At the frequency of the [C II] line, the main beam of the instrument's Airy pattern has a width of 14'' (FWHM), which is merely 10% wider than the beam at the frequency of the  $^3P_1 \rightarrow ^3P_0$  [C I] transition and thus facilitates the comparison of the line profiles.

## 3. Results

### 3.1. [C I] emission

Since the CO emission from the envelope is largely centrosymmetric (Cernicharo et al. 2015), and C<sup>0</sup> and C<sup>+</sup> are products of photochemistry, we averaged the spectra from the half-beam sampled, equivalent offsets from the star (Fig. 1). Evidence for deviations from this symmetry is discussed below; individual spectra, extending to up to 78'' from the star, are shown in Fig. A.1. We have analysed the spectra using various methods, from a simple phenomenological description assuming constant excitation to a radiative transfer model of the non-local thermodynamic equilibrium (non-LTE) excitation of [C I] throughout a homogeneous envelope, characterised by constant gradients in temperature and density, and expanding at a constant velocity.

### 3.2. [C I] emission: Line profile fitting

The emission from the centre and the innermost sightlines (up to a 13'' projected distance) displays well-separated blue- and red-shifted peaks (horn-shaped line profiles) from the hemispheres expanding towards and away from the observer, respectively. Beyond the 19.5'' offset, the components start to merge because the sightline-projected expansion velocity decreases. We have fit the observations (up to 26'' offsets) with individual Gaussian profiles by masking the emission component at the respective opposite velocity. The resulting parameters are reported in Table A.1. At 39'' significant emission can only be detected after smoothing these spectra to a resolution of 3 km s<sup>-1</sup> with a rather flat-topped profile of 0.08 K and rms noise of 31.8 mK. For closer inspection, we provide the spectrum of the sightline in Fig. A.2. At the 52'' offset and beyond, we see no significant emission anymore.

The individual spectra (Fig. A.1) observed at the same distance from the star show no strikingly remarkable differences. The central sightline features a slightly asymmetric double-peak profile, which can be attributed to a weak absorption in the blue wing, because in the corresponding hemisphere the sightline crosses layers of decreasing excitation. We note, however, that the blue- and red-shifted fractions of the line area display the opposite behaviour. The same holds for the observations of Keene et al. (1993) at 15'' (FWHM) resolution, who reported peak temperatures of less than 0.4 K, falling 0.3 K below ours. While the discrepancy may be partly due to the individual coupling of the [C I] emission to the different main beams or due to residual pointing or calibration errors, we note that our line flux of 3.1 K km s<sup>-1</sup> is in agreement with that of Keene et al. (1993). We concede that with the  $\approx 30$  yr time span between these observations and ours, the [C I]-emitting shell has expanded by almost 90 AU (or 0.7'' at the adopted distance of 130 pc). While such a distance is too short to be noticeable in the beams of single-dish sub-millimetre telescopes, it may be long enough (17 pulsation periods of 630 days, Menten et al. 2012) to possibly alter the line profiles if the shell and its photochemistry are not in a steady state. From the asymmetry of the line profile, which is weak at most, we conclude that opacity effects cannot be very important in the formation of the line. At offsets of -19'' and -26'' (in either right ascension or declination), the spectra show more centre-filling emission than the direct fits do (i.e. around the systemic velocity of -26.5 km s<sup>-1</sup>).

### 3.3. C<sup>0</sup> excitation modelling

Given the ad hoc approach of the direct fitting, we now use a more sophisticated method to model the excitation of [C I]

<sup>4</sup> <https://www.iram.fr/IRAMFR/GILDAS/>

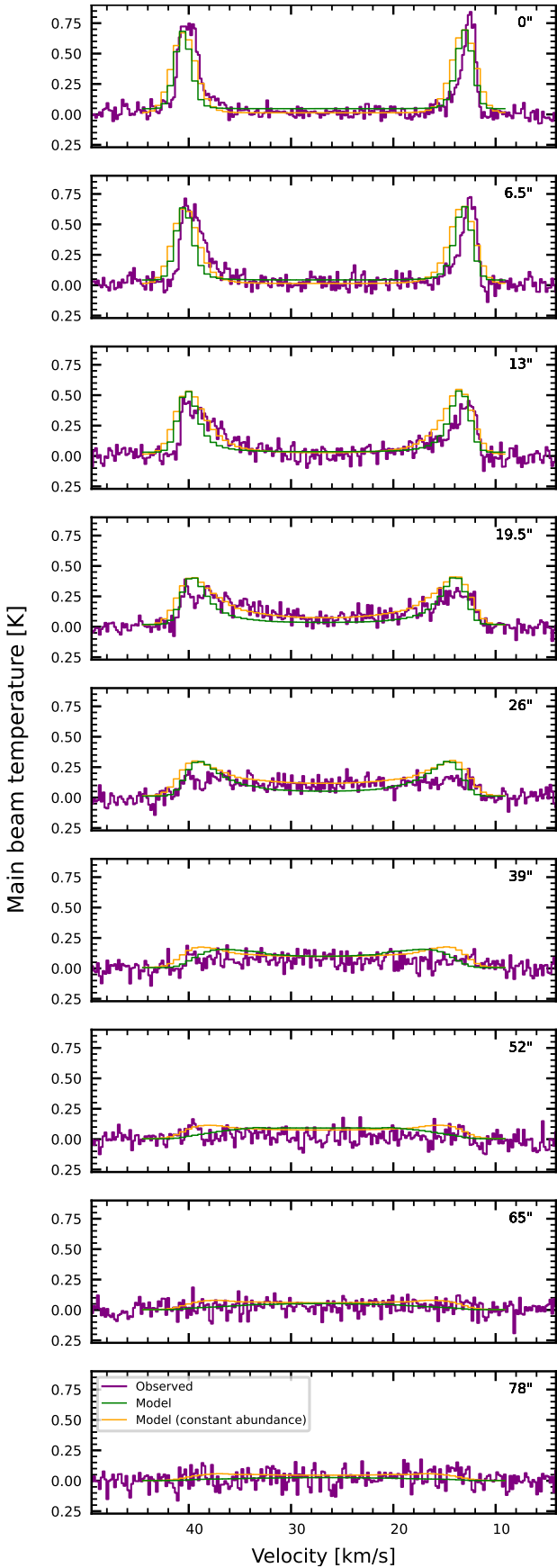


**Fig. 1.** [C I]  ${}^3\text{P}_1 \rightarrow {}^3\text{P}_0$  averaged spectra towards nine offsets from the star (in purple) overlaid with the RATRAN model for variable abundance (in green) and constant abundance (in orange).

**Table 1.** Input parameters for the RATRAN model of the [C I] emission.

$D$ (pc)	$\dot{M}$ ( $M_{\odot} \text{ yr}^{-1}$ )	$r_{\text{in}}$ (cm)	$r_{\text{out}}$ (cm)	$n_{\text{H}_2}(r_{\text{in}})$ ( $\text{cm}^{-3}$ )	$T(r_{\text{in}})$ (K)	$v_{\text{exp}}$ ( $\text{km s}^{-1}$ )	$\Delta v$
130	$2 \times 10^{-5}$	$2.3 \times 10^{16}$	$1.9 \times 10^{18}$	$4.5 \times 10^4$	156	14.0	1.0

**Notes.** The [C I] abundance profile is taken from Fig. 3 of Reach et al. (2022). A second model uses a constant abundance (with respect to hydrogen nuclei) of  $n(\text{C}^0)/n(\text{H}) = 4 \times 10^{-5}$  and  $r_{\text{in}} = 4 \times 10^{16}$  cm. We note that  $D$  is the distance to the source,  $r_{\text{in}}$  and  $r_{\text{out}}$  are the inner and outer radius of the shell, respectively,  $v_{\text{exp}}$  is the expansion velocity, and  $\Delta v$  is the line width ( $1/e$  half-width). The power-law indices for the fall-off of density and kinetic temperature (gas and dust temperature are assumed to be equal) with distance from the star are  $-2$  and  $-0.50$ , respectively. For comparison, the temperature power-law index for purely adiabatic cooling at a constant expansion velocity would be  $-4/3$  (Crosas & Menten 1997).

throughout an envelope characterised by density, abundance, and temperature gradients. We performed radiative transfer modelling to describe the observed spectral lines and determine the abundance and temperature profiles. We used the 1D radiative transfer code RATRAN<sup>5</sup> (Hogerheijde & van der Tak 2000), where a spherically symmetric model is assumed. For the model, we take a distance of 130 pc to the star with a mass-loss rate of  $2 \times 10^{-5} M_{\odot} \text{ yr}^{-1}$  (Cernicharo et al. 2015; Reach et al. 2022; Fonfria et al. 2022). Furthermore, the gas is expanding at a velocity of  $14 \text{ km s}^{-1}$ . The line profile function is Gaussian with a  $1/e$  width of  $2.0 \text{ km s}^{-1}$ . Under a turbulent contribution of  $1.5 \text{ km s}^{-1}$  (based on observations of CO and  $\text{C}_2\text{H}$ , De Beck et al. 2012), the resulting thermal width of  $(\sqrt{2.0^2 - 1.5^2} = 1.3) \text{ km s}^{-1}$  would be too large to be accounted for by our temperature profile. We note, however, that non-thermal line broadening in circumstellar envelopes is poorly constrained, and that magnetohydrodynamic turbulence cannot be ruled out on grounds of CN Zeeman measurements revealing significant deviations from a homogeneous magnetic field structure (Duthu et al. 2017). In such a picture, the fact that the emissions of CO and [C I] trace spatially distinct envelope regions could then reconcile the different estimates of turbulent line broadening. The excitation model accounts for far-infrared pumping by the dust emission (with an assumed gas-to-dust ratio of 100), and assumes that the temperatures of gas and dust are tightly coupled.

Reach et al. (2022) assume that the abundances of  $\text{C}^+$  and  $\text{C}^0$  in the outer envelope derive entirely from the photo-dissociation of CO (see their Fig. 3). The abundance of the latter is parameterised by the photo-destruction radius  $r_{\text{phot}}$  and steepness parameter  $\alpha$ ,

$$n(\text{CO})/n(\text{H}_2) = [\text{C}/\text{H}_2] \exp(-\ln 2(r/r_{\text{phot}})^{\alpha}). \quad (1)$$

Here we adopt their model with  $r_{\text{phot}} = 3.5 \times 10^{17}$  cm, and  $\alpha = 3.0$  (cf. Saberi et al. 2019), for an underlying elemental abundance of  $[\text{C}/\text{H}_2] = 8 \times 10^{-4}$ , of which at the inner boundary of the model 75% is contained in CO, while the remainder accounts for acetylene ( $\text{C}_2\text{H}_2$ ) and HCN. The model parameters are summarised in Fig. 4 and Table 1. While this model provides a satisfactory description of the azimuthally averaged spectra (Fig. 1, baseline noise 67–128 mK rms) or on individual positions (Fig. A.1), we have to test whether it entails uniqueness or not. We therefore overlay the corresponding spectra obtained from adjusting the spectra obtained from a constant-abundance

<sup>5</sup> <https://personal.sron.nl/~vdtak/ratran/frames.html>

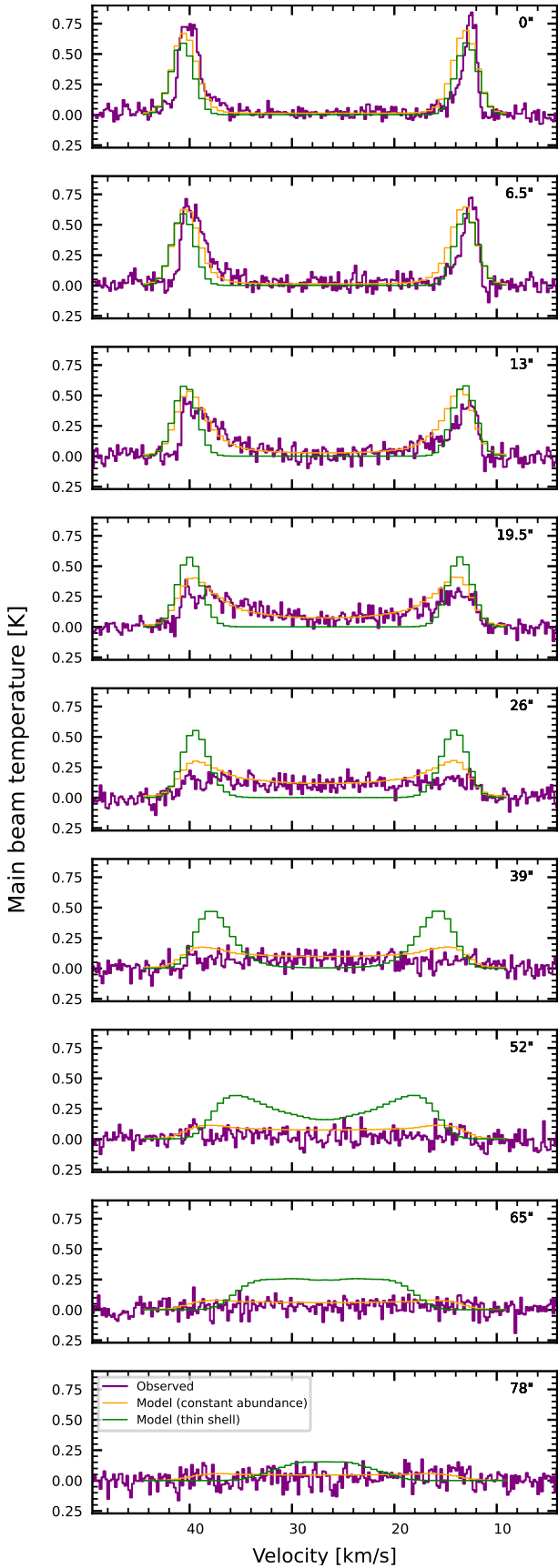


**Fig. 2.** As Fig. 1, except that the [C I] spectra are overlaid with those from the constant-abundance, thick-shell model (in orange), and a thin-shell model (in green). The latter clearly fails on all sightlines except for the two innermost ones.

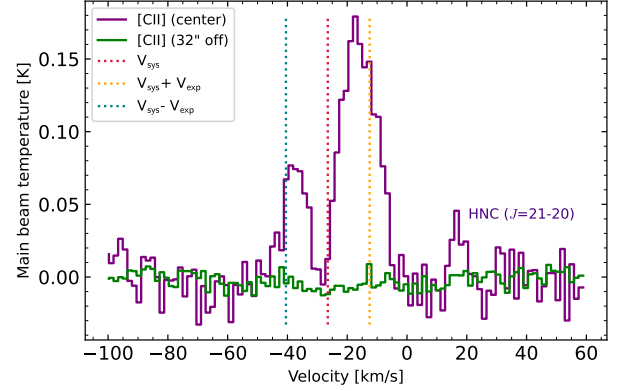


**Fig. 3.** [C II]  ${}^2P_{3/2} \rightarrow {}^2P_{1/2}$  spectrum (2015–2021 average) towards the central line of sight. The average off-centre spectrum (at 32'' from the centre) is overlaid in green. The systemic velocity ( $V_{\text{sys}}$ ) is marked with a red dotted line, and  $V_{\text{sys}}+V_{\text{exp}}$  and  $V_{\text{sys}}-V_{\text{exp}}$  values are marked with an orange and blue dotted line, respectively, where  $V_{\text{exp}}$  is the gas terminal expansion velocity. The emission feature at 15 km s $^{-1}$  could be from the HNC  $J = 21-20$  transition, and is marked as such.

model to the observed ones. A reasonable fit can be obtained with  $n(\text{C}^0)/n(\text{H}) = 4 \times 10^{-5}$  and  $r_{\text{in}} = 4 \times 10^{16}$  cm, but otherwise the model has the same parameters. This abundance falls an order of magnitude below that of elemental carbon (e.g.  $[\text{C}/\text{H}] = 2.1 \times 10^{-4}$  from young B-type stars, Nieva & Przybilla 2012), because it attributes elemental carbon to  $\text{C}^0$  at distances from the star where it should still be taken up by mainly CO.

Figure 1 shows both models overlaid on the observations, reproducing a weakly self-absorbed blue-shifted peak towards the centre and the overall distribution of the [C I] emission. On the innermost sightlines, both models reproduce the observed spectral profiles reasonably well. At 19.5'' from the star, the variable-abundance model somewhat underestimates the emission arising closer to the systemic velocity, by 1–2  $\sigma_{\text{rms}}$ , whereas the constant abundance model works well. Beyond this offset, both models agree with each other fairly well. We infer that the model of Reach et al. (2022) can be used to describe the inner boundary of the  $\text{C}^0$  shell; whereas, in the constant-abundance model, a  $\text{C}^0$  abundance that is a factor two higher could be compensated for by displacing the inner boundary from  $2.3 \times 10^{16}$  cm outwards to  $4 \times 10^{16}$  cm. Such a degeneracy reflects the scaling expected from the adopted density and temperature profiles and the spherical symmetry. Shifting the inner boundary even more towards the photo-destruction radius of CO indeed brings the abundance of  $\text{C}^0$  required for a good fit closer to the cosmic, elemental carbon abundance. However, an authoritative chemical model cannot be deduced from these observations alone. We, therefore, continue with a closer look at the [C II] emission from the central sightline.

### 3.4. [C II] emission

The average [C II]  ${}^2P_{3/2} \rightarrow {}^2P_{1/2}$  spectra from the central sightline and at 32'' from the star are shown in Fig. 3. Unlike the [C I]  ${}^3P_1 \rightarrow {}^3P_0$  emission, the [C II] emission is only detected towards the central pixel of the upGREAT array. The outer ring of the array’s hexagonal layout displays no detectable [C II] emission. This finding, and the broader components of the strongly asymmetric double-peak profile (FWHM 8.1 and 13.4 km s $^{-1}$  in the blue- and red-shifted peak, respectively), which are less pronounced than that of [C I], indicate that the emission cannot solely originate from the outer boundary of the circumstellar envelope, exposed to the interstellar radiation field. Additionally,

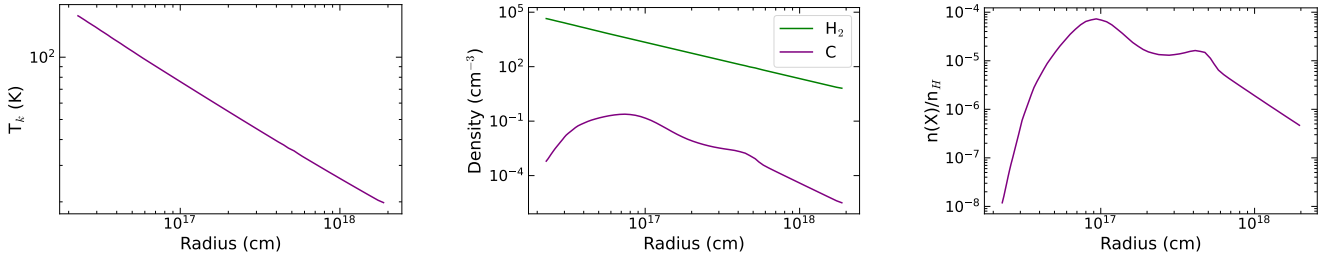


**Fig. 4.** Model profiles of (left) kinetic temperature, (centre) densities of  $\text{C}^0$  and  $\text{H}_2$  (the latter taken from Reach et al. 2022), and (right)  $\text{C}^0$  abundance (from Reach et al. 2022), used as input for the RATRAN model.

there is an emission feature present at  $15 \text{ km s}^{-1}$  velocity, which could be from the HNC  $J = 21-20$  transition. This line's small width ( $\sim 5 \text{ km s}^{-1}$ ), which is much smaller than the IRC+10216 CSE's terminal velocity, suggests an origin close to the stellar photosphere, following the conclusions Patel et al. (2009, 2011) drew for similarly narrow vibrationally excited lines from various molecules. Consistent with Reach et al. (2022), we do not detect any emission from the  $^{13}\text{C II}$  ion. Furthermore, the [C II] emission was found to be variable on a timescale corresponding to that of the stellar pulsation (paper II). This and the signature of self-absorption in the blue-shifted line component corroborate the presence of a contribution from within the envelope. Although with time the [C II] line profile shown in Fig. 3 varies both in strength and shape, its overall appearance (broad, strongly asymmetric peaks) is persistent.

#### 4. Discussion

The [C I]  $^3\text{P}_1 \rightarrow ^3\text{P}_0$  lines display profiles that are characteristic for optically thin emission from a geometrically extended, expanding envelope. The profiles towards the star, and towards the envelope's limb, could be readily explained by a spatially resolved optically thin shell, whose atomic carbon is produced from the dissociation of CO by the interstellar radiation field: towards the central position, the double-peaked "horn profile" is attributed to the front and rear part of the expanding envelope (the slight asymmetry between the blue- and red-shifted peaks is commented on below), while the single-peaked, flat-topped spectra beyond  $26''$  from the star are dominated by sightline elements of which the expansion velocity vector is mostly parallel to the sky plane. The interstitial positions, however, show that the shell cannot be geometrically thin, thanks to the emission close to the systemic velocity filling the double-horn profile. Indeed, a model consisting of a thin, constant-abundance shell extending from  $10^{17}$  to  $1.6 \times 10^{17}$  cm fits only the central spectrum and that at a  $6.5''$  distance; however, from a  $13''$  to  $39''$  distance, it cannot provide the emission observed close to systemic velocity (Fig. 2). At  $52''$  and beyond, where the shell starts to emit at a zero sightline-projected velocity, that is  $-26.5 \text{ km s}^{-1}$  in local standard of rest (LSR) velocity, the double-peak profile is still too pronounced and strong, while the observed emission starts to fall below the detection limit. Likewise, a thin shell extending from  $1.2 \times 10^{16}$  to  $1.6 \times 10^{16}$  cm, as advocated by Reach et al. (2022) to explain the [C II] observation of *Herschel*/HIFI, fails to reproduce our observations as well (see paper II).

Curiously, the [C II]  $^2\text{P}_{3/2} \rightarrow ^2\text{P}_{1/2}$  line towards the star (Fig. 3) does not show a narrow double-peak profile either (components  $\sim 10 \text{ km s}^{-1}$  wide at a corresponding half-maximum); although in a picture where  $\text{C}^+$  is produced by the exposure to an external radiation field, the line should originate outwards from the [C I] emitting layers. On the other hand,

producing the [C II] emission in a layer adjacent to the stellar photosphere is not easily understandable either, because the beam dilution there would require an unusually high emissivity.

The absence of detectable [C II] emission at a projected distance of  $\geq 20''-30''$  from the star and its presence towards it (Fig. 3) suggest that the environment of the inner shell harbours an additional source of ionisation. As a matter of fact, at a  $700 \text{ AU}$  distance, the star cannot drive any photo-chemistry ( $10^{16}$  cm, Fig. 5). This led Reach et al. (2022) to suggest that mass transfer from the star to a nearby companion locally enhances the UV radiation field, thanks to the shock forming in response to the accretion flow. The presence of such a companion, on a highly eccentric orbit, was indeed advocated by Cernicharo et al. (2015), searching for an explanation for the multiple, partial shells discovered in the optical by light scattering (Mauron & Huggins 1999) and, subsequently, in thermal dust emission (beyond  $1'$  from the star, Decin et al. 2011) and CO emission (Cernicharo et al. 2015; Decin et al. 2015; Guélin et al. 2018). The depth and extent of the CO studies demonstrate that a solar-like companion star would provide an explanation for the multiple shells, which form neither in response to thermal pulses, nor to the stellar pulsation, which would result in larger or shorter spacings, respectively. The binary hypothesis was also adopted by Siebert et al. (2022, further references therein), in support of a photo-chemical model of cyanoacetylene ( $\text{HC}_3\text{N}$ ) emission from the inner envelope, which would explain the presence of other molecules closer to the star than expected ( $\text{CH}_3\text{CN}$ ,  $\text{C}_4\text{H}_2$ ) or typical of O-rich stars ( $\text{H}_2\text{O}$ ). With the data at hand, and the restriction of our models to spherical symmetry, we cannot provide an argument favouring a binary system. We note that Matthews et al. (2018) confirm the proper motion determined for IRC +10216's by Menten et al. (2012) with longer time span data and find no evidence of statistically significant astrometric perturbations as would be expected from a binary companion, despite claims to the contrary. As discussed above, some asymmetry seen in the [C I] profiles is suggestive of a fingerprint of the multiple-shell structure. Given that it is evident in CO (2-1) emission observed at  $11''$  resolution (FWHM, Cernicharo et al. 2015), it should also be discernible in our  $13''$  resolution [C I] data. The Fourier transforms analysis of Guélin et al. (2018) reveals a  $16''$  shell spacing in all quadrants except in the south-eastern one, where our direct line-profile fits display larger residuals. Whether this observation is coincidental or not can only be settled by a full, critically sampled [C I] map.

#### 5. Conclusion

Following the pioneering observations of atomic carbon in IRC +10216 by Keene et al. (1993), we present more sensitive and more extensive observations of the  $^3\text{P}_1 \rightarrow ^3\text{P}_0$  emission from the [C I] fine structure triplet. Accounting for differences in the

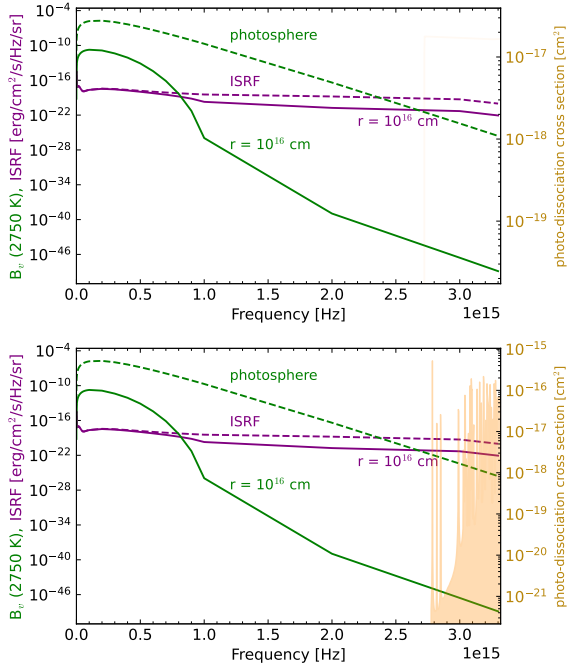


**Fig. 5.** Comparison of cross-sections from the Leiden Observatory database for photochemistry (Heays et al. 2017) for the photo-ionisation of C I and the photo-dissociation of CO (gold curves *top* and *bottom*, respectively, with right-hand ordinates) with SEDs of the attenuated stellar photosphere (green) and the interstellar radiation field (purple) at  $10^{16}$  cm from the star (with left-hand ordinate). The corresponding dotted curves refer to the unattenuated and undiluted radiations fields. Dust extinction coefficients were calculated from Rouleau & Martin (1991). The frequency scale is linear, so as to enhance its high-frequency end.

data quality, and allowing for an underlying variability which might show after the 30 yr time lapse between the observations, we notice an overall good agreement. We present a model employing an abundance gradient that best reproduces the lines profiles at increasing distance from the star; however, even a model employing a constant  $C^0$  abundance would work. We infer that the inner boundary of the [C I]-emitting shell is at  $\sim 10^{16}$  cm from the star, but cannot yet locate it more precisely. The fact that the [C II] line is seen only towards the inner sightlines through the circumstellar envelope ( $\leq 4000$  AU), while the outer envelope, ranging to up to  $\sim 10000$  AU, is void of [C II] emission, remains an enigma. Both findings call for a full map of the [C I] emission and deeper observations of the [C II] line. The line profiles obtained so far from both tracers exclude a picture in which atomic carbon is only produced in a thin low-density shell fully exposed to the interstellar radiation field.

**Acknowledgements.** This publication is based on data acquired with the Atacama Pathfinder EXperiment (APEX). APEX is a collaboration between the Max-Planck-Institut für Radioastronomie, the European Southern Observatory, and the Onsala Space Observatory. The authors thank the anonymous referee for thoughtful comments. M.J. thanks Ankit Rohatgi for making the WebPlotDigitizer tool open source (<https://automeris.io/WebPlotDigitizer/>). M.J. also thanks Ivalu Barlach Christensen for her help in fixing some python scripts. This research has made use of NASA's Astrophysics Data System. This work has also made use of Python libraries including NumPy (<https://www.numpy.org/>) (van der Walt et al. 2011), SciPy (<https://www.scipy.org/>) (Jones et al. 2001), and Matplotlib (<https://matplotlib.org/>) (Hunter 2007).

## References

Agúndez, M., Cernicharo, J., & Guélin, M. 2014, *A&A*, 570, A45  
 Agúndez, M., Martínez, J. I., de Andres, P. L., Cernicharo, J., & Martín-Gago, J. A. 2020, *A&A*, 637, A59

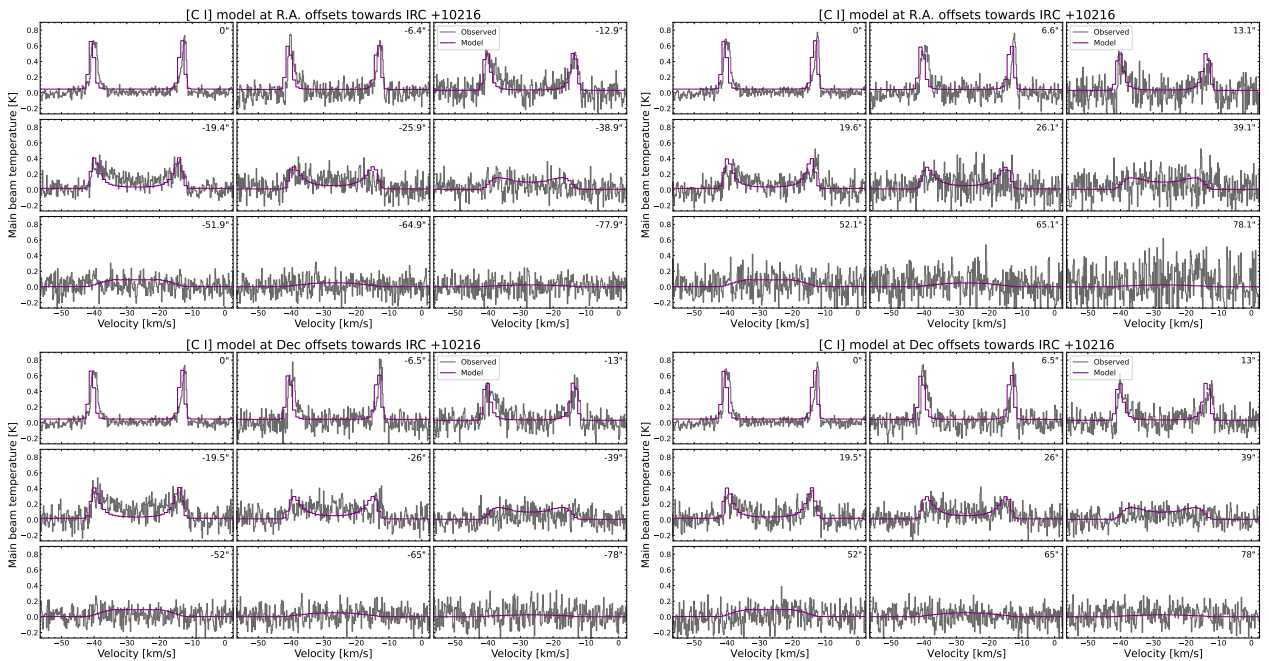
Bujarrabal, V., Castro-Carrizo, A., Alcolea, J., et al. 2016, *A&A*, 593, A92  
 Cernicharo, J., Guélin, M., & Kahane, C. 2000, *A&AS*, 142, 181  
 Cernicharo, J., Marcelino, N., Agúndez, M., & Guélin, M. 2015, *A&A*, 575, A91  
 Cerrigone, L., Menten, K. M., & Kamiński, T. 2012, *A&A*, 542, A15  
 Crosas, M., & Menten, K. M. 1997, *ApJ*, 483, 913  
 Darwent, B. 1970, *Bond Dissociation Energies in Simple Molecules*, NBS NSRDS (United States Department of Commerce)  
 De Beck, E., & Olofsson, H. 2018, *A&A*, 615, A8  
 De Beck, E., Lombaert, R., Agúndez, M., et al. 2012, *A&A*, 539, A108  
 Decin, L., Royer, P., Cox, N. L. J., et al. 2011, *A&A*, 534, A1  
 Decin, L., Richards, A. M. S., Neufeld, D., et al. 2015, *A&A*, 574, A5  
 Dharmawardena, T. E., Kemper, F., Scicluna, P., et al. 2018, *MNRAS*, 479, 536  
 Duthu, A., Herpin, F., Wiesemeyer, H., et al. 2017, *A&A*, 604, A12  
 Fonfría, J. P., DeWitt, C. N., Montiel, E. J., Cernicharo, J., & Richter, M. J. 2022, *ApJ*, 927, L33  
 Glab, W. L., Haris, K., & Kramida, A. 2018, *J. Phys. Commun.*, 2, 055020  
 Groenewegen, M. A. T. 2017, *A&A*, 606, A67  
 Groenewegen, M. A. T., Barlow, M. J., Blommaert, J. A. D. L., et al. 2012, *A&A*, 543, A8  
 Guélin, M., Patel, N. A., Bremer, M., et al. 2018, *A&A*, 610, A4  
 Haris, K., & Kramida, A. 2017, *ApJS*, 233, 16  
 Heays, A. N., Bosman, A. D., & van Dishoeck, E. F. 2017, *A&A*, 602, A105  
 Höfner, S., & Olofsson, H. 2018, *A&ARv*, 26, 1  
 Hogerheijde, M. R., & van der Tak, F. F. S. 2000, *A&A*, 362, 697  
 Hunter, J. D. 2007, *Comput. Sci. Eng.*, 9, 90  
 Jaffe, D. T., Harris, A. I., Silber, M., Genzel, R., & Betz, A. L. 1985, *ApJ*, 290, L59  
 Jentschura, U. D., Kotochigova, S., Le Bigot, E.-O., Mohr, P. J., & Taylor, B. N. 2005, *Phys. Rev. Lett.*, 95, 163003  
 Jones, E., Oliphant, T., Peterson, P., et al. 2001, SciPy: Open source scientific tools for Python  
 Karakas, A. I., & Lattanzio, J. C. 2014, *PASA*, 31, e030  
 Keene, J., Young, K., Phillips, T. G., Buettgenbach, T. H., & Carlstrom, J. E. 1993, *ApJ*, 415, L131  
 Klein, B., Philipp, S. D., Krämer, I., et al. 2006, *A&A*, 454, L29  
 Klein, B., Hochgürtel, S., Krämer, I., et al. 2012, *A&A*, 542, L3  
 Ladjal, D., Barlow, M. J., Groenewegen, M. A. T., et al. 2010, *A&A*, 518, L141  
 Li, X., Millar, T. J., Walsh, C., Heays, A. N., & van Dishoeck, E. F. 2014, *A&A*, 568, A111  
 Mamon, G. A., Glassgold, A. E., & Huggins, P. J. 1988, *ApJ*, 328, 797  
 Martin, D. C., Seibert, M., Neill, J. D., et al. 2007, *Nature*, 448, 780  
 Matthews, L. D., Reid, M. J., Menten, K. M., & Akiyama, K. 2018, *AJ*, 156, 15  
 Maun, N., & Huggins, P. J. 1999, *A&A*, 349, 203  
 McGuire, B. A. 2022, *ApJS*, 259, 30  
 Men'shchikov, A. B., Balega, Y., Blöcker, T., Osterbart, R., & Weigelt, G. 2001, *A&A*, 368, 497  
 Menten, K. M., Reid, M. J., Kamiński, T., & Claussen, M. J. 2012, *A&A*, 543, A73  
 Millar, T. J., & Herbst, E. 1994, *A&A*, 288, 561  
 Millar, T. J., Herbst, E., & Bettens, R. P. A. 2000, *MNRAS*, 316, 195  
 Morris, M., & Jura, M. 1983, *ApJ*, 264, 546  
 Nieva, M. F., & Przybilla, N. 2012, *A&A*, 539, A143  
 Papadopoulos, P. P., Thi, W. F., & Viti, S. 2004, *MNRAS*, 351, 147  
 Pardo, J. R., Cernicharo, J., Tercero, B., et al. 2022, *A&A*, 658, A39  
 Patel, N. A., Young, K. H., Brünken, S., et al. 2009, *ApJ*, 692, 1205  
 Patel, N. A., Young, K. H., Gottlieb, C. A., et al. 2011, *ApJS*, 193, 17  
 Pety, J. 2005, in *SF2A-2005: Semaine de l'Astrophysique Française*, eds. F. Casoli, T. Contini, J. M. Hameury, & L. Pagani, 721  
 Phillips, T. G., Huggins, P. J., Kuiper, T. B. H., & Miller, R. E. 1980, *ApJ*, 238, L103  
 Reach, W. T., Ruaud, M., Wiesemeyer, H., et al. 2022, *ApJ*, 926, 69  
 Richichi, A., Chandrasekhar, T., & Leinert, C. 2003, *New A*, 8, 507  
 Risacher, C., Güsten, R., Stutzki, J., et al. 2018, *J. Astron. Instrum.*, 7, 1840014  
 Rouleau, F., & Martin, P. G. 1991, *ApJ*, 377, 526  
 Saberi, M., Vlemmings, W. H. T., & De Beck, E. 2019, *A&A*, 625, A81  
 Sahai, R., & Chronopoulos, C. K. 2010, *ApJ*, 711, L53  
 Santoro, G., Martínez, L., Lauwaet, K., et al. 2020, *ApJ*, 895, 97  
 Schöier, F. L., & Olofsson, H. 2001, *A&A*, 368, 969  
 Siebert, M. A., Van de Sande, M., Millar, T. J., & Remijan, A. J. 2022, *ApJ*, 941, 90  
 Van de Sande, M., Sundqvist, J. O., Millar, T. J., et al. 2018, *A&A*, 616, A106  
 van der Veen, W. E. C. J., Huggins, P. J., & Matthews, H. E. 1998, *ApJ*, 505, 749  
 van der Walt, S., Colbert, S. C., & Varoquaux, G. 2011, *Comput. Sci. Eng.*, 13, 22  
 Weiss, A., & Ferguson, J. W. 2009, *A&A*, 508, 1343  
 Wolfire, M. G., McKee, C. F., Hollenbach, D., & Tielens, A. G. G. M. 2003, *ApJ*, 587, 278

## Appendix A: Individual results for directly fitted and modelled [C I] line profiles

**Table A.1.** Parameters deduced from direct fits to the observed spectra.

Offset	$V_1$ (km s <sup>-1</sup> )	$\int T_{\text{MB}}dV_1$ (K km s <sup>-1</sup> )	$\Delta V_1$ (km s <sup>-1</sup> )	$T_{\text{peak}1}$ (K)	$V_2$ (km s <sup>-1</sup> )	$\int T_{\text{MB}}dV_2$ (K km s <sup>-1</sup> )	$\Delta V_2$ (km s <sup>-1</sup> )	$T_{\text{peak}2}$ (K)
0''	-40 (0.03)	1.8 (0.04)	2.5 (0.07)	0.67	-12.2 (0.08)	1.3 (0.1)	1.7 (0.2)	0.69
<b>R. A. (negative)</b>								
-6.4''	-39.9 (0.1)	1.5 (0.15)	2.17 (0.2)	0.64	-12.9 (0.05)	1.3 (0.01)	1.9 (0.1)	0.66
-12.9''	-38.8 (0.4)	2.3 (0.3)	5.9 (0.9)	0.36	-13.8 (0.2)	1.4 (0.1)	3.2 (0.4)	0.43
-19.4''	-36.3 (0.3)	2.9 (0.2)	11.2 (0.7)	0.25	-16.2 (0.3)	2.07 (0.1)	8.4 (1)	0.23
-25.9''	-34.5 (1)	2.9 (0.3)	15.6 (2.1)	0.17	-20.3 (1.1)	1.9 (0.3)	12.4 (2.3)	0.15
<b>R. A. (positive)</b>								
6.6''	-39.6 (0.1)	1.67 (0.1)	2.7 (0.2)	0.57	-12.5 (0.1)	1.06 (0.1)	1.35 (0.2)	0.74
13.1''	-38.95 (0.2)	1.15 (0.1)	3.4 (0.3)	0.315	-12.92 (0.2)	0.85 (0.1)	2.19 (0.4)	0.36
19.6''	-36.9 (0.5)	1.97 (0.2)	9.02 (1.2)	0.21	-14.25 (0.5)	1.6 (0.3)	6.6 (1.5)	0.23
26.1''	-34.1 (0.9)	1.8 (0.2)	14.1 (2.1)	0.11	-18.5 (1.4)	1.43 (0.3)	13.2 (2.9)	1.01
<b>Dec (negative)</b>								
-6.5''	-39.6 (0.01)	1.74 (0.1)	2.7 (0.2)	0.6	-12.8 (0.01)	1.39 (0.1)	1.7 (0.2)	0.72
-13''	-38.8 (0.2)	1.95 (0.1)	5.5 (0.6)	0.35	-13.2 (0.1)	1.13 (0.1)	2.3 (0.2)	0.47
-19.5''	-36.6 (0.3)	2.95 (0.2)	10.1 (0.8)	0.27	-17.8 (0.5)	3.05 (0.2)	12.9 (1.1)	0.22
-26''	-32.5 (1.3)	3.02 (0.4)	17.2 (2.8)	0.17	-20.7 (1.4)	2.7 (0.4)	16.9 (2.7)	0.15
<b>Dec (positive)</b>								
6.5''	-39 (0.1)	1.6 (0.1)	2.3 (0.2)	0.6	-12.7 (0.1)	1.2 (0.01)	1.7 (0.1)	0.66
13''	-39.3 (0.3)	1.4 (0.2)	3.3 (0.6)	0.38	-13 (0.1)	1.3 (0.1)	3.0 (0.4)	0.39
19.5''	-37.53 (0.4)	1.83 (0.2)	8.3 (1)	0.21	-14.5 (0.3)	1.14 (0.1)	4.10 (0.7)	0.26
26''	-34.8 (0.8)	1.7 (0.2)	11.0 (1.6)	0.15	-17.4 (0.8)	1.9 (0.2)	11.9 (1.7)	0.15

**Notes.** The table summarises the physical parameters constrained at different offsets from the star. Subset 1 refers to the blue-shifted peak and subset 2 refers to the red-shifted peak. The parameters obtained for offsets away from the central position were calculated by fitting the Gauss method. We note that  $V$  is the LSR velocity,  $\int T_{\text{MB}}dV$  is the calculated integrated intensity,  $\Delta V$  refers to the line width calculated from the Gauss method, and finally  $T_{\text{peak}}$  is the peak temperature of the fitted line.


**Fig. A.1.** Observed [C I] spectra (in black) and line profiles modelled with RATRAN (in purple) at the sampled positions.

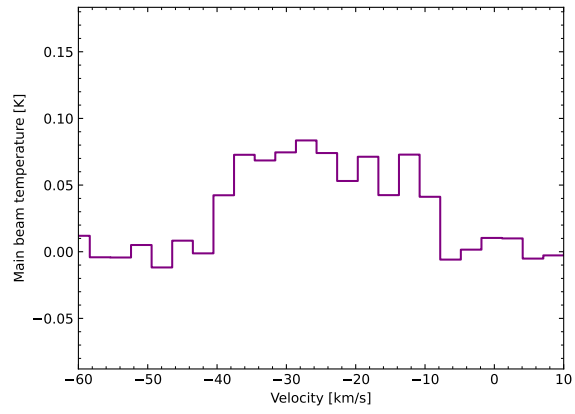


**Fig. A.2.** [C I] emission smoothed to  $3 \text{ km s}^{-1}$  at  $39''$  from the star.

---

## Bibliography

---

- Agúndez, M. et al. (2012), *Molecular abundances in the inner layers of IRC +10216*, [A&A 543, A48 A48](#).
- Agúndez, M. et al. (2014), *New molecules in IRC +10216: confirmation of C<sub>5</sub>S and tentative identification of MgCCH, NCCP, and SiH<sub>3</sub>CN*, [A&A 570, A45 A45](#).
- Appell, P. (1880), *Sur les séries hypergéométriques de deux variables et sur des équations différentielles linéaires aux dérivés partielles.*, French, C. R. Acad. Sci., Paris 90 296, 731, ISSN: 0001-4036.
- Atkins, P. and R. Friedman (2011), *Molecular Quantum Mechanics*, OUP Oxford, ISBN: 9780199541423.
- Aydi, E. and S. Mohamed (2022), *3D models of the circumstellar environments of evolved stars: Formation of multiple spiral structures*, [MNRAS 513 4405](#).
- Baud, B. and H. J. Habing (1983), *The maser strength of OH/IR stars, evolution of mass loss and the creation of a superwind.*, [A&A 127 73](#).
- Becklin, E. E. et al. (1969), *The Unusual Infrared Object IRC+10216*, [ApJL 158 L133](#).
- Belitsky, V. et al. (2018a), *ALMA Band 5 receiver cartridge. Design, performance, and commissioning*, [A&A 611, A98 A98](#).
- Belitsky, V. et al. (2018b), *SEPIA - a new single pixel receiver at the APEX telescope*, [A&A 612, A23 A23](#).
- Bernard-Salas, J. and A. G. G. M. Tielens (2005), *Physical conditions in Photo-Dissociation Regions around Planetary Nebulae*, [A&A 431 523](#).
- Bieging, J. H. et al. (2002), *CO 1st overtone spectra of cool evolved stars: Diagnostics for hydrodynamic atmosphere models*, [A&A 384 965](#).
- Bieging, J. H. (2001), *Discovery of Two New HCN Maser Lines in Five Carbon Stars*, [ApJL 549 L125](#).
- Billade, B. et al. (2012), *Performance of the First ALMA Band 5 Production Cartridge*, [IEEE Transactions on Terahertz Science and Technology 2 208](#).
- Bladh, S. et al. (2019), *An extensive grid of DARWIN models for M-type AGB stars. I. Mass-loss rates and other properties of dust-driven winds*, [A&A 626, A100 A100](#).
- Borexino Collaboration Agostini, M. et al. (2020), *Experimental evidence of neutrinos produced in the CNO fusion cycle in the Sun*, [587 577](#).

- Boyer, M. L. et al. (2015a), *An Infrared Census of DUST in Nearby Galaxies with Spitzer (DUSTiNGS). II. Discovery of Metal-poor Dusty AGB Stars*, [ApJ 800, 51–51](#).
- Boyer, M. L. et al. (2015b), *Identification of a Class of Low-mass Asymptotic Giant Branch Stars Struggling to Become Carbon Stars in the Magellanic Clouds*, [ApJ 810, 116–116](#).
- Brinkmann, N. et al. (2020), *An imaging line survey of OMC-1 to OMC-3-Averaged spectra of template regions*, *Astronomy & Astrophysics* 636 A39.
- Burbidge, E. M. et al. (1957), *Synthesis of the Elements in Stars*, [Reviews of Modern Physics 29 547](#).
- Cannon, C. J. (1985), *The transfer of spectral line radiation*, Cambridge: Cambridge University Press.
- Carter, M. et al. (2012), *The EMIR multi-band mm-wave receiver for the IRAM 30-m telescope*, [A&A 538, A89–A89](#).
- Cernicharo, J. et al. (2000), *A lambda 2 mm molecular line survey of the C-star envelope IRC+10216*, [142–181](#).
- Cernicharo, J. et al. (2011), *Probing the dust formation region in IRC +10216 with the high vibrational states of hydrogen cyanide*, [A&A 529, L3–L3](#).
- Cernicharo, J. et al. (2015a), *Molecular shells in IRC+10216: tracing the mass loss history*, [A&A 575, A91–A91](#).
- Cernicharo, J. et al. (2015b), *Molecular shells in IRC+10216: tracing the mass loss history*, [A&A 575, A91–A91](#).
- Chapman, J. M. and R. J. Cohen (1986), *MERLIN observations of the circumstellar envelope of VX Sagittarius.*, [MNRAS 220 513](#).
- Condon, J. J. and S. M. Ransom (2016), *Essential Radio Astronomy*, Princeton: Princeton University Press.
- Crosas, M. and K. M. Menten (1997), *Physical Parameters of the IRC +10216 Circumstellar Envelope: New Constraints from Submillimeter Observations*, [ApJ 483 913](#).
- Cutri, R. M. et al. (2003), *2MASS All Sky Catalog of point sources*.
- De Beck, E. and H. Olofsson (2018), *Circumstellar environment of the M-type AGB star R Doradus. APEX spectral scan at 159.0-368.5 GHz*, [A&A 615, A8–A8](#).
- De Beck, E. et al. (2010), *Probing the mass-loss history of AGB and red supergiant stars from CO rotational line profiles. II. CO line survey of evolved stars: derivation of mass-loss rate formulae*, [A&A 523, A18–A18](#).
- de Jong, T. (1973), *Water Masers in a Protostellar Gas Cloud*, [A&A 26 297](#).
- de Jong, T. (1983), *OH/IR stars : late stages of evolution of intermediate-mass stars.*, [ApJ 274 252](#).
- Decin, L. et al. (2006), *Probing the mass-loss history of AGB and red supergiant stars from CO rotational line profiles. I. Theoretical model - Mass-loss history unravelled in <ASTROBJ>VY CMa</ASTROBJ>*, [A&A 456 549](#).

- 
- Decin, L. et al. (2011), *Discovery of multiple dust shells beyond 1 arcmin in the circumstellar envelope of IRC +10216 using Herschel/PACS*, [A&A 534, A1 A1](#).
- Decin, L. et al. (2015), *ALMA data suggest the presence of spiral structure in the inner wind of CW Leonis*, [A&A 574, A5 A5](#).
- Decin, L. et al. (2020), *(Sub)stellar companions shape the winds of evolved stars*, [Science 369 1497](#).
- Decin, L. (2021), *Evolution and Mass Loss of Cool Ageing Stars: a Daedalean Story*, [59 337](#).
- Deguchi, S. (2007), “SiO maser survey of evolved stars in the Galaxy: various environments of maser sources”, *Astrophysical Masers and their Environments*, ed. by J. M. Chapman and W. A. Baan, vol. 242 200.
- Desch, S. J. et al. (2023), *Statistical chronometry of meteorites. I. A Test of  $^{26}\text{Al}$  homogeneity and the Pb-Pb age of the solar system’s  $t = 0$* , [402, 115607 115607](#).
- Dharmawardena, T. E. et al. (2018), *Extended Dust Emission from Nearby Evolved Stars*, [MNRAS 479 536](#).
- Downes, D. (1989), “Radio astronomy techniques”, *Evolution of Galaxies Astronomical Observations*, ed. by I. Appenzeller et al., Berlin, Heidelberg: Springer Berlin Heidelberg 351, ISBN: 978-3-540-46194-4.
- Einstein, A. (1917), *Zur Quantentheorie der Strahlung*, *Physikalische Zeitschrift* 18 121.
- Eker, Z. et al. (2018), *Interrelated main-sequence mass-luminosity, mass-radius, and mass-effective temperature relations*, [MNRAS 479 5491](#).
- Eker, Z. et al. (2024), *Fundamentals of Stars: A Critical Look at Mass-Luminosity Relations and Beyond*, [Physics and Astronomy Reports 2 41](#).
- Elitzur, M. et al. (1983), *A multilevel model for astronomical SiO masers*, [ApJ 274 210](#).
- Elitzur, M. (1982), *Physical characteristics of astronomical masers*, [Reviews of Modern Physics 54 1225](#).
- Elitzur, M. (1992), *Astronomical masers.*, [30 75](#).
- Fonfría, J. P. et al. (2018), *The Maser-emitting Structure and Time Variability of the SiS Lines  $J = 14-13$  and  $15-14$  in IRC+10216*, [ApJ 860, 162 162](#).
- Fonfría, J. P. et al. (2022), *Detection of the  $S(1)$  Rotational Line of  $\text{H}_2$  toward IRC+10216: A Simultaneous Measurement of the Mass-loss Rate and CO Abundance*, [ApJL 927, L33 L33](#).
- Fonfría Expósito, J. P. et al. (2006), *High- $J$   $v=0$  SiS Maser Emission in IRC +10216: A New Case of Infrared Overlaps*, [ApJL 646 L127](#).
- Foreman-Mackey, D. et al. (2013), *emcee: The MCMC Hammer*, [125 306](#).
- Freytag, B. and S. Höfner (2023), *Global 3D radiation-hydrodynamical models of AGB stars with dust-driven winds*, [A&A 669, A155 A155](#).

- Gaia Collaboration et al. (2016), *Gaia Data Release 1. Summary of the astrometric, photometric, and survey properties*, [A&A 595, A2 A2](#).
- Gail, H. -. (2003), “Formation and Evolution of Minerals in Accretion Disks and Stellar Outflows”, *Astromineralogy*, ed. by T. K. Henning, vol. 609 55.
- Glassgold, A. E. and P. J. Huggins (1986), *The Ionization Structure of the Circumstellar Envelope of Alpha Orionis*, [ApJ 306 605](#).
- Gong, Y. et al. (2017), *SiS in the Circumstellar Envelope of IRC +10216: Maser and Quasi-thermal Emission*, [ApJ 843, 54 54](#).
- Gottlieb, C. A. et al. (2022), *ATOMIUM: ALMA tracing the origins of molecules in dust forming oxygen rich M-type stars. Motivation, sample, calibration, and initial results*, [A&A 660, A94 A94](#).
- Gray, M. D. et al. (2005), *Evolution of 1612-MHz maser emission in expanding circumstellar shells*, [MNRAS 364 783](#).
- Gray, M. (2012), *Maser Sources in Astrophysics*.
- Greve, A. (2000), “Radio Antennas”, *Proceedings from IRAM Millimeter Interferometry Summer School 2*, ed. by A. Dutrey 1.
- Groenewegen, M. A. T. (1994), *A revised model for circumstellar molecular emission.*, [A&A 290 531](#).
- Groenewegen, M. A. T. and T. de Jong (1998), *CO observations and mass loss of MS- and S-stars*, [A&A 337 797](#).
- Groenewegen, M. A. T. et al. (2012), *An independent distance estimate to CW Leonis*, [A&A 543, L8 L8](#).
- Groenewegen, M. A. T. et al. (2016), *The ALMA detection of CO rotational line emission in AGB stars in the Large Magellanic Cloud*, [A&A 596, A50 A50](#).
- Guélin, M. et al. (2018), *IRC +10 216 in 3D: morphology of a TP-AGB star envelope*, [A&A 610, A4 A4](#).
- Guenther, D. B. (1989), *Age of the Sun*, [ApJ 339 1156](#).
- Guilloteau, S. et al. (1987), *A new strong maser : HCN.*, [A&A 176 L24](#).
- Güsten, R. et al. (2006), *The Atacama Pathfinder EXperiment (APEX) - a new submillimeter facility for southern skies -*, [A&A 454 L13](#).
- Habing, H. and H. Olofsson (2003), *Asymptotic giant branch stars*.
- Hastings, W. K. (1970), *Monte Carlo Sampling Methods using Markov Chains and their Applications*, [Biometrika 57 97](#).
- Henkel, C. et al. (1983), *SiS maser emission from IRC +10216.*, [ApJ 267 184](#).
- Höfner, S. (2008), *Winds of M-type AGB stars driven by micron-sized grains*, [A&A 491 L1](#).
- Höfner, S. and A. C. Andersen (2007), *Winds of M- and S-type AGB stars: an unorthodox suggestion for the driving mechanism*, [A&A 465 L39](#).

- 
- Höfner, S. et al. (2016), *Dynamic atmospheres and winds of cool luminous giants. I. Al<sub>2</sub>O<sub>3</sub> and silicate dust in the close vicinity of M-type AGB stars*, [A&A 594, A108 A108](#).
- Höfner, S. and H. Olofsson (2018), *Mass loss of stars on the asymptotic giant branch. Mechanisms, models and measurements*, [A&AR 26, 1 1](#).
- Hogerheijde, M. R. and F. F. S. van der Tak (2000), *An accelerated Monte Carlo method to solve two-dimensional radiative transfer and molecular excitation. With applications to axisymmetric models of star formation*, [A&A 362 697](#).
- Hubeny, I. (2003), “Accelerated Lambda Iteration: An Overview”, *Stellar Atmosphere Modeling*, ed. by I. Hubeny et al., vol. 288, Astronomical Society of the Pacific Conference Series 17.
- Huggins, P. J. and A. E. Glassgold (1982), *The photochemistry of carbon-rich circumstellar shells.*, [ApJ 252 201](#).
- Humphreys, E. et al. (2024), “(Sub)mm Observations of Evolved Stars”, *Cosmic Masers: Proper Motion Toward the Next-Generation Large Projects*, ed. by T. Hirota et al., vol. 380, IAU Symposium 309.
- Immer, K. et al. (2016), *SEPIA — A New Instrument for the Atacama Pathfinder Experiment (APEX) Telescope*, *The Messenger* 165 13.
- Infrared Astronomical Satellite (IRAS) Catalogs and Atlases. Volume 1: Explanatory Supplement.* (1988), vol. 1.
- Jacob, A. M. et al. (2020), *First detection of <sup>13</sup>CH in the interstellar medium*, [A&A 640, A125 A125](#).
- Jeste, M. et al. (2023), *[C I] and [C II] emission in the circumstellar envelope of IRC +10216. I. Observational data and NLTE modelling of the [C I] emission*, [A&A 675, A139 A139](#).
- Jeste, M. et al. (2022), *Vibrationally excited HCN transitions in circumstellar envelopes of carbon-rich AGB stars*, [A&A 666, A69 A69](#).
- Jorgensen, U. G. (1994), “Dominating Molecules in the Photosphere of Cool Stars”, *IAU Colloq. 146: Molecules in the Stellar Environment*, ed. by U. G. Jorgensen, vol. 428 29.
- Justanont, K. et al. (2012), *Herschel/HIFI observations of O-rich AGB stars: molecular inventory*, [A&A 537, A144 A144](#).
- Kaifu, N. et al. (1975), *Vibrationally excited SiO: a new type of maser source in the millimeter wavelength region.*, [ApJ 195 359](#).
- Karakas, A. and J. C. Lattanzio (2007), *Stellar Models and Yields of Asymptotic Giant Branch Stars*, [24 103](#).
- Karakas, A. I. and J. C. Lattanzio (2014), *The Dawes Review 2: Nucleosynthesis and Stellar Yields of Low- and Intermediate-Mass Single Stars*, [31, e030 e030](#).
- Kastner, J. H. et al. (1993), *Probing the AGB tip : luminous carbon stars in the galactic plane.*, [A&A 275 163](#).
- Keene, J. et al. (1993), *Atomic Carbon in the Envelope of IRC +10216*, [ApJL 415 L131](#).

- Kemper, F. et al. (2003), *Mass loss and rotational CO emission from Asymptotic Giant Branch stars*, [A&A 407 609](#).
- Kerschbaum, F. and H. Olofsson (1999), *Oxygen-rich semiregular and irregular variables. A catalogue of circumstellar CO observations*, [138 299](#).
- Khoury, T. et al. (2014), *The wind of W Hydrae as seen by Herschel. I. The CO envelope*, [A&A 561, A5 A5](#).
- Kippenhahn, R. et al. (2013), *Stellar Structure and Evolution*.
- Klein, T. et al. (2014), *FLASH<sup>†</sup> —A Dual-Channel Wide-Band Spectrometer for APEX*, [IEEE Transactions on Terahertz Science and Technology 4 588](#).
- Knapp, G. R. and M. Morris (1985), *Mass Loss from Evolved Stars. III. Mass Loss Rates for 50 Stars from CO J = 1–0 Observations*, [ApJ 292 640](#).
- Lagadec, E. and A. A. Zijlstra (2008), *The trigger of the asymptotic giant branch superwind: the importance of carbon*, [MNRAS 390 L59](#).
- Lane, A. P. et al. (1987), *H 2O Masers in Circumstellar Envelopes*, [ApJ 323 756](#).
- Langer, W. D. and A. A. Penzias (1990), *12C/ 13C Isotope Ratio across the Galaxy from Observations of 13C 18O in Molecular Clouds*, [ApJ 357 477](#).
- Lewis, B. M. (1989), *The Chronological Sequence of Circumstellar Masers: Identifying Proto-Planetary Nebulae*, [ApJ 338 234](#).
- Loup, C. et al. (1993), *CO and HCN observations of circumstellar envelopes. A catalogue - mass loss rates and distributions.*, 99 291.
- Lucas, R. and J. Cernicharo (1989), *Discovery of strong maser emission from HCN in IRC +10216.*, [A&A 218 L20](#).
- Maercker, M. et al. (2008), *Circumstellar water vapour in M-type AGB stars: radiative transfer models, abundances, and predictions for HIFI*, [A&A 479 779](#).
- Mamon, G. A. et al. (1988), *The Photodissociation of CO in Circumstellar Envelopes*, [ApJ 328 797](#).
- Massalkhi, S. et al. (2018), *Abundance of SiC<sub>2</sub> in carbon star envelopes*, [A&A 611, A29 A29](#).
- Matsuura, M. et al. (2016), *The mass-loss rates of red supergiants at low metallicity: detection of rotational CO emission from two red supergiants in the Large Magellanic Cloud*, [MNRAS 462 2995](#).
- Mauron, N. and P. J. Huggins (1999), *Multiple shells in the circumstellar envelope of IRC+10216*, [A&A 349 203](#).
- McDonald, I. and A. A. Zijlstra (2015), *Globular cluster interstellar media: ionized and ejected by white dwarfs*, [MNRAS 446 2226](#).
- McDonald, I. et al. (2018), *Pulsation-triggered dust production by asymptotic giant branch stars*, [MNRAS 481 4984](#).

- 
- Meledin, D. et al. (2022), *SEPIA345: A 345 GHz dual polarization heterodyne receiver channel for SEPIA at the APEX telescope*, [A&A 668, A2 A2](#).
- Mellau, G. C. (2011), *Complete experimental rovibrational eigenenergies of HCN up to 6880 cm<sup>-1</sup> above the ground state*, [134 234303](#).
- Menten, K. M. et al. (2012), *The size, luminosity, and motion of the extreme carbon star IRC+10216 (CW Leonis)*, [A&A 543, A73 A73](#).
- Menten, K. M. et al. (2018), *Widespread HCN maser emission in carbon-rich evolved stars*, [A&A 613, A49 A49](#).
- Metropolis, N. et al. (1953), *Equation of State Calculations by Fast Computing Machines*, [21 1087](#).
- Moran, J. M. et al. (1979), *VLBI observations of SiO masers at a wavelength of 7 millimeters in late-type stars.*, [ApJL 231 L67](#).
- Morris, M. (1975), *The IRC +10216 molecular envelope.*, [ApJ 197 603](#).
- Neri, R. et al. (1998), *A (12) CO (J=1-> 0) and (J=2-> 1) atlas of circumstellar envelopes of AGB and post-AGB stars*, [130 1](#).
- Neufeld, D. A. and G. J. Melnick (1991), *Excitation of Millimeter and Submillimeter Water Masers*, [ApJ 368 215](#).
- Neufeld, D. A. et al. (2017), *SOFIA/GREAT Discovery of Terahertz Water Masers*, [ApJ 843, 94 94](#).
- Neufeld, D. A. et al. (2021), *Terahertz Water Masers. II. Further SOFIA/GREAT Detections Toward Circumstellar Outflows, and a Multitransition Analysis*, [ApJ 907, 42 42](#).
- Nicolaes, D. et al. (2018), *PACS and SPIRE range spectroscopy of cool, evolved stars*, [A&A 618, A143 A143](#).
- Nyquist, H. (1928), *Thermal Agitation of Electric Charge in Conductors*, [Phys. Rev. 32 \(1\) 110](#).
- Olofsson, H. et al. (1982), *High sensitivity molecular line observations of IRC +10216.*, [A&A 107 128](#).
- Olofsson, H. et al. (1993), *A Study of Circumstellar Envelopes around Bright Carbon Stars. I. Structure, Kinematics, and Mass-Loss Rate*, [ApJS 87 267](#).
- Olofsson, H. et al. (2002), *Mass loss rates of a sample of irregular and semiregular M-type AGB-variables*, [A&A 391 1053](#).
- Olofsson, H. et al. (2017), *First detection of methanol towards a post-AGB object, HD 101584*, [A&A 603, L2 L2](#).
- Olofsson, H. et al. (2022), *CO line observations of OH/IR stars in the inner Galactic Bulge: Characteristics of stars at the tip of the AGB*, [A&A 665, A82 A82](#).
- Olofsson, H. (2004), "Circumstellar Envelopes", *Asymptotic Giant Branch Stars*, ed. by H. J. Habing and H. Olofsson 325.
- Pardo, J. R. et al. (2022), *Ultra-deep 31.0-50.3 GHz spectral survey of IRC+10216*, [A&A 658, A39 A39](#).

- Patel, N. A. et al. (2009), *Submillimeter Narrow Emission Lines from the Inner Envelope of IRC+10216*, [ApJ 692 1205](#).
- Patel, N. A. et al. (2011), *An Interferometric Spectral-line Survey of IRC+10216 in the 345 GHz Band*, [ApJS 193, 17 17](#).
- Pety, J. (2005), “Successes of and Challenges to GILDAS, a State-of-the-Art Radioastronomy Toolkit”, *SF2A-2005: Semaine de l’Astrophysique Francaise*, ed. by F. Casoli et al. 721.
- Ramstedt, S. et al. (2008), *On the reliability of mass-loss-rate estimates for AGB stars*, [A&A 487 645](#).
- Ramstedt, S. et al. (2009), *Circumstellar molecular line emission from S-type AGB stars: mass-loss rates and SiO abundances*, [A&A 499 515](#).
- Ramstedt, S. et al. (2020), *DEATHSTAR: Nearby AGB stars with the Atacama Compact Array. I. CO envelope sizes and asymmetries: A new hope for accurate mass-loss-rate estimates*, [A&A 640, A133 A133](#).
- Rau, G. et al. (2017), *The adventure of carbon stars. Observations and modeling of a set of C-rich AGB stars*, [A&A 600, A92 A92](#).
- Reach, W. T. et al. (2022), *Ionized Carbon around IRC+10216*, [ApJ 926, 69 69](#).
- Rees, N. R. et al. (2024), *Thermal pulses with MESA: resolving the third dredge-up*, [MNRAS 527 9643](#).
- Reid, M. J. et al. (1977), *The structure of stellar hydroxyl masers.*, [ApJ 214 60](#).
- Richards, A. M. S. et al. (2011), *Observational evidence for the shrinking of bright maser spots*, [A&A 525, A56 A56](#).
- Richichi, A. et al. (2003), *Milliarcsecond-resolution observations of IRC +10216*, [8 507](#).
- Riebel, D. et al. (2012), *The Mass-loss Return from Evolved Stars to the Large Magellanic Cloud. VI. Luminosities and Mass-loss Rates on Population Scales*, [ApJ 753, 71 71](#).
- Rybicki, G. B. and D. G. Hummer (1991), *An accelerated lambda iteration method for multilevel radiative transfer. I. Non-overlapping lines with background continuum*, [A&A 245 171](#).
- Rybicki, G. B. and D. G. Hummer (1992), *An accelerated lambda iteration method for multilevel radiative transfer. II. Overlapping transitions with full continuum.*, [A&A 262 209](#).
- Saberi, M. et al. (2019), *Photodissociation of CO in the outflow of evolved stars*, [A&A 625, A81 A81](#).
- Sahai, R. and S. Liechti (1995), *Circumstellar CO emission in S stars. I. Mass-loss with little or no dust.*, [A&A 293 198](#).
- Sahai, R. and C. K. Chronopoulos (2010), *The Astrosphere of the Asymptotic Giant Branch Star IRC+10216*, [ApJL 711 L53](#).
- Sargent, B. A. et al. (2011), *The Mass-loss Return from Evolved Stars to the Large Magellanic Cloud. IV. Construction and Validation of a Grid of Models for Oxygen-rich AGB Stars, Red Supergiants, and Extreme AGB Stars*, [ApJ 728, 93 93](#).

- 
- Schilke, P. and K. M. Menten (2003), *Detection of a Second, Strong Submillimeter HCN Laser Line toward Carbon Stars*, [ApJ 583 446](#).
- Schilke, P. et al. (2000), *A Submillimeter HCN Laser in IRC +10216*, [ApJL 528 L37](#).
- Schöier, F. L. and H. Olofsson (2001), *Models of circumstellar molecular radio line emission. Mass loss rates for a sample of bright carbon stars*, [A&A 368 969](#).
- Schöier, F. L. et al. (2007), *The Distribution of  $H^{13}CN$  in the Circumstellar Envelope around IRC+10216*, [ApJ 670 766](#).
- Scicluna, P. et al. (2022), *The Nearby Evolved Stars Survey II: Constructing a volume-limited sample and first results from the James Clerk Maxwell Telescope*, [MNRAS 512 1091](#).
- Serenelli, A. et al. (2021), *Weighing stars from birth to death: mass determination methods across the HRD*, [A&AR 29, 4 4](#).
- Shinnaga, H. et al. (2009), *IRC+10216'S Innermost Envelope—The eSMA'S View*, [ApJ 698 1924](#).
- Siebert, M. A. et al. (2022), *Investigating Anomalous Photochemistry in the Inner Wind of IRC+10216 through Interferometric Observations of  $HC_3N$* , [ApJ 941, 90 90](#).
- Snyder, L. E. and D. Buhl (1971), *Observations of Radio Emission from Interstellar Hydrogen Cyanide*, [ApJL 163 L47](#).
- Solomon, P. et al. (1971), *Observation of CO Emission at 2.6 Millimeters from IRC+10216*, [ApJL 163 L53](#).
- Soria-Ruiz, R. (2006), *Estudio de máseres circunestelares de monóxido de silicio con muy alta resolución espacial* *Estudio de máseres circunestelares de monóxido de silicio con muy alta resolución espacial* *Study of circumstellar silicon monoxide masers with very high spatial resolution*; PhD thesis: Spanish National Observatory, Madrid.
- Speagle, J. S. (2019), *A Conceptual Introduction to Markov Chain Monte Carlo Methods*, [arXiv e-prints, arXiv:1909.12313 arXiv:1909.12313](#).
- Srinivasan, S. et al. (2011), *The mass-loss return from evolved stars to the Large Magellanic Cloud. V. The GRAMS carbon-star model grid*, [A&A 532, A54 A54](#).
- Srinivasan, S. et al. (2016), *The evolved-star dust budget of the Small Magellanic Cloud: the critical role of a few key players*, [MNRAS 457 2814](#).
- Teyssier, D. et al. (2006), *CO line emission from circumstellar envelopes*, [A&A 450 167](#).
- Uttenthaler, S. et al. (2019), *Interplay between pulsation, mass loss, and third dredge-up: More about Miras with and without technetium*, [A&A 622, A120 A120](#).
- van der Veen, W. E. C. J. et al. (1998), *Atomic Carbon in the Circumstellar Envelopes of Evolved Stars*, [ApJ 505 749](#).
- van Leeuwen, F. (2007), *Validation of the new Hipparcos reduction*, [A&A 474 653](#).
- Vassiliadis, E. and P. R. Wood (1993), *Evolution of Low- and Intermediate-Mass Stars to the End of the Asymptotic Giant Branch with Mass Loss*, [ApJ 413 641](#).

## Bibliography

---

- Vlemmings, W. H. T. et al. (2003), *VLBI astrometry of circumstellar OH masers: Proper motions and parallaxes of four AGB stars*, [A&A 407 213](#).
- Weaver, H. et al. (1965), *Observations of a Strong Unidentified Microwave Line and of Emission from the OH Molecule*, [208 29](#).
- Wilson, R. W. et al. (1970), *Carbon Monoxide in the Orion Nebula*, [ApJL 161 L43](#).
- Wilson, T. L. et al. (2013), *Tools of Radio Astronomy*.
- Winters, J. M. et al. (2000), *Circumstellar dust shells around long-period variables. VIII. CO infrared line profiles from dynamical models for C-stars*, [A&A 359 651](#).
- Woitke, P. (2006), *Too little radiation pressure on dust in the winds of oxygen-rich AGB stars*, [A&A 460 L9](#).
- Wong, K. T. (2019), “HCN laser lines in carbon-rich evolved stars”, *ALMA2019: Science Results and Cross-Facility Synergies* 55 55.
- Young, K. (1997), *Neutral Carbon in the Protoplanetary Nebulae CRL 618 and CRL 2688*, [ApJL 488 L157](#).
- Ziurys, L. M. and B. E. Turner (1986), *Detection of Interstellar Vibrationally Excited HCN*, [ApJL 300 L19](#).
- Zuckerman, B. (1980), *Envelopes around late-type giant stars*, [18 263](#).
- Zuckerman, B. and H. M. Dyck (1986a), *Carbon Monoxide Emission from Stars in the IRAS and Revised AFGL Catalogs. I. Mass Loss Driven by Radiation Pressure on Dust Grains*, [ApJ 304 394](#).
- Zuckerman, B. and H. M. Dyck (1986b), *Dust Grains and Gas in the Circumstellar Envelopes around Luminous Red-Giant Stars*, [ApJ 311 345](#).
- Zuckerman, B. and H. M. Dyck (1989), *Outflow velocities from carbon stars.*, [A&A 209 119](#).
- Zuckerman, B. et al. (1986), *Carbon Monoxide Emission from Stars in the IRAS and Revised AFGL Catalogs. II. Massive Carbon Stars*, [ApJ 304 401](#).

---

# List of Figures

---

1.1	A simplified Hertzsprung-Russell (HR) diagram with surface temperature (in Kelvin) on the X-axis and luminosity (in solar units) on the Y-axis. Credit: Western Washington University ( <a href="https://astro101.wwu.edu/a101_hrdiagram.html">https://astro101.wwu.edu/a101_hrdiagram.html</a> ). . . . .	3
1.2	A sketch presenting a simplified version of the HR diagram. The figure shows the evolutionary path for a solar-mass star marked with its important phases. The Sun's current position is also illustrated on the HR diagram as a reference (Created based on <a href="https://www.astro.uu.se/deathstar/agb_stars.html">https://www.astro.uu.se/deathstar/agb_stars.html</a> ). . . . .	4
1.3	A schematic diagram of an AGB star and the composition of its CSE (Created based on Soria-Ruiz 2006; Höfner and Olofsson 2018). . . . .	8
1.4	Line area brightness distributions of $^{12}\text{CO}$ (1–0) ( <i>top</i> ) and $^{13}\text{CO}$ (1–0) ( <i>bottom</i> ) lines from the ALMA and IRAM-30m data (Credit: Guélin et al. 2018). . . . .	9
1.5	The figure presents the transmission through the earth's atmosphere for the electromagnetic radiation (Image from Wilson et al., 2013). . . . .	11
1.6	<i>Left:</i> A sketch of a single dish Cassegrain radio telescope. (Image created from Greve, 2000). <i>Right:</i> The figure represents the antenna power pattern with the main lobe and side lobes, along with the stray pattern generated due to non-uniformities of the dish. (Image is taken from Wilson et al., 2013). . . . .	12
1.7	APEX telescope at the Llano de Chajnantor in Chile. . . . .	15
1.8	The IRAM 30-m telescope in the Spanish Sierra Nevada (Credit: IRAM/ K. Zacher). . . . .	16
1.9	The JCMT telescope close to Mauna Kea, Hawai'i, USA (Credit: EAO observatory/ William Montgomerie). . . . .	16
1.10	The Onsala 20 m telescope (Credit: Chalmers/ J-O Yxell). . . . .	17
1.11	SOFIA with its telescope door open during a test flight (Credit: NASA/ Jim Ross). . . . .	17
1.12	The SEST telescope at La Silla, Chile (Credit: F. Kerschbaum/ ESO). . . . .	17
1.13	<i>Top:</i> Measurement of specific intensity. <i>Bottom:</i> Radiative transfer arrangement, here opacity refers to the optical depth ( $\tau$ ). Credit: Adapted from figures from Condon and Ransom (2016). . . . .	18
1.14	Energy diagram of the HCN molecule from Jeste et al. (2022) showing the rotational transitions, arising from vibrational states indicated by $J$ and $\nu$ , respectively. The splitting of every rotational level into two sub-levels, $1e$ and $1f$ , caused by the $l$ -type doubling is also indicated in the figure above. We also show the $J = 2-1$ ( $0, 1^{1e}, 0$ ) and $J = 2-1$ ( $0, 1^{1f}, 0$ ) transitions marked with blue and purple arrows, respectively. Cyan arrows denote the pumping photons from the ground state to highly vibrational excited states. Red arrows indicate the direct $l$ -type transitions. It is important to note that the separations of the $l$ -type transitions are not drawn to scale. . . . .	24
1.15	Abundances of CO, C, and $\text{C}^+$ in the outer envelope of IRC +10216 from the model presented in Reach et al. (2022). . . . .	26
1.16	Simple three-level maser. For clarity, only selected pathways for pumping and losses are shown and indicated by the arrows labelled with $P_3$ and $\Gamma_1 N_1$ respectively. Further details are mentioned in the text. . . . .	27

2.1	<i>Left</i> : Rotation diagram of IRC +10216 using vibrationally excited HCN lines. Some masers are plotted in the diagram for viewing purposes, shown by triangles, but are excluded from the linear least-square fit. <i>Right</i> : Temporal variations in the $J = 2-1$ ( $0, 1^{1e}, 0$ ) line in IRC +10216. The spectrum in black shows observations from 2018, cyan from 2021, red from 2015 (Menten et al., 2018), and blue from 1989 (Lucas and Cernicharo, 1989). Figures are taken from Jeste et al. (2022). . . . .	36
3.1	Cross-sections (right ordinates) for the photo-ionisation of C I and the photo-dissociation of CO, shown in <i>gold</i> (left and right figure, respectively). The solid <i>green</i> and <i>purple</i> lines show the SEDs (with left ordinates) of the attenuated stellar photosphere and ISRF respectively. The corresponding dashed lines are the unattenuated and undiluted radiation fields. The X-axis refers to the linear frequency scale. Figures are taken from Jeste et al. (2023). . . . .	39
3.2	$^3P_1 \rightarrow ^3P_0$ emission of [C I] towards 9 offsets from the star ( <i>in purple</i> ), overlaid with modelled profiles with constant abundance ( <i>in orange</i> ) and variable abundance ( <i>in green</i> ). Figure from Jeste et al. (2023). . . . .	41
4.1	<i>left</i> : Total sky coverage of the NESS sample and <i>right</i> : NESS sample in the distance and DPR space. Tiers 0 to 4 are shown in purple, blue, orange, green, and red, respectively. Images taken from Scicluna et al. (2022). . . . .	45
5.1	Sub-sample distribution (this work, in purple) overplotted on the complete sample of NESS. . . . .	50
5.2	Sketch (in projection, viewed from above the sightline) of a circumstellar envelope of outer radius $R$ , expanding at velocity $v_\infty$ . The emission at a given velocity $v_z$ originates from the surface of a cone with half opening angle $\alpha = a \cos \frac{v_z}{v_\infty}$ (hatched area). . . . .	53
5.3	Line profile of optically thin emission from a circumstellar envelope expanding at a constant speed ( $v_\infty$ ), normalised to unity at maximum, for a signal-to-noise ratio of 50 at peak, for (a) a spatially unresolved observation, and (b) $\theta = 0.6 R/D$ (from Eq. (5.6)), with an overlaid fit (green line profile) of the form $F_\nu(v) = a/(1-v^2)^{0.5}$ . . . . .	54
5.4	Optically thick emission ( $\tau_{R,0} = 4$ ) as observed in a beam of width $\theta = 2R$ (FWHM), for a signal-to-noise ratio of 50 at peak. The green line is a soft-parabola with $\beta = 1.7$ (from least-square fitting). . . . .	55
5.5	$^{12}\text{CO}$ (3–2) (left) and $^{13}\text{CO}$ (3–2) (centre) emission towards 18595-3947 (RAFGL 5552) observed with the APEX telescope. $^{13}\text{CO}$ (1–0) (right) emission towards RAFGL 712 observed with the IRAM-30m telescope. . . . .	57
5.6	<i>Left</i> : Histogram showing the distribution of $\log_{10}(^{12}\text{CO}/^{13}\text{CO})$ ratio for APEX observations. <i>Right</i> : $^{12}\text{CO}/^{13}\text{CO}$ ratio for IRAM observations . . . . .	58
5.7	(From left to right:) $\beta$ parameters for APEX, IRAM, SEST and OSO observations. . . . .	58
5.8	(Clockwise from top left:) MLR vs. expansion speed for APEX, IRAM, SEST/OSO, and JCMT observations. The latter are shown for completeness and discussed in Wallström et al. (in prep.). . . . .	60
5.9	Histograms showing the distribution of MLRs (figure on the <i>left</i> ), where blue indicates O-rich stars and grey indicates C-rich stars and (figure on the <i>right</i> ) expansion velocities segregated based on their chemical types. . . . .	61
5.10	MLR vs. expansion velocities. The errorbars for CO (3–2) are not plotted for clarity. For CO (2–1), which offers the largest sample, the double-logarithmic linear regression is overlaid for the whole sample, the oxygen-rich sub-sample, and the synthetic Darwin sample from Bladh et al. (2019). . . . .	63
5.11	DPR vs. MLR. In CO (3–2), MLR values with missing errorbars are to be considered upper limits (errorbars suppressed for clarity). For CO (2–1), which offers the largest sample, the double-logarithmic linear regression is overlaid for the whole sample (in black) and for the oxygen-rich sub-sample (in red). . . . .	64

5.12 Power-law exponent for expressing the dust-production rate through the mass-loss rate, as a function of the lower MLR cutoff. CO transitions are labelled by different colours, for the whole sample (filled circles) and for the oxygen-rich sample (filled triangles). . . . . 65

6.1 Integrated intensity map of IRC+10216 in CO (6–5) line emission observed with the APEX telescope. The contour levels are drawn at 5% intervals of peak emission. . . . . 70



---

## List of Tables

---

3.1	Input parameters for the RATRAN model of the [C I] emission . . . . .	39
5.1	Receiver setups for observations with APEX, IRAM-30m, OSO, and SEST telescopes. . . . .	51
5.2	Table describing line shape parameters for cases with different optical depths and spatial resolution of the source. . . . .	55
5.3	Correlation coefficients (Pearson $r$ ), false-alarm probabilities (Pearson $p$ ), and sample sizes for the double-logarithmic regression analysis of MLR vs. $\nu_\infty$ , and of DPR vs. MLR. . . . .	66
A.1	Results of the soft-parabola fitting. Errors are estimated with a Markov-Chain Monte Carlo method. For details and reference see text. . . . .	72



---

# Acknowledgements

---

As the PhD journey draws to a close, I would like to express my gratitude toward my mentors, colleagues, friends, and family who have helped and encouraged me along the way.

I would like to start with Prof. Dr. Karl Menten, who welcomed me into the sub-mm group many years ago as a master's student. Since that day, he has been very encouraging and excited for me to work on evolved stars, which has always kept me motivated. Thank you for providing me with an opportunity to work in this field, for the innovative ideas, and for the encouragement to participate in meetings and conferences even though I felt out-of-depth in the beginning. I have learned a lot from you and have always appreciated that you were only an email away whenever there were difficulties.

I also thank Prof. Dr. Pavel Kroupa for agreeing to be my second supervisor. I would also like to thank Prof. Akaki Rusetsky and Prof. Heiko Röglin for being part of my thesis committee.

I am deeply grateful to Dr. Helmut Wiesemeyer for his guidance in recent projects aiding me in understanding the radiative transfer modelling and analysis through our discussions. Thank you also for carefully reading the thesis and the manuscripts and providing your valuable suggestions.

Dr. Yan Gong and Dr. Ka Tat Wong have been guiding me since before my PhD and I want to express my many thanks to them for their support and encouragement. I have honed my proposal writing skills and fundamentals of single-dish and interferometry data reduction through your highly useful inputs and comments.

I would also like to mention my thanks to Dr. Peter Scicluna and Dr. Sofia Wallström for welcoming me into the NESS collaboration. I have enjoyed my time working on the project and have learned many new skills on the way through our many discussions.

I would like to thank Dr. Friedrich Wyrowski for the discussions regarding observations of AGB stars and constructive comments on the manuscripts, which have helped to make them better. I would also like to thank Dr. Arnaud Belloche for guiding me with observations at APEX and for making sure I felt welcomed at the base camp.

I want to thank Dr. Dirk Muders for always being available to solve any computer/IT problems so kindly and with the utmost patience. My time at the MPIfR would not have been possible without the help from Eva, Frau Tran, and Frau Menten for meticulous work and help with understanding the documents.

I would not have been here submitting the thesis without the encouragement and support of my friends and family that I have received along the way.

My sub-mm friends (past and current; in no particular order): Ivalu (fellow HP fan), Laure, Hans (aka the macaron friend), Rohit, Nina, Dat, Shampa, Niki, Maitraiye, Arshia, and many others; lunching and hanging out with you have made me aware of very vast (and questionable?) topics. Thank you for making the PhD journey in MPIfR more memorable. Ivana, I am so glad that you contacted me to be roommates in Granada because I now have gained such a caring friend. Thank you for being a cheerleader even when you are not in Bonn. I hope we 'meet up next week' with Dat! Laure, I very much appreciate our time in Bonn, especially during the pandemic. I enjoyed our Tuesday breakfasts (with the tasty pain au chocolat) in the week and wine nights on the weekends!

## Acknowledgements

---

I want to thank Jan Luca, without whose encouragement and trust I would not have started this PhD journey. I am deeply grateful for the unwavering support I received from you and your family during my time in Bonn, which made everything happier these past many years.

I would also like to thank two of my first Bonn friends, Vyoma and Devina, for the movie nights and spontaneous support texts during this journey, leaving me with a sense of camaraderie.

I want to mention my thanks to the close friends who have been there to get me to the finish line. Arunabh, you have been the oldest friend I have had in Bonn, and since day one, you have been a person full of positivity and support during these years. I want to thank you for being there, especially these past months, and for sharing your positive attitude. Whenever I was low on motivation, you made sure there was a plan to achieve the goals with enthusiasm and excitement, which is something that I will always cherish. I also want to thank Sonia for the late-night walks in Endenich, which left me feeling lighter. You have been a good listener and I hope I have been able to do the same for you. Ivalu, I know I can't deny it anymore but you're kind of funny (though I will roll my eyes if you mention this again). Your jokes and witty remarks have left me with belly-laugh, wheezing-laugh, snorting-laugh, and well, all kinds of laughs. Thank you for being like this, it has certainly made me giggle a lot more.

And most important of all, I am deeply grateful to my parents and family for being there through my journey. This accomplishment is possible only because of the unconditional love and support I receive from you. I am lucky to have you as my constant source of motivation, inspiration, and encouragement which has helped me immensely, and will continue to do so in whatever path I choose.